CHARACTERISATION OF SUB-RADIANT MODES OF METASURFACES

by

Panji Achmari

ORCID ID: orcid.org/0000-0002-7934-5380

A thesis submitted in total fulfillment for the requirements of
Master of Philosophy

November 2016

School of Physics

The University of Melbourne

Abstract

Metallic nanostructures can be utilised as optical antennas: devices to assist the conversion between localised (near-field) and propagating (far-field) light. Optical antennas possess sub-radiant modes which cannot be easily coupled to propagating fields and have the advantages of longer life-times and higher Q resonances. This project has involved the computational and experimental investigation of the properties of sub-radiant modes of various nanoantennas that form the basis of a metasurface. These modes were found to be excited by off-normally incident light with a specific polarisation or vector beams with radial or azimuthal polarisation. It was also shown through studies of the optical far-field that the angular spectrum of the reflected fields was modified through interaction via a sub-radiant mode.

Declaration

(i) This thesis comprises only the original work by the author towards the Master of Philosophy candidature except where indicated in the preface and in the text.

(ii) Acknowledgements to previous work by other people have been made in the text to all materials used.

(iii) This thesis contains fewer than the 50,000 words in length, exclusive of tables, bibliographies, and appendices.

Preface

This thesis was submitted as a requirement for the degree of Master of Philosophy (M.Phil) in School of Physics, Faculty of Science, The University of Melbourne. The research activities behind this thesis were performed under the supervision of Prof. Ann Roberts.

This thesis contains unpublished original work by the author except where acknowledgments and references are made to previous work. Contributors to this project were Dr. Timothy James who helped with the sample fabrication of the metasurfaces designed by the author, and Dr. Timothy Davis who helped providing suggestions in using the electrostatic eigenmode method (EEM).

The M.Phil candidature of the author was supported by the scholarships from The University of Melbourne in the form of Melbourne International Fee Remission Scholarships (MIFRS) and Melbourne International Research Scholarships (MIRS).

Acknowledgements

I would like to express my sincere gratitude to my supervisor, Prof Ann Roberts, for her continuous support and guidance throughout my candidature. Her invaluable encouragements were crucial in nurturing me as a young researcher. I have developed my knowledge and skills in research, particularly in optics, under her supervision.

I would like to acknowledge Dr. Timothy James and Dr. Timothy Davis for all helpful discussions about the work presented in this thesis. I would also like to thank Prof. Robert Scholten as the chair of my advisory committee, and Dr. Brett Johnson who lent me an important optical equipment. I would also like to thank Prof. Raymond Volkas and Prof. Stuart Wyithe as former and current Head of School, all people in School of Physics, and people in The University of Melbourne, who provided pleasant academic environment.

I would like to thank my colleagues, Stuart Earl, Kalpana Singh, Jasper Cadusch, Evgeniy Panchenko, and Jasmine Hughes, for all the discussions, suggestions, and encouragements during my years of study and beyond.

Special thanks to my beloved wife, Leni Indah Sri Fitri Yani, and son, Senandika Aidan Achmari, who were always supporting me throughout my candidature. I would also like to thank my parents, Budi Yuwono and Yuyun Yunarsih, father-in-law, Sujari Suprapto, and relatives who has supported me this far. Big thanks to everyone who I could not mention one by one, who helped me through anything in making this work possible.

All praise is due to God, Lord of the worlds. Without His permission, this work would never have taken place.

Contents

Abstract ii

Declaration iii

Preface iv

Acknowledgements v

Contents vi

List of Figures x

List of Tables xxvi

1 Introduction 1

1.1 Metallic Nanostructures for Manipulating and Sensing Light . . 1

1.2 Optical Antennas and Metasurfaces 3

1.2.1 Optical Antennas 3

1.2.2 Metasurfaces 5

1.3 An Overview of the Thesis 6

2 Optical Antennas and Metasurfaces: Background 10

2.1 Metasurfaces 10

2.1.1 Examples of Metasurfaces 11

2.2 Metals at Optical Frequencies 14

2.2.1 Surface Plasmon Polaritons 15

2.2.2 Localised Surface Plasmons 17

2.3 Optical Antennas 18

2.3.1 Basic Theory of Optical Antennas 18

2.3.2 Examples of Optical Antennas 19

2.3.3 Modes of Optical Antennas 22

2.4 Chapter Conclusion 27

3 Methods for Modelling Optical Antennas and Metasurfaces 29

3.1 Methods for Solving Electromagnetic Problems 29

3.2 The Finite-Difference Time-Domain (FDTD) Method 31

3.2.1 Implementation of Maxwell's Equations in the FDTD Method 33

3.2.2 Boundary Conditions 35

3.2.3 The Plane Wave Source 38

3.2.4 Modelling the Optical Properties of Metals 39

3.2.5 Simulations in Lumerical FDTD Solutions 41

3.3 The Electrostatic Eigenmode Method (EEM) 44

3.3.1 EEM Formulation 45

3.3.2 Implementing the EEM for Nanorod Trimer and Tetramer Antennas 49

3.3.3 Scattering from Periodic Arrays of Metal Nanostructures 50

3.4 Plane Waves and Optical Beams for Excitation of the Metasurfaces 52

3.4.1 Plane Wave Illumination 52

3.4.2 The Vector Beam Illumination 53

3.4.3 Focussed Beam Illumination 55

3.5 Chapter Conclusion 57

4 Modelling and Investigating Metasurface Resonances 59

4.1 Optical Antenna Designs and Strategies for Exciting Sub-radiant Modes 59

4.2 Modelling with The Finite-Difference Time-Domain Method . . 62

4.2.1 Preliminary Modelling 64

4.2.2 Corner Rounding Effects 67

4.2.3 Modelling Results 71

4.3 Modelling with The Electrostatic Eigenmode Method (EEM) . . 83

4.3.1 Scattering from Metasurfaces Composed of Radial Antennas 87

4.3.2 Scattering from Metasurfaces Composed of Azimuthal Antennas 98

4.3.3 Scattering from Metasurfaces at Resonances 106

4.4 Chapter Conclusion 110

5 Experimental Characterisation of Metasurfaces 113

5.1 Fabrication of Metasurfaces 113

5.1.1 Electron Beam Lithography 114

5.1.2 Fabricated Samples 115

5.2 Experimental Characterisation 118

5.3 Transmission and Reflection Spectra 124

5.3.1 Radial Trimer Metasurfaces 125

5.3.2 Radial Tetramer Metasurfaces 140

5.3.3 Azimuthal Trimer Metasurfaces 149

5.3.4 Azimuthal Tetramer Metasurfaces 154

5.4 Fourier Plane (Far-Field) Images of Reflected Beams at Resonances 158

5.5 Chapter Conclusion 172

6 Conclusion **174**

Bibliography **177**

A The Experimental Data of Transmission and Reflection Spectra **A-2**

A.1 Transmission Spectra A-2

A.2 Reflection Spectra A-22

B Far-Field Images of the Reflected Beams from the Metasurfaces **A-39**

B.1 Beam Profiles at Resonances of Radial and Dipole Modes A-39

B.2 Beam Profiles at Various Wavelengths A-53

List of Figures

1.1 Optical antennas designs: (a) radial trimer, (b) radial tetramer, (c) azimuthal trimer, and (d) azimuthal tetramer. 7

2.1 The metasurface made of nanoholes with spatially variation of geometry acts as a hologram producing two different patterns at two different wavelengths [32]. 12

2.2 A metasurface-based device for converting circularly polarised beam into azimuthally polarised beam [34]. 13

2.3 Plasmonic circuits consisting of metal nanorods to sense phase difference of the incident fields. 13

2.4 Complex refractive index of gold, silver, and copper as a function of photon energy [42]. 15

2.5 The schematic showing surface plasmon excitation at metal/ dielectric boundaries, using prism coupling [8]. 16

2.6 The dispersion relation of surface plasmons at silver/air and silver/silica interfaces [8]. 16

2.7 The influence of particle shape and size on the surface plasmon resonance of (a) silver [46] and (b) gold nanoparticles. [47]. . . . 17

2.8 Scheme of optical antenna for the enhancement of (a) transmission process and (b) receiving process. 19

2.9 The scattering intensity of single gold and silver nanospheres measured by dark-field microscopy and fitted with theoretically Lorentzian shape. 20

2.10 The scattering spectra and field profiles at resonances of a single nanocube with variation of its position to the dielectric substrate. 20

2.11 Two silver spheroids acts as a dimer antenna to enhance the emission of quantum dot placed in the gap. 21

2.12 A schematic, spectrum, and intensity profiles of the cross optical antenna made of four tipped-end nanorods 22

2.13 A nanogap for enhancing the emission rate of emitting material placed in the gap [60]. 22

2.14 The excitation of (a) bright and (b) dark modes in two identical cylindrical particles [63]. 23

2.15 The excitation of bright and dark modes in two gold octahedra using prism coupling [64]. 24

2.16 The excitation of bright and dark modes using asymmetric nanorods with different lengths [20]. 25

2.17 All possible modes are on silver nanodisk trimer [65]. 25

2.18 Nanostructures consisting of six symmetrically arranged gold nanodisks. 26

2.19 Hybridization for gold nanostructure consisting of a disk inside a thin ring. 26

2.20 The radially arranged nanorod trimer is excited with radially polarised light. Some results may arise for different modes of the excited state [21]. 27

2.21 Heptamer antenna structure is excited with (a) azimuthally and (b) radially polarised light [68]. 27

2.22 The higher-order Fano resonances at spherical metal nanoparticle in its radar back scattering and forward scattering [69]. 28

3.1 The PML on 2D xy-slice at $z = 0$ inside the simulation region [75]. 36

3.2 Example of periodic BCs implementation where the structures are periodic along x directions with normally incident fields. . . 37

3.3 The simulation using TFSF boundaries. 39

3.4 The scheme for injecting plane wave source into the simulation using TFSF boundaries. 40

3.5 Three dimensional view of simulation set-up in Lumerical FDTD Solutions. 41

3.6 The two dimensional slice of the simulation set-up. 42

3.7 Structures under study: (a) radial trimer, (b) radial tetramer, (c) azimuthal trimer, and (d) azimuthal tetramer, to be solved by EEM. 49

3.8 The schematic for (a) p-polarised and (b) s-polarised plane waves. 53

3.9 The schematic for (a) linearly, (b) radially, and (c) azimuthally polarised beams [93]. 54

3.10 Schematic showing polarisation changes in a focussed beam. . . 56

3.11 The local distribution of polarisation of focussed beams with (a) linearly, (b) radially, and (c) azimuthally polarisation. 57

4.1 Designs of optical antennas as the basis of metasurfaces supporting radial and azimuthal modes with symmetric radial and azimuthal arrangements. 60

4.2 The length L, width w, and height h of a single nanorod. 60

4.3 The dominant mode in a single nanorod is the dipole mode parallel to its long axis. 60

4.4 The surface charge distribution of *radial modes* of radially-arranged (a) trimer and (b) tetramer optical antennas. 61

4.5 The surface charge distribution of *azimuthal modes* of azimuthally-arranged (a) trimer and (b) tetramer optical antennas. 61

4.6 The surface charge distribution of sub-radiant modes of tetramer antennas other than the radial or azimuthal modes. 62

4.7 The surface charge distribution of radiant modes of optical antennas of radial trimer, radial tetramer, azimuthal trimer, and azimuthal tetramer. 62

4.8 A schematic for an incident plane wave at an angle θ with respect to the normal and the plane of incidence at an angle ϕ with respect to the x-axis. 63

4.9 The scattering spectra from a radial trimer, simulated using the 'home-made' FDTD. 65

4.10 The scattering spectra from an azimuthal trimer, simulated using the 'home-made' FDTD. 65

4.11 Comparison of spectra of a single radial trimer between that simulated using the 'home-made' FDTD and that simulated using LFS. 67

4.12 Comparison of (a) transmission through and (b) reflection from an array of periodic radial trimers between results simulated using the 'home-made' FDTD and LFS. 68

4.13 The schematic for corner rounding of the nanorod in FDTD modelling. 69

4.14 The (a) transmission through and (b) reflection from an array of silver nanorods with sharp and rounded corners, illuminated with a normally incident plane wave. 69

4.15 The (a) transmission through and (b) reflection from an array of radial trimer antennas for the sharp and rounded corner nanorods, illuminated with a normally incident plane wave. 70

4.16 The (a) transmission through and (b) reflection from an array of radial trimer antennas with an off-normally incident at an angle of 20°, p-polarised plane wave. 71

4.17 The (a) transmission through and (b) reflection from a metasurface consisting of radial trimer antennas with different illumination of plane waves. 72

4.18 The surface charge distribution of (a) radial mode ($\lambda = 625$ nm) and (b) dipole mode ($\lambda = 725$ nm) resonances of a metasurface consisting of radial trimer antennas, on the top surface. 72

4.19 The (a) transmission through and (b) reflection from a radial tetramer metasurface with different illumination of plane waves. 73

4.20 The surface charge of (a) radial mode ($\lambda = 670$ nm), (b) dipole mode ($\lambda = 815$ nm), and (c) breathing mode ($\lambda = 860$ nm) of a metasurface consisting of radial tetramer antennas with *p-polarised* plane wave illumination. 73

4.21 The surface charge at (a) 720 nm, and (b) 910 nm on a metasurface consisting of radial tetramer antennas with *s-polarised* plane wave illumination. 74

4.22 The (a) transmission through and (b) reflection from radial trimer metasurfaces by p-polarised plane wave for different nanorod lengths L and the gap size $\delta = 20$ nm is kept constant. . . . 75

4.23 The (a) transmission through and (b) reflection from radial tetramer metasurfaces by a p-polarised plane wave for different nanorod lengths L and the gap size $\delta = 30$ nm is kept constant. 75

4.24 The (a) transmission through and (b) reflection from radial trimer metasurfaces by p-polarised light for different off-set distance s. The periodicity is $p = 300$ nm for each metasurface. . . 76

4.25 The (a) transmission through and (b) reflection from radial tetramer metasurfaces by p-polarised plane wave for different off-set distances s. 77

4.26 The (a) transmission through and (b) reflection from a metasurface consisting of radial trimer antennas by p-polarised plane waves with different angles of incidence θ. 77

4.27 The (a) transmission through and (b) reflection from a metasurface consisting of radial trimers with variation of azimuthal angle ϕ of incident fields. 78

4.28 The scattering from a single radial trimer with variation of azimuthal angle ϕ of incident fields. 79

4.29 The (a) transmission through and (b) reflection from a metasurface consisting of azimuthal trimers with different illumination of plane waves. 80

4.30 The (a) transmission through and (b) reflection from a metasurface consisting of azimuthal tetramer antenna with different excitations with angle of incidence 20° for s- and p-polarised illumination. 80

4.31 The surface charge distribution of (a) dipole mode ($\lambda = 680$ nm) and (b) azimuthal mode ($\lambda = 805$ nm) resonances of azimuthal trimer antennas. 81

4.32 The surface charge of (a) dipole mode ($\lambda = 640$ nm) and (b) azimuthal mode ($\lambda = 815$ nm) resonances of azimuthal tetramer antennas. 82

4.33 The (a) transmission through and (b) reflection from azimuthal tetramer antenna with different excitations and angle of incidence at 30°. 82

4.34 The (a) transmission through and (b) reflection from azimuthal trimer metasurfaces with s-polarised plane wave illumination for different nanorod lengths L but the gap size $\delta = 71$ nm is kept constant. 83

4.35 The (a) transmission through and (b) reflection from azimuthal tetramer metasurface by s-polarised light for different nanorod length L but the gap size $\delta = 30$ nm is kept constant. 83

4.36 The (a) transmission through and (b) reflection from the metasurface of azimuthal trimer antennas by s-polarised light for different off-set distance s. 84

4.37 The (a) transmission through and (b) reflection from azimuthal tetramer metasurfaces with s-polarised plane wave illumination for different off-set distances s. 84

4.38 The scattering from a single isolated nanorod with various sizes calculated using the FDTD method. 85

4.39 The transmission though and reflection from a periodic array of nanorods with various sizes calculated using the FDTD method. 86

4.40 Reproducing the spectrum of silver nanorod from the FDTD simulation result with the EEM. 87

4.41 The assumed direction of *uncoupled* dipole modes of the nanorods of radial trimer, used for calculating the mode interactions. 88

4.42 Reproducing the scattering from radial trimer metasurface from FDTD simulation with the EEM. 89

4.43 The scattering by the metasurface of radial trimer antennas when excited by normally and off-normally incident plane waves (p- and s-polarised). 90

4.44 The excitation amplitudes of the nanorods in radial trimers when excited by the off-normally incident p-polarised light. . . . 91

4.45 The scattering spectra of radial trimer metasurface for (a) different coupling constants $|G|$ and (b) off-set distances s while keeping the other parameters fixed. 92

4.46 The scattering spectra of the radial trimers using p-polarised light with 30° angle of incidence where the plane of incidence makes an angle ϕ with respect to the x-axis. 93

4.47 The scattered power of the metasurface with radial trimer antennas when excited by p-polarised light with various angle of incidence. 94

4.48 The assumed direction of *uncoupled* dipole modes of the nanorods of radial tetramer, used for calculating the mode interactions. 94

4.49 The scattering of a single radial trimer antenna with the radially polarised beam coaxially with the antenna. 95

4.50 The scattering of plane waves from the metasurface of radial tetramers at normal and off-normal incidence. 96

4.51 The real part of the amplitudes of excitation of the metasurface of radial tetramers with p-polarisation at 30° angle of incidence. 97

4.52 The scattering of the p-polarised plane wave from the metasurface of radial tetramers with various angle of incidence. 98

4.53 The scattering of plane waves with p-polarisation from the metasurface of radial tetramers with various orientation ϕ of plane of incidence with respect to the x-axis. 98

4.54 The scattering of plane waves with s-polarisation from the metasurface of radial tetramers with various orientation ϕ of plane of incidence with respect to the x-axis. 99

4.55 The assumed direction of *uncoupled* dipole modes of the nanorods of azimuthal trimer, used for calculating the mode interactions. 99

4.56 The scattering of a metasurface with azimuthal trimer antennas when excited by normally and off-normally incident plane waves (p- and s-polarised). Inset: zoomed-in spectra at azimuthal mode resonance. 100

4.57 The real part of the amplitudes of excitation of the metasurface of azimuthal trimers with p-polarisation at 30° angle of incidence. 101

4.58 The scattering by triangle trimer antennas with different angle of incidence by s-polarised light. Inset: zoomed-in spectra showing azimuthal mode resonances. 102

4.59 The scattering by triangle trimer antennas with various orientation of plane of incidence with an angle ϕ respect to the x-axis with s-polarised plane wave illumination. 102

4.60 The scattering by a single azimuthal trimer antenna with the azimuthally polarised beam coaxial with the antenna. (a) The scattering spectrum and (b) the amplitudes of excitation. 103

4.61 The assumed direction of *uncoupled* dipole modes of the nanorods of azimuthal tetramer, used for calculating the mode interactions. 103

4.62 The scattering of plane waves from the metasurface of azimuthal tetramers at normal and off-normal incidence. 104

4.63 The real part of the amplitudes of excitation of the metasurface of azimuthal tetramers with s-polarisation at 30° angle of incidence. 105

4.64 The scattering of the s-polarised plane wave from the metasurface of azimuthal tetramers with various angle of incidence. . . . 105

4.65 The scattering of plane waves with p-polarisation from the metasurface of azimuthal tetramers with various orientation ϕ of plane of incidence with respect to the x-axis. 106

4.66 The scattering of plane waves with s-polarisation from the metasurface of azimuthal tetramers with various orientation ϕ of plane of incidence with respect to the x-axis. 107

4.67 The spatial frequency distribution of the radial trimers excitation at (a) radial mode and (b) dipole mode resonances using a focussed beam with linear polarisation input. 108

4.68 The spatial frequency distribution of the radial trimers excitation at (a) radial mode and (b) dipole mode resonances using focussed beam with radial polarisation input. 109

4.69 The scattering spectra of the metasurface consisting of radial trimers using a focussed beam with (a) linear and (b) radial polarisation input, for various NAs. 110

5.1 The fabrication steps using electron beam lithography. 115

5.2 A few SEM images of the metasurfaces fabricated for experimental characterisation. 118

5.3 The experimental set-up for measuring transmission spectra. . . 119

5.4 The experimental set-up for measuring reflection spectra. 119

5.5 The photograph of objective lenses used in the spectra measurements. 123

5.6 Photograph of experimental set-up for measuring transmission. . 124

5.7 Photograph of experimental set-up for measuring reflection. . . 124

5.8 The coordinate systems defined for each metasurface design. . . 125

5.9 The transmission through the radial trimer metasurface #R13 with linearly polarised light illumination through objective lenses with different NA. 126

5.10 The transmission through the radial trimer metasurface #R13 with radially polarised light illumination through objective lenses with different NA. 127

5.11 The transmission through the radial trimer metasurface #R13 with (a) linearly x- and y-polarised light and (b) radially and azimuthally polarised light illumination, using objective lens with NA=0.75. 127

5.12 The transmission through the radial trimer metasurface #R15 with (a) linearly and (b) radially polarised light illumination through the objective lens with different NA. 129

5.13 The transmission through the radial trimer metasurface #R15 with (a) linearly x- and y-polarised light and (b) radially and azimuthally polarised light illumination using objective lens with NA=0.75. 129

5.14 The transmission through the radial trimer metasurface #R11 with (a) linearly and (b) radially polarised light illumination through the objective lens with different NA. 130

5.15 The transmission through the radial trimer metasurface #R11 with (a) linearly x- and y-polarised light and (b) radially and azimuthally polarised light illumination,using objective lens with NA=0.75. 130

5.16 The transmission of light through the radial trimer antennas of different L and s with radially polarised light focussed by the objective lens of NA=0.65. 131

5.17 The reflection from the radial trimer metasurface #R11 with (a) linearly and (b) radially polarised light illumination through the objective lens with different NA. 131

5.18 The reflection from the radial trimer metasurface #R13 with (a) linearly and (b) radially polarised light illumination through the objective lens with different NA. 132

5.19 The reflection from the radial trimer metasurface #R15 with (a) linearly and (b) radially polarised light illumination through the objective lens with different NA. 132

5.20 The reflection from the radial trimer metasurface with different L and s (#R11, #R13, #R15) illuminated with focussed radially polarised light with NA=0.75. 133

5.21 The (a) transmission though and (b) reflection from radial trimer metasurface #R13 with linearly x- and y-polarised illumination compared with the FDTD simulation results. 134

5.22 The (a) transmission though and (b) reflection from radial trimer metasurface #R15 with linearly x- and y-polarised illumination compared with the FDTD simulation results. 135

5.23 The (a) transmission through and (b) reflection from the metasurfaces #R13 and #R15 compared with the FDTD results with the geometric parameters taken from the SEM images. 136

5.24 The comparison between the experimental data of metasurfaces #R13 and #R15 with radially polarised illumination and the simulation results with the EEM. 137

5.25 The (a) transmission through and (b) reflection from the radial trimer metasurfaces with $L = 90$ nm and different off-set distance s with radially polarised light. Code: #R11; #R12 . . 138

5.26 The (a) transmission through and (b) reflection from the radial trimer metasurfaces with $L = 100$ nm and different off-set distance s with radially polarised light. Code: #R13; #R14 . . 138

5.27 The (a) transmission through and (b) reflection from the radial trimer metasurfaces with $L = 120$ nm and different off-set distance s with radially polarised light. Code: #R13; #R14 . . 139

5.28 The (a) transmission through and (b) reflection from radial trimer metasurfaces with $L = 100$ nm, $s = 70$ nm, and different nanorod width w (#R13, #R17, #R18). 140

5.29 The (a) transmission through and (b) reflection from radial trimer metasurfaces with $L = 120$ nm and different nanorod width w (#R15, #R19, #R1A). 140

5.30 The (a) transmission through and (b) reflection from the radial tetramer metasurface #R25 with linearly polarised light illumination through the objective lens with different NA. 141

5.31 The (a) transmission through and (b) reflection from the radial tetramer metasurface #R25 with radially polarised light illumination through the objective lens with different NA. 142

5.32 The (a) transmission through and (b) reflection from the radial tetramer metasurfaces #R25 with linearly x- and diagonal-polarised light illumination. 143

5.33 The (a) transmission through and (b) reflection from the radial tetramer metasurfaces #R25 with radially and azimuthally polarised light illumination. 143

5.34 The comparison between the experimental data of metasurface #R25 and the FDTD simulation results. 144

5.35 The (a) transmission trough and (b) reflection from metasurface #R25 modelled by the FDTD with p- and s-polarisation. 145

5.36 The comparison between the experimental data of metasurfaces #R25 under radially polarised illumination and the simulation results with the EEM. 146

5.37 The (a) transmission through and (b) reflection from the radial tetramer metasurfaces with various L (#R21,#R23,#R25) with radially polarised light illumination. 147

5.38 The (a) transmission through and (b) reflection from the radial tetramer metasurfaces with $L = 90$ nm and different off-set distance s (#R21 & #R22) with radially polarised light. 147

5.39 The (a) transmission through and (b) reflection from the radial tetramer metasurfaces with $L = 100$ nm and different off-set distance s (#R23 & #R24) with radially polarised light. 148

5.40 The (a) transmission through and (b) reflection from the radial tetramer metasurfaces with $L = 120$ nm and different off-set distance s (#R25 & #R26) with radially polarised light. 148

5.41 The (a) transmission through and (b) reflection from the radial tetramer metasurfaces with various width for L =100 nm (#R27 & #R23) with radially polarised light illumination using objective lens with NA=0.75. 149

5.42 The (a) transmission through and (b) reflection from the radial tetramer metasurfaces with various width for $L = 120$ nm (#R28 & #R25) with radially polarised light illumination using objective lens with NA=0.75. Device code: 149

5.43 The (a) transmission through and (b) reflection from the azimuthal trimer metasurface #A15 with linearly polarised light illumination through the objective lens with different NA. 150

5.44 The (a) transmission through and (b) reflection from the azimuthal trimer metasurface #A15 with azimuthally polarised light illumination through the objective lens with different NA. . 151

5.45 The(a) transmission through and (b) reflection from the azimuthal trimer metasurfaces #A15 with linearly x- and y-polarised light polarised light illumination. 151

5.46 The(a) transmission through and (b) reflection from the azimuthal trimer metasurfaces #A15 with radially and azimuthally light polarised light illumination. 152

5.47 The(a) transmission through and (b) reflection from the azimuthal trimer metasurfaces with code #A12, #A14, and #A16 with linearly x-polarised light polarised light illumination. . . . 152

5.48 The(a) transmission through and (b) reflection from the azimuthal trimer metasurfaces with code #A12, #A14, and #A16 with azimuthally polarised light polarised light illumination. . . 153

5.49 Comparison between experimental results and FDTD simulation for the (a) transmission through and (b) reflection from the azimuthal trimer metasurfaces. 153

5.50 Comparison between the experimental data of metasurfaces #A15 with radially polarised illumination and the simulation results with the EEM. 154

5.51 The (a) transmission through and (b) reflection from the azimuthal tetramer metasurface #A25 with linearly polarised light illumination through the objective lens with different NA. 155

5.52 The (a) transmission through and (b) reflection from the azimuthal tetramer metasurface #A25 with azimuthally polarised light illumination through the objective lens with different NA. . 155

5.53 The (a) transmission through and (b) reflection from the metasurface #R25 from the experiment compared with the FDTD simulation. 156

5.54 Comparison between the experimental data of metasurface #A25 with azimuthally polarised illumination and the simulation results with the EEM. 157

5.55 The (a) transmission through and (b) reflection from the azimuthal tetramer metasurfaces with various L (#A21,#A23,#A25) with azimuthally polarised light illumination. 158

5.56 The scattered light intensity from radial trimer antennas at (a) radial and (b) dipole mode, under illumination of focussed light with linearly x-polarisation. 159

5.57 The reflected light intensity from radial trimer antennas at (a) radial and (b) dipole mode, under illumination of focussed light with radial polarisation. 160

5.58 The experimental set-up for imaging the Fourier-plane reflected beams from the metasurfaces. 161

5.59 The spectrum of the laser, filtered with monochromator, centred at various wavelengths. 162

5.60 The Fourier plane images of reflected beams from metasurface #R13 with linearly x-polarised illumination, at radial mode resonance (620 nm). 163

5.61 The Fourier plane images of reflected beams from metasurface #R13 with linearly y-polarised illumination, at radial mode resonance (620 nm), ... 164

5.62 The reflection coefficient of the plane waves with p-polarised (R_p) and s-polarised (R_s) plane waves propagating in the air ($n_1 = 1$) and being reflected by an interface of the glass ($n = 1.5$) surface, calculated with Fresnel equations [108]. 165

5.63 The Fourier plane images of reflected beams from metasurface #R13 with linearly x-polarised illumination, at dipole mode resonance (750 nm). 165

5.64 The Fourier plane images of reflected beams from metasurface #R13 with linearly y-polarised illumination, at dipole mode resonance (750 nm). 166

5.65 The Fourier plane images of reflected beams from metasurface #R13 with radially polarised illumination, at radial mode resonance (620 nm). 167

5.66 The Fourier plane images of reflected beams from metasurface #R13 with radially polarised illumination, at dipole mode resonance (750 nm). 168

5.67 The normalised reflected beams from metasurface #R13 with radially polarised beam illumination at various wavelengths. . . 168

5.68 The normalised reflected beams from metasurface #R13 with linearly x-polarised beam illumination at various wavelengths. . 169

5.69 The Fourier plane images of normalised beams reflected from metasurface #R18 with (a) radially, (b) linearly x-, and (c) linearly y-polarised illumination, at radial mode resonance (650 nm). 170

5.70 The Fourier plane images of normalised beams reflected from metasurface #R18 with (a) radially, (b) linearly x-, and (c) linearly y-polarised illumination, at **dipole mode** resonance (750 nm). 170

5.71 The Fourier plane images of normalised beams reflected from metasurface #R25 with (a) radially, (b) linearly x-, and (c) linearly y-polarised illumination, at radial mode resonance (675 nm). 171

5.72 The Fourier plane images of normalised beams reflected from metasurface #R25 with (a) radially, (b) linearly x-, and (c) linearly y-polarised illumination, at 820 nm (near **dipole mode** resonance). 172

List of Tables

4.1 The parameters used in the EEM calculation for the spectra of single nanorods in Figure 4.40. 86

4.2 The EEM parameters for calculating spectra in Figure 4.42. . . 89

5.1 Codes for metasurface designs. 116

5.2 The geometric parameters of fabricated metasurfaces. 117

5.3 Optical components used in experiments. 120

5.4 Light sources used in experiments. 121

5.5 Objective lens used. 122

5.6 The fitting parameters of the EEM for experimental data of metasurfaces #R13 and #R15, for comparison shown in Figure 5.24. 136

5.7 Best fit parameters for the EEM for experimental data of metasurface #R25, for comparison shown in Figure 5.36. 146

5.8 The fitting parameters of the EEM for experimental data of metasurfaces #R13 and #R15, for comparison shown in Figure 5.50. 154

5.9 Best fit parameters for the EEM for experimental data of metasurface #A25, for comparison shown in Figure 5.54. 156

Chapter 1

Introduction

1.1 Metallic Nanostructures for Manipulating and Sensing Light

Light propagates in different ways through different media and its properties can change as a result of its interaction with various media or objects [1]. Recently, there has been a growing interest in analysing the interaction of light with artificial media composed of sub-wavelength structures [2–4]. These media can be made of various types of materials, including metals, dielectrics, semiconductors, and different combinations. These artificial materials are called metamaterials and they are able to provide optical responses and properties that are not available in natural media [5]. They have attracted widespread interest for manipulating and sensing light.

The term 'light' is generally used to describe a part of the electromagnetic spectrum that can be roughly divided into ultraviolet, visible, and near-infrared regions. These correspond to free-space wavelengths ranging from approximately 100 nm to 1500 nm (or frequencies from 200 THz to 3000 THz). The propagation of light through homogeneous linear and isotropic media is usually described in terms of its electric permittivity, ε, and magnetic permeability, μ. The speed of light in a medium is given by $v = c/n = 1/\sqrt{\varepsilon\mu}$ and the

refractive index n of a medium is defined via

$$n = \sqrt{\frac{\varepsilon\mu}{\varepsilon_0\mu_0}} \tag{1.1}$$

where $c = 1/\sqrt{\varepsilon_0\mu_0}$ is the speed of light in vacuum, and ε_0 and μ_0 are permittivity and permeability of vacuum.

In general, the refractive index is a complex number. Its real part determines the phase velocity and the imaginary part characterises the loss via absorption. At radio and microwave frequencies (∼3 kHz to 300 GHz), the imaginary part of the refractive index of metal has a very large value so that metals are opaque and reflective to radio and microwave frequencies. At optical frequencies, however, its imaginary part is much smaller than at radio frequencies so that metals are not completely opaque to light although they remain absorbing. Furthermore, metals at optical frequencies are non-magnetic so that they can be described by considering only their permittivity.

In the visible part of the spectrum, the free electrons of metal behave as a plasma or free electron gas. Their response to the electromagnetic field is very dispersive. At frequencies below a characteristic frequency (the plasma frequency), the materials retain their metallic properties having a negative value for the real part of the permittivity. At frequencies above the plasma frequency, however, the material behaves more as a lossy dielectric. For silver, the plasma frequency is ∼3.9 eV, corresponding to a free space wavelength of ∼320 nm, while for gold the corresponding figure is ∼2.4 eV (∼520 nm) [6, 7].

The boundary between a dielectric and a metal can support surface waves known as surface plasmon polaritons (SPPs). SPPs are confined to the surface and their amplitude decays evanescently in a direction perpendicular to the surface. Under particular conditions and using special techniques, these SPPs can be excited by an incident field when impedance matching occurs between SPPs and the exciting waves. Prism coupling, grating coupling, and highly focussed beams are a few example of techniques that can be used to excite SPPs [8].

On metal nanoparticles, surface charge oscillations are localised, forming standing waves resulting in localised surface plasmons (LSPs). At resonance, the intensity near the metal nanoparticle surface is significantly higher. The prop-

erties of LSPs depend strongly on the geometry of a nanoparticle and nanoparticles with different shapes and sizes produce different resonances. LSPs are also able to interact via near-field coupling; the excitations on one particle are coupled with its neighbours. On an ensemble of nanoparticles, the resonances of the system of particles depends strongly on their arrangement as well as their individual geometric and dielectric properties. The metal nanoparticles as well as the optical properties of background media also contribute to the frequency of resonances and change the field distributions at the resonances. LSPs play a very important role in this thesis.

The LSPs of metal nanoparticles can alter the properties of light such as its intensity, polarisation, and phase and can also sense those properties. As a result, metamaterials and their two dimensional counterparts, metasurfaces, which consist of metallic nanostructures can be used for manipulating or sensing light, provided that designs and materials are appropriately tailored to suit the specific purposes. For example, metamaterials have been demonstrated to have a negative refractive index, arising from simultaneously negative permittivity and permeability [5], and these metamaterials have potential for imaging beyond the diffraction limit [9].

1.2 Optical Antennas and Metasurfaces

1.2.1 Optical Antennas

Optical antennas are optical scatterers with sub-wavelength sizes, designed to have a specific response to electromagnetic waves in the optical region of the spectrum. The optical antennas can be arranged in a two dimensional array, forming a metasurface, a flat device with the ability to control or sense the light. Metasurfaces are the flat (2D) counterpart of bulk (3D) metamaterials and have the potential to replace bulk optical devices such as lenses, polarisers, and holograms [10].

Antennas are devices for converting between propagating electromagnetic (EM) waves (far-field) and localised EM fields (near-field). Antennas at radio frequencies are well-understood and are widely used in many electronic devices,

such as mobile phones, laptops, televisions, radios, radars, GPS, and many other devices. They are able to couple signals from radio waves and convert them into electrical signals. They are also used for transmitting radio waves to send information.

Antennas take advantage of different designs with different geometries, sizes, and arrangements of antenna elements. There are, for example, dipole antennas, Yagi-Uda antennas, parabolic dish antennas, and bow-tie antennas. They are designed to operate over different frequency ranges as well as with different types of signal transmissions [11, 12].

Antennas that are designed for use at optical frequencies are still a topic of active investigation and their operating wavelength is much shorter than that for radio frequencies. The geometry of these antennas must be made on sub-wavelength scales corresponding to typical dimensions from tens to hundreds of nanometer. State-of-the-art technologies such as electron beam lithography (EBL) and focussed ion beam (FIB) milling for making structures on the sub-micrometer scale have made the investigation of the optical antennas possible over the past decade [13].

In order to extend the concept of RF antennas to optical frequencies, a further consideration must be addressed. Metals behave differently at optical frequencies as well as when patterned on sub-microscopic sizes. They need to be modelled as an electron plasma rather than as a (nearly) perfect conductor and they are also very dispersive at optical frequencies. All antennas have a range of different resonances depending on their dimensions and geometry. By altering these parameters, optical antennas can be designed to have various operating frequencies and their interaction with light can be varied.

There are many applications envisaged for optical antennas [14]. They can be used in imaging and spectroscopy for their ability to enhance image quality via near-field coupling. As photovoltaic devices, they are able to help generate charge carriers in semiconductors. Low-efficiency light emitters (e.g. quantum dots) can be enhanced with the presence of optical antennas as they act as light emission enhancement devices. They are also able to change the polarisation and directionality of emitter radiation [15].

1.2.2 Metasurfaces

Metasurfaces are flat optical devices composed of periodic arrangements of nanostructures that have the ability to sense or modify optical wavefronts with sub-wavelength resolution [10]. These devices are made of light scatterers or optical antennas arranged in two dimensional arrays [14, 16, 17]. Spatial variations between unit cells may be introduced into a metasurface so that the phase, amplitude, or polarisation of the light passing through or reflected from the metasurface can be modified into desired properties [18]. Metasurfaces have been shown to have the potential to replace bulk optical devices such as lenses, waveplates, and holograms in a device with a thickness of the order of 100 nm [10].

On a metasurface, optical antennas determine the basic properties of the structure. For example, an optical antenna consisting of three nanorods [19] has been shown to sense the phase gradient of an incident field. A periodic arrangement of these structures into a metasurface demonstrated that the antenna property extended to the array.

Since the geometry of the antennas is critical, the shape can be used to tailor the device to have resonances at specific design wavelengths. The resonances correspond to the modes of surface charge oscillations on the metallic nanostructures composing the antennas. Dipole modes, consisting of a simple oscillating charge separation, are easily excited by linearly polarised light at normal incidence. They are also called radiant or bright modes as they are easily coupled to propagating plane waves. Antennas can sustain higher order modes but many of these are more difficult to couple to propagating light. These modes are called sub-radiant or dark modes. To couple them to propagating light, a normally-incident linearly-polarised plane wave is not sufficient. Tailored beams of light can be used, such as vector beams with radially or azimuthally polarisation or even plane waves at off-normal incidence.

Symmetry breaking is an important aspect of probing sub-radiant modes. This can be done in two ways, by breaking the symmetry of the structures, or by breaking the symmetry of the excitation field. An example is a sub-radiant mode in dimer metamaterials [20], where the anti-symmetric mode can be excited by introducing different lengths for each nanorod of the dimer. Similarly,

in trimer arrangements of nanorods, a geometric asymmetry has been shown to produce a quasi-dark mode [21].

In this study, the excitation of sub-radiant modes of arrays of optical antennas, particularly radial and azimuthal modes in a metasurface, is investigated. Radial modes are modes corresponding to charge oscillations on the antennas that are oscillating along a radial line with respect to a central point. Azimuthal modes, on the other hand, oscillate circularly or azimuthally around the centre of the structure.

The optical antennas under study in this project, consist of radial and azimuthal ensembles of nanorods, are arranged in an array forming a metasurface. Each antenna design has radiant and sub-radiant modes that are excited under different illumination conditions. The excitation of sub-radiant modes was performed by illumination with a highly focussed beam and the off-normal components of the focussed field are able to excite the sub-radiant modes of the metasurface. The polarisation components of the incident light also plays an important role in the excitation of the sub-radiant modes. For example, radial modes are excited with p-polarised light and azimuthal modes are excited with s-polarised light.

1.3 An Overview of the Thesis

This project covers the computational and experimental investigation of sub-radiant modes of metasurfaces, particularly radial and azimuthal modes of radially and azimuthally arranged nanorod ensembles. The metasurfaces studied are periodic arrays of optical antennas composed of silver nanorods on a glass substrate, encapsulated by a polymethyl methacrylate (PMMA) layer. A single unit cell of a metasurface consists of a single optical antenna composed of two or three nanorods. There were four different designs of optical antenna considered, with three or four nanorods arranged radially or azimuthally. The arrangements studied are shown in Figure 1.1.

The designs were modelled using two methods, the electrostatic eigenmode method (EEM) and the finite-difference time-domain (FDTD) method. The EEM is an approximate method while the FDTD is a more rigorous full-

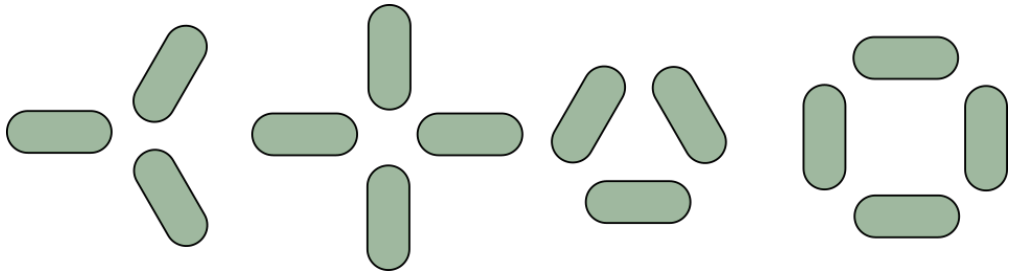

Figure 1.1: Optical antennas designs: (a) radial trimer, (b) radial tetramer, (c) azimuthal trimer, and (d) azimuthal tetramer.

field method. The response of metasurfaces to the incident fields was studied computationally using linearly polarised off-normally incident plane waves. A focussed beam can then be constructed as a sum of plane waves with different wavevectors and polarisations. The spectral information describing reflection and transmission was obtained from the modelling and both radiant and sub-radiant modes were able to be identified. The far-field properties of the reflected beam at resonances were also investigated.

Experimental characterisation was performed via transmission and reflection measurements using broadband light sources. The broadband sources used were a tungsten-halogen light and a high-intensity supercontinuum laser. Linearly polarised light, as well as radially and azimuthally polarised vector beams were used to excite the metasurfaces and high numerical aperture (NA) beams used to probe different angles of incidence. Spectral information was obtained and once radiant and sub-radiant modes were identified, the metasurfaces were illuminated with a narrowband source[1] centred on particular resonances. The far-zone reflected beams at the resonances were then imaged to confirm the nature of the resonance.

The main goal of this project was to **characterise the sub-radiant modes of metasurfaces**. These sub-radiant modes have unique properties, including high sensitivity to wavelength and angle of incidence, longer life-times, and higher Q resonances. The characterisation of these sub-radiant modes is an initial step before they can be used for many potential applications in manipulating and sensing light. In order to achieve that goal, several sub-goals were

[1]Narrowband source was the supercontinuum laser filtered with a tunable monochromator.

required. The sub-goals were:

1. to design metasurfaces supporting sub-radiant modes in the visible region of the spectrum,
2. to investigate strategies to separate the spectral locations of radiant and sub-radiant modes,
3. to model the optical properties of sub-radiant modes of metasurfaces,
4. to establish methods to experimentally probe sub-radiant mode excitation, and
5. to obtain the far-field properties of the reflected light via the excitation of sub-radiant modes.

Chapter 2 provides a literature review discussing optical antennas and metasurfaces. The properties of metallic nanostructures at optical frequencies and localised surface plasmons (LSPs) are discussed. LSPs are used as the basis for the extension of concepts from radio frequency to optical frequency antennas. Several examples of geometries of optical antennas including their properties and potential applications are discussed. These antennas are then considered as the unit cell of arrays to form two dimensional nanostructures for controlling and sensing light, called metasurfaces. Optical antennas and metasurfaces can sustain several modes of oscillations, including radiant and sub-radiant modes. Several examples of mode excitation of optical antennas and metasurfaces are also discussed.

Chapter 3 provides a detailed explanation of the methods used for modelling in this project. The electrostatic eigenmode method (EEM) uses the electrostatic approximation and incorporates interparticle mode coupling. The other method used in this project is the finite-difference time-domain (FDTD), a more rigorous and computationally intensive method for solving electromagetic problems. This algorithm solves both electric and magnetic field distributions as a function of time and this information can be used to construct spectral information.

Chapter 4 includes the results of modelling metasurfaces with the FDTD and EEM methods. Several different excitation strategies for each design of metasurface are discussed. The metasurfaces were designed to have spectrally separated resonances of radiant and sub-radiant modes. Modelling was initially

performed using the FDTD method to predict the spectral behaviour of the metasurfaces. Further modelling using the EEM provided insight for different types of excitation on each metasurface. As a result of the faster calculation times compared to the FDTD method, the EEM can also be used to produce maps of the spatial frequency response of the resonances.

Chapter 5 discusses the fabrication and characterisation of metasurfaces. Devices were fabricated using EBL and the measurements performed using a bench-top optical set-up to measure their transmission and reflection. The exciting light used in the characterisation was focussed and beams with linear, radial, and azimuthal polarisation were used as inputs. Radiant and sub-radiant modes were able to be identified by looking at the transmission and/or reflection spectra of the metasurfaces. Sub-radiant modes were found to be excited using strongly focussed light with high numerical aperture objective lenses. The use of vector beams as input was shown to increase the strength the of sub-radiant mode excitations relative to neighbouring radiant modes. The far-field profiles of the reflected beams at the resonances were then investigated by capturing their images with a camera. The angular properties of the beams were found to be modified via sub-radiant mode excitation. Some of modelling results from Chapter 4 are also presented in this chapter supporting this evidence of sub-radiant mode excitation.

Chapter 6 provides a conclusion along with recommendations for further work.

Chapter 2

Optical Antennas and Metasurfaces: Background

Metasurfaces are attracting increasing interest for their capacity to sense and control electromagnetic radiation in a device that can be as thin as several tens of nanometres. As discussed in the previous chapter, the basic building block of a metasurface is a sub-wavelength structure that interacts strongly with electromagnetic radiation – an optical antenna. In this thesis, arrays of optical antennas are investigated and this chapter provides an overview of antenna and metasurface properties.

Optical antennas can be single or an ensemble of metallic nanostructures, which can be nanoparticles or nanoapertures, that are designed to have a specific optical response. Their modes of charge oscillation can be divided into two types, radiant (or bright) modes and sub-radiant (or dark) modes. The modes are excited collectively on a metasurface when it is illuminated by electromagnetic waves.

2.1 Metasurfaces

Bulk optical devices such as lenses and polarisers rely on the propagation of light through a medium with a thickness much larger than the wavelength of the light. These devices are based on basic optical principles like refraction,

reflection, and diffraction. Metasurfaces provide an ultrathin alternative for these optical devices taking advantage of interactions on the sub-wavelength scale [10, 22]. Compared to metamaterials, metasurfaces have the advantages of requiring less physical space, are simpler to fabricate, and many applications of metamaterials can be achieved using metasurfaces [23].

With suitable design, metasurfaces are able to introduce a tailored phase variation at a surface to manipulate the phase, amplitude, and/or polarisation of light passing through or reflected from one of the devices [10]. Metasurface components can therefore be designed to achieve desired optical properties equivalent to popular bulk optical devices. At a metasurface, optical scatterers or optical antennas interact strongly with an incident field and a phase jump is introduced within tens to hundreds nanometers. Phenomena related to the phase jump introduced by a metasurface can be demonstrated using the generalised law of refraction [24].

2.1.1 Examples of Metasurfaces

Various devices have been demonstrated using metasurfaces [10]. By using V-shaped antennas, a flat lens can be realised to focus a light beam without spherical aberration at telecom wavelengths [25]. The reported efficiency is, however, very small. The efficiency can be increased by matching its impedance to that of free space. This has been demonstrated by using spatially varying copper traces supporting electric and magnetic polarisation currents to match the free space impedance [26]. This was demonstrated using microwaves but the concept can be extended to the optical region.

Metasurfaces have also been demonstrated as polarising elements such as quarter wave plates [27, 28], and also as devices to generate vector beams [29,30]. Furthermore, devices that can discriminate between orthogonal states of circular polarisation have been produced [31].

Introducing a spatial variation into metasurfaces can be used for wavefront shaping of the light beam. Figure 2.1 shows a metasurface made of varying size apertures with spatially varying transmission coefficients that can be used as a hologram [32]. The metasurface has two different operating wavelengths that produce two different holograms. A word 'META' is created in the far-

field at $\lambda_1 = 905$ nm and a word 'CGH' at $\lambda_2 = 1385$ nm. Another example is a metasurface made of spatially varying V-shaped antennas which has a spatial variation to generate an optical vortex beam carrying orbital angular momentum [33]. The vortex beam wavefronts appear in a spiral interferogram produced by the interference between the beam and a co-propagating Gaussian beam.

Figure 2.1: The metasurface made of nanoholes with spatially variation of geometry acts as a hologram producing two different patterns at two different wavelengths [32].

A metasurface consisting of slot apertures with radial orientation in a metal film has also been designed to create an azimuthally polarised optical vortex beam from an incident circularly polarised beam [34]. A schematic of the device is shown in Figure 2.2. This occurs because a slit aperture in a metallic film acts as a miniature polariser that transmits light with polarisation perpendicular to its long axis. Based on the same principle, U-shaped antennas are arranged so that left circular polarised light at normal incidence is converted into a focussed beam with right handed circular polarisation [35,36]. Another design with rod antennas demonstrated a phase plate that can generate a broadband optical vortex beam [37].

Despite the considerable developments in using metasurfaces to manipulate the phase of an incident electromagnetic wave, there have been relatively few reports of using metasurfaces to sense the phase, specifically the phase gradients, of an incident wavefield by converting this information to intensity. The ability to do this would open up applications such as ultracompact spatial filters for image processing, all-optical chips for real-time mathematical operations, new approaches for wavefront sensing and novel methods for visualising transparent objects such as cells.

An example of a phase gradient detection scheme is a plasmonic circuit consisting of three coupled nanorods [38], arranged as in Figure 2.3a and b. Two nano-

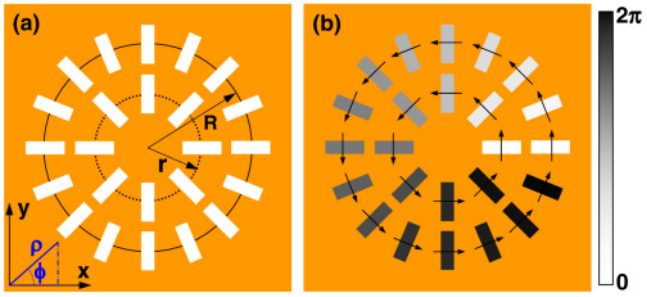

Figure 2.2: A metasurface-based device for converting circularly polarised beam into azimuthally polarised beam [34]. (a) The arrangement of a metasurface made of radially-arranged apertures. (b) The resulting transmission through the device where the arrow indicates the local polarisation and gray-scale filling indicates the phase.

rods, labelled as inputs, are excited by incident fields with a phase difference or a field with a phase gradient. The out-of-phase plasmon excitation on these two nanorods is then detected through evanescent coupling by a third nanorod arranged perpendicular to both of the inputs. The polarisation of input and output beams are expected to be orthogonal, and the scattered beam from the output can then be analysed. A further scheme based on a similar principle can be achieved in two dimensions by the more complex arrangement [39] shown in Figure 2.3c. With this metasurface, phase gradients along both x- and y-axis can be detected. Phase-gradient sensing can also be performed through the sub-radiant/ dark modes excitation of gold nanorings [40]. Dark modes are very sensitive to the phase gradient of incident angle due to retardation.

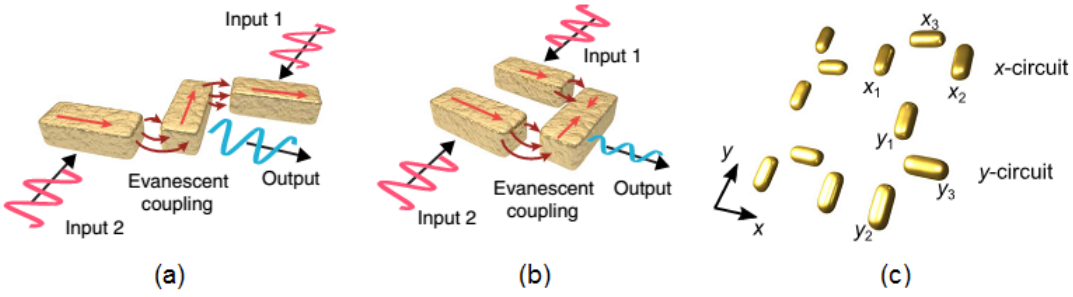

Figure 2.3: Plasmonic circuits consisting of metal nanorods to sense phase difference of the incident fields. (a,b) Two possible arrangement of plasmonic circuits [38], and (c) the unit cell of a metasurface to perform two dimensional mathematical operation based on phase difference [39].

Metasurfaces investigated in this study are arrays of optical antennas that

possess sub-radiant modes. The excitation of these dark modes is sensitive to the angle of incidence and polarisation of the exciting light. Furthermore, the linewidths of dark modes are narrower than bright modes, leading to a potentially improved sensing. The spectral location of the resonances of these modes can be altered by changing the geometry of the individual optical antennas, i.e. by changing the size, orientation and position of the constituent nanorods.

2.2 Metals at Optical Frequencies

Metals are generally regarded as good conductors of electricity as they have free electrons that permit electrical current to flow within them. At radio frequencies, metals are highly non-penetrable by electromagnetic (EM) waves because of the presence of these free electrons which rearrange themselves to cancel the penetrating electric and magnetic fields of EM waves. The fields within conductors strongly decay exponentially into the bulk from the metal surface. As a result, the overall EM behaviour of metals can be modelled as near-perfect conductors at radio frequencies.

At optical frequencies, metals can no longer be modelled this way. The free electrons of metals instead behave as a free electron gas or plasma. The plasma oscillates with the incident electromagnetic fields and they are very dispersive.

Naturally occuring media including metals are non-magnetic at optical frequencies [41]. Their response to EM fields then can be described by considering only their electrical properties. A plasma of free electrons responds to the incident EM waves by oscillating a with strong dependence on the frequencies of the EM waves. The optical properties of bulk gold, silver, and copper were experimentally investigated in Ref. [42] by Johnson and Christy and the properties of other bulk metals, such as aluminium, can be found in Ref. [43] by Palik. The properties are described via the complex refractive index n,

$$n(\omega) = n_r(\omega) + in_i(\omega). \tag{2.1}$$

where ω is the frequency of the incident EM fields. The complex refractive index of a few metals is shown in Figure 2.4.

For non-magnetic materials, a very good approximation at optical frequencies, is that the relative permittivity of metals is simply the square of the complex refractive index, $\varepsilon(\omega) = \tilde{n}^2$.

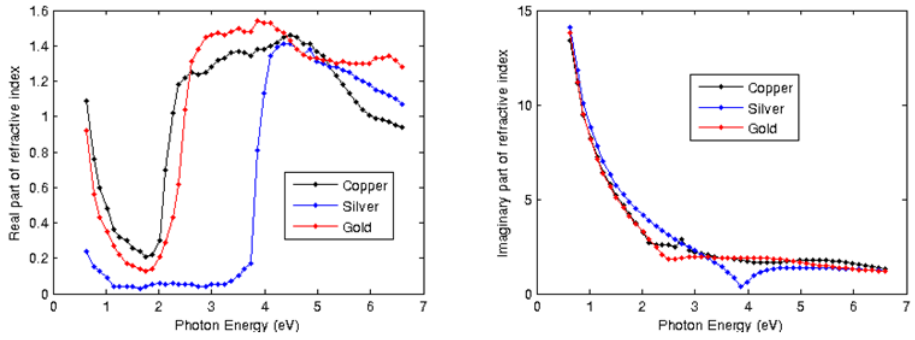

(a) (b)

Figure 2.4: Complex refractive index of gold, silver, and copper as a function of photon energy [42]. The real part is shown in Fig. (a) and imaginary part in Fig. (b).

2.2.1 Surface Plasmon Polaritons

The free electrons of metal tend to repel to each other, resulting in free electrons being located at metal/dielectric interfaces. These free electrons interact with an applied external EM wave and respond to the oscillations of the external electric field from the exciting EM wave.

As a result of this interaction between electrons and external EM waves, some of the energy of the EM waves is converted to a surface EM wave that propagates along the metal/dielectric interface. The EM waves excited on metal/dielectric boundaries by external EM waves are called surface plasmon polaritons (SPPs) or simply surface plasmons (SPs). For the SPs to be excited, the momentum (or phase) of the SPs along the direction of propagation needs to be matched with those of incident EM fields. One common technique is the Kretchmann configuration [44], in which a thin metal film is evaporated on the surface of a glass prism. The incident fields come through the glass side of prism and fall onto the glass/metal interface under total internal reflection condition. This will excite the SPs on the air/metal interface. Another similar technique is the Otto configuration [45], in which the thin metal layer is sep-

arated from the prism by a thin air gap. Both schemes are shown in Figure 2.5.

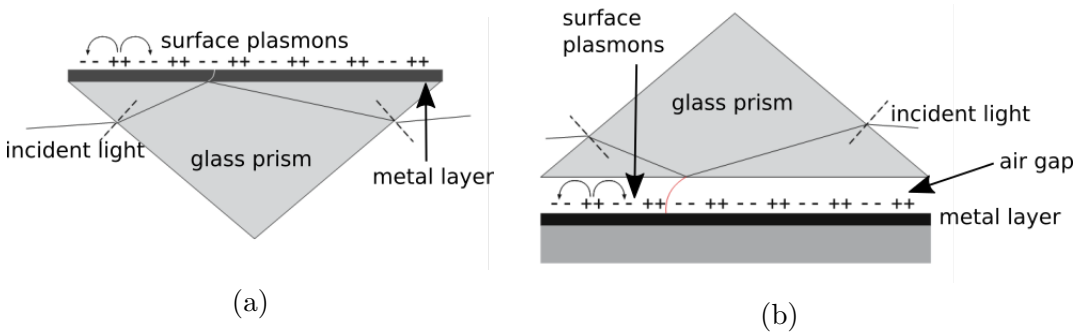

(a) (b)

Figure 2.5: The schematic showing surface plasmon excitation at metal/ dielectric boundaries, using prism coupling [8] with the (a) Kretchmann [44] and (b) Otto [45] configurations. An attenuated EM wave from the total internal reflection exciting the surface charge oscillations on a metal/ dielectric (air) interface. The wave is confined on the surface with exponential strength decay of the fields along normal of the surface.

Figure 2.6 shows the dispersion relation of surface plasmons at a silver/air and a silver/silica interface. A resonance at a specific frequency that depends on the optical properties of the metal and dielectric involved is apparent. For gold, silver, and copper, this plasma frequency occurs in the visible part of the spectrum. For aluminium, this lies in the ultraviolet.

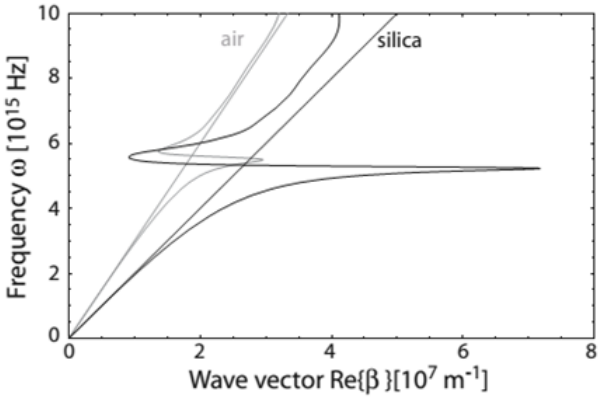

Figure 2.6: The dispersion relation of surface plasmons at silver/air and silver/silica interfaces [8].

2.2.2 Localised Surface Plasmons

On nanoparticles, SPs do not propagate but instead are localised at the nanoparticle surface. The free electron gas of the metal oscillates along a line parallel to the incident electric field. This movement leads to an oscillating separation of charge on the particle. When linearly polarised light is used, a dipole moment will be excited on the particles. This surface plasmon phenomenon causes significantly higher intensity regions of the electromagnetic fields around the particles. At one or more specific light frequencies, the amount of scattered and/or absorbed light is at a maximum corresponding to a resonance. This condition is often referred as localised surface plasmon resonance.

The shape and size of the particle as well as the optical properties of its surrounding medium, have an influence on the frequency of the surface plasmon resonance. If a different metal is used, this also changes the resonance. Figure 2.7 shows the dependence on the nanoparticle shape and sizes on silver and gold nanoparticles [46, 47].

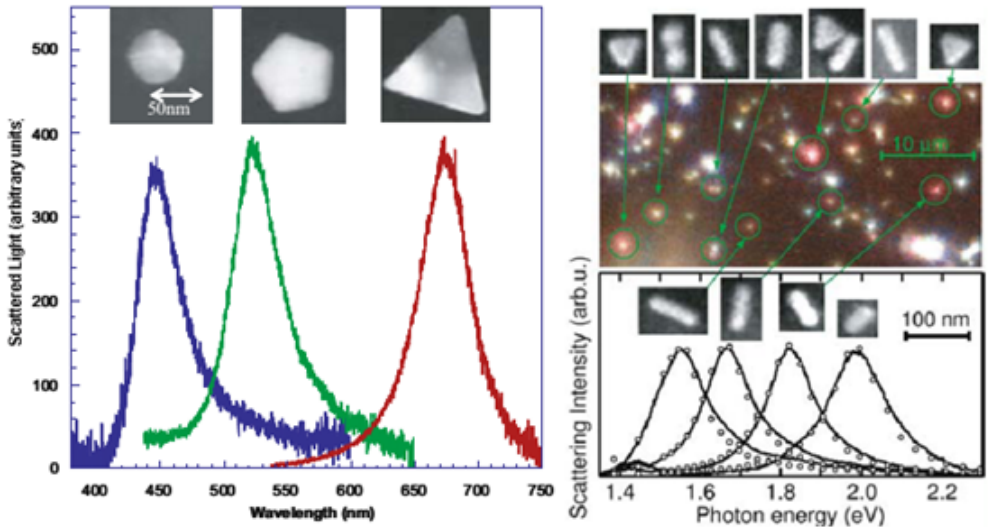

(a) (b)

Figure 2.7: The influence of particle shape and size on the surface plasmon resonance of (a) silver [46] and (b) gold nanoparticles. [47].

In an array or some other arrangement of particles, the localised surface plasmon of one particle can be coupled to the surface plasmon of other particles.

This surface plasmon interaction can be utilised for certain applications. Some of those are plasmon waveguides, the transmission of radiation through apertures and films, the enhancement of emission process and nonlinearities, spectroscopy, sensing, and metamaterials imaging [8]. For reviews, see Ref. [48–50].

2.3 Optical Antennas

2.3.1 Basic Theory of Optical Antennas

Electromagnetic radiation can be manipulated by, and coupled to and from, devices called antennas. In general, antennas are devices to assist the receiving and/or radiation of electromagnetic waves. In receiving processes, antennas convert free-propagating electromagnetic waves to electrical currents which flow through the antennas and connect to other electrical devices. On the other hand, antennas perform the counterpart in the electromagnetic transmission processes, where electric currents are converted to free-propagating electromagnetic waves. Antennas are widely used for a range of electronic devices, such as television, radio, and mobile phones, where data are sent via electromagnetic waves. These applications mainly lie in the radio and microwave frequency range where the theory of antennas has been well-established for decades.

Although antennas used at radio and microwave frequencies are already very well-understood and a wide range of designs have been developed for various applications, this is not true at optical frequencies. In particular, the behaviour of metals (as the material of the antenna) at optical frequencies is far from a perfect conductor but instead, as already discussed, acts as a plasma or free electron gas [51]. Apart from that, antennas need also to be scaled down to a sub-wavelength size which is of the order of hundreds of nanometer for use at optical frequencies. Thus, a different theory for antennas at optical frequencies has been developed. The understanding of surface plasmons is one of the steps leading to the development of antennas at optical frequencies. Despite the differences, the basic ideas of optical antennas are essentially analogous to the those of radio and microwave antennas.

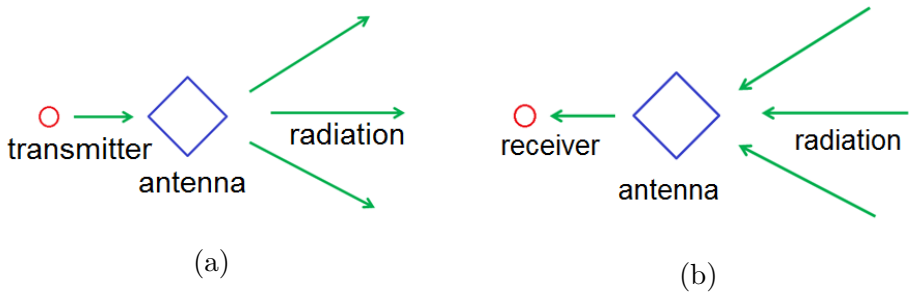

(a) (b)

Figure 2.8: Scheme of optical antenna for the enhancement of (a) transmission process and (b) receiving process.

As in the case of antennas for radio and microwave frequencies, the design of optical antennas has an important influence on their performance. This includes the choice of the material used for the antenna, its shape and the size of metal nanoparticles or nanoapertures composing the antenna, as well as the arrangement or overall structure of the antenna. The design is informed by the envisaged application for the antennas.

There are several parameters used to describe optical antennas, adapted from those developed for radio and microwave antennas. These include radiation efficiency, directivity, gain, radiative enhancement, and antenna aperture [51].

The efficiency of radiation of light emitted or received, by quantum elements such as quantum dots, fluorescent molecules, or defects in diamond can be enhanced using optical antennas. Increasing the power radiated by an emitter is one of the potential advantages of using optical antennas.

2.3.2 Examples of Optical Antennas

An optical antenna may be composed of a single metal nanoparticle. This can be any shape, such as a nanosphere, nanorod, or nanocube. At resonance, this particle is surrounded by an electric field that is significantly (by an order of magnitude or more) greater than that of the excitation field and typically extends over a distance of a few tens of nanometers [52]. A quantum emitter such as a dye molecule, quantum dot, or NV centre in diamond can be placed near the nanoparticle in this high intensity region. It will then interact with the confined EM field due to plasmon excitation on the metal nanoparticle.

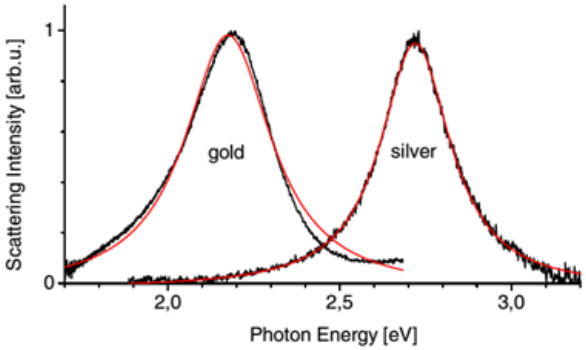

Figure 2.9: The scattering intensity of single gold and silver nanospheres of diameter 60 nm, measured by dark-field microscopy (black lines) and fitted with theoretically Lorentzian shape (red lines) [53].

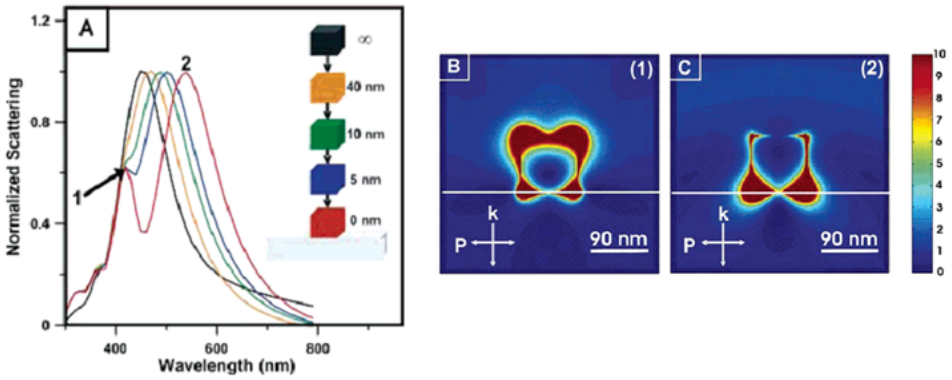

Figure 2.10: (a) The scattering spectra of a single nanocube with variation of its position to the dielectric substrate. (b) and (c) The field profile on resonance condition 1 and 2 indicated on the spectra [54].

The resonance of single gold and silver nanospheres was investigated in [53] (Figure 2.9) showing their ability to scatter and or absorb light at particular frequencies. Figure 2.10 shows the results of simulations of scattering by a silver nanocube placed near a dielectric substrate [54]. There is a clear peak in the scattering spectrum that is split when the cube is moved close to the substrate. The nanocube close to the substrate shows two peaks in its scattering spectrum. This shows that the resonances are affected by the surrounding media and conversely that metal nanoparticles can be used for sensing the refractive index of a material.

Another example of the use of a single metal nanoparticle as an optical antenna is an octahedral shape of silver nanoparticle [55]. This is designed to enhance the emission process of graphene quantum dots placed at various locations

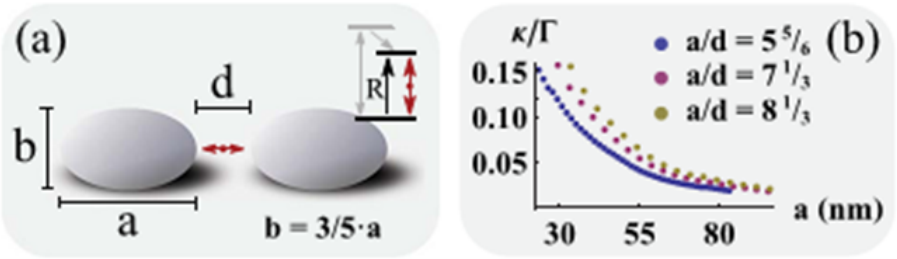

Figure 2.11: (a) Two silver spheroids acts as a dimer antenna to enhance the emission of quantum dot placed in the gap. (b) The coupling strength dependency on the ratio a/d [56].

near the nanoparticle.

To have stronger localisation of the EM field distribution, two nanoparticles can be arranged close to each other to produce a dimer antenna. A strong EM field enhancement will be formed in the gap between the particles. Figure 2.11 shows a dimer antenna that consists of two silver spheroids. A quantum dot is then placed in-between them as a transmitter. The coupling strength depends on the ratio of the particle size to the gap width (a/d) of the antenna structure [56].

A bow-tie antenna is another widely used type of dimer antenna that has also been used as an element in a metasurface [57]. This is made of two nanoprisms placed with their tips adjacent. The localised EM field distribution is now more strongly confined between these tips than in the case of spheroidal particles [58]. An example of a more complex structure is four nanorods with pointed ends, shown in Figure 2.12, that form a cross optical nano-antenna that excites EM localization at its centre and has reduced sensitivity to polarization [59].

For the purpose of emission over a broad wavelength range, the gap between silver nanospheres and an extended silver film is used to enhance the radiation of emitting material inside the gap in ref. [60]. The scheme is illustrated in Figure 2.13. The spontaneous emission using this nanogap leads to an enhancement over the whole visible range. However, when nanoparticles are too close to the metal film, the emission rate can be reduced – a phenomenon called quenching [61].

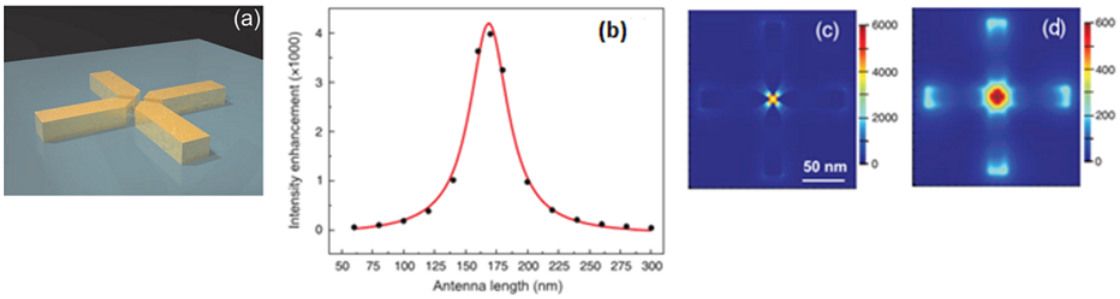

Figure 2.12: (a) The cross optical antenna made of four tipped-end nanorods (b) The intensity spectrum (c) the intensity profile of this antenna at mid-height plane and (d) at 5 nm above the antenna surface [59]

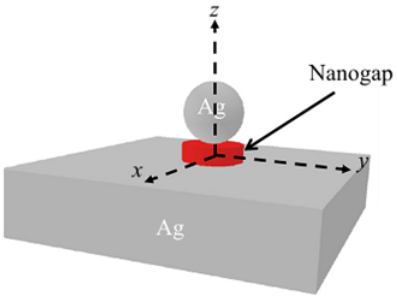

Figure 2.13: A nanogap for enhancing the emission rate of emitting material placed in the gap [60].

2.3.3 Modes of Optical Antennas

When illuminated with light, surface charge oscillations are induced on optical antennas. Depending on the nature of the excitation field, different modes of optical antennas can be excited. Modes can generally be divided into two types: (1) radiant (or 'bright') modes and (2) sub-radiant (or 'dark') modes.

Radiant modes couple easily to propagating electromagnetic waves. They can be excited with normally incident plane waves and have a non-zero net electric dipole moment. Dipole oscillations correspond to the polarisation of the excitation field.

Sub-radiant modes couple weakly to propagating light and are more difficult to excite since their net dipole moment is zero. Symmetry breaking is required to probe these modes using radiation. This can be performed by either breaking the geometric symmetry of the antennas or that of the excitation field. An antenna asymmetry can be introduced by using an asymmetric geometry such

as the shape of a single-element antenna or their sizes and/or orientations of a multi-element antenna. An asymmetric excitation field can be introduced by illuminating the antennas with off-normally incident plane waves or more complex vector beams such as radially or azimuthally polarised light.

When the symmetry of an antenna structure is broken, higher multipolar modes such as the quadrupole and octupole can be excited with normally incident plane waves [62]. These modes have no net dipole moment and are often called dark or sub-radiant modes. Both bright and dark modes can appear together depending on the antenna structure and the exciting radiation used. On the other hand, directly dipole-active higher order modes appear on larger antennas due to retardation effects and their properties changed by the angle of incidence of the exciting radiation [40, 63].

An example demonstrating the excitation of bright and dark modes on particle dimers are shown in Figure 2.14 [63]. Two cylinders are placed closely to each other with a small gap. If the incident field falls symmetrically, as shown in Figure 2.14a, the plasmons excited on both particles are in-phase. The excited plasmons have a net electric dipole moment, which is parallel to the electric field, hence a bright mode. When the incident field has a phase difference across the structure (due to retardation), as shown in Figure 2.14b, the excited plasmons are anti-symmetric, leading to another mode excitation. This mode is dark because the net dipole moment is zero. The excitation of dark modes were demonstrated in the experiment using a dimer consisting two gold octahedra, excited using prism coupling [64], shown in Figure 2.15. The dark mode was excited with p-polarisation, where the wavevector of the incident field is parallel to the dimer axis (Figure 2.15a) whereas the bright mode was excited when the wavevector of the incident field was perpendicular to the dimer axis.

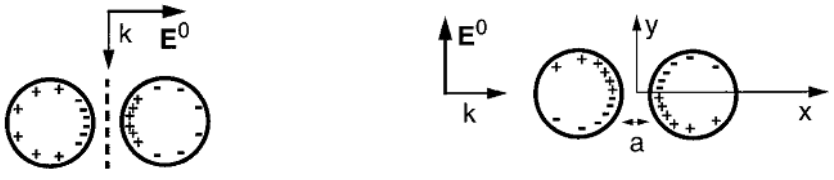

(a) (b)

Figure 2.14: The excitation of (a) bright and (b) dark modes in two identical cylindrical particles [63].

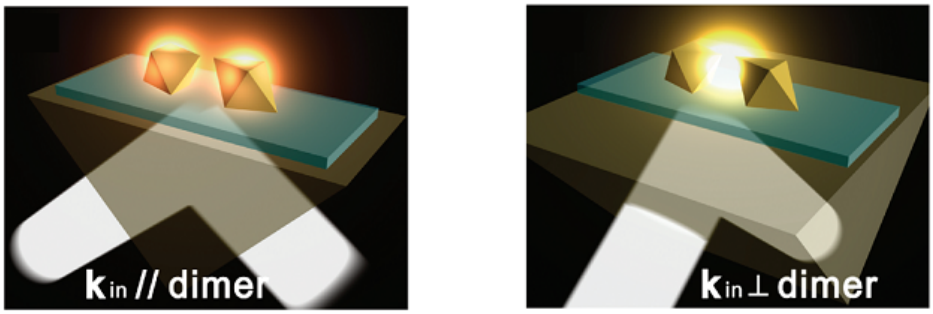

(a) (b)

Figure 2.15: The excitation of bright and dark modes in two gold octahedra using prism coupling [64]. The dark mode was excited with arrangement in Fig. (a) whereas the bright mode was excited with arrangement in Fig. (b), both using p-polarisation.

Dark modes on a dimer can also be excited using asymmetric particles. An example is shown in Figure 2.16a, where two asymmetric rods are closely located with a small gap between them [20]. Two modes can be excited with normally incident plane wave. Figure 2.16b shows the simulated transmission spectra through the array of dimers. Black solid line is the spectrum when the length difference of the particles $\alpha = \Delta L = 0$, where it exhibits only the bright mode. When $\alpha \neq 0$, represented by red dashed line, two modes are excited. The anti-symmetric (dark) mode is resonant at a shorter wavelength compared to the symmetric (bright) mode.

An example in Figure 2.17 can be used to demonstrate radial and azimuthal modes. Consider a trimer structure consist of three nanodisks arranged symmetrically [65]. By calculation using the discrete dipole approximation, all possible modes of the structures are obtained. Depending on the exciting light one or more modes may be excited.

Modes B (breathing) and R (rotation) have no net dipole moments so that they are not easily coupled to propagating light. Mode B is a radial mode since it oscillates radially and mode R is an azimuthal mode because the oscillations circulating around the centre.

Another example is given in nanostructures made of six nanodisks [66], shown in Figure 2.18(a). The structures were modelled by assuming illumination with a radially polarised beam, resulting in excitation of the radial mode.

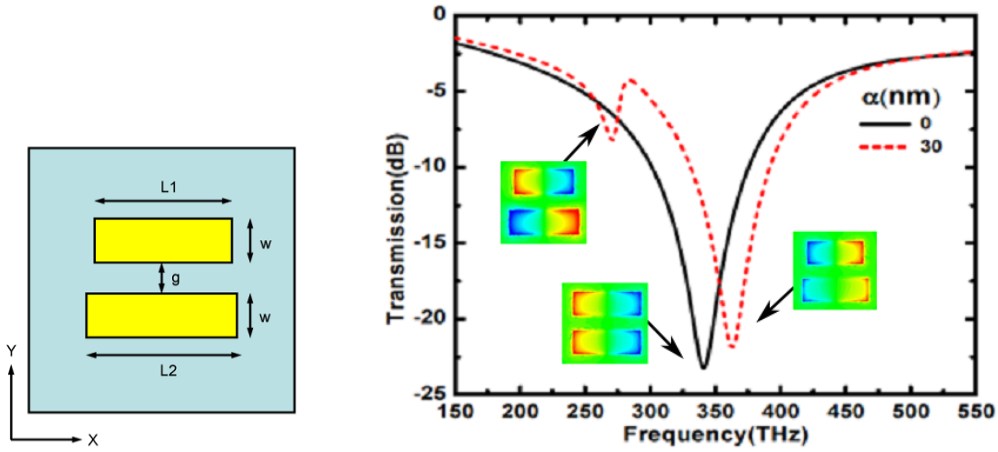

(a) (b)

Figure 2.16: The excitation of bright and dark modes using asymmetric nanorods with different lengths [20]. (a) Schematic of the dimer and (b) the transmission spectra using normally incident plane wave, where black solid line represents symmetric rods and red dashed line represents asymmetric rods. Inset in (b): corresponding surface charge at the resonances.

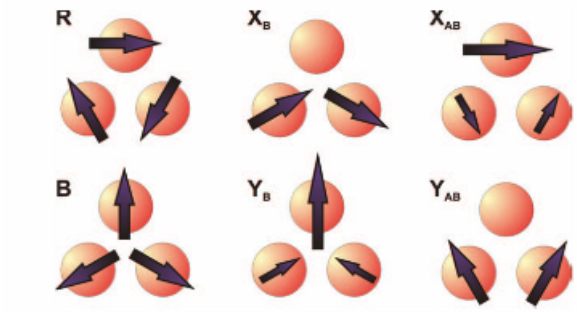

Figure 2.17: All possible modes are on silver nanodisk trimer [65]. B stands for the collective breathing-mode, R for the rotation mode, X_B/Y_B for the bonding (low energy) modes polarised along x/y and X_{AB}/Y_{AB} stands for the corresponding anti-bonding (high energy) mode

This equivalently produced an azimuthal magnetic field (Figure 2.18(b)) on and around the structures and this mode is also referred to as a toroidal dipole mode.

Sub-radiant mode excitation is also observed on a nanostructure consisting of a gold disk inside a thin gold ring [67]. Both dark and bright modes appear and the structure is very sensitive to the refractive index. A sub-radiant mode exists in a radial structure of three nanorods, a radial trimer excited with radi-

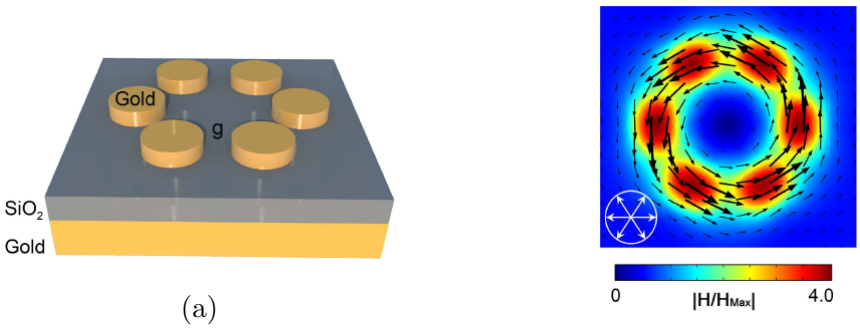

(a) (b)

Figure 2.18: (a)Nanostructures consisting of six symmetrically arranged gold nanodisks and (b) the magnetic field on the structures when excited with radially polarised beam [66].

ally polarised light [21], shown in Figure 2.20. The radial mode on the nanorod trimer was found to have a greater energy compared to the dipole mode so that its resonance frequency is shorter than that of the dipole mode.

On the other hand, structures with azimuthal symmetry may also be excited using azimuthally polarised light. An oligomer consisting of seven nanoparticles (a heptamer), shown in Figure 2.21, has both radial and azimuthal symmetry. These modes can be excited either by radial or azimuthal polarised beams, affecting the location of the hot spots within the structure [68].

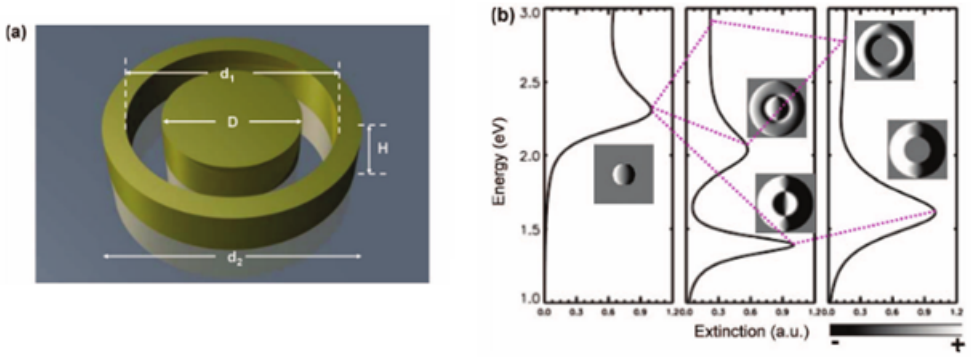

Figure 2.19: (a) Geometry of nanostructure consisting of a disk inside a thin ring. (b) Hybridization diagram for gold nanostructure in vacuum showing both sub-radiant and super-radiant modes, calculated by simulation [67].

Fano-resonance [69] plays an important role in characterisation of modes of metasurfaces. A Fano resonance exhibits an asymmetric resonance lineshape, in contrast to a Lorentzian lineshape. This type of resonance occurs due to

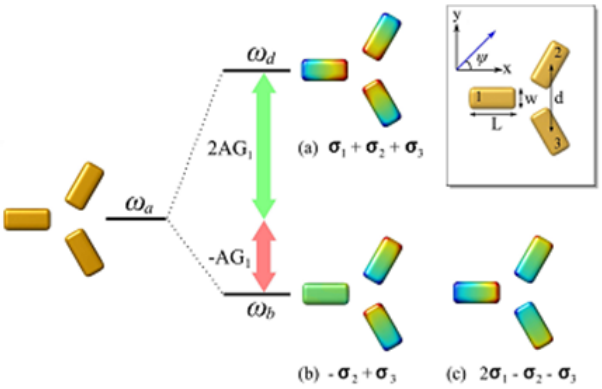

Figure 2.20: The radially arranged nanorod trimer is excited with radially polarised light. Some results may arise for different modes of the excited state [21].

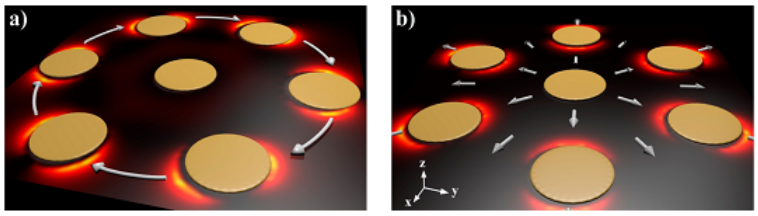

Figure 2.21: Heptamer antenna structure is excited with (a) azimuthally and (b) radially polarised light, producing enhancement of the intensity in different arrangement [68].

the interference between the directly excited and modes excited by near-field interactions, which in this case, are the radiant and sub-radiant modes. The incident light mainly interacts with the radiant mode (via the far-field), and this excitation leads to an excitation of the sub-radiant mode (via the near-field), provided there is some degree of spectral overlap between these modes. An example in Figure 2.22 shows the scattering spectrum of a solid spherical metal nanoparticle, exhibiting higher order Fano resonances, which are the dipole, quadrupole, and octupole modes. Similar resonances can be found in an ensemble of nanoparticles in a metasurface.

2.4 Chapter Conclusion

Metasurfaces consist of sub-wavelength structures arranged in a plane that have a strong interaction with electromagnetic waves. The building blocks of

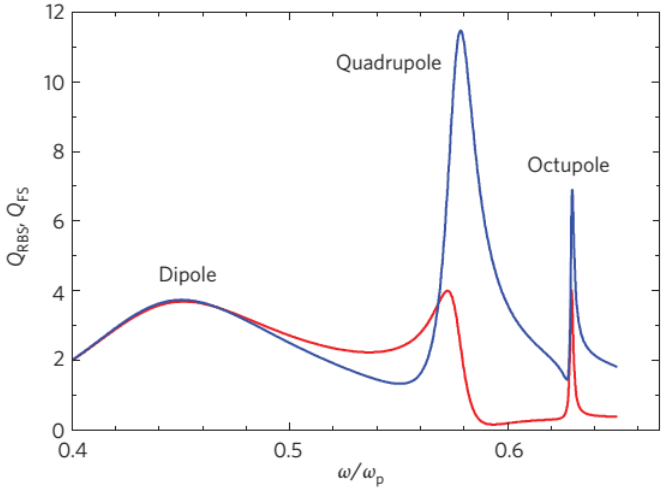

Figure 2.22: The higher-order Fano resonances at spherical metal nanoparticle in its radar back scattering (red) and forward scattering (blue) [69].

metasurfaces are optical antennas, consisting of one or more metallic nanoparticles or nanoapertures designed to have a specific optical response. Using these devices, electromagnetic waves can be controlled over a sub-wavelength distance. Several examples of metasurfaces were also discussed.

Optical antennas consist of some arrangement of metallic nanoparticles or nanoapertures with typical sizes in the range of tens to hundreds of nanometers for operation at optical frequencies. An optical antenna has the ability to couple propagating radiation into localised fields, or vice-versa, mimicking antennas at radio and microwave frequencies. Optical antennas utilise localised surface plasmons on nanoparticles which are very dispersive and very sensitive to light.

Optical antennas can sustain modes of surface charge oscillation that can be categorised into radiant and sub-radiant modes. Examples of modes on optical antennas were discussed. In the next chapter, methods for modelling and designing metasurfaces are discussed. Two modelling methods used in this thesis are summarised and types of illumination to excite the modes are also presented.

Chapter 3

Methods for Modelling Optical Antennas and Metasurfaces

3.1 Methods for Solving Electromagnetic Problems

The interaction between metasurfaces and electromagnetic waves can be analysed by solving Maxwell's equations for the system. To solve the equations, analytical or numerical approaches may be used. The range of problems that can be solved analytically, however, is very limited. Many numerical methods can be computationally intensive and approximate techniques can be a useful complement that may also provide additional insight into antenna and metasurface performance. In this chapter the methods used in this project are introduced.

Mie theory is an analytic method for modelling spherical nanoparticles embedded in homogeneous medium by expanding the fields into a set of normal modes [6]. This is a rigorous approach and can be used for spherical antennas of arbitrary size and composition. It also provides a useful method for validating computational results. Metal nanoparticles with ellipsoidal shapes may also be calculated using this analytical approach [70].

One example of an analytical approximation method to describe optical antennas is the quasi-static approximation [8]. In this method, the structure size

is assumed to be much smaller than the wavelength used. Locally homogeneous oscillating electric and magnetic fields that act on the nanostructures are used to calculate the excitation. Other analytic approaches rely heavily on the symmetry of the structures under study to simplify the problem.

The electrostatic eigenmode method (EEM) is one approximate method used in this study [71, 72]. This method begins with solving for the self-sustained surface charge oscillations that satisfy the eigenvalue problem. A small number of dominant modes of oscillation are then used for calculating the interaction of the fields from one particle with neighbouring nanoparticles. These dominant modes are usually the lowest energy modes in the form of dipole modes. The interaction between neighbouring nanoparticles can be described via near-field coupling and the coupled amplitudes of excitation are then found by solving a matrix equation. This matrix equation uses the amplitudes of modes of uncoupled nanoparticles and the size of matrix to be solved is $N \times N$, where N is the number of particles. Once the coupling is known, their interaction with incoming electromagnetic waves can be determined. EEM assumes that the size of the nanoparticles and their separations are much smaller than the wavelength used so that phase variations are neglected.

In order to use the EEM, some knowledge of the resonances of individual particles must be assumed. In order to determine input quantities such as the resonance frequency and linewidth of a nanoparticle resonance, a more precise computational method is required. The amplitudes of excitation on the ensemble of particles can then be used to identify the modes excited.

Maxwell's equations can be written in either integral or differential form. Based on these forms, two distinct types of numerical methods can be used to solve the equations for the full field. The discrete dipole approximation (DDA) [73] and boundary element method (BEM) [74] are two examples of numerical methods solving the integral forms of Maxwell's equations. On the other hand, the differential forms of Maxwell's equations are solved numerically by methods such as the finite-difference time-domain (FDTD) method [75, 76] and the finite-element method (FEM) [77, 78].

The FDTD method is used to solve Maxwell's equations in the time domain by discretising the equations in both space and time. This method mainly uses the Ampere-Maxwell law and Faraday's law to calculate the change in

electromagnetic fields with time while implicitly implementing the other two laws within the simulation. More details are provided in Section 3.2 in this chapter.

In this research, two different implementations of the FDTD method were used. The first was written by me using MATLAB which was used to perform preliminary calculations. The 'home-made' FDTD tool consists of a three dimensional simulation with PML (Perfectly Matched Layers) boundary conditions which can be changed into periodic boundary conditions if needed. PML is used to terminate infinite boundary conditions so that the outgoing waves will not be reflected back into the simulation. Periodic boundary conditions are used for simulating periodic structures (Section 3.2.2).

A limitation of the original implementation of the 'home-made' FDTD code was that it was limited to normally incident plane waves. Rather than develop this program further, the commercial FDTD software produced by Lumerical Solutions was used. This permitted more flexibility than the 'home-made' code to excite the structures with plane waves with various angle of incidence and polarisations. Other advantages include non-uniform meshing for better use of memory and processor efficiency as well as superior modelling visualisation tools.

For those reasons, most modelling results appearing in this thesis were calculated using a commercial implementation of FDTD produced by Lumerical Solutions. The version used was FDTD Solutions 8.9. The self-written codes, however, provided invaluable insights into the fundamentals of FDTD, its limitations, and key features. In particular, treating simulation software as a 'black box' can lead to erroneous input and misinterpretation of results.

3.2 The Finite-Difference Time-Domain (FDTD) Method

Electromagnetic waves propagate in space as self-sustaining oscillations of electric and magnetic fields. By performing simulations with the FDTD method, the nature of electromagnetic waves propagating through any media or interacting with any objects can be analysed by solving Maxwell's equations. The

Ampere-Maxwell law and Faraday's law of induction are solved as coupled equations for the electric and magnetic fields as a function of space and time. The other two of Maxwell's equations (Gauss' law for electricity and magnetism) are not used explicitly for solving the problem. They are intrinsically satisfied, however, by the choice of grid used in the simulation which is selected to satisfy the divergence-free condition when no charge is present. Both electric and magnetic fields are solved in the time-domain, i.e. $\vec{E} = \vec{E}(\vec{r}, t)$ and $\vec{H} = \vec{H}(\vec{r}, t)$, where $\vec{r}$ is the vector position and t is time.

The FDTD method is very flexible and can be used to model a wide variety of structures as the properties of the materials are placed on the desired grid cells to fit any shapes or structures. The Cartesian coordinate grids, however, used in the FDTD usually lead to a curved material boundary becoming staircased which will affect the accuracy of the simulation. In order to overcome this problem, finer meshing can be used but this requires more memory, requiring a trade off between accuracy and numerical considerations.

The sub-cell updating algorithm on material boundaries can be applied to fix the staircasing problem [79, 80]. The stability of these algorithms for metal and dielectric boundaries must be checked prior to use. It is usually safer to keep the stair-cased boundaries than to use sub-cell algorithm for metal and dielectric interfaces.

Any type of electromagnetic source can be used in the FDTD simulation, from a dipole point source to a plane wave source. They are introduced via a defined electric current density $\vec{J}$. There is however the requirement of time-step in the simulation to satisfy the Courant - Friedrichs - Lewy (CFL) condition to achieve convergence of the results. The condition is

$$\Delta t \leq \Delta t_{max} = \frac{1}{c\sqrt{\frac{1}{\Delta x^2} + \frac{1}{\Delta y^2} + \frac{1}{\Delta z^2}}}, \tag{3.1}$$

where $\Delta t, \Delta x, \Delta y,$ and Δz is the meshing (or step) in time and $x, y,$ and z directions respectively, and c is the speed of light in vacuum. The maximum time-step reduces to $\Delta t_{max} = \Delta s/(c\sqrt{3})$ when meshes are equal in all directions, $\Delta x = \Delta z = \Delta z = \Delta s$. Finer meshing of the grids makes the required time-step smaller, but making the computation time n^4-times longer if the meshing is n-times smaller in three dimensional simulations.

3.2.1 Implementation of Maxwell's Equations in the FDTD Method

In linear media, the Ampere-Maxwell and Faraday laws are given by

$$\nabla \times \vec{H} = \vec{J} + \varepsilon \frac{\partial \vec{E}}{\partial t}, \tag{3.2}$$

$$\nabla \times \vec{E} = -\mu \frac{\partial \vec{H}}{\partial t}, \tag{3.3}$$

where $\vec{E}$ and $\vec{H}$ are the electric and magnetic fields, $\vec{J}$ is the electric current density, and ε and μ are the electric permittivity and magnetic permeability of the medium. Others have introduced magnetic current $\vec{J_m}$ in Equation 3.3 to make two equations appear more equivalent. Applying this, the right hand side of the equation becomes $\vec{J_m} - \mu \partial \vec{H}/\partial t$. The electric and magnetic currents are respectively given by

$$\vec{J} = \sigma \vec{E} + \vec{J}_{ext} \tag{3.4}$$

$$\vec{J_m} = \sigma_m \vec{H} + \vec{J}_{m,ext} \tag{3.5}$$

where σ and σ_m are electric and magnetic conductivity of materials, and $\vec{J}_{ext}$ and $\vec{J}_{m,ext}$ are external electric and magnetic current sources.

The FDTD was initially developed for use at radio and microwave frequencies and metals are described by their conductivity σ which is usually large. However, at optical frequencies, metals are far from a perfect conductor and they are very dispersive. As a result, they will need to be treated differently and a special algorithm is used for describing them in optical frequencies. Most materials are non-magnetic at optical frequencies so the $\vec{J_m}$ term can be omitted.

To implement these two equations in the simulation, all the derivatives need to be converted into finite-difference form. For example, $\partial \vec{E}/\partial t$ becomes $\Delta \vec{E}/\Delta t$, where $\Delta \vec{E}$ is the change of $\vec{E}$ in time-interval Δt. After converting Equation 3.2 and 3.3 into finite-difference form, the equations become:

$$\begin{vmatrix} \hat{i} & \hat{j} & \hat{k} \\ \frac{1}{\Delta x} & \frac{1}{\Delta x} & \frac{1}{\Delta x} \\ \Delta H_x & \Delta H_y & \Delta H_z \end{vmatrix} = (J_x\hat{i} + J_y\hat{j} + J_z\hat{k}) + \varepsilon \left(\frac{\Delta E_x\hat{i} + \Delta E_y\hat{j} + \Delta E_z\hat{k}}{\Delta t} \right) \quad (3.6)$$

$$\begin{vmatrix} \hat{i} & \hat{j} & \hat{k} \\ \frac{1}{\Delta x} & \frac{1}{\Delta x} & \frac{1}{\Delta x} \\ \Delta E_x & \Delta E_y & \Delta E_z \end{vmatrix} = -\mu \left(\frac{\Delta H_x\hat{i} + \Delta H_y\hat{j} + \Delta H_z\hat{k}}{\Delta t} \right). \quad (3.7)$$

By splitting the above equations for each of the vector components ($\hat{i}, \hat{j},$ and $\hat{k}$), the two equations now become six. After re-arranging the terms, the equations become

$$\frac{\Delta E_x}{\Delta t} = \frac{1}{\varepsilon}\left(\frac{\Delta H_z}{\Delta y} - \frac{\Delta H_y}{\Delta z} - J_x \right) \quad (3.8a)$$

$$\frac{\Delta E_y}{\Delta t} = \frac{1}{\varepsilon}\left(\frac{\Delta H_x}{\Delta z} - \frac{\Delta H_z}{\Delta x} - J_y \right) \quad (3.8b)$$

$$\frac{\Delta E_z}{\Delta t} = \frac{1}{\varepsilon}\left(\frac{\Delta H_y}{\Delta x} - \frac{\Delta H_x}{\Delta y} - J_z \right) \quad (3.8c)$$

$$\frac{\Delta H_x}{\Delta t} = \frac{1}{\mu}\left(\frac{\Delta E_z}{\Delta y} - \frac{\Delta E_y}{\Delta z} \right) \quad (3.9a)$$

$$\frac{\Delta H_y}{\Delta t} = \frac{1}{\mu}\left(\frac{\Delta E_x}{\Delta z} - \frac{\Delta E_z}{\Delta x} \right) \quad (3.9b)$$

$$\frac{\Delta H_z}{\Delta t} = \frac{1}{\mu}\left(\frac{\Delta E_y}{\Delta x} - \frac{\Delta E_x}{\Delta y} \right) \quad (3.9c)$$

The above equations are six updating equations for electric and magnetic fields ready for implementation in an FDTD simulation. These six equations are used for calculating the changes in electric and magnetic fields as a function of time.

All six equations in Equation 3.8 and 3.9 are used in the FDTD simulation for calculating the electric and magnetic fields. The implementation of these equations into the simulation grid is done by using the Yee algorithm [75,76,81]. This algorithm efficiently solves for both electric and magnetic fields altogether, not separately. In the implementation, the electric and magnetic fields are updated alternately in each time-step. The $\vec{E}$ fields are updated at half time-steps

between the updates of the $\vec{H}$ fields, and vice versa. This takes the advantages of coupled electric and magnetic equations from Ampere-Maxwell and Faraday laws. Solving for both electric and magnetic fields gives more accurate results rather than solving for the electric or magnetic fields separately. As a result, the FDTD method is very flexible for modelling any structures without losing information about the fields if solved separately.

3.2.2 Boundary Conditions

3.2.2.1 Perfectly Matched Layers (PML)

Any computer has limited memory to process simulations. As a result, the size of the modelled region is also limited. However, it is usually of interest to model a situation where incoming waves interact with objects and then scatter to infinity. The problem is those waves will be reflected back into the simulation region after scattering from the edge or boundary of the simulation region. In order to prevent this, something must be put at the boundaries that can absorb outgoing waves. The established boundaries for this purpose are called perfectly matched layers (PML). These layers absorb waves of any frequency and polarisation coming at any angle to the simulation boundaries. The effectiveness of PML, however, still depends on the frequency and angle of incidence, but the variation can be minimised by optimising the PML parameters.

PMLs use anisotropic layers for absorbing all possible outgoing waves propagating at any angle, polarisation, and frequency. The outgoing waves are absorbed gradually until they reach zero amplitude at the boundaries so ideally nothing is reflected back. The lossy parameters of PML are σ_e and σ_m for absorbing electric and magnetic fields respectively. There is also a parameter a to handle low-frequency wave reflections and κ to stretch the meshing inside the PML. All these parameters are anisotropic and the conditions for each boundary can be solved with Berenger's split-field formulation [82].

PMLs are placed inside the simulation regions at the boundaries. Figure 3.1 shows the location of the PML inside the simulation region, on a two dimensional xy-slice at $z = 0$. A similar configuration also applies along the

z-direction. There are overlap regions of boundaries at the edges to absorb the outgoing wave component parallel to the boundary. At the corners, there are overlapping PML regions for the $x, y,$ and z sides. These PMLs are applied on all three dimensional boundaries when 'infinity boundary conditions' are needed in all directions. In the case of two dimensional periodic structures, PMLs are applied in only one direction with the other boundaries being periodic boundary conditions

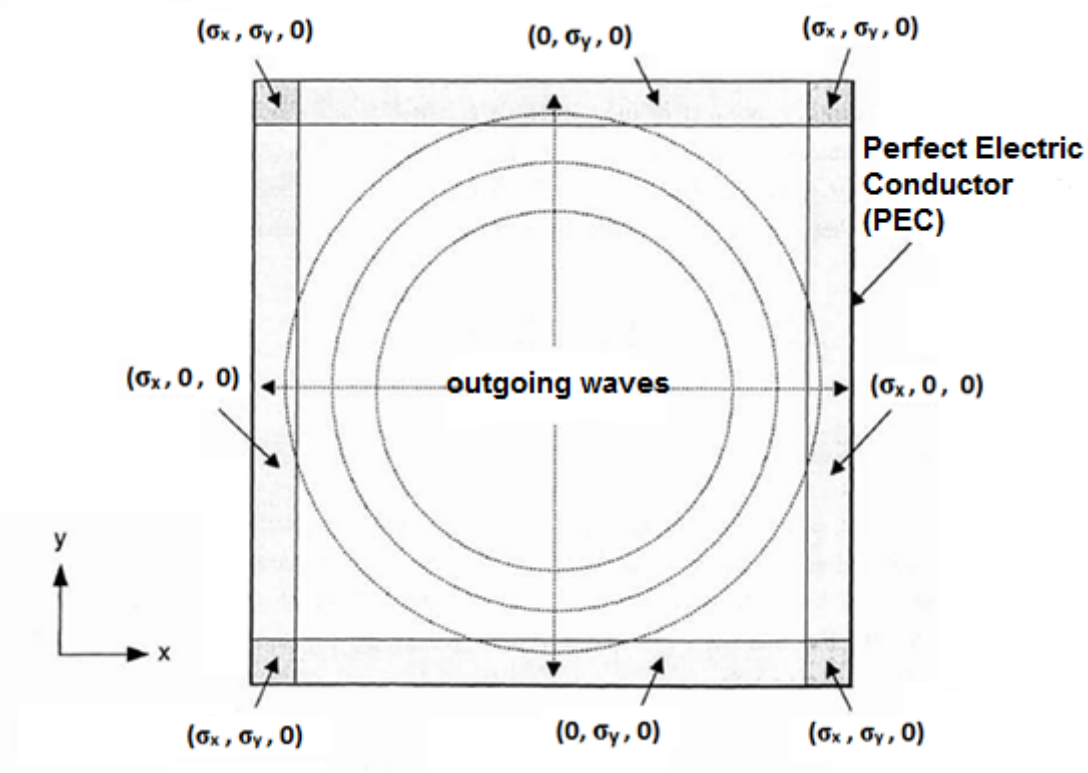

Figure 3.1: The PML on 2D xy-slice at $z = 0$ inside the simulation region [75].

3.2.2.2 Periodic Boundary Conditions

Periodic boundary conditions (BCs) are used for modelling periodic structures where the structures are assumed to be infinite. These BCs are applied in the direction(s) in which the structures are periodic and they can be combined with PML BCs on the direction(s) where there is no periodicity. The implementation of periodic BCs for normally (parallel to one of the main axes) and off-normally (making an oblique angle to this axis) incident waves are different. More complex algorithms are used for modelling off-normal excitation of

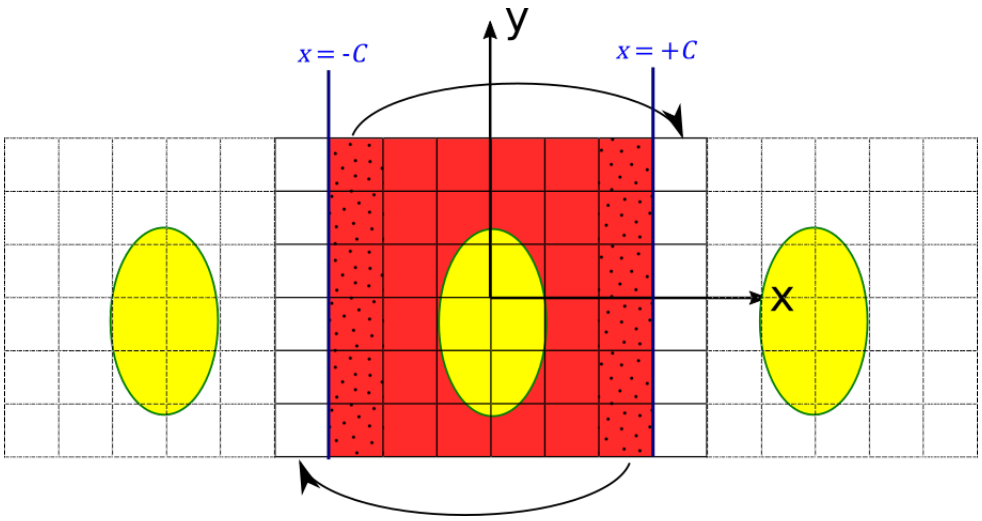

Figure 3.2: Example of periodic BCs implementation where the structures are periodic along x directions with normally incident fields. Red region is the simulation region with an oval object inside. White regions are neighbouring unit cells of the periodic structures.

periodic structures.

For normally incident waves on periodic structures, the implementation of the periodic BCs is simple. This can be done by copying the known fields from the opposite boundary. A scheme is shown in Figure 3.2 for two dimensional slice along z = constant, simulating periodic structures along $x-$axis with the incident wave propagating along the $z-$axis (into or out of the page). The red-coloured area is the simulation region and the blue lines are the periodic boundaries of the simulation. The fields known at $x = -C$ boundary (red dotted layer) are copied into $x = +C$ boundary, and the other way around, from $x = +C$ to $x = -C$. By doing this, simulation of periodic arrays requires a solution for only one FDTD unit cell. Similar steps can also be done if the structures are periodic in two dimensions.

There are many methods for solving prolems involving oblique incidence waves on periodic structures. Each method has its limitations. One method called the sine-cosine method is relatively easy to implement but it works only for a single frequency [75]. The other alternative method that works with broadband fields is the angle-update method, but the maximum angle of incidence it can handle is 45° [75]. The electromagnetic (EM) fields used in FDTD are generally real-valued. The complex-valued EM fields are to be used only for special cases

because they take more computer memory and calculation time. Modelling off-normally incident plane waves on periodic structures are available in Lumerical FDTD Solutions software. As it has proprietary license, the method used for off-normally incidence in this software is not described in the documentation and it is not possible to state which algorithm is used.

3.2.3 The Plane Wave Source

In an FDTD simulation, various type of sources can be used to investigate the response of the objects and surrounding media with the incident fields. This includes dipole point sources, plane waves, and Gaussian beams. In this study, the only sources used were plane waves. Although experiments were performed using focussed optical fields, these beams can be written as a superposition of plane waves with different wavevectors and polarisations. To calculate the reflectance of focussed beams from periodic surfaces would have required a large number of computationally intensive calculations, so the use of FDTD was restricted to being used to find parameters to input into the EEM model and to verify its results.

Plane waves can be generated in FDTD simulations using the 'total field/ scattered field' (TFSF) technique. The TFSF boundaries separate the simulation region into two regions called the total field (TF) region and the scattered field (SF) region. A schematic showing TFSF regions and boundaries is shown in Figure 3.3. The object being modelled lies inside the TF region and the excitation field exists only in the TF region. As the incident field interacts with the objects and is scattered and absorbed, the field inside this box is the total field. When the field enters the SF region, the incident/undisturbed fields are subtracted from the total field, so that the field in this region is the scattered field. Only the field nodes located next to these boundaries require TFSF correction so that the algorithm does not require a lot of computer memory and processing time.

To inject a plane wave source into the total field region, a one dimensional auxiliary simulation is used. This auxiliary simulation runs simultaneously with the main simulation and its direction is parallel to the propagation direction of the plane waves. A schematic of the TFSF technique in a two dimensional slice

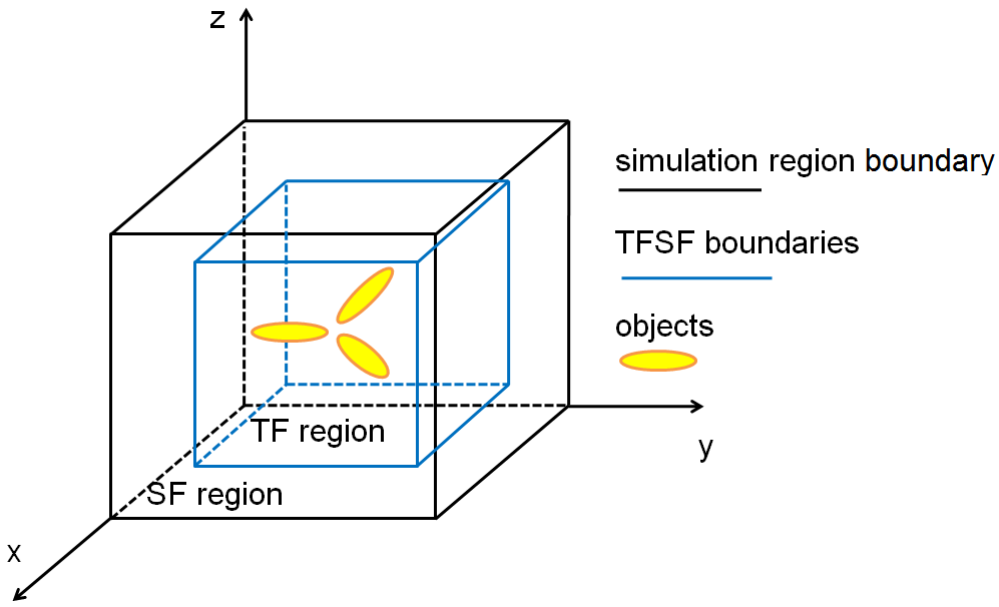

Figure 3.3: The simulation using TFSF boundaries.

through the boundaries is shown in Figure 3.4. The arrowed line corresponds to the propagation of the injected plane wave. Along that line, there are field nodes for the auxiliary one dimensional simulation. Only the incident field is included in that auxiliary simulation. The corrections on the TFSF boundaries in the main simulation are done based on the incident field simulated in the auxiliary simulation. Each node to be corrected corresponds to one node in the auxiliary simulation, where the dotted lines are drawn. The corrections are performed for all six boundaries separating the TF and SF regions. In general, the incident field can be chosen to be in any direction with respect to the main axis of the main simulation.

3.2.4 Modelling the Optical Properties of Metals

In the FDTD method, the modelling of highly dispersive materials such as metals is critical. To describe metal dispersive properties at optical frequencies, various models can be used. The Drude model uses a semi-classical approach where free electrons in the materials are modelled as a plasma or a free electron gas. The plasma is driven by the oscillating electric field from an electromagnetic wave and is defined by a plasma frequency, ω_D, and damping

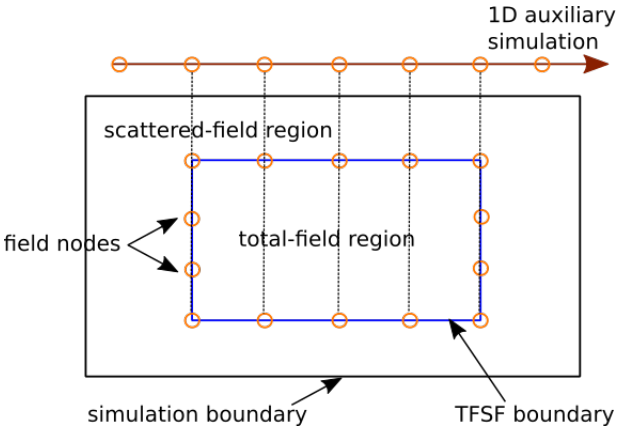

Figure 3.4: The scheme for injecting plane wave source into the simulation using TFSF boundaries, shown at the two dimensional slice of simulation region, where the field nodes on the TFSF boundaries are corrected based on the auxiliary simulation.

constant, γ. The permittivity $\varepsilon(\omega)$ of metals using this model is given by

$$\varepsilon(\omega) = \varepsilon_\infty - \frac{\omega_D^2}{\omega^2 + i\gamma\omega} \tag{3.10}$$

where ε_∞ is the background permittivity.

The Drude model is, however, valid in only certain frequency ranges as it fails to reproduce the dielectric function of metals at higher frequencies. This is caused by the interband transition of electrons which is not included in the model [8]. At wavelengths shorter than a critical value, the Drude model is no longer valid. This failure occurs at wavelengths below approximately 600 nm for gold and 400 nm for silver.

The failure of the Drude model at short wavelengths can be addressed by modifying the formula by adding more terms to the simple Drude models. The new parameters, together with the (previous) Drude model parameters, are fitted to experimental data. The modification of the Drude models for FDTD implementation are, for example, the Drude-Lorentz (DL) model [83, 84] and the Drude-Critical Points (DCP) model [85–87]. The performance of the DCP model for gold and silver with specific fitting parameters was studied to be more efficient than the DL model [88].

Lumerical FDTD Solutions does not disclose in detail the approach used for modelling the metal properties. It uses a database of the complex permittivity

of various materials obtained experimentally. Once the simulation bandwidth is established, the software uses multi-coefficients model to fit the properties within the simulation bandwidth. The formulation of this model is not described in any detail in the documentation. The approach is potentially similar to the one discussed here. The coefficients are calculated to fit the ranges of provided data and the updating formulations are modified by including all the coefficients calculated previously.

3.2.5 Simulations in Lumerical FDTD Solutions

Lumerical FDTD Solutions (LFS) is a commercial simulation engine for solving electromagnetic problems with the FDTD method. Here the simulation set-up used for modelling the metasurfaces under study are discussed. The version used was LFS 8.9. Figure 3.5 shows an example of three dimensional view of the set-up used.

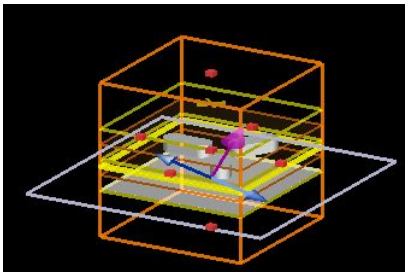

Figure 3.5: Three dimensional view of simulation set-up in Lumerical FDTD Solutions.

Two dimensional slices through the set-up used in this project are shown in Figure 3.6. The set-up consists of four important components: the FDTD simulation region (A), electromagnetic source (B), objects (C), and detectors (D-1 to D-4). The FDTD simulation region sets the simulation region to be calculated and this includes boundary conditions. The sources define the excitation of electromagnetic waves into the simulation region. Objects are the structures to be studied consisting of either trimer or tetramer arrangements of nanorods, with either radial or azimuthal symmetry. Detectors are placed on locations where data will be recorded, for example, to calculate the transmittance and reflectance, two 2D-detectors are placed sandwiching the antennas.

The general parameters of the simulation are set in the FDTD simulation re-

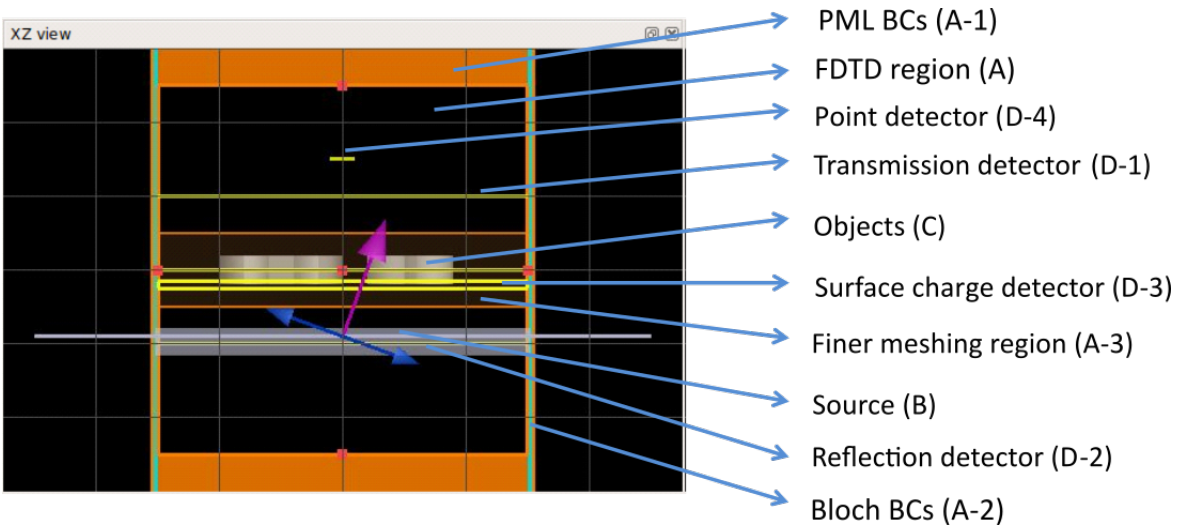

(a)

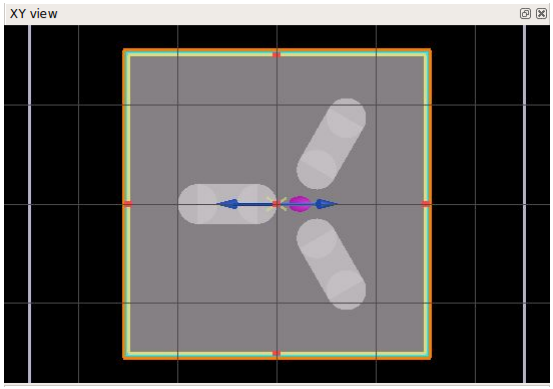

(b)

Figure 3.6: The two dimensional slice of the simulation set-up at (a) $xz-$plane and (b) $xy-$plane. The metasurface is located at $xy-$plane and the light propagates at an angle to the $z-$axis.

gion (A). These include the size of the simulation region, refractive index of the background media, meshing options, and boundary conditions. The simulation region has a cross-section of a unit cell of the metasurface being modelled. The background media, which is $n = 1.5$ for the case studied here, can be set under this FDTD simulation region set-up. The size of the simulation region parallel to the metasurface (along x- and y-directions) is equal to the periodicity of the structures and in the direction normal to the metasurface (the z-direction), the size was 1000 nm.

There are many options for meshing and they include 'uniform', 'auto non-uniform', and 'manual non-uniform'. 'Uniform' means the mesh throughout

the simulation region is uniform and 'auto non-uniform' corresponds to graded meshing with automatic selection of parameters. 'Manual non-uniform' meshing was used in this project so that meshing parameters can be controlled. Finer meshing can be set in the region near the structure under investigation (A-3). The meshing was uniform along the x- and y-directions and graded along z-direction. Metasurfaces are placed parallel to the $xy-$plane. In the case of off-normally incident illumination, the wavevector makes an angle θ with respect to the z-axis.

There are many boundary conditions available in LFS. The ones that were used in this study were PML BCs, periodic BCs, and Bloch BCs. These boundary conditions were discussed in Section 3.2.2. PML BCs are used at z- boundaries (A-1) and periodic or Bloch BCs are used at x- and y-boundaries (A-2). In LFS, both periodic BCs and Bloch BCs are used for periodic structures but the usage is different. Periodic BCs are used for periodic structures illuminated by normally incident waves, e.g. metasurfaces on xy-plane illuminated by plane waves propagating along the z-direction. Bloch BCs are used for simulating periodic structures with off-normally incident illumination. If Bloch BCs are used, all the fields in the simulation use complex values. All other BCs calculate only real-valued fields. This means that simulations using periodic BCs are calculated faster than those with Bloch BCs for normal incidence.

The source used in the modelling in this study is a plane wave source (B). The manual states that the size of the source must be extended up to the edge of the simulation region so that a perfect plane wave is produced. The source size was set to be larger than the FDTD region so that the source always extended up to the edge of the simulation boundaries. The component of the plane wave source outside the FDTD region is not calculated by the program.

The objects in each unit cell are silver-nanorod antennas (C). Nanorods were modelled to have rounded corners. This can be done by overlapping one block with two cylinders, shown in Figure 3.6(b). The antenna material was silver (Ag) with data taken from Johnson and Christy data [42] and fitted over the range of wavelength used (500 nm to 1000 nm). More detailed information about the designs investigated are available in Chapter 4.

The last components defined in the model are detectors. There were several detectors used in the simulation for modelling the metasurfaces. There are two

dimensional detectors for recording transmission (D-1) through and reflection (D-2) from the metasurfaces, indicated by yellow lines. These detectors convert signals into the frequency domain. There is also a detector for recording the surface charges on the nanorods (D-3), also in the frequency domain. There is a point detector behind the structures to record the amplitude and power of the electromagnetic waves in time domain (D-4), used for checking the convergence of the simulation. If the simulation is converged, the amplitudes and power approach zero at the end of simulation for large times.

3.3 The Electrostatic Eigenmode Method (EEM)

The electrostatic eigenmode method uses the electrostatic approximations. This means that only electric fields are considered in the calculation and magnetic fields are assumed to follow the same behaviour as electric fields. The spatial variation of the propagating waves is also neglected by assuming the wavelength is much larger than the particle size so that retardation over the particle is neglected. As a result, this method is not as accurate as rigorous full-field methods such as the FDTD or the finite element method (FEM). The model contains several fitting parameters and will not be able to precisely predict the spectral locations or linewidths of resonance.

Since the EEM relies on the electrostatic approximation, it requires the length scale to be very small, i.e. $kd << 1$, where k is the wavelength in the medium, and d is the dimension of the particle. The accuracy of the EEM compared to the FDTD has been demonstrated for a silver nanorod with the shape of hemispherically capped cylinder in [89]. The EEM was shown to be particularly good at predicting the spectral location of higher multipolar modes of the particles. For example, it was reported in the literature that a rod with a length of 230 nm ($kd = 1.6$) has errors below 8% in calculating the spectral location of the second order mode and higher, but the fundamental mode had an error of 18%.

With those limitations, however, this method is extremely useful because it provides physical insight into mode excitation and coupling between particles. It describes the interactions between the modes of surface charge oscillations

of nanoparticles and the incident fields and their near-field interactions with neighbouring nanoparticles. The interactions are solved to obtain the coupled excitation amplitudes in response to incident electromagnetic fields. The EEM is also relatively simple to implement in calculations and a large amount of computer memory is not required since simulations are not time-consuming.

3.3.1 EEM Formulation

Here the formulation for the EEM method developed in refs. [71, 72, 90] is summarised for completeness. The formulation begins with Coloumb's law that describes the relationship between the electric field $\vec{E}(\vec{r})$ at position $\bar{r}$ produced by electrical charge $q(\vec{r'}) = \sigma(\vec{r'})dS'$ at position $\vec{r'}$ from a piece of surface with area dS'.

$$\vec{E}(\vec{r}) = \frac{1}{4\pi\varepsilon_0} \oint \sigma(\vec{r'}) \frac{(\vec{r} - \vec{r'})}{|\vec{r} - \vec{r'}|^3} dS' \tag{3.11}$$

Using Gauss' law, the normal component of electric displacement fields $\vec{D} = \varepsilon\vec{E}$ is continuous across boundary so that the relationship between electric field on the metal $\vec{E}_m$ and electric field on the dielectric background $\vec{E}_b$ can be written as

$$\varepsilon_m \vec{E}_m \cdot \hat{n} = \varepsilon_b \vec{E}_b \cdot \hat{n} \tag{3.12}$$

where ε_m and ε_b is the permittivity of the metal and dielectric background respectively, and $\hat{n}$ is the unit vector normal to the surface at $\vec{r}$.

The electric field at position $\bar{r}$ originates from surface charge at $\vec{r}$, plus surface charges from all over the surface. Taking the normal component of electric field, Equation 3.11 becomes

$$\vec{E}_{m,b}(\vec{r}) \cdot \hat{n} = \mp \frac{\sigma(\vec{r})}{2\varepsilon_0} + \frac{1}{4\pi\varepsilon_0} \oint \sigma(\vec{r'}) \frac{(\vec{r} - \vec{r'}) \cdot \hat{n}}{|\vec{r} - \vec{r'}|^3} dS' \tag{3.13}$$

The electric fields in Equation 3.13 is then substituted into Equation 3.12,

giving the eigenvalue problem for surface charge, given by

$$\sigma(\vec{r}) = \frac{\gamma}{2\pi} \oint \sigma(\vec{r'}) \frac{(\vec{r} - \vec{r'}) \cdot \hat{n}}{|\vec{r} - \vec{r'}|^3} dS', \tag{3.14}$$

where

$$\gamma = \frac{\varepsilon_m(\omega) - \varepsilon_b}{\varepsilon_m(\omega) + \varepsilon_b}. \tag{3.15}$$

Equation 3.14 is used in the EEM for solving the surface plasmon from the self-sustaining surface charge oscillations on individual uncoupled (isolated) particles. The equation to be solved is an eigenvalue problem describing surface charge interactions within a particle. The surface charge modes of oscillations $\sigma(\vec{r})$ are the eigenfunction solutions $\sigma_p^k(\vec{r})$ of a particle-p for the k-th that satisfy the Equation 3.14 with eigenvalue $\gamma = \gamma_p^k$. The equation can then be re-written as

$$\sigma_p^k(\vec{r}) = \frac{\gamma_p^k}{2\pi} \oint \sigma_p^k(\vec{r}_p) \frac{(\vec{r} - \vec{r}_p) \cdot \hat{n}}{|\vec{r} - \vec{r}_p|^3} dS_p \tag{3.16}$$

and can be described as the surface charge $\sigma_p^k(\vec{r})$ is induced at point $\bar{r}$ as a result of the electric field produced by $\sigma_p^k(\vec{r}_p)$ at all points $\vec{r}_p$ on the surface of nanoparticle-p.

The resonance frequency ω_p^k of the nanoparticle satisfies the following relationship:

$$\mathrm{Re}[\varepsilon_m(\omega_p^k)] = \varepsilon_b \left(\frac{1 + \gamma_p^k}{1 - \gamma_p^k} \right), \tag{3.17}$$

where $\varepsilon_m(\omega)$ is the permittivity of the metal and ε_b is the permittivity of the background medium, which is assumed to have a real value.

When the nanoparticle interacts with external electromagnetic fields, one or more resonance modes can be excited. The excited modes then produce surface charge distributions which can be expressed as the sum of individual resonance modes,

$$\sigma_p(\vec{r}, \omega) = \sum_k a_p^k(\omega) \sigma_p^k(\vec{r}). \tag{3.18}$$

The amplitude a_p^k of particle-p of mode-k can be written as

$$a_p^k(\omega) = f_p^k(\omega)\vec{p_p^k} \cdot \vec{E}_0 \tag{3.19}$$

where

$$f_p^k(\omega) = \frac{2\gamma_p^k \varepsilon_b(\varepsilon(\omega) - \varepsilon_b)}{\varepsilon_b(\gamma_p^k + 1) + \varepsilon(\omega)(\gamma_p^k - 1)}, \tag{3.20}$$

and $\vec{p_p^k}$ is the dipole moment of particle p for the k-th mode, and $\vec{E}_0$ is the electric field of the incident electromagnetic wave. If the Drude model is used to describe the metal, the term $f_p^k(\omega)$ can be simplified and approximated as

$$f_p^k(\omega) \approx \frac{-A_p^k}{\omega - \omega_p^k + i\Gamma_p^k/2} \tag{3.21}$$

where A_p^k is a constant, ω_p^k is the resonance frequency of particle p of mode k, and Γ_p^k is the full width at half maximum of the resonance (the damping constant).

Using Equation 3.18, one can derive the total dipole moment $\vec{p}_p(\vec{r}, \omega)$ of nanoparticle p, which is

$$\vec{p}_p(\vec{r}, \omega) = \sum_k a_p^k(\omega)\vec{p_p^k}(\vec{r}). \tag{3.22}$$

When metal nanoparticles are placed close together, their excitation fields will influence other particels and the modes of all the particles are coupled. Their interaction can be described by a matrix equation described below. The coupled amplitudes $\tilde{a}_p^k$ of particle p excited in the k-th mode is calculated from its interaction with particle q in the j-th mode. Suppose there are N nanoparticles interacting, the equation for the coupled excitation amplitudes is

$$\tilde{a}_p^k = \sum_{q=1}^{N} \sum_j (\delta_{pq}\delta^{kj} - C_{pq}^{kj})^{-1} a_q^j, \tag{3.23}$$

where δ_{pq} and δ^{kj} are Kronecker delta functions for particle p and q and mode k and j, and C_{pq}^{kj} is the coupling or interaction between particle p for the k-th mode and particle q for the j-th mode.

The term C_{pq}^{kj} can be written as,

$$C_{pq}^{kj} = \frac{f_p^k}{4\pi\varepsilon_b} G_{pq}^{kj}, \tag{3.24}$$

where f_p^k is the spectral response of particle p in mode k as in Equation 3.20 and 3.21. The coupling constant G_{pq} between particle p and particle q for particles with dominant dipolar modes can be approximated as

$$G_{pq}^{kj} \approx \frac{1}{4\pi\varepsilon_b d_{pq}^3} \left(3(\vec{p_p^k} \cdot \hat{d}_{pq})(\vec{p_q^j} \cdot \hat{d}_{pq}) - \vec{p_p^k} \cdot \vec{p_q^j}\right) \tag{3.25}$$

where $\vec{d}_{pq} = d_{pq}\hat{d}_{pq}$ is a vector from the location of particle q to the location of particle p.

The matrix equation for solving the coupled amplitude (Equation 3.23) can be simplified in the case of only one dominant mode on each nanoparticle. This is the case for metal nanorods where the dominant mode is the dipole mode with a dipole moment along its long axis. The matrix equation for the coupled amplitudes if there are N nanoparticles is

$$\begin{pmatrix} \tilde{a}_1 \\ \tilde{a}_2 \\ \vdots \\ \tilde{a}_n \end{pmatrix} = \begin{pmatrix} 1 & f_1 G_{12} & f_1 G_{13} & \cdots & f_1 G_{1N} \\ f_2 G_{21} & 1 & f_2 G_{23} & \cdots & f_2 G_{2N} \\ \vdots & \vdots & \vdots & \ddots & \vdots \\ f_N G_{N1} & f_N G_{N2} & f_N G_{N3} & \cdots & 1 \end{pmatrix}^{-1} \begin{pmatrix} a_1 \\ a_2 \\ \vdots \\ a_n \end{pmatrix}. \tag{3.26}$$

The off-diagonal elements describe the coupling strength between the particles. This depends on the individual response f_p of each particle and the coupling G_{pq} of the p-th and q-th particles.

The net dipole moment of each of the nanoparticles can be used to calculate the electric field radiated in direction $\hat{r}$ for wavenumber k via the equation: [91]:

$$\vec{E} = \frac{e^{ikr}}{4\pi\varepsilon_0 r^3} \left[(kr)^2(\hat{r} \times \vec{p}) \times \hat{r} - ikr(3\hat{r}(\hat{r} \cdot \vec{p}) - \vec{p})) + (3\hat{r}(\hat{r} \cdot \vec{p}) - \vec{p})\right]. \tag{3.27}$$

In the far-field where $kr >> 1$, the first term is dominant and is used for calculating the far-field scattering. The total scattered electric field can be found be summing over the contributions from each dipole.

The scattered power can be determined by taking the square of electric field found in Equation 3.27. The scattered power per unit solid angle is:

$$\frac{dP_{scat}}{d\Omega} = \frac{ck^4}{32\pi^2\varepsilon_b}|\hat{r} \times \vec{P}|^2. \tag{3.28}$$

3.3.2 Implementing the EEM for Nanorod Trimer and Tetramer Antennas

The matrix equation of Equation 3.26 can be more easily solved when the nanoparticles of the optical antennas are arranged symmetrically. In this project, the structures under study are identical metal nanorods arranged radially or azimuthally (circularly). The unit cells of the arrays are made of three or four nanorods, as shown in Figure 3.7.

Because all particles are the same and their arrangement is symmetric, the coupling strength is $G_{pq} = G$ for trimer arrangements. There are two different values of G_pq in the tetramer arrangements. The sign of G depends on whether the mode interaction is head-to-head (same charges) or head-to-tail (opposite charges), as calculated using Equation 3.25. If the dipole moments of uncoupled nanorods are assumed to be as given in Figure 3.7, the radial trimer has $G < 0$ and azimuthal trimer has $G > 0$. Based on symmetry, there are two different values of G in tetramer arrangements. The signs of the coupling constants in tetramer follow the same rules as in radial and azimuthal trimers.

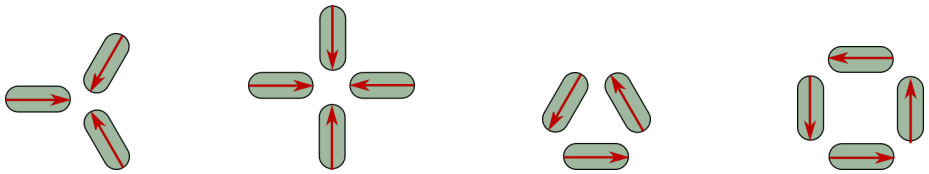

Figure 3.7: Structures under study: (a) radial trimer, (b) radial tetramer, (c) azimuthal trimer, and (d) azimuthal tetramer, to be solved by EEM. Red arrows indicate the uncoupled dipole moments of every nanorod.

Assuming all particles are identical, the matrix equations to be solved for

trimer and tetramer structures for Equation 3.26 are respectively

$$\begin{pmatrix} \tilde{a}_1 \\ \tilde{a}_2 \\ \tilde{a}_3 \end{pmatrix} = \begin{pmatrix} 1 & -fG & -fG \\ -fG & 1 & -fG \\ -fG & -fG & 1 \end{pmatrix}^{-1} \begin{pmatrix} a_1 \\ a_2 \\ a_3 \end{pmatrix} \tag{3.29}$$

and

$$\begin{pmatrix} \tilde{a}_1 \\ \tilde{a}_2 \\ \tilde{a}_3 \\ \tilde{a}_4 \end{pmatrix} = \begin{pmatrix} 1 & -fG_A & -fG_B & -fG_A \\ -fG_A & 1 & -fG_A & -fG_B \\ -fG_B & -fG_A & 1 & -fG_A \\ -fG_A & -fG_B & -fG_A & 1 \end{pmatrix}^{-1} \begin{pmatrix} a_1 \\ a_2 \\ a_3 \\ a_4 \end{pmatrix}. \tag{3.30}$$

where $f = f(\omega)$ is the spectral function of each particle as a response to an incident field $\vec{E_0}$, described in Equation 3.21, and G, G_A, and G_B are the coupling constants between each pair of nanoparticles. In Equation 3.29, G corresponds to the interaction between any two nanoparticles in a trimer arrangement and in Equation 3.30 for tetramer arrangements , G_A corresponds to the interaction between any two closest neighbouring particles, i.e. two perpendicular nanorods, and G_B corresponds to the interaction between any two opposing particles, i.e. two parallel nanorods. The coupled amplitudes $\tilde{a_p}$ of particle p can be solved by calculating the inverse matrix of the above equations that involves the uncoupled amplitudes a_p for all particles ($p = 1...3$ for trimer and $p = 1...4$ for tetramer). The uncoupled amplitudes will be proportional to $\vec{p} \cdot \vec{E_0}$, where $\vec{E_0}$ is the incident field.

3.3.3 Scattering from Periodic Arrays of Metal Nanostructures

The structures investigated here are periodic arrays of antennas to form metasurfaces. In this case, the modelling is performed for one unit cell (or one single structure) and the effect of arrays can be considered as follow [92].

Suppose the incident field at the metal nanostructures has the form of $E_0 = \psi_i e^{i\vec{k_i}\cdot\vec{r_s}}$ where ψ_i is the amplitude, $\vec{k_i}$ is the incident wavevector, and $\vec{r_s}$ is the location of the structures. The wave is then scattered with an efficiency Q_s

and the scattered wave ψ_s is given by

$$\psi_s = \frac{Q_s \psi_i}{R} e^{(i\vec{k_i}\cdot\vec{r_s}+ikR)} \tag{3.31}$$

where $R = |\vec{r} - \vec{r_s}|$ is the distance of observation point at $\vec{r}$ from the scatterer and $k = |\vec{k_i}|$.

Assuming that the observation distance is large compared to the nanostructure size, R can be approximated as

$$R = r\left(1 + \left(\frac{r_s}{r}\right)^2 - \frac{2\hat{r}\cdot\vec{r_s}}{r}\right)^{1/2} \approx r - \hat{r}\cdot\vec{r_s}, \tag{3.32}$$

where $\hat{r} = \vec{r}/r$. With this approximation, $kR = kr - \vec{k_s}\cdot\vec{r_s}$ where $\vec{k_s} = k\hat{r}$ is the wavevector in the direction of scattering. The scattered wave then becomes

$$\psi_s \approx \frac{Q_s \psi_i}{r} e^{ikr - i(\vec{k_s}-\vec{k_i})\cdot\vec{r_s}} = \psi_0 e^{(ikr - i\vec{q}\cdot\vec{r_s})} \tag{3.33}$$

Here the scattering wavevector has been defined as $\vec{q} = \vec{k_s} - \vec{k_i}$. If the periodicity of the array is $\vec{a}$, the nanostructure n is located at $\vec{r_s} = n\vec{a}$. The total scattered field from the array is

$$\psi_{tot} \approx \psi_0 e^{ikr} \sum_{n=0}^{N-1} e^{-in\vec{q}\cdot\vec{a}} = \psi_0 e^{ikr}\left(\frac{1 - e^{-iN\vec{q}\cdot\vec{a}}}{1 - e^{-i\vec{q}\cdot\vec{a}}}\right). \tag{3.34}$$

The term in the bracket averages to zero for large N except when $\vec{q}\cdot\vec{a} = 2n\pi$ where n in an integer. This is the condition for strong scattering from the array.

If the periodicity is much smaller than the wavelength, only terms with $n = 0$ will contribute. At this condition, $\vec{k_s} = \vec{k_i}$ which means the transmitted wave has the same wavevector as the incident wave. This means that we consider only coupling of the coupled dipoles to a specularly reflected plane wave to determine the scattering coefficient.

3.4 Plane Waves and Optical Beams for Excitation of the Metasurfaces

There are several techniques that can be used to excite and observe the modes in a metasurface consisting of an array of optical antennas. The radiant modes are relatively easy to excite since the net dipole moment excited on the antennas scatter light easily, with strong and broad resonances. Linearly polarised plane waves with normal incidence is sufficient for dipole mode excitation.

The sub-radiant modes studied in this project cannot be excited with linearly-polarised normally-incident plane waves. They, however, can be excited with either off-normally incident plane waves, highly focussed beams, or vector beams such as radially or azimuthally polarised beams. In the modelling, the investigation of metasurfaces were performed by using off-normally incident plane waves, either with p- or s-polarisation. The off-normally incident plane waves introduce an asymmetry with a spatial phase gradient in the fields across the antenna.

By using Fourier analysis, any general optical beam can be expanded as a sum over plane waves with various wavevectors, polarisations, and amplitudes. The excitation of the metasurfaces with p- and s-polarised plane waves in the modelling can then be used as the basis for analysing the excitation with focussed beams.

3.4.1 Plane Wave Illumination

The modelling in this study relies heavily on the excitation of the metasurfaces with off-normally incident plane waves. Plane waves with p-polarisation have the electric field parallel to the plane of incidence and plane waves with s-polarisation have the electric field perpendicular to the plane of incidence. The schematic for p- and s-polarised plane waves are shown in Figure 3.8.

Suppose the normal direction is the z-axis and the plane wave is incident at an angle θ with respect to the z-axis (normal axis) and at an angle ϕ with respect to the x-axis as in spherical coordinates. The electric field of a p-polarised

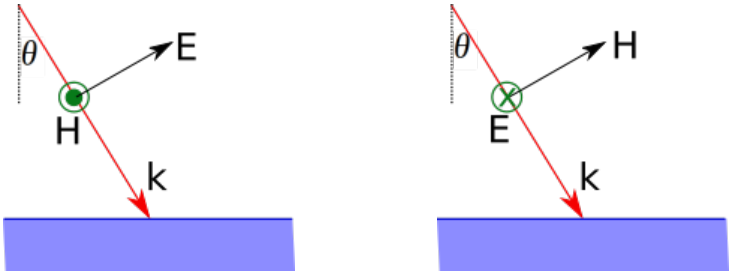

(a) (b)

Figure 3.8: The schematic for (a) p-polarised and (b) s-polarised plane waves.

plane wave can be written as:

$$\vec{E}(\vec{r},t) = E_0 e^{i(\vec{k}\cdot\vec{r}-\omega t)}(\cos\theta\cos\phi\hat{x} + \cos\theta\sin\phi\hat{y} - \sin\theta\hat{z}). \tag{3.35}$$

where

$$\vec{k} = k_x\hat{x} + k_y\hat{y} + k_z\hat{z} = k_0(\sin\theta\cos\phi\hat{x} + \sin\theta\sin\phi\hat{y} + \cos\theta\hat{z}) \tag{3.36}$$

is the wavevector of the plane wave. On the other hand, the electric field of an s-polarised plane wave can be written as:

$$\vec{E}(\vec{r},t) = E_0 e^{i(\vec{k}\cdot\vec{r}-\omega t)}(-\sin\phi\hat{x} + \cos\phi\hat{y}). \tag{3.37}$$

The magnetic field components follow Maxwell's equations and can be calculated from the known electric field $\vec{E}$ using the following relationship.

$$\vec{B} = \frac{1}{\omega}(\vec{k}\times\vec{E}) \tag{3.38}$$

where $\vec{k}$ is the wavevector and ω is the angular frequency of the plane wave.

3.4.2 The Vector Beam Illumination

Radially and azimuthally polarised beams are states of polarised light which have spatially varying polarisation of fields oscillation. The electric field is directed radially or azimuthally within the light beam which has a radially symmetric intensity distribution. In contrast, linearly or circularly polarised light has a uniform polarisation over the entire beam. The schematic for

linearly (or circularly), radially, and azimuthally polarised light are shown in Figure 3.9.

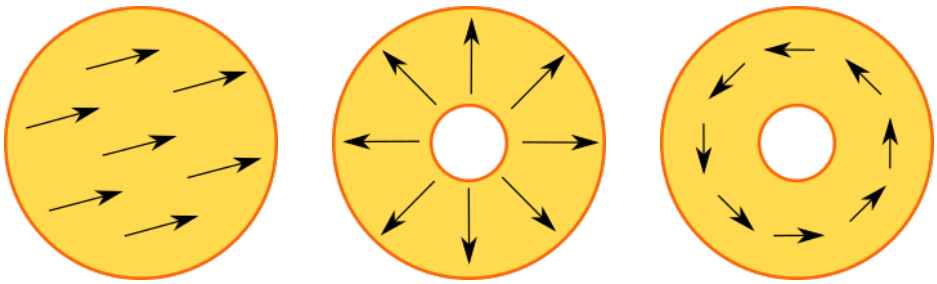

(a) (b) (c)

Figure 3.9: The schematic for (a) linearly, (b) radially, and (c) azimuthally polarised beams [93]. Arrows indicate the local polarisation throughout the beams. Radially and azimuthally polarised beams have zero intensity at the centre.

Suppose the light is propagating in a direction parallel to the z-axis. The electric field of a linearly polarised plane wave as a function of position and time can be written as

$$\vec{E}(\vec{r},t) = E_0(\cos\varphi_0\hat{x} + \sin\varphi_0\hat{y})e^{i(kz-\omega t)}. \tag{3.39}$$

where E_0 is electric field amplitude and φ_0 is the polarisation angle with respect to the x-axis. Circularly and elliptically polarised light has a phase difference between the x- and y-components, making the angle φ_0 vary with time.

The expressions for the field of radially and azimuthally polarised light are, on the other hand, more complicated [94]. The electric field of radially polarised light however can be simplified as being approximately:

$$\vec{E}(\vec{r},t) = E_0\sqrt{r}e^{-(r/a)^2}\hat{r}e^{i(kz-\omega t)} = E_0\sqrt{r}e^{-(r/a)^2}\left(\frac{x}{r}\hat{x} + \frac{y}{r}\hat{y}\right)e^{i(kz-\omega t)} \tag{3.40}$$

where $r = \sqrt{x^2+y^2}$ and $\hat{r}$ is radial unit vector in cylindrical coordinates and a is a constant describing the width of the beam. Azimuthally polarised light can also be approximated as:

$$\vec{E}(\vec{r},t) = E_0\sqrt{r}e^{-(r/a)^2}\hat{\phi}e^{i(kz-\omega t)} = E_0\sqrt{r}e^{-(r/a)^2}\left(-\frac{y}{r}\hat{x} + \frac{x}{r}\hat{y}\right)e^{i(kz-\omega t)}. \tag{3.41}$$

where $r = \sqrt{x^2+y^2}$ and $\hat{\phi}$ is azimuthal unit vector in cylindrical coordinates and a is a constant.

Radially and azimuthally polarised beams have z components as well to satisfy the Gauss' laws for magnetic and electric fields. These are not included in Equations 3.40 and 3.41. Again, the magnetic field follows Maxwell's equations and can be calculated using Equation 3.38. Note that radially and azimuthally polarised light could also be described in terms of approximate angular spectra. This is useful once the angular response to plane wave illumination is known.

3.4.3 Focussed Beam Illumination

Focussed beams are interesting and technologically important type of illumination in optical studies. Focussed beam illumination enables far-field excitation of sub-radiant modes within a simple and compact optical measurement set-up and the experimental characterisation of the metasurfaces undertaken as part of this project relies heavily on focussed beam illumination. The off-normal angular components of the beams of the focussed beams are responsible for the sub-radiant mode excitation.

When a plane wave is transmitted through a lens, the polarisation of the beam will change and the effect increases at higher refraction angles. The diagrams shown in Figure 3.10 explain the change of the direction due to beam focussing leading to a change in the polarisation. This interpretation also holds for objective lenses where a complex set of lenses are present inside. The area near the centre of the beam is transmitted with only a small change in direction and can be considered near-normal incidence. The area closer to the edge of the beam, however, is strongly refracted by the lens and its polarisation is affected, as noted by the red arrows in the figures. The output focussed beam can be written as a linear combination of off-normally incidence plane waves with p- and s-polarisation.

Suppose an incident linearly polarised beam propagates parallel to the z-axis with its polarisation axis parallel to the the x-axis. The focussed beam that illuminates the metasurface consists of plane wave with different angle of incidence and different polarisations. The near normal incident light has the same polarisation as the incident field.

Figure 3.11a shows the dominant plane wave components of the focussed field if the incident polarisation is linearly x-polarised. The refractions as illustrated

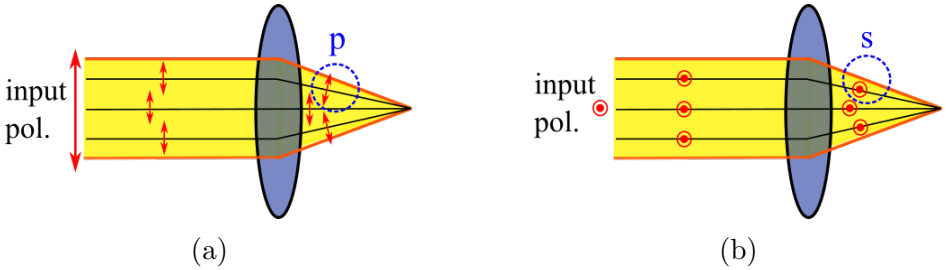

(a) (b)

Figure 3.10: Schematic showing polarisation changes in a focussed beam for input polarisation (a) parallel to the page and (b) perpendicular to the page.

in Figure 3.10 can be used to determine the dominant components throughout the beam. For angular components near σ_x-axis, the dominant plane wave components have p-polarisation and on the other hand, for angular components near σ_y-axis, they are dominated by s-polarised plane wave components. If the polarisation is rotated by 90°, the dominant components are interchanged.

The amplitudes of the components of the focussed electric field as a function of spatial frequencies σ_x, σ_y and σ_z when a lens is illuminated by a plane wave polarised in the x-direction are given by [95, 96]:

$$E_x = \frac{\sigma_x^2(1-\sigma_x^2-\sigma_y^2)+\sigma_y^2}{\sqrt{\sigma_z}(\sigma_x^2+\sigma_y^2)} \tag{3.42a}$$

$$E_y = \frac{-\sigma_x\sigma_y[1-(1-\sigma_x^2-\sigma_y^2)^{1/2}]}{\sqrt{\sigma_z}(\sigma_x^2+\sigma_y^2)} \tag{3.42b}$$

$$E_z = -\sigma_x/\sqrt{\sigma_z} \tag{3.42c}$$

where $\sigma_x = k_x/k_0$ and $\sigma_y = k_y/k_0$ are the normalised spatial frequency components along x- and y-axis and k_0 is the wavenumber. The z-component can be calculated using $\sigma_z = (1-\sigma_x^2-\sigma_y^2)^{1/2}$. For values of σ_x and σ_y with $\sqrt{\sigma_x^2+\sigma_y^2} > NA$, the amplitudes of the focussed field are zero.

Using an appropriate device or optical system, a, linearly polarised beam can be converted into either a radially or azimuthally polarised beam. In both cases, a very low intensity is observed at the centre of the beam. If the incident light is radially polarised, the rays undergo a polarisation change as illustrated in Figure 3.11(a). As a result, a focussed, perfect, radially polarised beam is purely p-polarised as shown in Figure 3.11(b). In contrast, if the incident beam is azimuthally polarised, focussed beam is purely s-polarised as shown

in Figure 3.11(c).

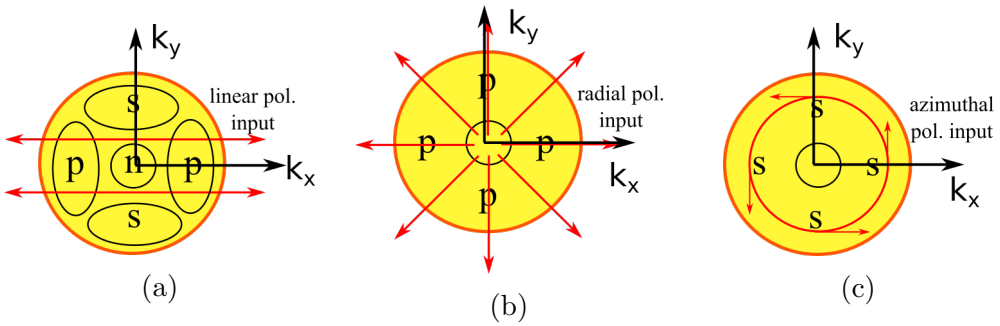

Figure 3.11: The local distribution of polarisation of focussed beams with (a) linearly, (b) radially, and (c) azimuthally polarisation.

3.5 Chapter Conclusion

There are two methods used for simulating and designing the metasurfaces in this study, the FDTD method and the EEM. The FDTD method is a rigorous full-field method which solves for both electric and magnetic fields as a function of space and time for any arbitrary geometry. The EEM uses the electrostatic approximation to solve for coupled modes of oscillation in ensembles of nanoparticles. The formulation for both methods was discussed.

The FDTD method mainly uses the coupled equations for electric and magnetic fields from Ampere-Maxwell's law and Faraday's law. The electric and magnetic fields are solved as a function of space and time, i.e. $\vec{E}(\vec{r},t)$ and $\vec{H}(\vec{r},t)$ giving accurate results but requiring significant large computer memory and calculation time.

On the other hand, the EEM solves for the amplitudes of excitation of all particles involved when interacting with an incident field and mode coupling between neighbouring particles via the near-field. The calculation is performed by solving an inverse matrix equation with a size of $N \times N$ for N particles. This is less accurate but the calculation is quick and requires little computer memory. This permits integration over a range of incidence angles providing deep insight into the interaction of beams of various kinds with metasurfaces. The far-field beam profiles at resonances are more easily produced by this

method. To improve its accuracy, spectral information from the FDTD simulation can be used to determine input parameters for the EEM calculation.

In the experiments undertaken here, the metasurfaces were excited using a focussed beam of light. Any optical fields can be written as a sum of plane waves with various wavevectors and polarisations. Modelling were performed using off-normally incident plane waves with either p- (electric field parallel to the plane of incidence) or s-polarisation (electric field perpendicular to the plane of incidence). These can then be used to gain insight into the interaction of more complex focussed fields with metasurfaces. In the next chapter, the results of simulations performed using the methods introduced here will be presented.

Chapter 4

Modelling and Investigating Metasurface Resonances

4.1 Optical Antenna Designs and Strategies for Exciting Sub-radiant Modes

The goal of this study was to explore the sub-radiant modes of metasurfaces, particularly *radial* and *azimuthal* modes. The metasurfaces are made of *periodic arrays of optical antennas*. To obtain these sub-radiant modes, optical antennas composed of radially and azimuthally arranged metal nanorods have been designed.

The geometric parameters play an important role in determining the spectral location of the resonances. The parameter s, the off-set distance of nanorods from the centre of the entire antenna, for each metasurface design studied here are shown in Figure 4.1. The defined gap size δ for each metasurface is also shown. Each nanorod has length L, width w, and height h, shown in Figure 4.2 and is arranged symmetrically. The antennas were made of silver, embedded in a medium with a refractive index of $n = 1.5$.

The optical antennas with three nanorods are referred to here as *trimer antennas* and those with four nanorods as *tetramer antennas*. The dominant, lowest energy mode of a single nanorod is the dipole mode parallel to the long axis, shown in Figure 4.3. By arranging the nanorods with radial and azimuthal

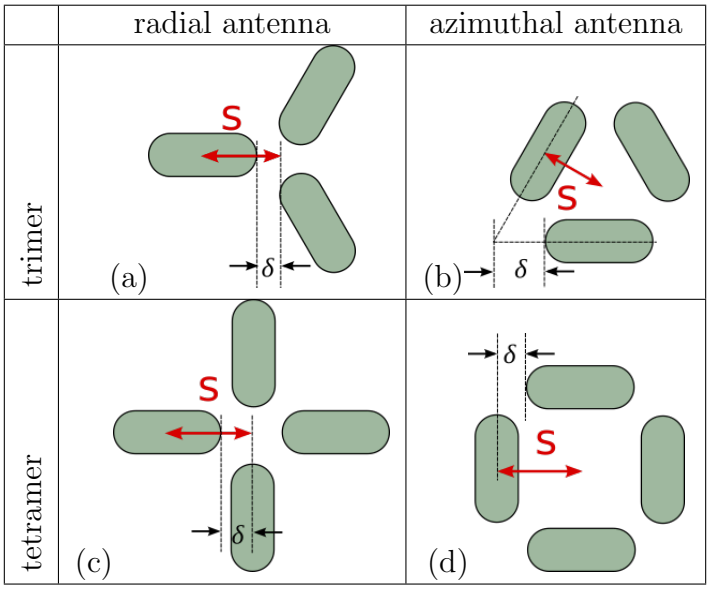

Figure 4.1: Designs of optical antennas as the basis of metasurfaces supporting radial and azimuthal modes with symmetric radial and azimuthal arrangements. (a) radial trimer, (b) azimuthal trimer, (c) radial tetramer, and (d) azimuthal tetramer. The off-set distance s, from the antenna centre to the centre of one of the nanorod, and gap size δ, are shown for each design.

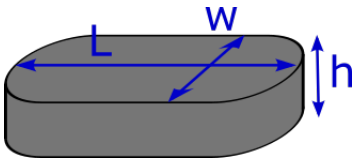

Figure 4.2: The length L, width w, and height h of a single nanorod.

symmetry, the sub-radiant modes of interest exhibit the same geometry as the optical antennas, i.e. radial and azimuthal modes. These modes correspond to the electric charge oscillations, thus the terms radial and azimuthal modes refer to the radially and azimuthally oscillations of electric field rather than magnetic field.

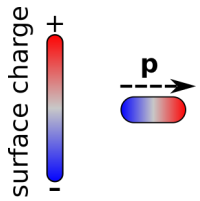

Figure 4.3: The dominant mode in a single nanorod is the dipole mode parallel to its long axis (with the colourbar for the surface charge on the left).

If these sub-radiant modes are excited on the antennas, the surface charges

appear as in Figure 4.4 for radial modes and Figure 4.5 for azimuthal modes. These modes have zero net electric dipole moment and are thus not easily coupled to propagating waves. As a result, these modes are referred to as *sub-radiant* or *dark* and need specific techniques to be excited.

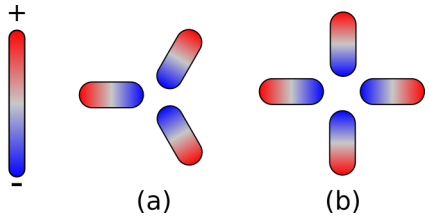

Figure 4.4: The surface charge distribution of *radial modes* of radially-arranged (a) trimer and (b) tetramer optical antennas.

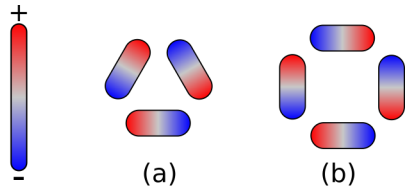

Figure 4.5: The surface charge distribution of *azimuthal modes* of azimuthally-arranged (a) trimer and (b) tetramer optical antennas.

There are other sub-radiant modes that exist in the tetramer antennas and figure 4.6 shows other modes of tetramer antennas with zero net electric dipole moment. Although these modes can be excited along with radial or azimuthal modes, the resonances are too close to those of radiant or bright modes, limiting their visibility in the spectra.

Figure 4.7 shows some radiant modes of the antennas. These modes are also referred to as dipole modes because there is a net dipole moment induced in the excitation. As depicted here, the net electric dipole moment of the modes are parallel either to the x- or y-axis. In general, a superposition of modes will be excited. The amplitude of each mode will depend on the illumination conditions including the frequency, polarisation and angle of incidence.

Sub-radiant modes do not couple to normally incident plane waves but they can be excited by a point source placed near the antenna. [97]. In this study, excitation was achieved instead using focussed light beams. These beams (and any general optical beams) can be written as a sum of plane waves with various wavevectors and polarisations [98]. Modelling was performed by simulating

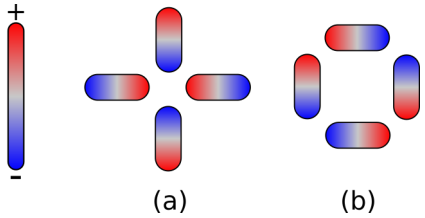

Figure 4.6: The surface charge distribution of sub-radiant modes of tetramer antennas other than the radial or azimuthal modes. Mode in Fig.(a) referred as breathing mode and mode in Fig.(b) referred as quadrupole mode.

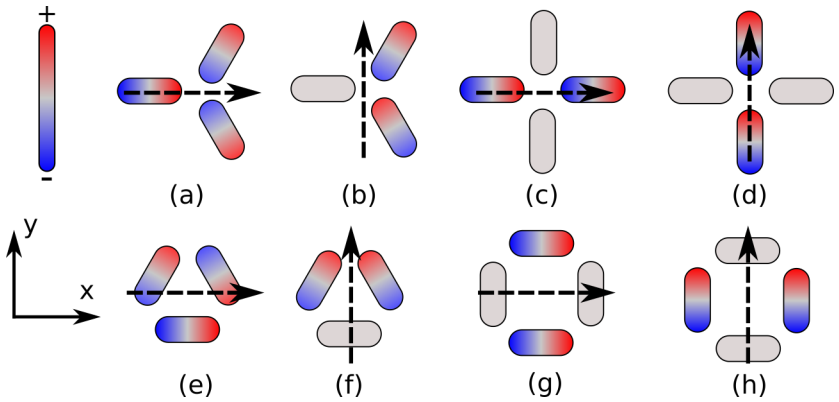

Figure 4.7: The surface charge distribution of radiant modes of optical antennas of: (a-b) radial trimer, (c-d) radial tetramer, (e-f) azimuthal trimer, and (g-h) azimuthal tetramer. Modes have the dipole moments parallel to the (a,c,e,g) x-axis and (b,d,f,h) y-axis, with the coordinate defined in the inset. Dashed lines indicate the net electric dipole moments.

the metasurfaces (arrays of optical antennas) with plane wave illumination with different angles of incidence and polarisations. The schematic in Figure 4.8 shows the incident plane wave at an angle θ with respect to the normal direction with the plane of incidence at an azimuthal angle ϕ with respect to the x-axis for a plane wave incident. The schematic for the p- and s-polarised plane wave was shown in Figure 3.8.

4.2 Modelling with The Finite-Difference Time-Domain Method

The focus of this study is radial and azimuthal modes of metasurfaces consisting of nanorod trimers or tetramers. The FDTD modelling was undertaken to investigate the excitation of these modes with off-normally incident plane

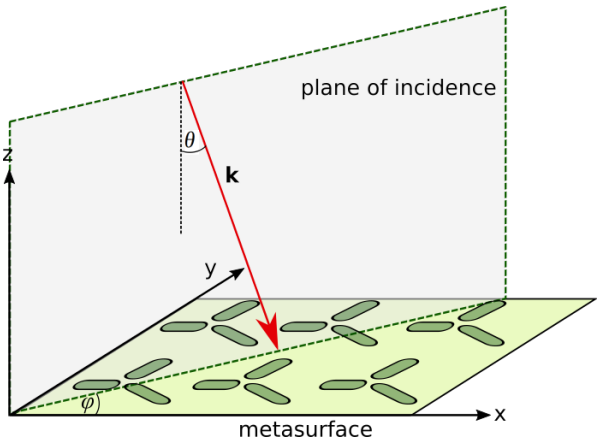

Figure 4.8: A schematic for an incident plane wave at an angle θ with respect to the normal and the plane of incidence at an angle ϕ with respect to the x-axis. $\phi = 0°$ and $\phi = 90°$ corresponds to xz- and yz-plane of incidence respectively.

waves. Plane waves with p-polarisation excite radial modes whereas those with s-polarisation excite azimuthal modes. In Fourier analysis, a focussed radially polarised light corresponds to a superposition of p-polarised plane waves and focussed azimuthally polarised light corresponds to a superposition of s-polarised plane waves. The antenna properties were investigated by varying the geometry of the antennas, i.e. modifying the length of nanorods and the separation between them. The FDTD implementation used in this study was developed by Lumerical FDTD Solutions[1].

The results discussed in this section are provided in the form of transmission and reflection spectra, as these were actually measured in the experiments. The FDTD could also calculate the scattering and absorption spectra, but these are not included here. The resonances of the metasurfaces are sufficiently described using the transmission and reflection spectra.

The first goal was to obtain optical antenna geometry parameters of metasurfaces suitable for investigating radiant and sub-radiant modes. The resonances of the radiant and sub-radiant modes were set to have a spectral separation close to 100 nm so that they could be discriminated in experiments.

The FDTD simulations in this study were performed in a server computer

[1]Lumerical FDTD Solutions (LFS) is a commercial FDTD solver from Lumerical Solutions Inc. The version used was 8.9.

(Dell PowerEdge R620 x8 Chassis) with dual processors, Intel Xeon E5-2650v2 2.6GHz, and 256 GB of RAM. When the computer was used only to run LFS, one simulation took 10 to 20 minutes to finish. One simulation corresponds to a metasurface illuminated with a plane wave with a specific polarisation and an angle of incidence for a range of wavelengths (usually 550 nm to 950 nm). The meshes were non-uniform where the minimum mesh size is 4 nm near the structures and extended to a maximum 20 nm away from the structures. The total FDTD Yee nodes for modelling the metasurfaces with a periodicity $p = 300$ nm is 2.38×10^5 nodes and those with a periodicity $p = 400$ nm is 6.45×10^5 nodes.

4.2.1 Preliminary Modelling

Preliminary study of sub-radiant mode excitation was performed using an FDTD software written by the author in MATLAB. The modelling was performed on a single antenna by calculating the scattering cross section. An investigation of an array of optical antennas (a metasurface) was also performed with a normally incident plane wave. Further use of this software was limited due to the unavailability of excitation at oblique angles of incidence and it was decided that software modification would be too time consuming.

Examples of the spectra produced using this version of FDTD are shown in Figures 4.9 and 4.10 for radial and azimuthal trimers. Each of the simulations was performed on a single antenna using two different types of illumination, a linearly and a radially polarised light incident on a radial trimer, and a linearly and an azimuthally polarised light incident on a azimuthal trimer. The size of each nanorod is $L = 100$ nm and $w = 40$ nm, with no corner rounding. Both figures show two variation in the off-set distance s. The linearly polarised beam has the polarisation axis parallel to the x-axis (refer to Figure 4.7) and the radially and azimuthally polarised beams are concentric with the centre of the antenna. The simulations were performed with a meshing size of 5 nm, and time-steps at $0.99\Delta t_{max}$ from the CFL condition.

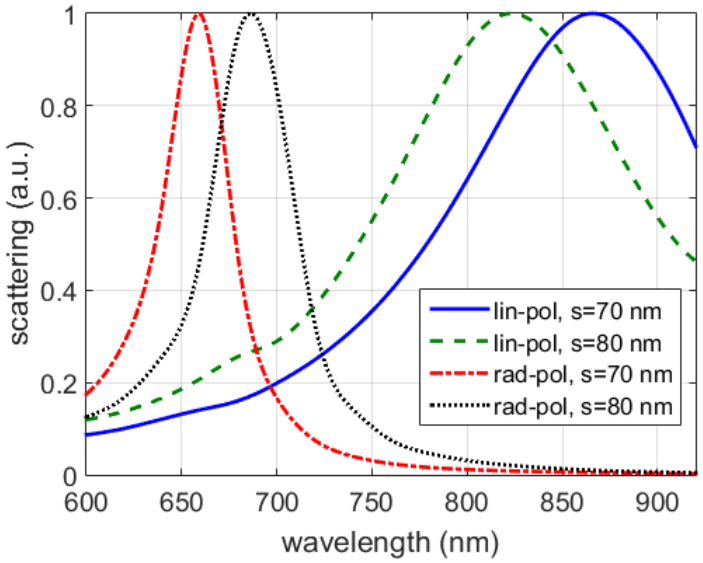

Figure 4.9: The scattering spectra from a radial trimer with nanorod length $L = 100$ nm, width $w = 40$ nm, and two different off-set distance s. The simulation was performed using the 'home-made' FDTD, with linearly and radially polarised beams.

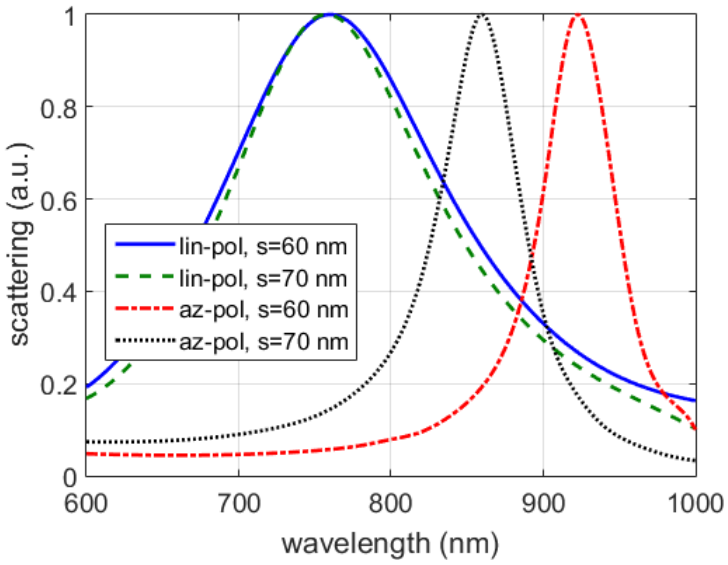

Figure 4.10: The scattering spectra from an azimuthal trimer with nanorod length $L = 100$ nm, width $w = 40$ nm, and two different off-set distance s. The simulation was performed using the home-made FDTD, with linearly and azimuthally polarised beams.

Figure 4.9 shows that two different spectra were produced from a radial trimer using different illumination. The spectra produced with a linearly polarised beam shows the excitation of the dipole modes characterised by broad resonances, located at 825 nm and 870 nm for $s = 70$ nm and $s = 80$ nm respectively. Sub-radiant modes, which are the radial modes, are resonant at shorter wavelengths compared to the dipole modes and they have the characteristic of narrower resonances, located at 660 nm and 690 nm for $s = 70$ nm and $s = 80$ nm respectively. An increase in s leads to the red-shifting of both modes.

Figure 4.10 also shows different resonances produced by different illumination of an azimuthal trimer. The dipole modes are excited at shorter wavelengths compared to the sub-radiant modes (azimuthal modes). A variation in s does not shift the spectral location of the dipole mode at 760 nm. The azimuthal modes are located at 860 nm and 920 nm for $s = 60$ nm and $s = 70$ nm respectively. Like the radial modes, the azimuthal modes have the characteristic of narrower resonances compared to the dipole modes.

The comparison of the spectra produced using this 'home-made' FDTD and the commercially available Lumerical FDTD Solutions (LFS) are shown in Figure 4.11 for radial trimers illuminated with a linearly polarised beam. The trimers have nanorod lengths $L = 100$ nm, widths $w = 40$ nm, and off-set distances $s = 70$ nm. The lineshape of the spectra and the spectral location of the resonances are in fairly good agreement. The spectral lineshape are fairly similar with the resonances located at 865 nm and 880 nm using home-made FDTD and LFS respectively.

Further modelling of an array of antennas (metasurface) is shown in Figure 4.12. The structure was illuminated with a normally incident beam, with polarisation aligned parallel to the x-axis (refer to Figure 4.7). The transmission and reflection spectra calculated using the candidates own version of FDTD are shown along with the results produced using LFS. The spectra produced using the home-made FDTD are in a good agreement with those produced using LFS with very similar lineshapes. The dipole mode resonances in the transmission spectra are located at 785 nm using the home-made FDTD, and

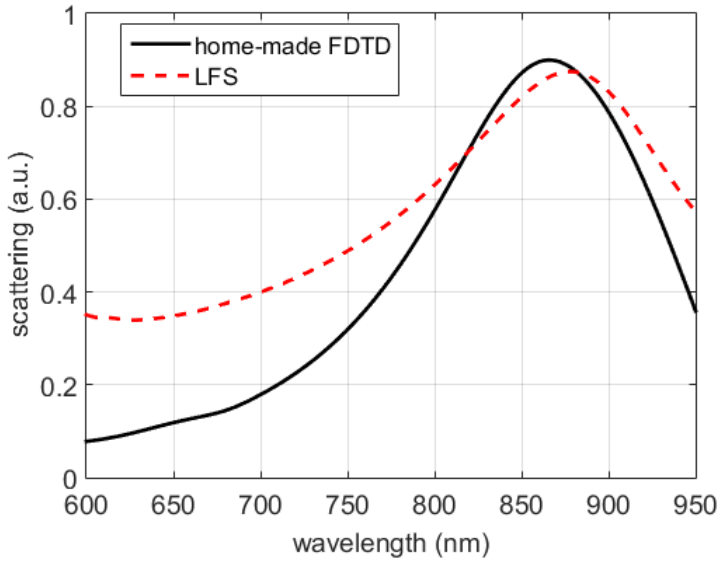

Figure 4.11: Comparison of spectra of a single radial trimer with nanorod lengths $L = 100$ nm, widths $w = 40$ nm, and off-set distances $s = 70$ nm, between that simulated using the 'home-made' FDTD and that simulated using LFS.

at 775 nm using LFS. In the reflection spectra, the resonances are at 795 nm and 780 nm using the home-made FDTD and LFS respectively. These resonances are blue-shifted compared to those on a single antenna due to interaction between neighbouring antennas.

4.2.2 Corner Rounding Effects

An important influence in FDTD modelling is the effect of rounding of the antenna corners. Nanorods can be modelled either as a rectangular block with sharp corners or a "pill-shape" that has rounded corners. The corner rounding was implemented as shown in Figure 4.13a. The structures with rounded corners provide a more realistic approximation to structures fabricated using electron beam lithography discussed in Chapter 5.

The gaps between nanorods are altered by corner rounding, as shown in Figure 4.13b. Since the gap size is actually very small, around 15 to 30 nm for nanorod sizes of $100 \times 40 \times 40$ nm, the smallest distance between nanorods is

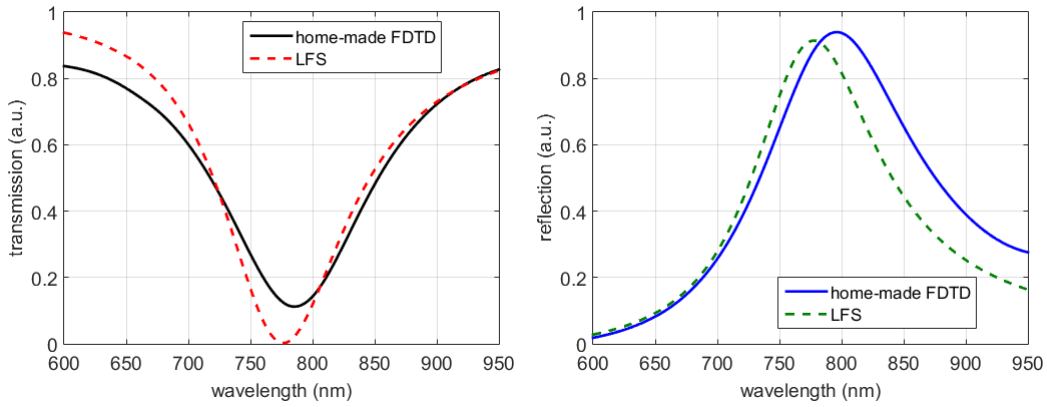

(a) (b)

Figure 4.12: Comparison of (a) transmission through and (b) reflection from an array of periodic radial trimers with nanorod lengths $L = 100$ nm, widths $w = 40$ nm, off-set distances $s = 70$ nm, and periodicity $p = 300$ nm between results simulated using the 'home-made' FDTD and LFS.

strongly influenced by their corners, indicated by the red arrow in the figure. Rounded corners make the gap slightly larger and, as a result, the coupling interaction between nanorods changes as well. This leads to shifts in the resonance frequencies in the spectra.

The corner rounding was performed by overlapping two cylinders at both ends of a rectangular block, shown in Figure 4.13c. The cylinder has a diameter equal to the width of the nanorod. The height of those cylinders was equal to the thickness of nanorod. The overlapping regions do not affect the computation as all regions are treated as a uniform index region. The fabricated nanorods are actually rounded in three dimensions and also have other artefacts. The corner rounding in two dimensions used in the modelling only partly compensates irregularities in the actual fabricated shapes and is reasonably accurate as will be shown in the next chapter.

Figure 4.14 shows the results of corner rounding on a single nanorod with dimensions $100 \times 40 \times 40$ nm illuminated with a linearly-polarised plane wave at normal incidence. The polarisation is aligned parallel to the axis of the nanorod and the length of the nanorod is kept constant for comparison. It is apparent that the resonance peak is shifted to a shorter wavelength. This is primarily due to the nanorod size becoming slightly smaller as a result of

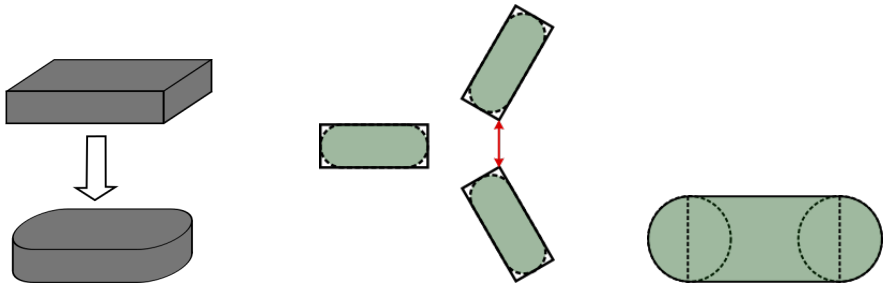

(a) (b) (c)

Figure 4.13: The schematic for corner rounding of the nanorod in FDTD modelling. (a) Nanorod corners are rounded in two dimensions. (b) The gaps between nanorods are changed by corner rounding, indicated by the red arrow. (c) Rounding was done by placing two cylinders at both ends of a rectangular block (top view).

corner rounding.

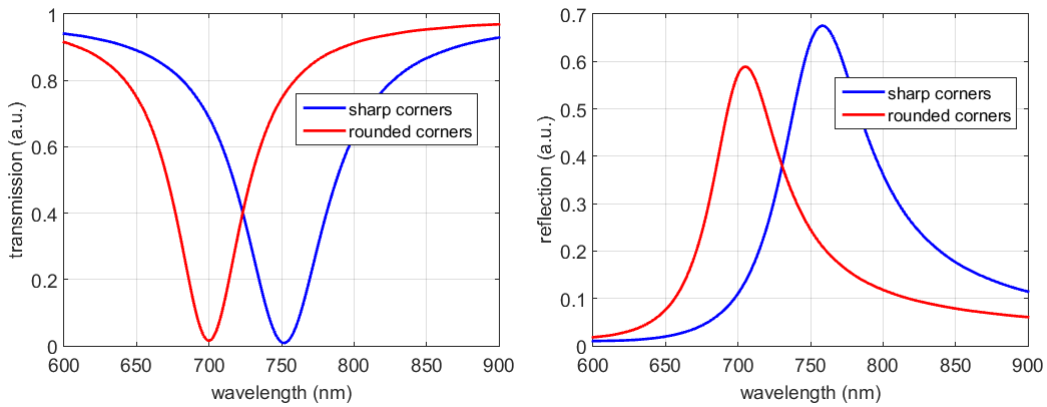

(a) (b)

Figure 4.14: The (a) transmission through and (b) reflection from an array of silver nanorods with sharp and rounded corners, illuminated with a normally incident plane wave, linearly polarised parallel to the long axis of nanorods. The rod size is $L = 100$ nm and $w = h = 40$ nm, and the background medium has the refractive index of $n = 1.5$.

Following this, the effect of corner rounding on scattering by radial trimers was considered. Figure 4.15 shows the spectrum obtained when the nanorods have sharp or rounded corners. The resonance of a single nanorod is already blue-shifted. When they are combined into an antenna, this will shift the whole spectrum as well to a shorter wavelength. The radial mode is not clearly present in this plot because the illumination was performed at normal incidence. A weak signature of the excitation of radial mode is observed in the spectrum of the radial trimer metasurface illuminated with a normally

incident plane wave at a shorter wavelength than the dipole mode spectral location. This excitation is possible though the near-field coupling of the bright mode [99].

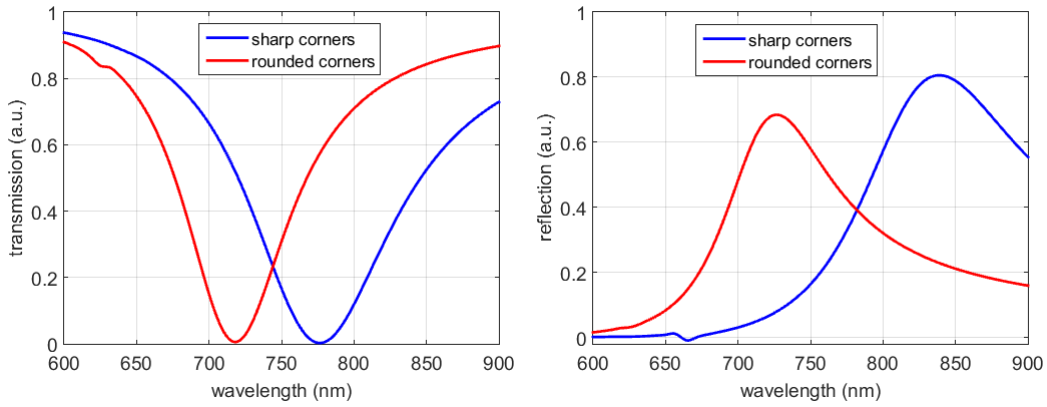

(a) (b)

Figure 4.15: The (a) transmission through and (b) reflection from an array of radial trimer antennas for the sharp and rounded corner nanorods, illuminated with a normally incident plane wave, linearly polarised parallel to one of the nanorods. The antenna is radial trimer with an off-set distance $s = 70$ nm. The nanorod sizes are $100 \times 40 \times 40$ nm.

To see the effect on the radial mode, we need to use an oblique angle of incidence with p-polarisation. Figure 4.16 shows the same radial trimer as in Figure 4.15 but excited with p-polarised light at 20° angle of incidence to the normal. Both the radial and dipole modes are blue-shifted but the shift is different for each mode. This is due to the fact that the radial and dipole modes have a different dependence on the size of the gap. When the gap size is increased, the radial mode is red-shifted while the dipole mode is blue-shifted. The total effect can be considered as the combined effects of the centre spectrum being blue-shifted due to the decreasing size of the nanorod with the dipole mode is being further blue-shifted than the radial mode due to increasing size of the gap.

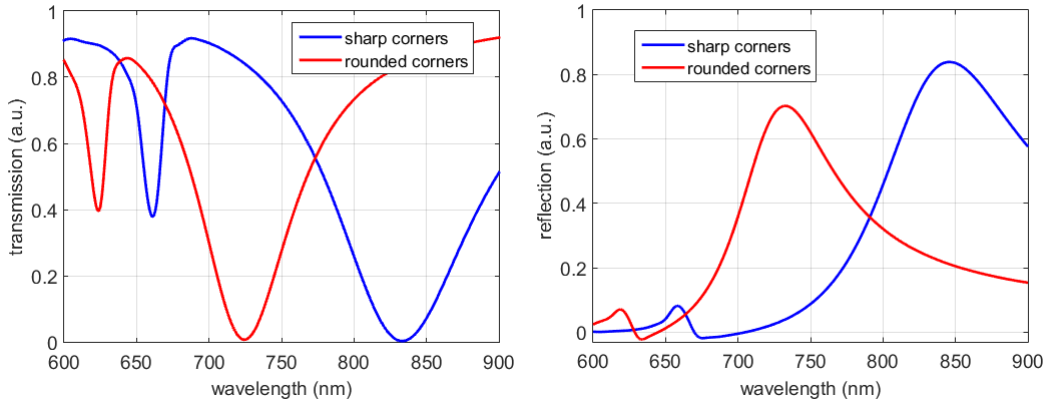

(a) (b)

Figure 4.16: The (a) transmission through and (b) reflection from an array of radial trimer antennas with nanorod sizes of $100 \times 40 \times 40$ nm and $s = 70$ nm with an off-normally incident at an angle of 20°, p-polarised plane wave.

4.2.3 Modelling Results

4.2.3.1 Metasurfaces with Radial Antennas

The first tests were performed for a metasurface composed of arrays of radial trimer antennas with nanorod lengths[2] of $L = 100$ nm, width and height of $w = h = 40$ nm. The off-set distance is $s = 70$ nm and the periodicity is $p = 300$ nm. Different excitation strategies were used to test this particular structure.

Figure 4.17 shows the transmission through a metasurface of radial trimers when excited by normally and off-normally incident plane waves. When a linearly polarised plane wave is normally incident, only one peak appears in the spectrum in the range of interest, the dipole mode. When the incident propagation vector is tilted from the normal by 20°, an incident p-polarised plane wave produces two peaks. In this case, both dipole and radial modes were excited. A plane wave with s-polarisation does not excite the radial mode of this particular antenna. This shows that, as expected, a p-polarised plane wave is needed to excite the radial mode.

The surface charge distribution on the nanorods at the corresponding resonances can help identifying the modes, as shown in Figure 4.18 for the metasur-

[2]See Figures 4.1 and 4.2 for diagrams showing L, w, h, and s.

face of radial trimers. Figure 4.18a shows the surface charge distribution for the radial mode at 625 nm. Figure 4.18b shows the surface charge distribution for the dipole mode with a net dipole moment parallel to the x-axis at 725 nm.

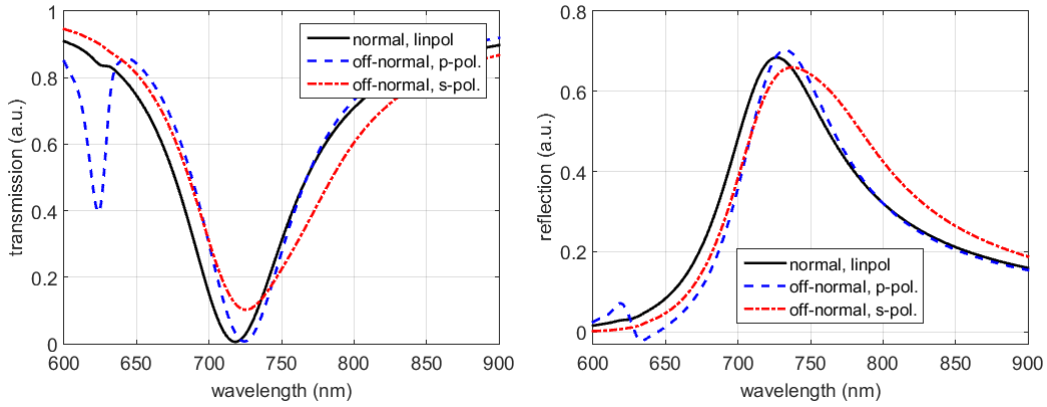

(a) (b)

Figure 4.17: The (a) transmission through and (b) reflection from a metasurface consisting of radial trimer antennas with different illumination of plane waves. Nanorods have the sizes $100 \times 40 \times 40$ nm, off-set distance $s = 70$ nm, and periodicity $p = 300$ nm. The radial mode is excited by p-polarised light.

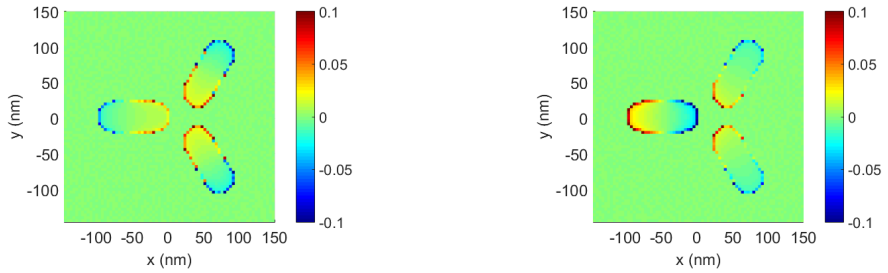

(a) (b)

Figure 4.18: The surface charge distribution of (a) radial mode ($\lambda = 625$ nm) and (b) dipole mode ($\lambda = 725$ nm) resonances of a metasurface consisting of radial trimer antennas, on the top surface. Nanorods have the sizes$100 \times 40 \times$ nm, off-set distance $s = 70$ nm, and periodicity $p = 300$ nm.

The results for the metasurface of radial tetramers are shown in Figure 4.19. The nanorod size is $120 \times 40 \times 40$ nm and the off-set distance is $s = 90$ nm. The array has a periodicity of 400 nm. Off-normal p-polarised light excites the radial mode and another dark mode and the surface charge distribution on the antennas is shown in Figure 4.20 for p-polarised excitation. The radial mode resonance is the shortest wavelength feature in the frequency region shown. Another dark mode, which is a breathing mode is located very close

to the dipole mode resonance. The resonance of this mode may disappear for particular geometries as the dipole mode influence is very strong and the appearance of breathing modes is strongly affected by interference with dipole modes.

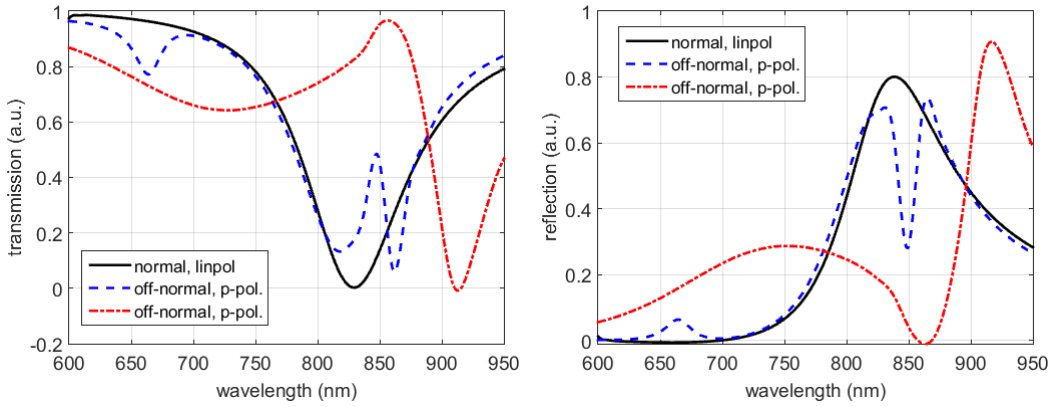

(a) (b)

Figure 4.19: The (a) transmission through and (b) reflection from a radial tetramer metasurface with different illumination of plane waves. The radial mode is excited by p-polarised light. The parameters are mentioned in the text.

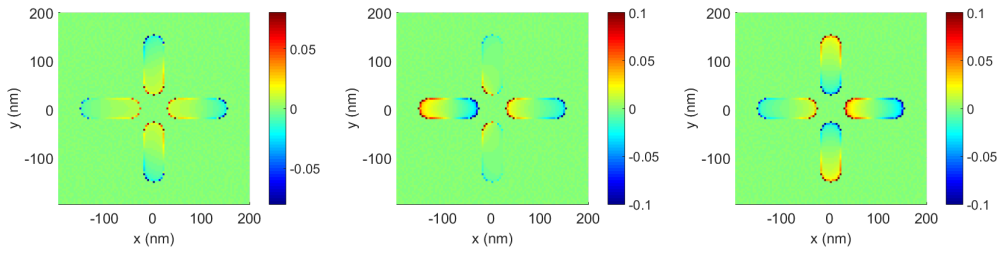

(a) (b) (c)

Figure 4.20: The surface charge of (a) radial mode ($\lambda = 670$ nm), (b) dipole mode ($\lambda = 815$ nm), and (c) breathing mode ($\lambda = 860$ nm) of a metasurface consisting of radial tetramer antennas with *p-polarised* plane wave illumination. The parameters as in Figure 4.19, mentioned in the text.

If a metasurface consisting of radial tetramers is illuminated with an s-polarised plane wave, a Fano resonance lineshape [69] was observed at the wavelength near the dipole mode resonance. The transmission spectrum has a local maximum and a local minimum at 860 nm and 910 nm respectively for the metasurface described above. Equivalently, the reflection spectrum has a local minimum and a local maximum at those wavelengths. This produces a broad peak centred at 720 nm mimicking the radial mode resonance. By looking at

the surface charge at this wavelength, shown in Figure 4.21a, no radial mode is excited. The surface charge distribution at 910 nm is also provided in Figure 4.21b.

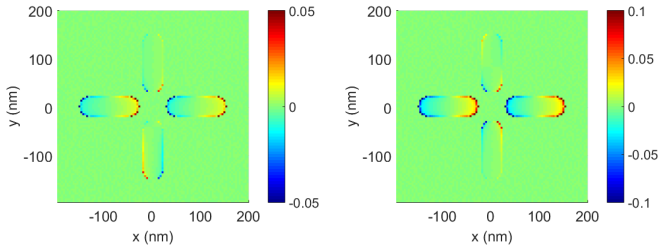

Figure 4.21: The surface charge at (a) 720 nm, and (b) 910 nm on a metasurface consisting of radial tetramer antennas with *s-polarised* plane wave illumination. The parameters as in Figure 4.19, mentioned in the text.

An investigation of the effect of nanorod length L on the scattering spectrum from the metasurface of radial trimers was undertaken. The gaps between the nanorods are kept fixed along with the nanorod width and height. To maintain the gap size, the antenna with $L = 100$ nm and $w = h = 40$ nm has an off-set distance of $s = 70$ nm and the antenna with $L = 120$ nm has the off-set distance set at $s = 80$ nm. The illumination has p-polarisation and the angle of incidence is 20°.

The transmission and reflection spectra are shown in Figure 4.22. Both the radial and dipole resonances are red-shifted due to the longer nanorod. Longer nanorods lead to an overall larger antenna size that resonates at longer wavelengths. The results for the metasurface of radial tetramers are shown in Figure 4.23. The simulations were performed with a similar set-up as in Figure 4.22, but with a periodicity of 400 nm since the antenna size is larger and more space in a unit cell is needed. The metasurface of radial tetramers gives a similar result for the variation in nanorod length. The breathing mode is very close to the dipole mode for $L = 100$ nm and interferes with the dipole mode producing a Fano resonance line-shape at 750 nm.

The coupling between nanorods is determined by how close the nanorods are to each other. The interaction is stronger when the nanorods are placed as close as possible. The gap, however, cannot be made arbitrarily small because in fabrication of nanostructures, reliably producing a very small gap is difficult.

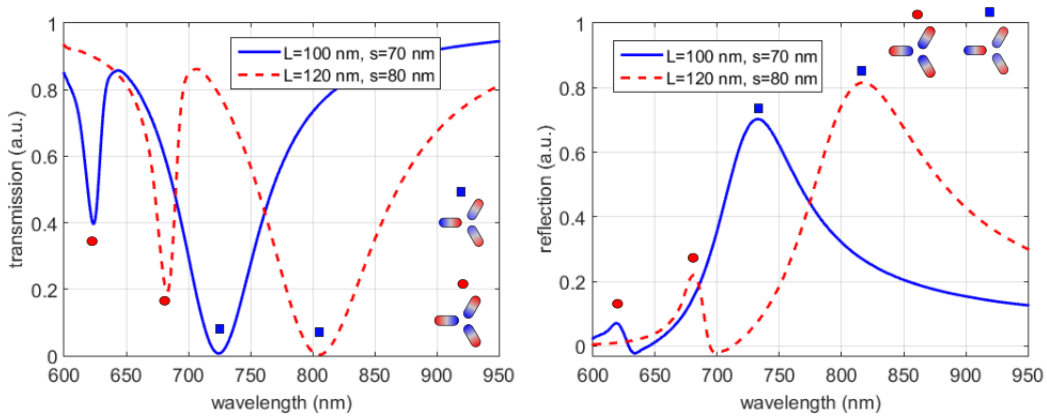

Figure 4.22: The (a) transmission through and (b) reflection from radial trimer metasurfaces by p-polarised plane wave for different nanorod lengths L and the gap size $\delta = 20$ nm is kept constant.

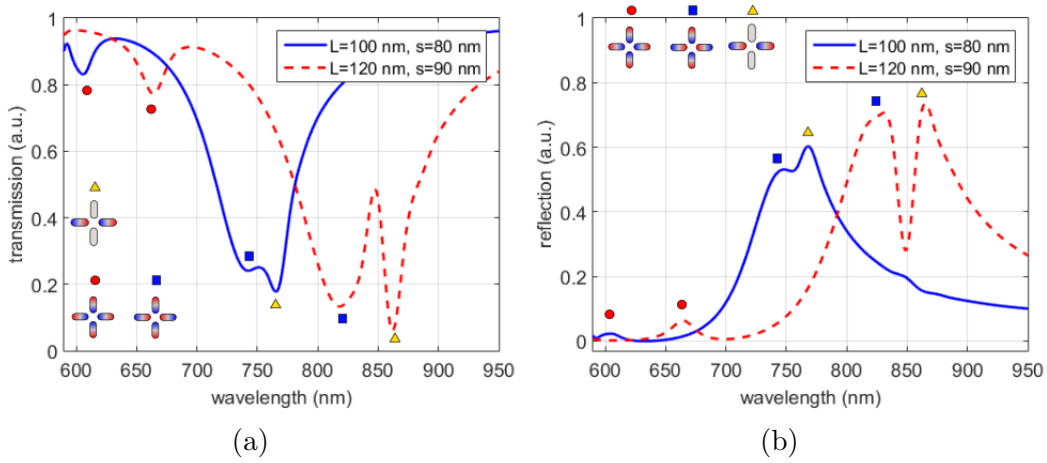

Figure 4.23: The (a) transmission through and (b) reflection from radial tetramer metasurfaces by a p-polarised plane wave for different nanorod lengths L and the gap size $\delta = 30$ nm is kept constant.

As the gaps become smaller, fabricated nanorod-ends tend to join leaving no gap and the minimum possible gap is typically around 10 to 15 nm.

Figure 4.24 shows the radial trimer spectrum with various off-set distances s. The nanorod size is $100 \times 40 \times 40$ nm and the periodicity is 300 nm. A p-polarised plane wave is incident at 20°. As the gap size decreases, the nanorod-coupling increases leading to splitting between radial and dipole modes. This

pushes the radial mode resonance to a shorter wavelength and the dipole mode resonance to a longer wavelength. Similar results for the radial tetramer are shown in Figure 4.25 where the smaller gap pushes the radial mode to a shorter wavelength. As seen in the previous section, reducing the gap increases the coupling, red-shifting the dipole mode and blue-shifting the radial mode. For $s = 130$ nm, however, no breathing mode is apparent in the spectrum. This mode interferes with the dipole mode resonance, producing a Fano resonance line-shape at a longer wavelength.

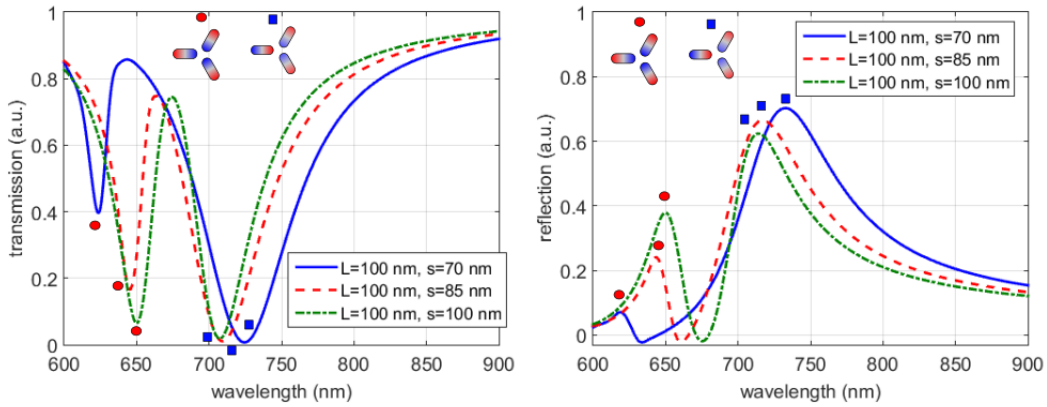

(a) (b)

Figure 4.24: The (a) transmission through and (b) reflection from radial trimer metasurfaces by p-polarised light for different off-set distance s. The periodicity is $p = 300$ nm for each metasurface.

As discussed previously, the radial mode is sensitive to the angle of incidence of an excitation plane wave, or equivalently, the transverse spatial frequency of the incident light. At normal incidence, it is not excited. As the angle of incidence is increased, the strength of the radial mode relative to the dipole mode increases. Consider a metasurface consisting of radial trimer antennas where $L = 100$ nm, $w = h = 40$ nm, and $s = 70$ nm. The radial mode resonance is at 620 nm. The simulations were performed with p-polarised light with different angles of incidence at the resonance wavelength. The results are shown in Figure 4.26 where it can be seen that the strength of radial mode excitation becomes stronger with increasing angle of incidence. The valley in the transmission spectrum also becomes deeper and the peak in the reflection spectrum increases. The radial mode resonances are slightly blue-shifted with increasing angle of incidence.

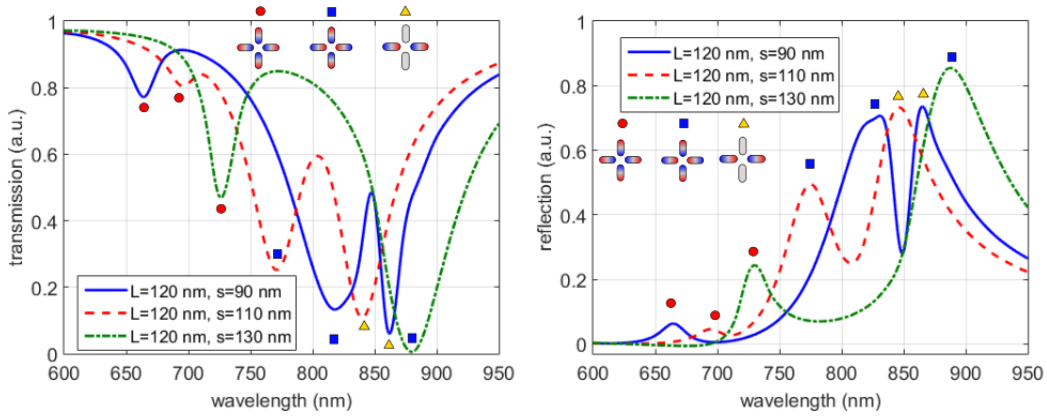

(a) (b)

Figure 4.25: The (a) transmission through and (b) reflection from radial tetramer metasurfaces by p-polarised plane wave for different off-set distances s. The periodicity is $p = 400$ nm for each metasurface.

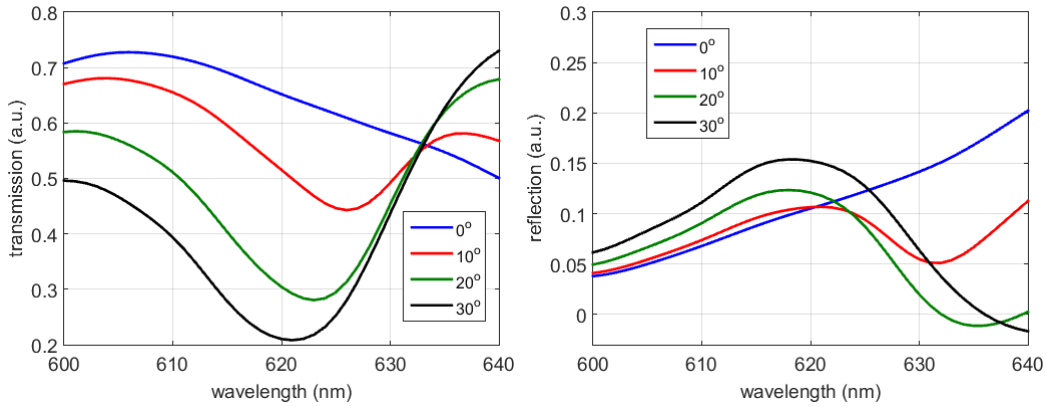

(a) (b)

Figure 4.26: The (a) transmission through and (b) reflection from a metasurface consisting of radial trimer antennas by p-polarised plane waves with different angles of incidence θ. The nanorod sizes are $100 \times 40 \times 40$ nm, the off-set distance is $s = 70$ nm, and periodicity is $p = 300$ nm.

The metasurface was also investigated as the azimuthal angle ϕ of the incident field was varied, i.e. the angle of the plane of incidence with respect to the x-axis, keeping the angle of incidence $\theta = 20°$ constant. The results are shown in Figure 4.27, where the parameters are the same as in Figure 4.26 for a metasurface consisting of radial trimers illuminated with a p-polarised plane wave. There is no significant shift in the radial mode in both the trans-

mission and reflection spectra. The dipole mode, however, shifts to a longer wavelength with increasing ϕ. The interaction between neighbouring unit cells is responsible in the asymmetry. The rods are closer along the y axis rather than along the x-axis. This is, however, is not the only cause of the shifting of dipole mode resonance, as shown with the simulation on a single antenna.

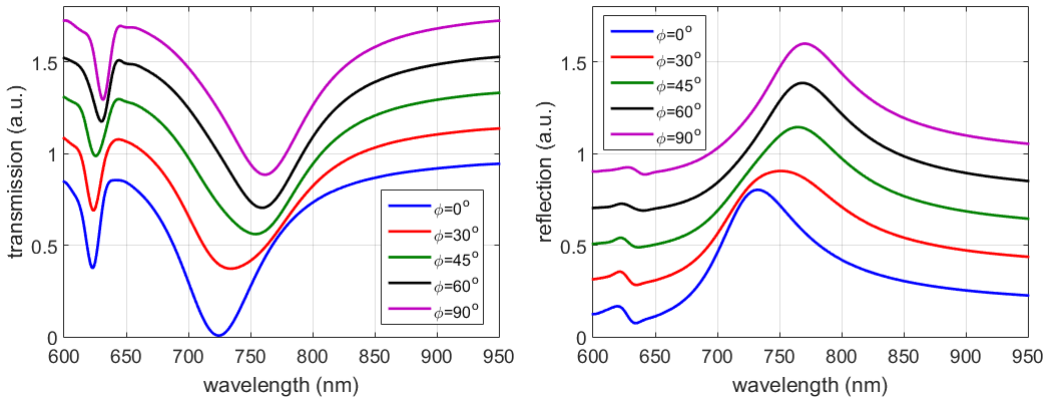

(a) (b)

Figure 4.27: The (a) transmission through and (b) reflection from a metasurface consisting of radial trimers with $L = 100$ nm, $w = 40$ nm, $s = 70$ nm, and $p = 300$ nm with variation of azimuthal angle ϕ of incident fields. The spectra are shifted upward for clarity.

To further understand the origin of shift in the dipole mode, a simulation was also performed with a single antenna, a radial trimer. The radial trimer has 60° symmetry of rotation and the spectra are expected to exhibit symmetry with respect to 60° rotation of ϕ. The scattering from a single radial trimer with variation of ϕ is shown in Figure 4.28. The spectra do not show the expected 60° symmetry, as shown with the differences between $\phi = 0°$ and 60° as well as between $\phi = 30°$ and 90°. This effect can be explained due to the meshing in the FDTD that is shaped as rectangular grids, so that the illumination of antenna at $\phi = 0°$ and 60°, with the same angle of incidence θ, do not produce same spectra. The whole effect on the metasurfaces simulated using the FDTD can be explained by the combination between the two effects, asymmetric coupling between neighbouring unit cells and rectangular grids on the FDTD algorithm.

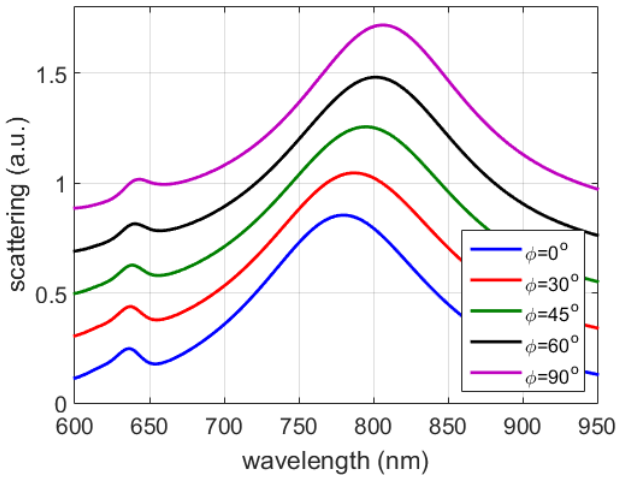

Figure 4.28: The scattering from a single radial trimer with $L = 100$ nm, $w = 40$ nm, and $s = 70$ nm with variation of azimuthal angle ϕ of incident fields. The spectra are shifted upward for clarity.

The sub-radiant modes dependence on angle of incidence is discussed more thoroughly in Section 4.3.3 where the modelling was performed with the EEM. Although an approximation including various 'fit' parameters, the EEM can be used to rapidly perform calculations that would be prohibitive using the FDTD method.

4.2.3.2 Metasurfaces with Azimuthal Antennas

Further investigation of metasurfaces made of arrays of optical antennas in an azimuthal configuration was performed to study azimuthal modes. As previously discussed, the excitation of this mode can be done by using either an azimuthally polarised beam or an off-normal s-polarised plane wave (at 20°). Figure 4.29 and 4.30 shows plots of the transmission and reflection spectra from metasurface of azimuthal trimers and tetramers with various types of illumination calculated using the FDTD. The nanorod dimensions in all trimers are $100 \times 40 \times 40$ nm, the off-set distance is $s = 70$ nm, and periodicity is $p = 300$ nm. The tetramers have an off-set distance of $s = 80$ nm with the same nanorod sizes as the trimers. The periodicity is larger, $p = 400$ nm as tetramers have a larger size than the trimers. The dark modes resonant near 800 nm appear under s-polarisation excitation for both trimers and tetramers.

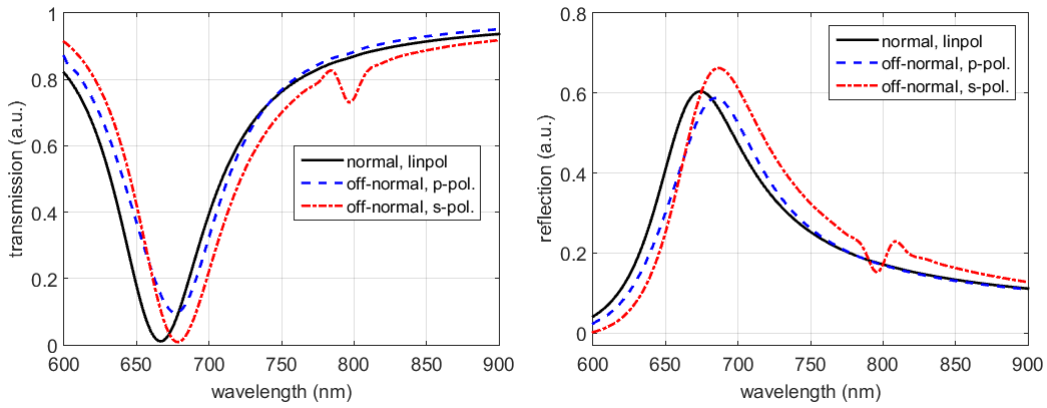

(a) (b)

Figure 4.29: The (a) transmission through and (b) reflection from a metasurface consisting of azimuthal trimers with different illumination of plane waves. The azimuthal mode is excited by s-polarised plane wave.

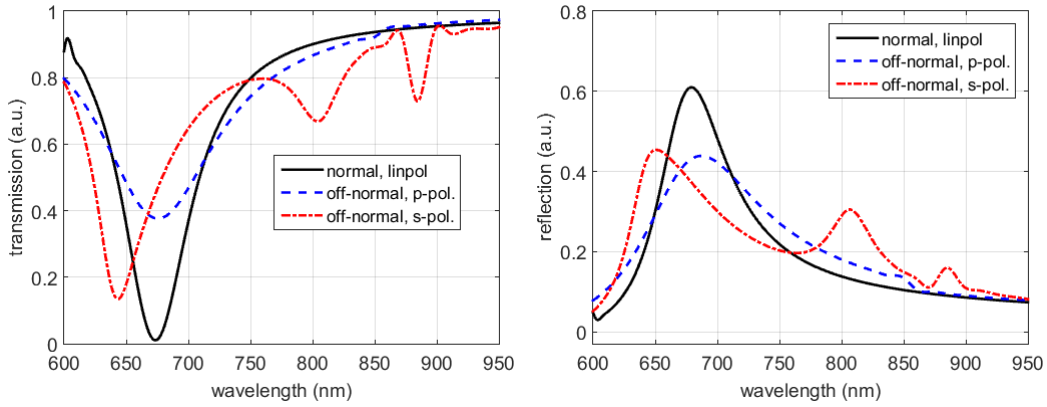

(a) (b)

Figure 4.30: The (a) transmission through and (b) reflection from a metasurface consisting of azimuthal tetramer antenna with different excitations with angle of incidence 20° for s- and p-polarised illumination. The azimuthal mode is excited by s-polarised plane wave.

Two resonances can be seen in the metasurface of azimuthal trimers. One resonance is the dipole mode at 680 nm and the other is an azimuthal mode at 810 nm. The dipole mode is a bright mode excited with both normal and off-normal incident light but the azimuthal mode can be excited only with s-polarised light due to the normal component of the magnetic field and the phase gradient in the electric field introduced by the oblique angle.

The modes can be identified by looking at the surface charge distribution

on the nanorods at each of the resonances. Figure 4.31 shows the surface charge at the central wavelengths of the dipole and azimuthal resonances. In Figure 4.31a, the dipole mode has a net electric dipole moment along the x-axis, aligned with the polarisation of the incident light. In Figure 4.31b, the azimuthal mode has zero dipole moment and the surface charge distribution has azimuthal symmetry across the antenna.

In the azimuthal tetramer, there are potentially three resonances which could be observed, which are associated with the dipole, azimuthal, and quadrupole modes. The modes can identified again by looking at the surface charge at the corresponding wavelength. Figure 4.32 shows the surface charge distribution at resonances. In this frequency range, the dipole mode has a resonance at 680 nm and the azimuthal mode occurs at 815 nm. The peak at 885 nm is a numerical artefact and does not correspond to another mode. This artefact can be reduced by decreasing the mesh sizes or by using a larger angle of incidence. Another simulation was performed with a larger angle of incidence, 30°, as shown in Figure 4.33. The peak at 885 nm then disappears as expected. There is no clear indication that the quadrupole mode is excited.

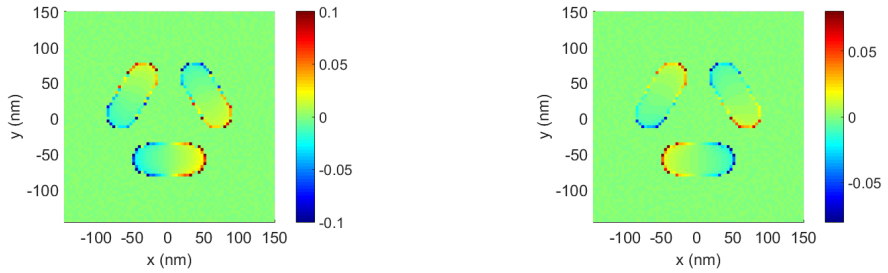

Figure 4.31: The surface charge distribution of (a) dipole mode ($\lambda = 680$ nm) and (b) azimuthal mode ($\lambda = 805$ nm) resonances of azimuthal trimer antennas. The parameters as in Figure 4.29.

The effects of increasing nanorod size on the resonances of the metasuface of azimuthal trimer antennas are shown in Figure 4.34. The gap size is fixed and the periodicity is $p = 300$ nm. Larger nanorods lead to the resonance shifting to a longer wavelength due to the resonance of the individual nanorods being red-shifted with increasing size. The azimuthal mode is red-shifted more than the dipole mode so larger antennas have a larger separation between these modes with the azimuthal mode occuring in the red or near-infrared regions.

(a) (b)

Figure 4.32: The surface charge of (a) dipole mode ($\lambda = 640$ nm) and (b) azimuthal mode ($\lambda = 815$ nm) resonances of azimuthal tetramer antennas. The parameters as in Figure 4.30.

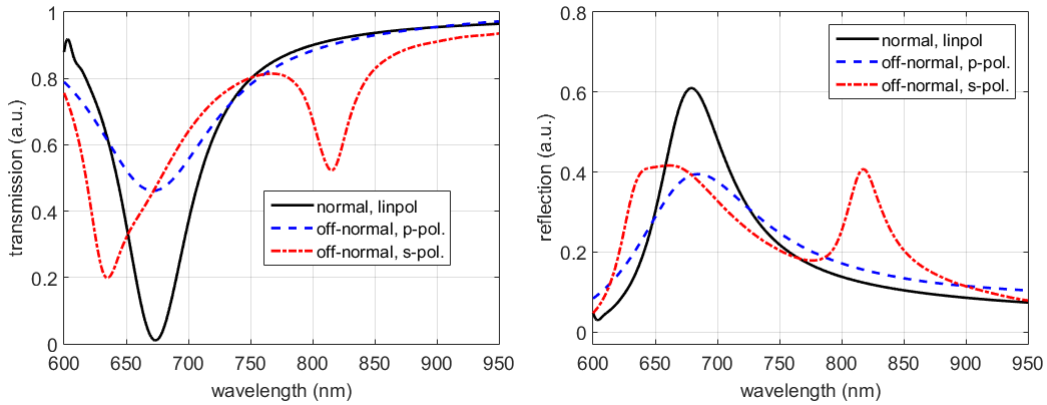

(a) (b)

Figure 4.33: The (a) transmission through and (b) reflection from azimuthal tetramer antenna with different excitations. The angle of incidence of p- and s-polarised plane wave is 30°.

The results of investigating tetramers composed of nanorods of different lengths with the periodicity $p = 400$ nm are shown in Figure 4.35. Dipole and azimuthal mode resonances are red-shifted for longer nanorods.

A larger separation distance between the nanorods leads to weaker coupling and this is not an exception for the metasurface of azimuthal antennas. The trimer and tetramer results are shown in Figures 4.36 and 4.37. The periodicities are $p = 300$ nm for trimers and $p = 400$ nm for tetramers. As their off-set distance s increases, the resonances approach that of an individual nanorod. The dipole mode is red-shifted and the azimuthal mode is blue-shifted, opposite to the shifting seen in metasurfaces of radial antennas.

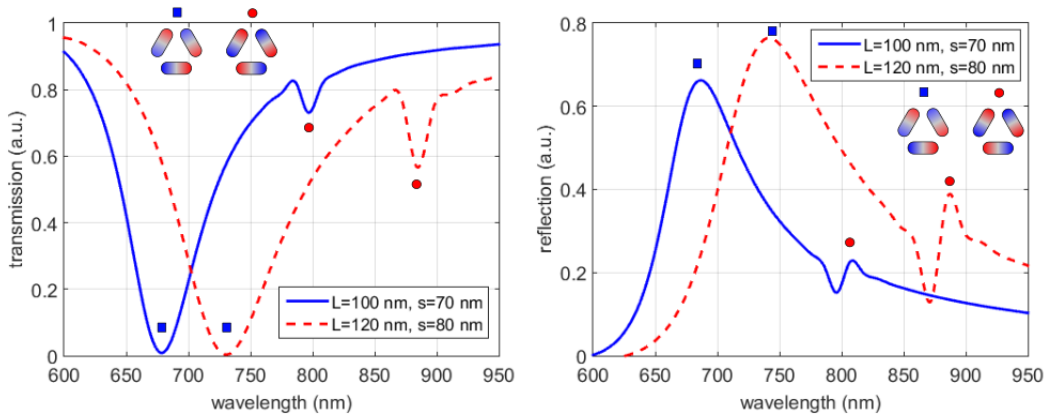

(a) (b)

Figure 4.34: The (a) transmission through and (b) reflection from azimuthal trimer metasurfaces with s-polarised plane wave illumination for different nanorod lengths L but the gap size $\delta = 71$ nm is kept constant. The periodicity is $p = 300$ nm.

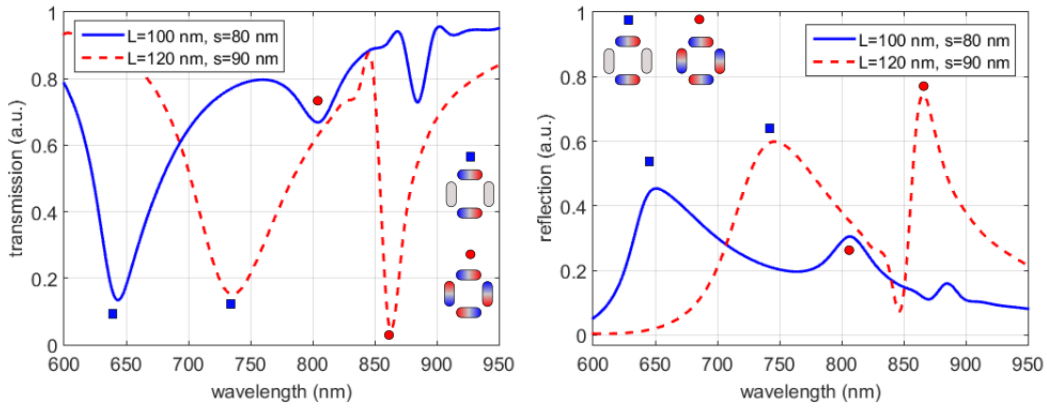

(a) (b)

Figure 4.35: The (a) transmission through and (b) reflection from azimuthal tetramer metasurface by s-polarised light for different nanorod length L but the gap size $\delta = 30$ nm is kept constant. The periodicity is $p = 400$ nm.

4.3 Modelling with The Electrostatic Eigenmode Method (EEM)

EEM modelling initially involves solving for the intrinsic electromagnetic properties of a single metal nanoparticle. The charges on the nanoparticle have oscillation modes that depend on the type of material and the geometry of the

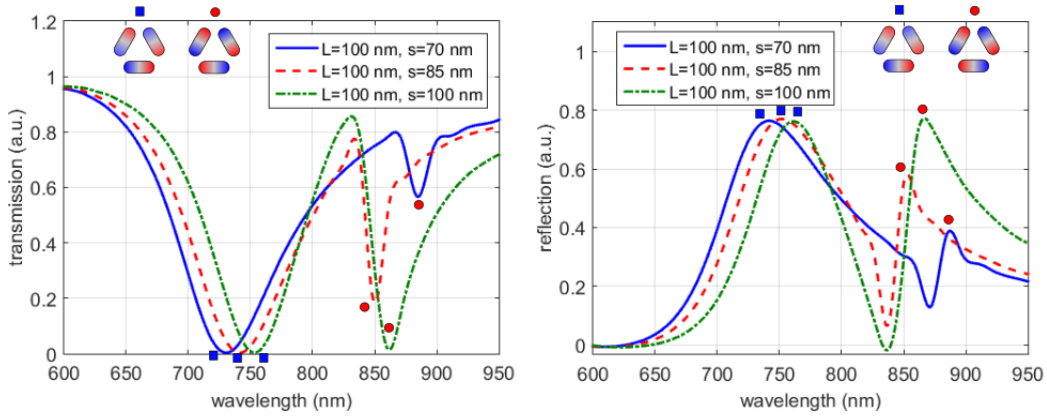

(a) (b)

Figure 4.36: The (a) transmission through and (b) reflection from the metasurface of azimuthal trimer antennas by s-polarised light for different off-set distance s. The periodicity is $p = 300$ nm.

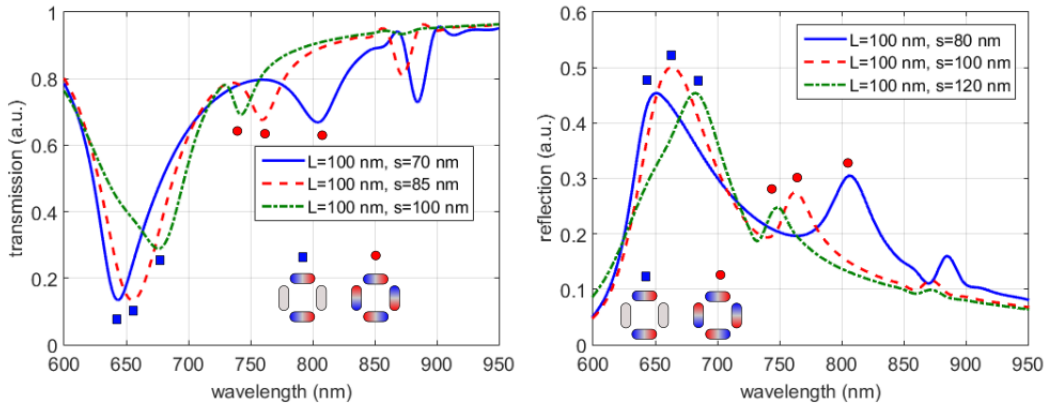

(a) (b)

Figure 4.37: The (a) transmission through and (b) reflection from azimuthal tetramer metasurfaces with s-polarised plane wave illumination for different off-set distances s. The periodicity is $p = 400$ nm.

particles. These modes can be coupled to the incident field and each mode resonates at different frequencies or wavelengths. The dipole mode of a single particle has the lowest energy and is the dominant mode.

For a rod-shaped metal nanoparticle, the lowest order dipole mode has its electric dipole moment parallel to its long axis [19]. When several nanorods are placed together to form an optical antenna, the modes on each particle

interact with each other. Their interactions determine the entire scattering properties of the optical antenna.

The analysis provided here are for optical antennas arranged in periodic arrays or metasurfaces. The interactions between plasmonic modes and the scattering of waves were analysed within each unit cell. The scattering properties of the array were subsequently determined by finding the coupling between the nanorods and the dominant scattered wave from the metasurface. This component of the scattered field is the wave with the same transverse (k_x, k_y) wavevector component as the incident field. Hence specular transmission or reflection is assumed. A detailed explanation was provided in Section 3.3.3.

The results from FDTD can be used to assist in choosing suitable parameters for EEM modelling. Figure 4.38 shows the simulated scattering from silver nanorod as a single particle and Figure 4.39 shows the transmission and reflection spectra of a two dimensional periodic nanorods ($p = 300$ nm), both calculated with the FDTD method. The transmission spectra are shifted upward for clarity. The resonance wavelength as well as the full-width at half-maximum can then be used in EEM calculations. The rods are assumed to be embedded in a medium with refractive index $n = 1.5$.

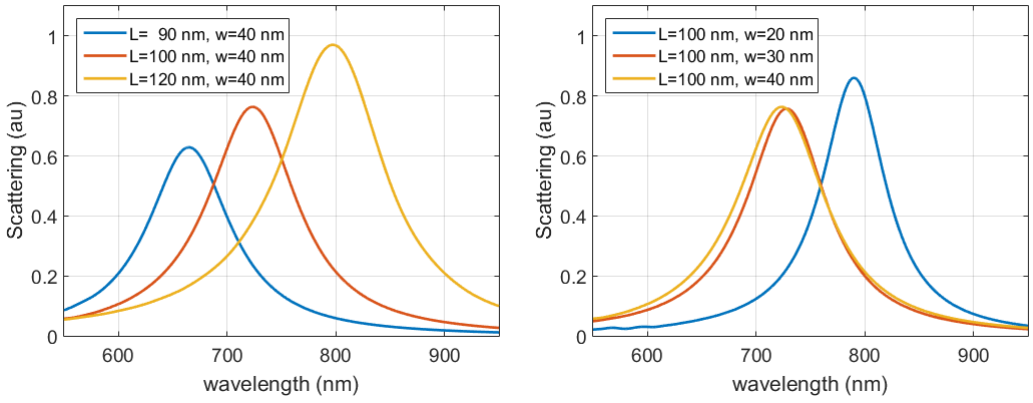

(a) (b)

Figure 4.38: The scattering from a single isolated nanorod with various sizes, (a) various lengths L and widths $w = 40$ nm and (b) various widths w and lengths $L = 100$ nm, calculated using the FDTD method. The heights are $h = 40$ nm.

From those figures, a silver nanorod with $L = 100$ nm and $w = h = 40$ nm has a long-axis dipole resonance at ∼730 nm when isolated. If the rods are

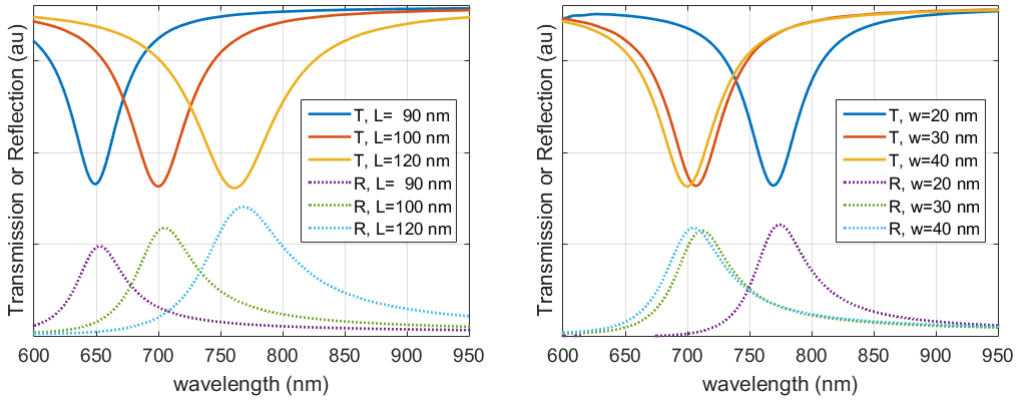

(a) (b)

Figure 4.39: The transmission though and reflection from a periodic array of nanorods with various sizes, (a) various lengths L and widths $w = 40$ nm and (b) various widths w and lengths $L = 100$ nm, calculated using the FDTD method. The heights are $h = 40$ nm and periodicity is $p = 300$ nm.

Figure	λ_p (nm)	ω_p (rad/s)	Γ (rad/s)
4.40a	730	2.58×10^{14}	3.50×10^{14}
4.40b	709	2.66×10^{14}	2.44×10^{14}

Table 4.1: The parameters used in the EEM calculation for the spectra of single nanorods in Figure 4.40.

arranged in an array with a periodicity of 300 nm, the resonance is blue-shifted to ∼710 nm and its linewidth also becomes smaller. This blue-shifting and narrowing of the resonance also occur for nanorods with different sizes. The spectrum produced by the FDTD can be reproduced by the EEM with normal incidence plane wave illumination. By fitting the results of Figures 4.31 and 4.32 to Lorentzian lineshapes, it is possible to obtain suitable parameters to use in the EEM. The parameters generated from those simulation for nanorod with $L = 100$ nm and $w = h = 40$ nm are provided in Table 4.1. For an array of nanorods, fitting was performed on the reflection spectrum.

Figure 4.40 shows a comparison of the scattering spectra from a single rod obtained from the EEM with fit parameters obtained using the FDTD. Figure (a) corresponds to a single isolated nanorod and Figure (b) corresponds to the array of single nanorods. The lineshape produced by the EEM in Figure (b) is different to that from the FDTD, despite having the same peak and linewidth. The spectrum from the FDTD is asymmetric as a result from

the interaction between the nanorods in the array, whereas in the EEM, the interactions between unit cells are neglected. These two set of parameters are discussed further in the following sub-section.

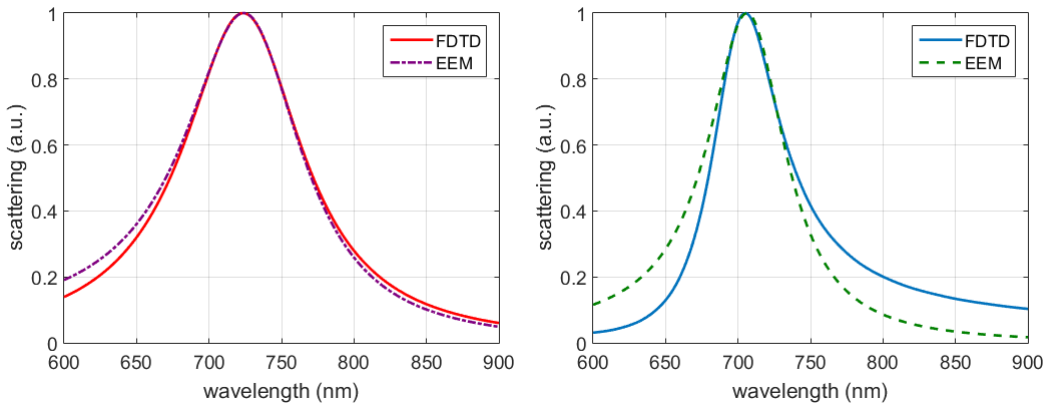

(a) (b)

Figure 4.40: Reproducing the spectrum of silver nanorod from the FDTD simulation result with the EEM. (a) A single isolated nanorod and (b) array of nanorods with periodicity 300 nm. The size is $L = 100$ nm $w = h = 40$ nm with background refractive index $n = 1.5$

.

4.3.1 Scattering from Metasurfaces Composed of Radial Antennas

Consider a metasurface consisting of radial trimer antennas. The nanorods are placed to form a symmetric radial trimer which has an off-set distance of $s = 70$ nm. The direction of the uncoupled dipole modes are set to be inward to the centre[3]. As they are symmetric, the interaction between any two nanorods is equal, so that we can define a common coupling constant G for all of the interactions, i.e. $G_{12} = G_{13} = G_{23} = G$. The value of G is negative because we have arranged the dipole orientations between any two nanorods to be 'head-to-head'. Figure 4.41 shows a schematic of the dipole orientations of the particles in a radial trimer antenna used for calculating the mode interactions with EEM.

[3]The direction can be set in any direction along the axis of each nanorod, but the coupling constant G_{ij} between i-th and j-th particle will then have the opposite sign.

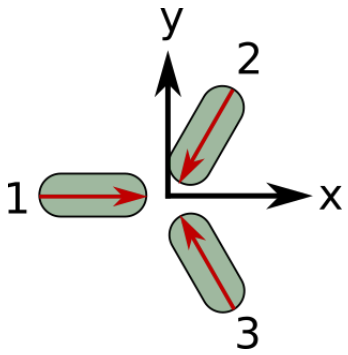

Figure 4.41: The assumed direction of *uncoupled* dipole modes of the nanorods of radial trimer, used for calculating the mode interactions.

The metasurfaces were investigated using several different plane-wave excitations described in Section 3.4. To obtain a far-field radial mode excitation, either radially polarised or p-polarised off-normally incident light needs to be used.

Recall the simulation results with the FDTD method for radial trimer metasurface from Figure 4.17. The nanorod size is $100 \times 40 \times 40$ nm, off-set distance $s = 70$ nm and periodicity 300 nm. The spectrum with p-polarised plane wave illumination is to be reproduced. The resonance wavelength and linewidth of a single nanorod can be obtained either from the spectrum of a single isolated nanorod or array of single nanorods. Scattering from the FDTD was obtained from the reflection spectrum.

Figure 4.42 shows the scattering spectrum reproduced by the EEM using the resonance wavelengths and linewidths obtained from the FDTD simulation. The coupling constant G is set to produce a resonance of radial mode at 620 nm. There are two calculations of the spectra using two different sets of parameters which are listed in Table 4.2. The first was calculated based on the resonance of an isolated nanorod and the second was based on the resonance of an array of nanorods mentioned previously.

The first spectrum has a dipole resonance at 768 nm and the second spectrum at 737 nm while the FDTD result is at 724 nm. From this calculation, it can be concluded that the second spectrum has a better agreement with the FDTD result. Note that the EEM is an approximate method so that precise results are not expected. The radial mode calculated from the EEM is significantly weaker, despite the angle of incidence being larger, 49°, compared to 20° in

Parameters (Units)	Values	
	EEM-1	EEM-2
λ_p (nm)	730	709
A (rad/s)	1×10^{14}	1×10^{14}
Γ (rad/s)	3.50×10^{14}	2.44×10^{14}
G	-1.9	-1.6
s (nm)	70	70

Table 4.2: The EEM parameters for calculating spectra in Figure 4.42.

FDTD calculation.

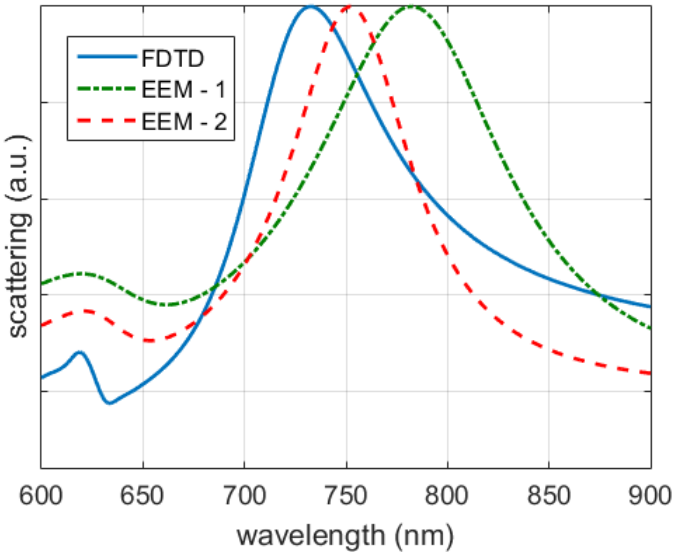

Figure 4.42: Reproducing the scattering from radial trimer metasurface from FDTD simulation with the EEM. Parameters from (1) isolated single nanorod and (2) array of single nanorods were used.

This suggests that to produce the reasonably accurate spectra of the metasurface as an array of antennas, the suitable single nanorod spectral parameters to be used are the ones from an array of nanorods instead of an isolated particle. This is potentially due to the effect of neighbouring antennas on the mode excitations which is assumed intrinsically from the use of the resonance wavelength λ_p and linewidth Γ.

For the purpose of illustration using the EEM to investigate the key properties of the metasurfaces, the parameters used in the following EEM modelling are different to those found above. For example, the coupling constant for

radial trimer metasurface discussed above is set to be $G = -3$ instead of $G = -1.6$ and linewidth Γ is slightly smaller to show well-separated radial and dipole mode resonances. The values of the parameters used in the following calculations can be shifted and fitted with the FDTD simulation results and/or the experimental data to obtain more accurate spectra if required.

Figure 4.43 shows the results of calculated scattering spectra from a metasurface when excited with several different incident plane waves. Off-normally incident plane waves were set at 30° angle of incidence. In this example, the parameters are set to $\lambda_p = 700$ nm, $G = -3$, $A = 1 \times 10^{14}$ s^{-1}, and $\Gamma = 2 \times 10^{14}$ s^{-1}. The plane of incidence is aligned parallel to the x-axis, along one of the nanorods.

The scattering spectrum with a normally incident linearly-polarised plane wave has a peak at 785 nm. This corresponds to the excitation of the dipole mode. The resonance appears at a longer wavelength compared to the single nanorod (at 700 nm).

To excite the radial mode, an off-normally incident plane wave with p-polarisation is used. The effects of the excitation of both radial and dipole modes appear in the spectrum as two peaks. The radial mode resonance occurs at 570 nm, a shorter wavelength than the dipole mode resonance.

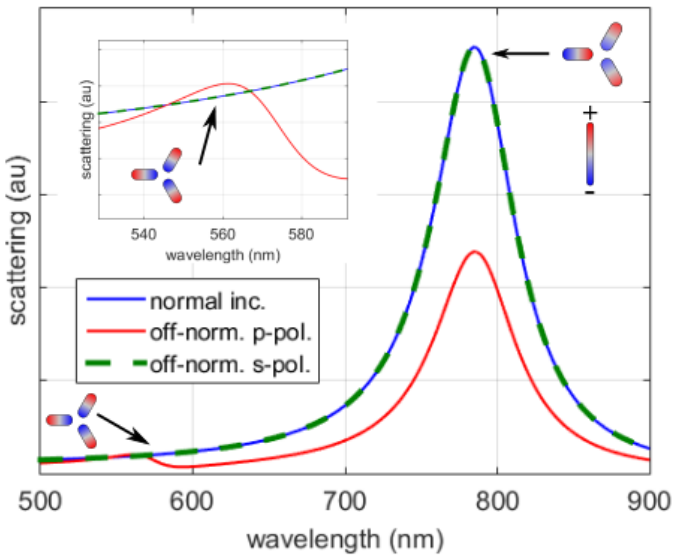

Figure 4.43: The scattering by the metasurface of radial trimer antennas when excited by normally and off-normally incident plane waves (p- and s-polarised).

The modes of excitation can be analysed by looking at the coupled amplitudes of excitation of the nanorods forming a single antenna in a unit cell. It was initially defined that the uncoupled dipole modes on each nanorod have moments aligned inward toward the centre of the antenna. The modes are then coupled to each other when illuminated by incident plane waves. Looking at the mode amplitudes at specific wavelengths, i.e. the resonance wavelengths, the symmetry of the excitation can be determined.

Figure 4.44 shows the real part of the coupled amplitudes of each mode on each rod on a metasurface with radial trimer antennas. The incident wave is a normally incident p-polarised plane wave. Each nanorod is assigned a number as shown in Figure 4.41. The amplitudes undergo a phase change at 785 nm, indicating the resonance of the dipole mode. At just below 785 nm, nanorod 1 has a positive amplitude while the other two nanorods have a negative amplitude. This shows an electric net dipole moment in the $+x$-direction, as shown in the inset diagram. At just above 785 nm, the amplitudes change sign and the net electric dipole moment is still parallel to the x-axis but in the opposite direction ($-x$). At 570 nm, the signs of all rod mode amplitudes are the same (all negatives), forming radially outward dipole moments and this indicates the radial mode excitation.

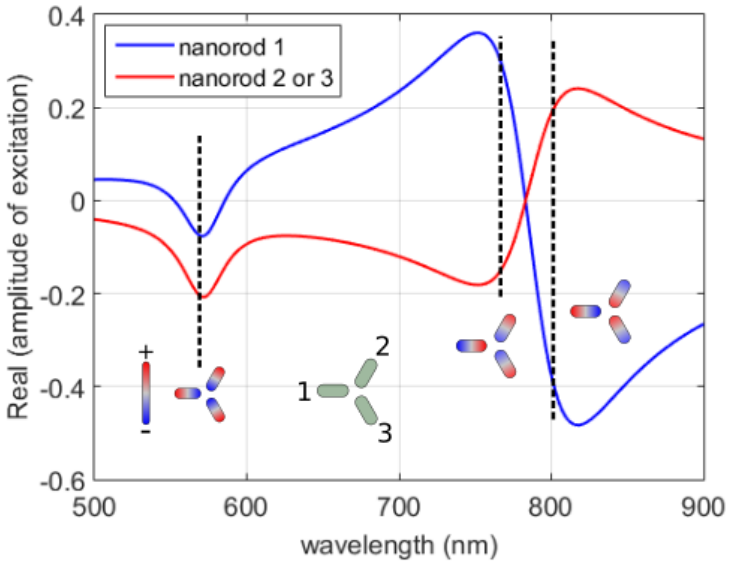

Figure 4.44: The excitation amplitudes of the nanorods in radial trimers when excited by the off-normally incident p-polarised light.

To see the roles played by the coupling constant, G, and off-set distance,

s, in changing the scattering spectra, the graphs of scattering from a radial trimer metasurface with various G and s are shown in Figure 4.45. The other parameters are kept fixed and the peak scattering is normalised to 1 for each parameter.

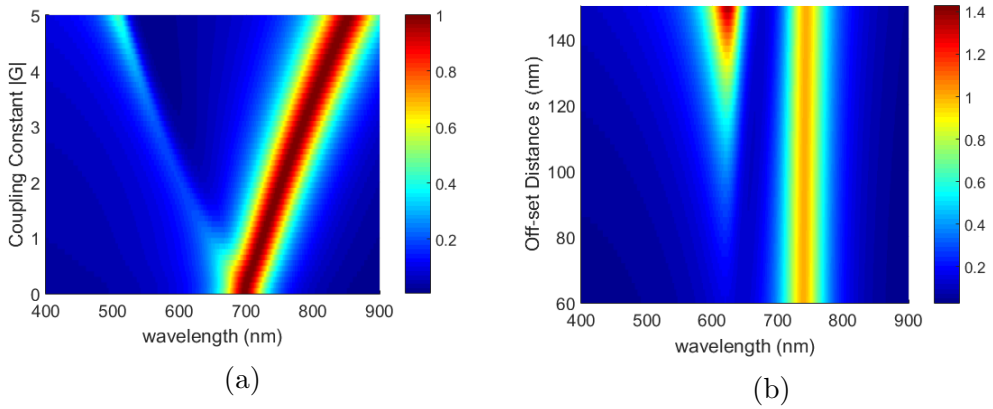

(a) (b)

Figure 4.45: The scattering spectra of radial trimer metasurface for (a) different coupling constants $|G|$ and (b) off-set distances s while keeping the other parameters fixed.

The result of looking at the variation in G (Figure 4.45a) suggests that as expected, increasing the coupling constant increases the spectral separation between radial and dipole mode resonances. The weaker radial mode is blue-shifted while the dipole mode is red-shifted. This means that to produce well-separated resonances of radial and dipole modes, nanorods composing the antennas must be placed as close as possible to maximise the coupling constant.

By increasing the off-set distance s (Figure 4.45b), the radial mode strength increases. This occurs because the spatial phase variation is larger between antennas that are further apart. In practice, however, a larger value of s reduces the coupling constant G, making the resonances of radial and dipole modes spectrally closer. In other words, parameters s and G are not independent.

The modes produced by radial trimer antennas can be considered as splitting of the modes of individual nanorods, known as plasmon hybridization [100]. The individual properties of the particle are determined by ω_p and Γ in the calculation. As the particles get closer to each other, the coupling constant G increases, leading to an increase in the mode splitting, where in this case,

the dipole mode on individual particles produces the dipole (bright) and radial (dark) modes on the antennas.

For p-polarisation, the excitation of the modes is independent of the orientation of the plane of incidence. A variation in the orientation of the plane of incidence was achieved by defining the orientation angle ϕ with respect to the x-axis. The plane wave used has p-polarisation with 30° angle of incidence. The results are shown in Figure 4.46. This is in contrast to the results obtained using the FDTD simulation, shown in Figure 4.27 and 4.28, where the radial modes are unaltered with variations of ϕ, but the dipole modes are red-shifted as ϕ increases from 0° to 90°. Using the EEM, the coupling between the neighbouring unit cells are neglected and the calculation is not performed with rectangular grids, leading to the disappearance of shifting of resonances as observed in the FDTD.

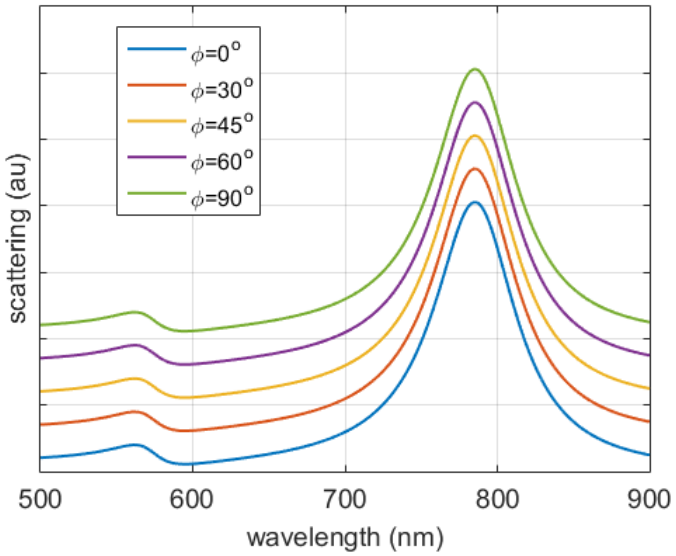

Figure 4.46: The scattering spectra of the radial trimers using p-polarised light with 30° angle of incidence where the plane of incidence makes an angle ϕ with respect to the x-axis. The spectra are shifted (upward) for clarity.

To investigate the phase sensitivity of radial mode excitation, the metasurface was investigated with plane-wave illumination with various angles of incidence. Figure 4.47 shows the scattering spectra from trimer antenna with p-polarised light. As the angle of incidence increases, the radial mode intensity becomes stronger and the intensity compared to the dipole mode increases with angle

of incidence. The angle dependence is parametrised using the σ_x component of the incident plane wave and σ_y is set to zero. The angle of incidence can be calculated by $\theta = \sin^{-1}(\sigma_x)$.

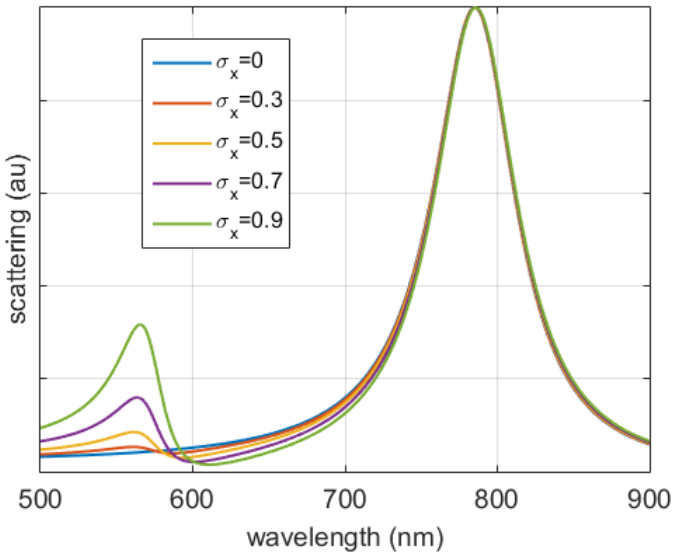

Figure 4.47: The scattered power of the metasurface with radial trimer antennas when excited by p-polarised light with various angle of incidence, where $\theta = \sin^{-1}(\sigma_x) = \sin^{-1}(k_x/k_0)$. The spectra are normalised to their respective dipole mode resonances.

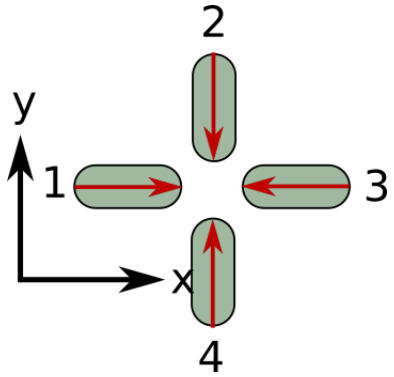

Figure 4.48: The assumed direction of *uncoupled* dipole modes of the nanorods of radial tetramer, used for calculating the mode interactions.

The response of an antenna to a radially polarised beam at normal incidence was then investigated. The radially polarised beam was modelled according to Equation 3.40 with the spatial profile parameter of $a = 150$ nm. In this case, a single antenna was assumed instead of an array. This calculation is performed to show that radially polarised light coaxial with the antenna can excite the

radial mode as well as suppress the strong dipole mode.

The results of a single radial trimer antenna illuminated with a radially polarised beam is shown in Figure 4.49. In Figure (a), no dipole mode is excited with the illumination and scattering at the radial mode resonance at 570 nm is observed. The amplitudes of excitation in Figure (b) indicate the radial symmetry of the modes because all nanorods either all have negative amplitudes or all have positive amplitudes at radial mode resonance. This is the case for a single antenna and for an array of antennas, the dipole mode would still be excited alongside the radial mode due to its bulk effect.

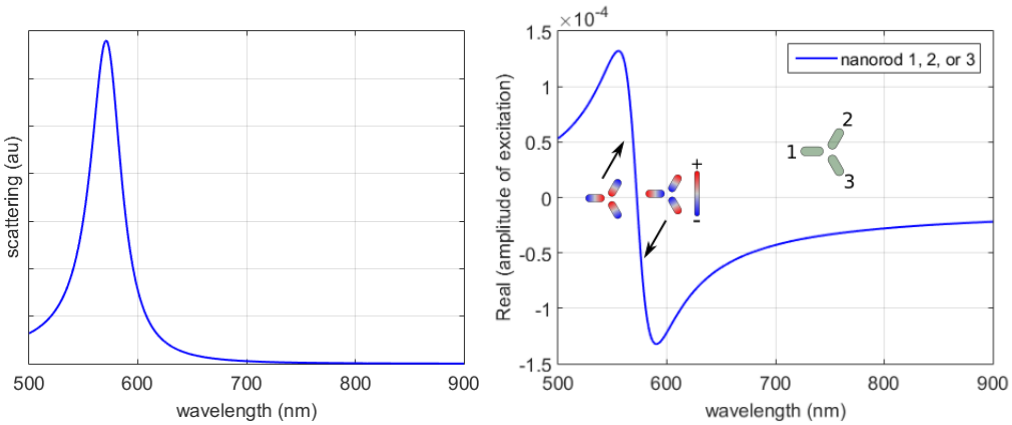

(a) (b)

Figure 4.49: The scattering of a single radial trimer antenna with the radially polarised beam coaxially with the antenna. (a) The scattering spectrum and (b) the amplitudes of excitation.

The other arrangement of radially symmetric antennas considered here are radial tetramers. Consider a metasurface composed of radial tetramer antennas. The properties of these antennas are similar to the radial trimers, but with another sub-radiant mode called the breathing mode (refer to Figure 4.6). The nanorods have sizes of $L = 100$ nm, $w = h = 40$ nm, and $s = 70$ nm. The uncoupled modes of the nanorods are assumed to have dipole moments shown in Figure 4.48. The EEM parameters are $G_A = -3$, $G_B = -1.5$, $A = 1 \times 10^{14}$ s^{-1}, and $\Gamma = 2 \times 10^{14}$ s^{-1}. G_A corresponds to the interaction between any two closest neighbours, e.g. nanorod 1 and 2. G_B corresponds to the interaction between any two opposing nanorods, e.g. nanorod 1 and 3, and has a smaller magnitude due the further distance and weaker coupling. Off-normally incident plane waves were set at 30° angle of incidence.

Figure 4.50 shows the power scattered by the metasurface with normal and off-normal incidence p- and s-polarised plane waves. As expected, normally incident plane waves produce only one peak, the dipole mode resonance at 740 nm. There are two peaks observed in the spectra with p-polarised light plane wave illumination. The corresponding modes are radial and dipole modes at 540 nm and 740 nm respectively. The breathing mode is not visible in the spectrum because a larger angle of incidence and, hence, a large phase variation across the antenna is required.

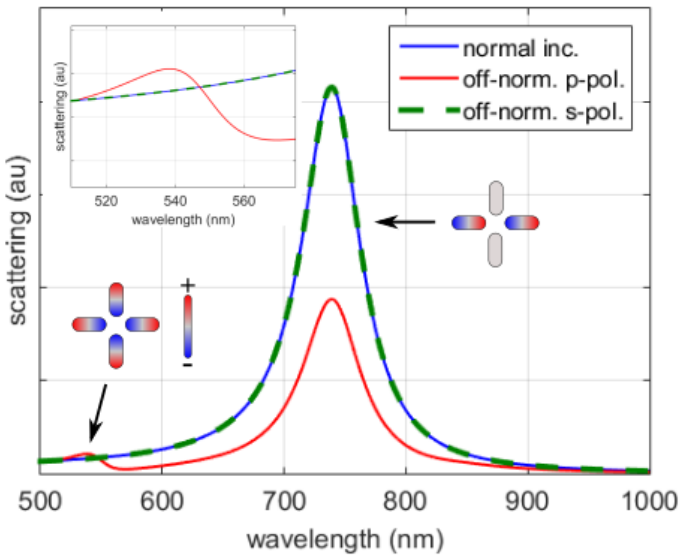

Figure 4.50: The scattering of plane waves from the metasurface of radial tetramers at normal and off-normal incidence. The off-normally incidence plane waves are p- and s-polarised. Inset: zoomed-in spectra to the radial mode resonance.

Figure 4.51 shows the real part of the coupled amplitudes of each nanorod in a unit cell of the metasurface. The radial modes are evidenced by the negative amplitude of excitation of every nanorod, at 540 nm. The dipole mode is excited parallel to the incident polarisation, i.e. parallel to the x-axis. Nanorods 1 and 3 are excited to produce a dipole mode at 740 nm. Despite no evidence of the breathing mode in the spectra, the excitation amplitudes show that there is evidence of weak excitation at 830 nm. At this wavelength with 30° angle of incidence, nanorod 1, however, does not exhibit the property of breathing mode excitation where its amplitude should be negative. This happens due to interference with the dominant dipole mode.

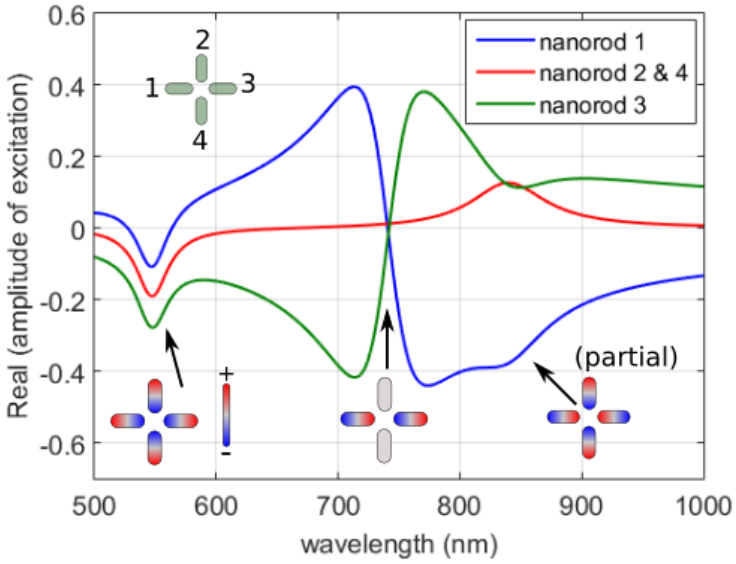

Figure 4.51: The real part of the amplitudes of excitation of the metasurface of radial tetramers with p-polarisation at 30° angle of incidence.

Figure 4.52 shows the influence of a variation of the angle of incidence, parametrised by $\sigma_x = \sin(\theta)$ where $\sigma_x = k_x/k_0$ is the unit propagation vector parallel to the x-axis and $\sigma_y = k_x/k_0 = 0$ is the unit propagation vector parallel the y-axis which is set to zero here. The spectra are normalised to that of their respective dipole modes so that the comparison of relative strength between the modes can be analysed more easily. As the angle of incidence increases, the relative strength of the radial mode at 540 nm increases. The breathing mode appears at 840 nm at values of σ_x of 0.7 and above.

The radial mode of radial tetramers can be excited with p-polarised but not not s-polarised plane waves. Unlike the radial mode, the breathing mode can be excited with either p- or s-polarised light with a specific plane of incidence orientation. Figures 4.53 and 4.53 show the effect of changing the plane of incidence orientation with respect to the x-axis by changing the angle ϕ for p- and s-polarised illumination. The spectra are shifted upward for clarity. The breathing mode is most clearly excited with p-polarisation when the plane of incidence is aligned with two of the nanorods (at $\phi = 0°$ and $\phi = 90°$) and excited with s-polarisation when the plane of incidence is not aligned with any nanorods (at $0° < \phi < 90°$).

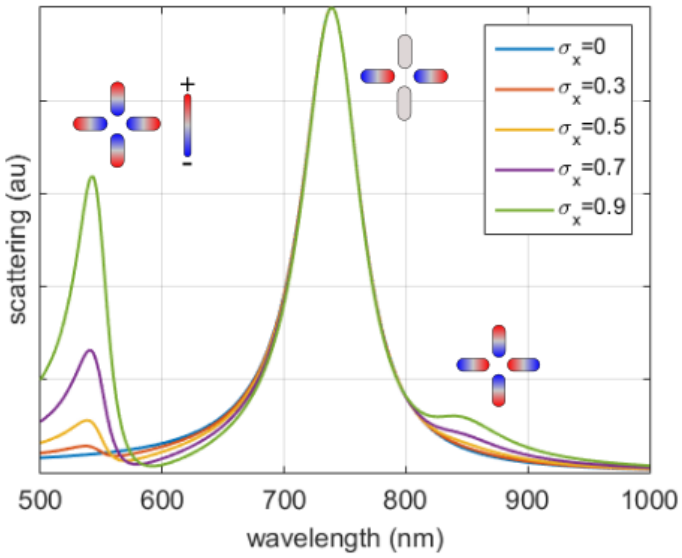

Figure 4.52: The scattering of the p-polarised plane wave from the metasurface of radial tetramers with various angle of incidence. The angle of incidence is determined by $\theta = \sin^{-1}(\sigma_x)$. The spectra are normalised to the dipole mode resonances.

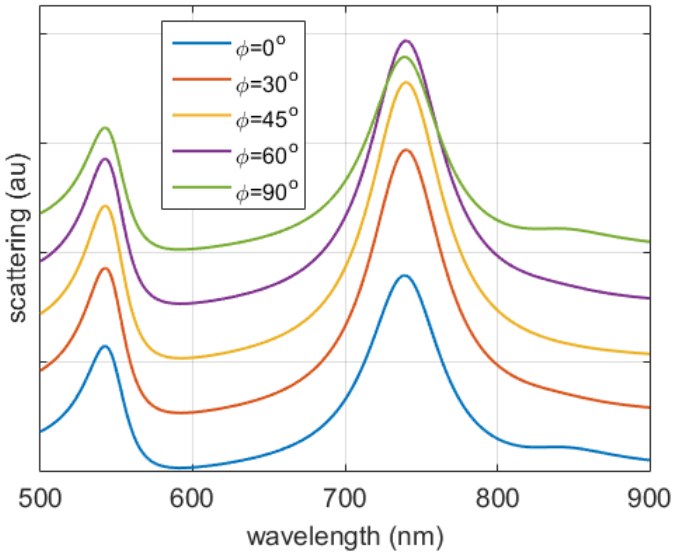

Figure 4.53: The scattering of plane waves with p-polarisation from the metasurface of radial tetramers with various orientation ϕ of plane of incidence with respect to the x-axis.

4.3.2 Scattering from Metasurfaces Composed of Azimuthal Antennas

Consider a metasurface with azimuthal trimer antennas. The uncoupled dipole moment of each nanoparticle is set to be directed counter-clockwise. The

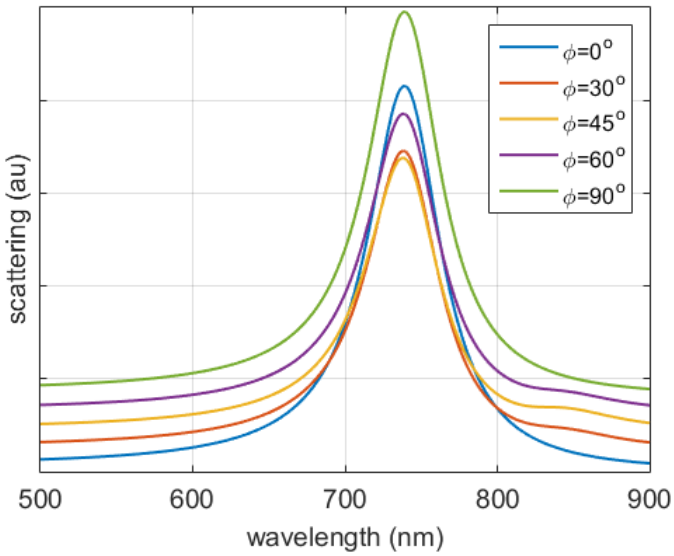

Figure 4.54: The scattering of plane waves with s-polarisation from the metasurface of radial tetramers with various orientation ϕ of plane of incidence with respect to the x-axis.

coupling constant has a positive value due to the dipole moments of the neighbouring nanoparticle being coupled 'head-to-tail' instead of 'head-to-head'. The arrangement of the assumed dipole modes on each uncoupled nanorod is shown in Figure 4.55. The parameters describing the azimuthal trimers are $G = 1.5$, $A = 1 \times 10^{14}$ s^{-1}, and $\Gamma = 2 \times 10^{14}$ s^{-1}. The angle of incidence was set to be 30° or $\sigma_x = k_x/k_0 = 0.5$ and $\sigma_y = k_y/k_0 = 0$.

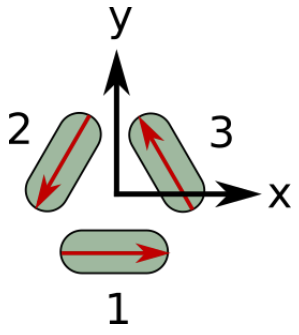

Figure 4.55: The assumed direction of *uncoupled* dipole modes of the nanorods of azimuthal trimer, used for calculating the mode interactions.

The resonance of the dipole mode can be identified by looking at the spectra produced by a normally incident, linearly polarised plane wave. The excitation of the azimuthal mode is produced by either the off-normally incident s-polarised plane wave or through azimuthally polarised beam excitation. The

results of plane wave excitation are shown in Figure 4.56. The plane of incidence for the off-normally incident plane wave is parallel to the x-axis.

For a metasurface of azimuthally arranged trimers, the lowest energy sub-radiant mode, i.e. the azimuthal mode, appears at a longer wavelength than the dipole mode. The dipole and azimuthal modes are at 660 nm and 790 nm respectively. No sub-radiant mode is excited by a p-polarised plane wave for this type of antenna. The phase difference across the antenna introduced by an oblique angle of incidence as well as the anti-parallel oscillation of the electric field of s-polarisation are responsible for the azimuthal mode excitation.

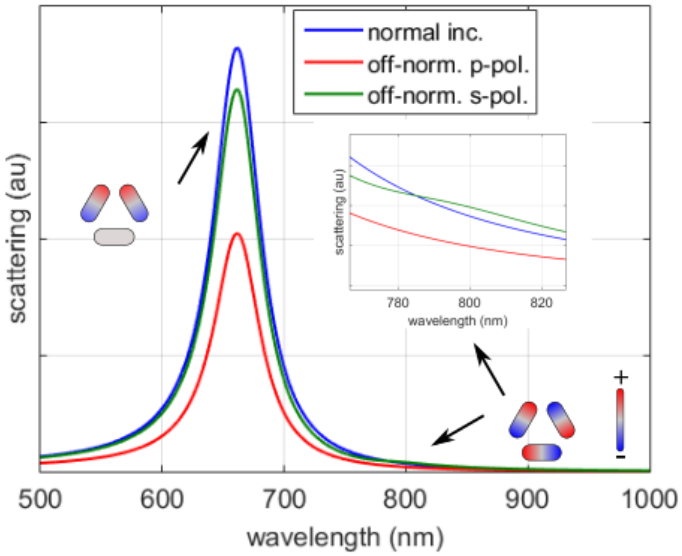

Figure 4.56: The scattering of a metasurface with azimuthal trimer antennas when excited by normally and off-normally incident plane waves (p- and s-polarised). Inset: zoomed-in spectra at azimuthal mode resonance.

The real part of the coupled excitation amplitudes are plotted in Figure 4.57 for s-polarised plane wave incidence. The phase change occurs at the dipole mode resonance at 660 nm. At just below and above this wavelength, the amplitude of nanorod 1 has opposite sign to the amplitudes of nanorod 2 and 3, indicating a net dipole moment perpendicular to the plane of incidence, or parallel to the x-axis. At 790 nm, the azimuthal mode can be identified, although the amplitudes are modified by interference with dipole mode excitation. At this wavelength, all nanorods have the same dipole moment orientation with the assumed counter-clockwise arrangement shown in Figure 4.55.

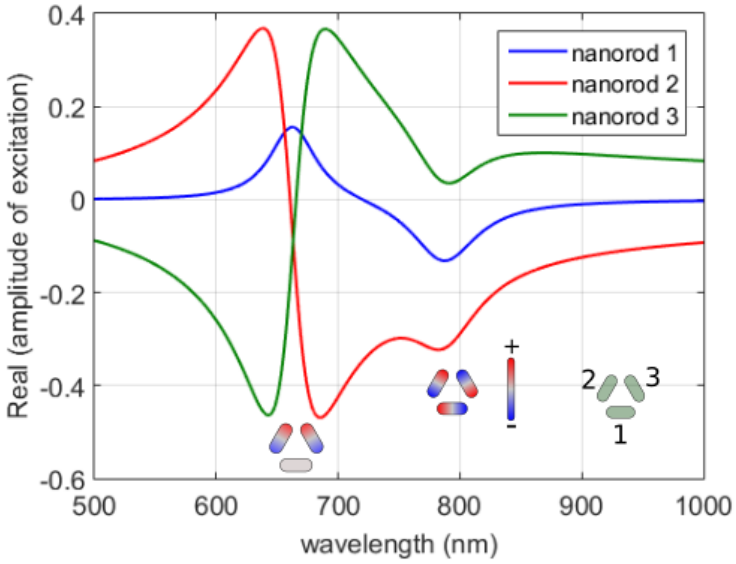

Figure 4.57: The real part of the amplitudes of excitation of the metasurface of azimuthal trimers with p-polarisation at 30° angle of incidence.

Figure 4.58 shows the sensitivity of the azimuthal mode to different angles of incidence of s-polarised light. The azimuthal mode becomes relatively stronger as the angle (or σ_x) increases. This is parallel to the excitation of the radial modes on radial trimer antennas where the modes are also sensitive to the angle of incidence and the spatial frequency of the incident light. The excitation is independent of the orientation of the plane of incidence with respect to the x-axis, shown in Figure 4.59.

The same approach was performed when investigating the azimuthal trimer antenna excited using azimuthally polarised light. Instead of an array, a single antenna is illuminated coaxially to the beam with an azimuthally polarised beam as described in Equation 3.41 with $a = 150$ nm. An azimuthal mode peak is observed at 790 nm with azimuthally polarised beam excitation with no dipole mode excited. The scattering spectra and the excitation amplitudes are shown in Figure 4.60.

Now consider a metasurface consisting of azimuthal tetramer antennas. Four nanorods are arranged azimuthally in a square arrangement as shown in Figure 4.61. The arrows indicate the uncoupled dipole moment of the dipole mode excitation on each nanorod, used for calculating the mode interactions. The interactions are then solved with the parameters $G_A = 3$, $G_B = 0$, $A = 1 \times 10^{14}$

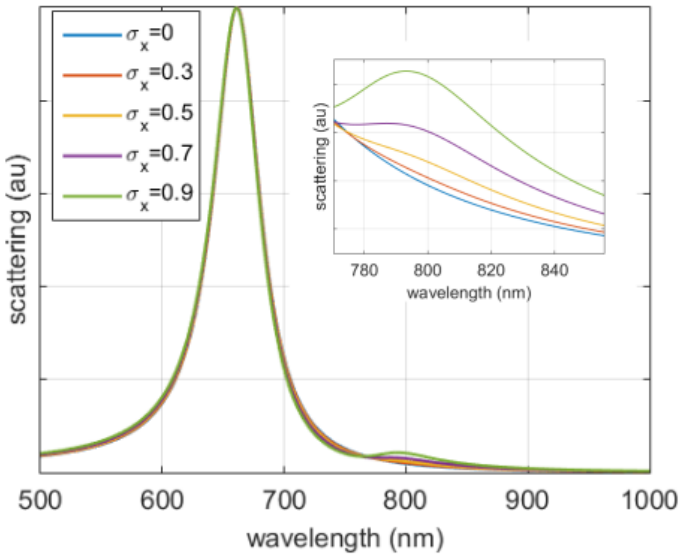

Figure 4.58: The scattering by triangle trimer antennas with different angle of incidence by s-polarised light. Inset: zoomed-in spectra showing azimuthal mode resonances.

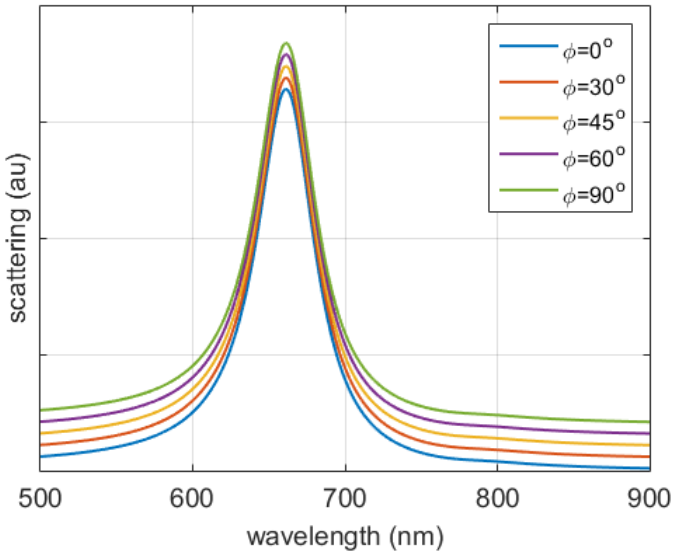

Figure 4.59: The scattering by triangle trimer antennas with various orientation of plane of incidence with an angle ϕ respect to the x-axis with s-polarised plane wave illumination.

s^{-1}, and $\Gamma = 2\times10^{14}$ s^{-1} and the angle of incidence is 30° ($\sigma_x = 0.5$ and $\sigma_y = 0$). G_A is the interaction between two closest neighbouring particles, e.g. nanorod 1 and 2 and G_B is the interaction between opposing nanorods, e.g. nanorod 1 and 3. The value of G_2 is set to zero due to the assumed very weak coupling

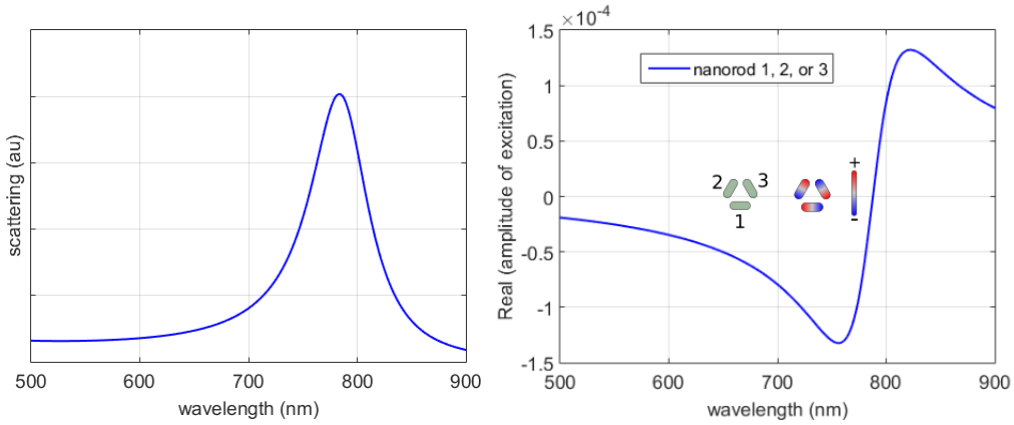

(a) (b)

Figure 4.60: The scattering by a single azimuthal trimer antenna with the azimuthally polarised beam coaxial with the antenna. (a) The scattering spectrum and (b) the amplitudes of excitation.

between opposing nanorods in this particular design. The plane of incidence is aligned parallel to the x-axis.

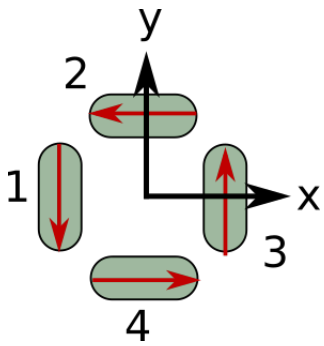

Figure 4.61: The assumed direction of *uncoupled* dipole modes of the nanorods of azimuthal tetramer, used for calculating the mode interactions.

Figure 4.62 shows the excitation of the metasurface of azimuthal tetramers with different incident plane waves. The normally incident plane wave excites only the dipole mode of the metasurface and this occurs for all metasurface designs investigated in this study over the spectral range considered. The sub-radiant mode of the azimuthal-tetramer metasurface is excited with s-polarised light. With this polarisation, there are three resonances observed in the spectrum. These correspond to the quadrupole, dipole, and azimuthal modes. The dipole mode, as a radiant mode, clearly has the strongest scattering. The azimuthal mode has the longer resonance wavelength and the quadrupole mode has a shorter resonance wavelength. These modes can be identified by looking at

amplitudes of excitation and the distribution of surface charge.

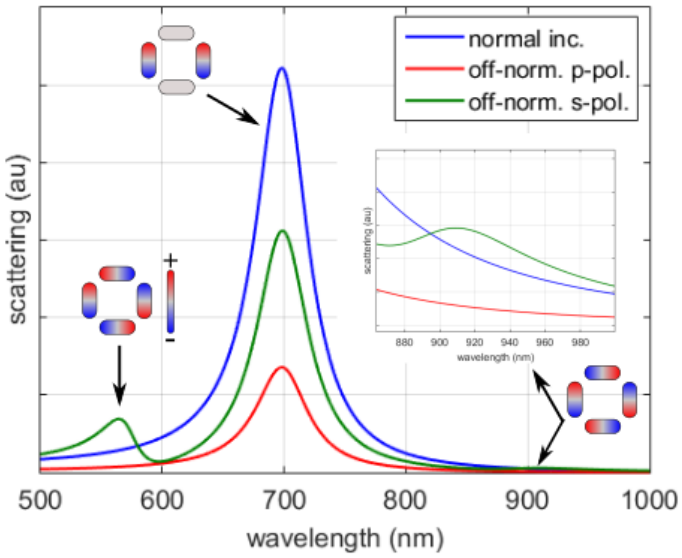

Figure 4.62: The scattering of plane waves from the metasurface of azimuthal tetramers at normal and off-normal incidence. The off-normally incidence plane waves are p- and s-polarised. Inset: zoomed-in spectra to the azimuthal mode resonance.

Figure 4.63 shows the real part of the excitation amplitudes of the metasurface of azimuthal tetramers with s-polarised plane wave illumination. The defined positive direction of the uncoupled mode of each nanorod is shown in Figure 4.61. At 570 nm, the surface charge distribution forms the quadrupole mode by producing negative amplitudes on nanorod 1 and 3 and positive amplitudes on nanorod 2 and 4. The metasurface exhibits a dipole mode resonance at 700 nm where the surface charges excited on nanorod 1 and 3 have the dipole moment parallel to the y-axis, or perpendicular to the plane of incidence, for s-polarisation. At 900 nm, all nanorods have negative amplitudes which means the dipole moments are aligned clockwise. This corresponds to azimuthal mode excitation.

To analyse the sensitivity of sub-radiant modes to the angle of incidence, the metasurface was illuminated with plane waves at various angles of incidence. Figure 4.64 shows normalised spectra showing the scattered power when the array is illuminated with an s-polarised plane wave. The spectra are normalised to have a maximum of one. The spectra show the increase in the strength of both sub-radiant modes compared to the dipole mode, with increasing angle

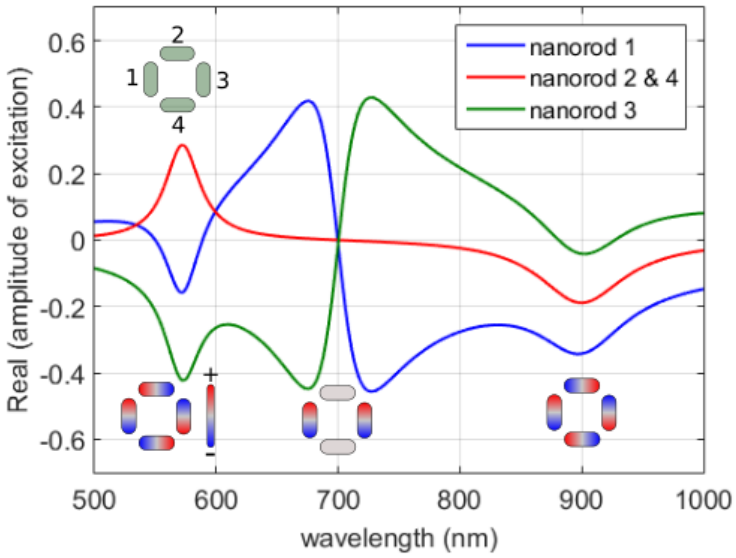

Figure 4.63: The real part of the amplitudes of excitation of the metasurface of azimuthal tetramers with s-polarisation at 30° angle of incidence.

of incidence.

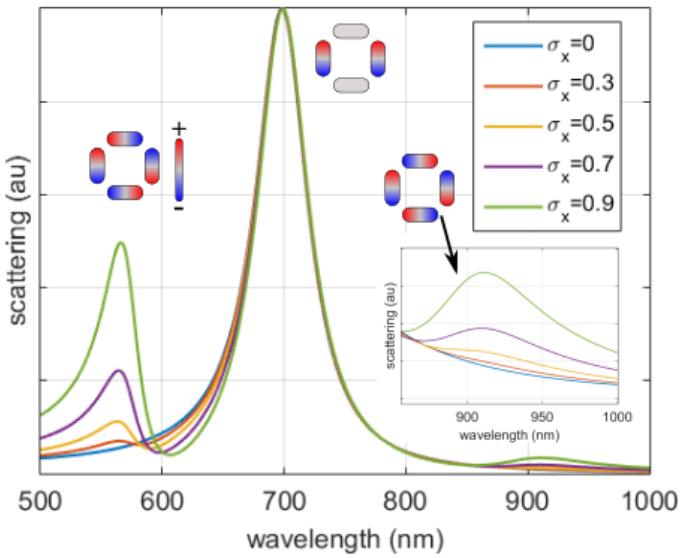

Figure 4.64: The scattering of the s-polarised plane wave from the metasurface of azimuthal tetramers with various angle of incidence. The angle of incidence is determined by $\theta = \sin^{-1}(\sigma_x)$. The spectra are normalised to the dipole mode resonances.

The quadrupole modes of azimuthal tetramers have the same behaviour as the breathing modes of radial tetramers. They can be excited with p- or

s-polarisation but the excitation depends on the orientation of the plane of incidence. When the plane of the incidence is parallel to none of the nanorods, p-polarised light excites the quadrupole modes, as shown in Figure 4.65. On the other hand, s-polarised plane waves do not excite the quadrupole mode when the plane of incidence makes an angle of 45° to the x-axis, as shown in Figure 4.66.

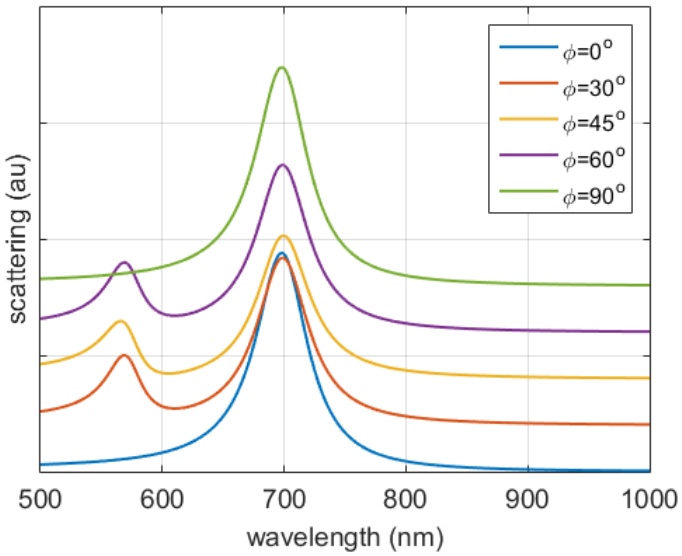

Figure 4.65: The scattering of plane waves with p-polarisation from the metasurface of azimuthal tetramers with various orientation ϕ of plane of incidence with respect to the x-axis. The spectra are shifted upward for clarity.

4.3.3 Scattering from Metasurfaces at Resonances

From EEM modelling, we can obtain insight into the excitation of radiant and sub-radiant modes of metasurfaces with radial and azimuthal antennas. The dipole modes are strongly excited by linearly polarised light, at both normal and off-normal incidence. To achieve sub-radiant mode excitation, a tailored incident plane wave is needed. Radial modes can be excited with either a radially polarised beam or off-normally incident, p-polarised plane waves. The resonance is at a shorter wavelength than the dipole mode. On the other hand, the azimuthal mode can be excited with either an azimuthally polarised beam or an off-normal s-polarised plane wave. The azimuthal mode resonance occurs at a longer wavelength than the dipole mode of the antenna.

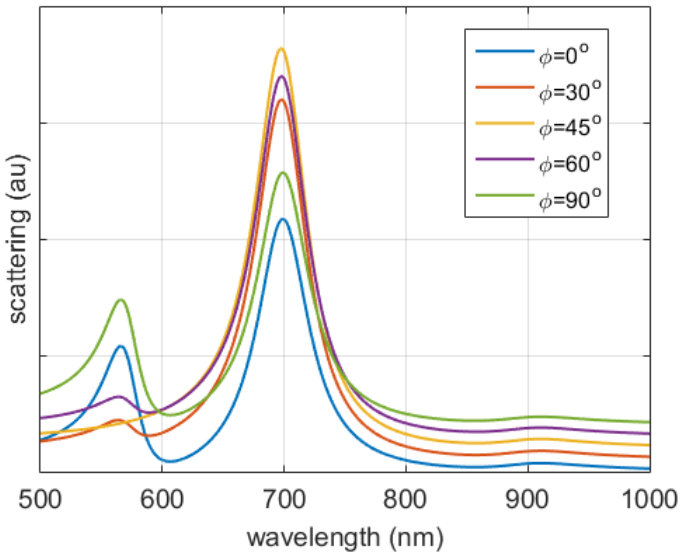

Figure 4.66: The scattering of plane waves with s-polarisation from the metasurface of azimuthal tetramers with various orientation ϕ of plane of incidence with respect to the x-axis. The spectra are shifted upward for clarity.

Further analysis can be performed by looking at the excitation of the metasurfaces at the resonances of the radiant and sub-radiant modes with various plane wave illumination conditions. The spatial frequencies studied here are for focussed beams with an input linear polarisation or radial (or azimuthal) polarisation. The electric field components of the focussed light with linear polarised input is given in Equation 3.42 from [95]. A specific wavelength (at resonance) is taken and the results are presented in a two dimensional plot as a function of $\sigma_x = k_x/k_0$ and $\sigma_y = k_y/k_0$ i.e. in the spatial frequency domain.

The example provided in this section is for the metasurface with radial trimer antennas, either at the radial (sub-radiant) and dipole (radiant) resonances. The properties of radiant and sub-radiant modes of metasurfaces with different designs are expected to exhibit similar behaviour. The differences are primarily the spectral location of the resonances and the polarisation required to excite them.

The radial and dipole mode resonances of the metasurface of radial trimers presented in Section 4.3.1 are located at 570 nm and 785 nm respectively (with $\lambda_p = 700$ nm, $G = -3$, $A = 1 \times 10^{14}$ s^{-1}, and $\Gamma = 2 \times 10^{14}$ s^{-1}). Figure 4.67 shows the scattering intensity produced by illumination corresponding to radial

and dipole modes by a focussed beam with a linear polarisation input parallel to the x-axis. The radial and dipole modes exhibit different spatial frequency distribution patterns. The strength of radial mode increases as the angle of incidence increases whereas the dipole mode scattering strength decreases with angle of incidence along the direction of polarisation.

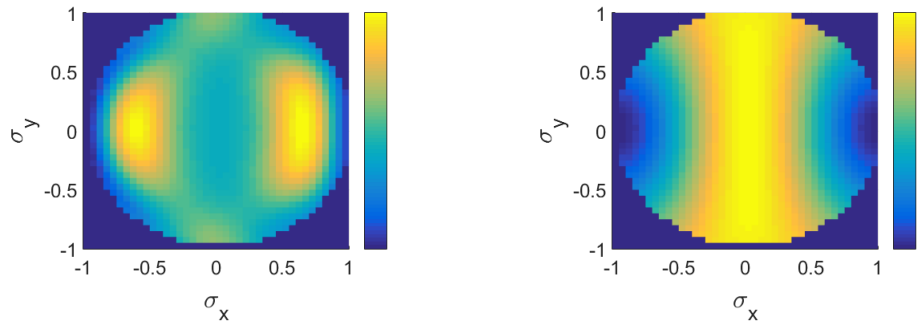

Figure 4.67: The spatial frequency distribution of the radial trimers excitation at (a) radial mode and (b) dipole mode resonances using a focussed beam with linear polarisation input. The parameters are $\lambda_p = 700$ nm, $G = -3$, $A = 1 \times 10^{14}$ s^{-1}, and $\Gamma = 2 \times 10^{14}$ s^{-1}.

In Figure 4.67a, along the line $\sigma_y = 0$, the incident plane wave is p-polarised so that the radial mode strength increases with increasing angle of incidence and σ_x. Along the line $\sigma_x = 0$, on the other hand, the incident field is s-polarised and, therefore, does not excite the radial mode. The figures show that the excitation of radial modes occurs with plane wave components with dominant p-polarisation components, i.e. along the σ_x-axis.

The metasurface was further investigated with different input polarisations. When radially polarised light is focussed by an objective lens, the plane wave components of the beam all have p-polarisation. Figure 4.68 shows the scattering by the metasurface with focussed radial polarisation. The EEM parameters are the same as in the previous example with a linearly polarised beam. In Figure (a), it shows that the radial mode excitation is weaker for smaller angles of incidence (i.e. low spatial frequencies σ_x and σ_y) and reaches a maximum at an angle of incidence of 45° ($\sqrt{\sigma_x^2 + \sigma_y^2} = 0.7$). The pattern has a doughnut shape due to the symmetry of the radially polarised beam. In Figure (b), on the other hand, the excitation at the dipole mode resonance produces a bright pattern at near-normal angles of incidence, in contrast to that at radial mode

resonance.

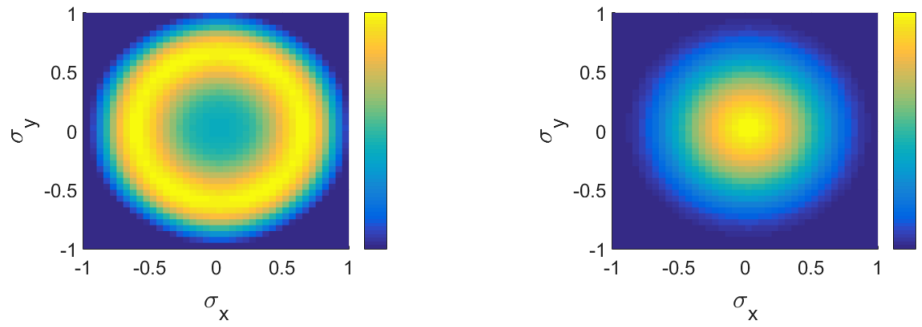

Figure 4.68: The spatial frequency distribution of the radial trimers excitation at (a) radial mode and (b) dipole mode resonances using focussed beam with radial polarisation input. The parameters are $G = -3$, $A = 1 \times 10^{14}$ s^{-1}, and $\Gamma = 2 \times 10^{14}$ s^{-1}.

In the next chapter, measured spectra obtained when metasurfaces are illuminated with focussed beams of light are presented. In these cases, the result is a sum over all angles of incidence composing the beam. These need to further modified to take into account changes in polarisation introduced by the lens. The ability of a lens to focus light is determined by its numerical aperture (NA). NA is defined as NA$= n \sin\theta$, where $n = 1$, is the refractive index of surrounding medium of the objective, which is air for the set-up used in this study and θ is the half cone-angle of the focussed beam. Once the beam transmitted into the substrate with $n = 1.5$, the components have smaller angles of incidence θ.

From Figure 4.67 and 4.68, scattering spectra produced by a focussed beam excitation can be calculated and these are shown in Figure 4.69. The plane waves included are those up to a various NAs of 0.90, 0.65, and 0.40. The spectra were calculated with a flat distribution of amplitudes, i.e. all plane waves have $|\vec{E}| = 1$ and the spectra are normalised to the dipole mode resonance.

From this figure, it can be concluded that the radial mode strength increases with larger NA of the focussed beam. As expected, this is due to the nature of the larger angle of incidence components included when the NA is larger. This property is further investigated in experimental measurements in the next chapter where the samples were illuminated with various NA objectives.

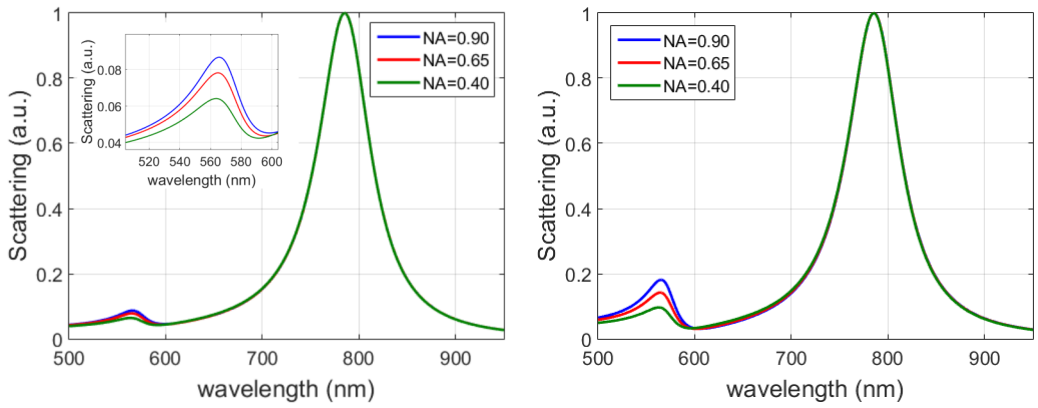

Figure 4.69: The scattering spectra of the metasurface consisting of radial trimers using a focussed beam with (a) linear and (b) radial polarisation input, for various NAs, with parameters are the same as in Figures 4.67 and 4.68.

A focussed beam with radial polarisation input produces a stronger radial mode peak compared to linear polarisation input for the same NA. Note that the dipole resonance excited on antennas not centred with the beam axis can still be seen in the case of radial mode illumination, therefore, the bulk effect is that the strong dipole mode is still present in the spectrum for focussed radially polarised beam.

4.4 Chapter Conclusion

Four different arrangements of nanorods forming the unit cell of metasurfaces have been considered in this chapter. Here, the EEM, an approximate analytic method that provides significant physical insight along with the opportunity to study a broad range of parameters, was used as well as a more computationally-intensive, full-field FDTD approach. These different designs provide rich properties to be explored. Two radially-arranged optical antennas have radial modes alongside dipole modes in the visible spectrum. The radial modes have zero net dipole moments and each of the dipole moment of nanorod are radially oriented. The other two azimuthally-arranged optical antennas provide a structure that exhibit azimuthal modes. Azimuthal modes can be identified as the dipole moment of each nanorod aligned circularly within the antenna. The radial and azimuthal modes are dark or sub-radiant and they

are relatively difficult to excite and do not couple easily to propagating plane waves and they have narrower bandwidth than the dipole mode.

As the radial and azimuthal modes are sub-radiant modes, they need specific excitation strategies. The radial modes can be excited using either a radially polarised beam or off-normal incident p-polarised plane waves. The azimuthal modes, on the other hand, can be excited by azimuthally polarised light or off-normally incident s-polarised light.

The electric dipole mode with its dipole moment the long-axis of nanorod is the dominant and most significant mode on a single uncoupled nanorod. In the case of optical antennas consisting of ensembles of nanorods, the rods are placed close together and the dipole modes of each nanorod couple to each other. The result is a resonance splitting where two or more modes of the antenna can be produced.

The radial mode is resonant at a shorter wavelength than the dipole mode while the azimuthal mode has its resonance at a longer wavelength. When the distance between these nanorods is decreased, the spectral separation between the modes increases and each mode can be observed independently. Stronger coupling in radial antennas will blue-shift the radial mode and red-shift the dipole mode. The azimuthal antennas, on the other hands, have the opposite behaviour, as the azimuthal mode is red-shifted with increasing separation and the dipole mode is pushed to a shorter resonance wavelength.

On metasurfaces with radial tetramer antennas, another dark mode is observed called the breathing mode. This mode appears at a longer wavelength than the dipole mode resonance. This mode can be altered by the strong dipole mode leading to the mode interference producing Fano resonance line-shape.

The metasurfaces were seen to be sensitive to the transverse spatial frequency of the incident field with the sensitivity depending on the nature of any resonance. It was also observed that if a metasurface is illuminated with a linearly polarised focussed beam, then the angular spectrum of the scattered field is strongly dependent on the wavelength and the NA of the focussing objective.

In the next chapter, the experimental characterisation of the metasurfaces is discussed. Based on the simulation results obtained in this chapter, the sample metasurfaces were fabricated to exhibit radiant and sub-radiant resonances in

the visible. The characterisation was performed in a bench-top optical set-up with the focussed beam illumination and this chapter concluded with showing that by illuminating a metasurface with a high NA focussed beam, sub-radiant modes can be seen in the far-field scattering spectra and that they exhibit a characteristic angular spectrum dependence.

Chapter 5

Experimental Characterisation of Metasurfaces

5.1 Fabrication of Metasurfaces

The simulations discussed in the previous chapter were used to design metasurfaces with interesting optical properties. Metasurfaces were then fabricated with varying geometries and the resulting devices were optically characterised by obtaining the reflection and transmission spectra with linearly, radially and azimuthally polarised light illuminating the structures through objectives with different numerical apertures. Furthermore, at wavelengths where distinct resonances were identified, images of the reflected beams in the far-field were also investigated.

The metasurfaces were fabricated using electron-beam lithography (EBL) at the Melbourne Centre for Nanofabrication (MCN) by Dr Timothy James [1]. The substrate for the sample was fused silica glass with a thickness 0.3 mm. The refractive index of the fused silica in the visible spectrum ranges from 1.45 to 1.48 over the wavelength range from 300 nm to 1000 nm [101].

[1]Except the fabrication, all designs and layouts of metasurfaces to be fabricated were performed by the candidate. Furthermore, development of optical systems and characterisation of these metasurfaces, which are discussed in this chapter, were also performed by the candidate.

5.1.1 Electron Beam Lithography

The substrate was cleaned by sonication in a solvent bath and then rinsed in de-ionised water. The resist layer, polymethyl methacrylate (PMMA), was then spun onto the substrate at 4000 rpm, and the resulting film was baked at 180° for 5 minutes. This created a layer of PMMA on top of the glass substrate (Figure 5.1a). A conductive layer is needed for the EBL process with a non-conductive substrate and a chromium layer with 30 nm thickness was evaporated on top of the PMMA. The conductive layer provided a path for the electrons to disperse when the structures were written, otherwise there would be significant charging that would ruin the pattern[2].

The structures to be written on the sample were prepared using K-Layout [102] and saved in GDS (Graphic Data System) format. The structures were written into the PMMA by electron beam exposure with a Vistec EBPG 5000 EBL system. The area exposed to the electron beam changes its chemical properties (Figure 5.1b) so that it would be dissolved in the development process. Chromium layer was lift off prior to the development with a commercial chromium etchant and the sample was then developed in a 3:1 mixture of isopropanol:methyl isobutyl. After this development process, the regions exposed to the beam were dissolved, leaving a gap into which metal is deposited (Figure 5.1c).

Metallic films were then deposited via electron-beam evaporation. A 2 nm thick germanium layer acted as an adhesion film between a layer of silver and the substrate. The layer of silver was 40 nm-thick, which is the height of the resulting metal nanostructures (Figure 5.1d).

The next step was a lift-off process, where the remaining PMMA was removed by placing the sample in a heated bath of acetone (Figure 5.1e). Minimal agitation was used to remove the resist/metal layer from the substrate. The sample was then immediately encapsulated under a 750 nm-thick PMMA layer so that the resulting metallic nanostructures were embedded inside a nearly homogeneous media and the silver was protected from degradation resulting from exposure to air (Figure 5.1f). The refractive index of PMMA in the

[2]For similar reason, a conductive layer was also used in obtaining SEM images of the structures. A thin gold layer, with the thickness of 2-4 nm, was evaporated on top of the structures prior taking the images. The SEM images were taken on a used sample.

range 300-1000 nm is 1.49 to 1.55 [103]. Hence the refractive indices of the glass substrate and the PMMA in the visible to near-infrared regions of the spectrum are both approximately 1.5 which was assumed in calculations.

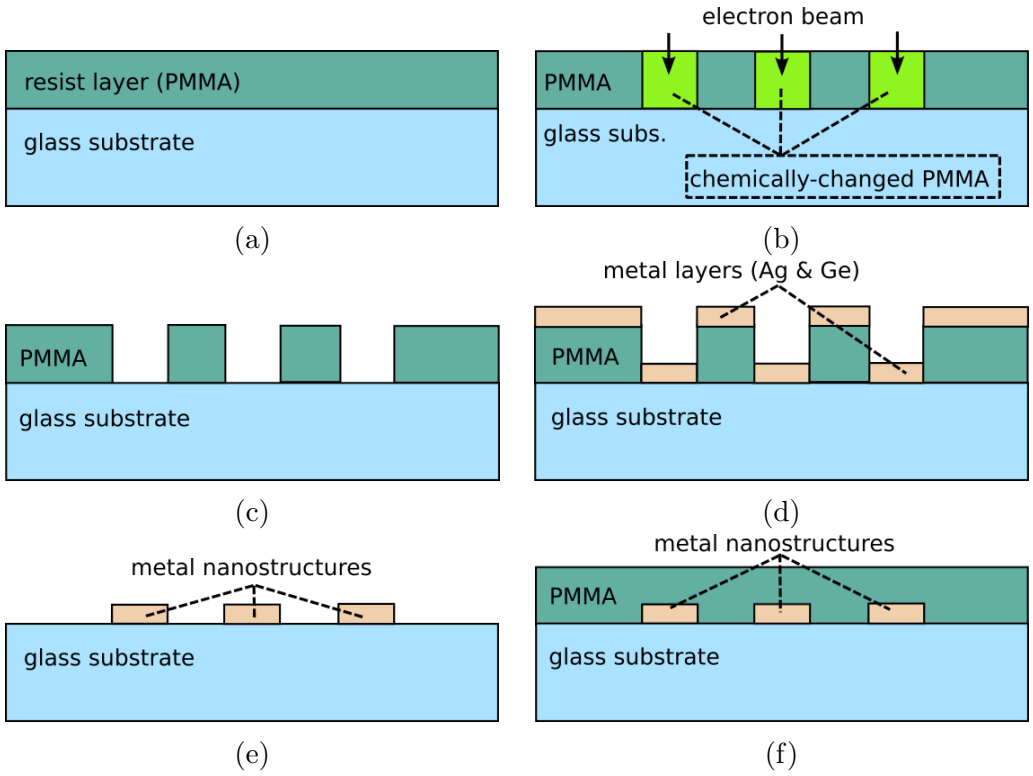

Figure 5.1: The fabrication steps using electron beam lithography. (a) The resist layer (PMMA) was spun onto the glass substrate. (b) The predefined regions (drawn with KLayout) were exposed to the electron beam, changing its chemical properties. (c) The sample was developed by dissolving exposed regions in acetone, leaving gaps for metallic nanostructures. (d) Metal layers (Ag and Ge) are deposited onto the sample via electron beam evaporation. (e) The remaining PMMA layer was lifted off, leaving only the metallic nanostructures. (f) The nanostructures were immediately encapsulated with a PMMA layer.

5.1.2 Fabricated Samples

Four different metasurface designs as discussed in the previous chapter were characterised. There were two series of samples fabricated. In the first series, each antenna configuration was fabricated with three different nanorod lengths, $L = 90$ nm, $L = 100$ nm, and $L = 120$ nm. For each L, two different off-set distances s were fabricated. The resulting metasurfaces had overall dimensions

X	m	Description
R	1	radial trimers
R	2	radial tetramers
A	1	azimuthal trimers
A	2	azimuthal tetramers

Table 5.1: Codes for metasurface designs.

of 100 µm × 100 µm. The periodicity was either 300 nm or 400 nm, depending on the size of a single antenna within the unit cell. After some preliminary measurements, a second series of samples was fabricated consisting of radial trimer and tetramer antennas with reduced nanorod widths w and smaller periodicities (250 nm and 350 nm). All fabricated antennas have the same nanorod heights (or metallic thickness) of $h = 40$ nm.

To make identification easier and simplify discussion, each metasurface was given a code. The code is in the format 'Xmn' where 'X' and 'm' correspond to the antenna configuration and 'n' corresponds to the geometric parameters. 'X' is either 'R' for radial antennas or 'A' for azimuthal antennas and 'm' is either '1' for trimer or '2' for tetramer. These are summarised in Table 5.1. The variation of geometric parameters, including nanorod length L, nanorod width w, off-set distance s, and periodicity p, are given by the parameter 'n'. The fabricated metasurfaces are summarised in Table 5.2. All metasurfaces with 'n' from 1 to 6 are from the first series of samples while the others are from the second series. The geometrical sizes of optical antennas given in this chapter to describe samples are the ***nominal sizes***, i.e. designed sizes when preparing the layout for fabrication.

Figure 5.2 shows a few SEM images of the fabricated samples for each design. The metasurfaces shown are #R13, #R23, #A13, and #A23. The average length L, width w, off-set distance s, and periodicity p of the fabricated metasurfaces were measured from the SEM images and they are summarised in Table 5.2 along with their respective nominal or designed sizes. Uncertainties were calculated from the standard deviation of 15 to 30 measurements of sizes.

n	Code	Nominal geometric parameters				Fabricated geometric parameters			
		L (nm)	w (nm)	s (nm)	p (nm)	L(nm)	w(nm)	s(nm)	p(nm)
1	R11	90	40	70	300	95±5	65±6	65±4	309±9
2	R12	90	40	85	300	108±8	67±5	75±8	311±9
3	R13	100	40	70	300	106±6	68±6	70±6	308±9
4	R14	100	40	85	300	106±6	68±6	82±8	310±8
5	R15	120	40	85	400	136±6	82±10	90±8	419±11
6	R16	120	40	100	400	132±6	71±5	97±7	412±10
7	R17	100	20	70	250; 300	108±6	50±6	70±7	252±9; 307±6
8	R18	100	30	70	250; 300	112±9	63±5	72±7	246±15; 300±10
9	R19	120	20	80	250; 300	121±7	52±5	84±6	245±9; 302±17
A	R1A	120	30	80	250; 300	127±11	75±9	75±9	249±15; 306±10
1	R21	90	40	75	400	101±7	70±7	77±6	411±6
2	R22	90	40	85	400	105±9	69±6	81±9	407±7
3	R23	100	40	80	400	109±9	69±6	83±5	411±7
4	R24	100	40	90	400	113±7	72±6	83±6	412±6
5	R25	120	40	90	400	129±5	74±5	92±5	410±5
6	R26	120	40	100	400	132±8	73±12	99±8	411±10
7	R27	100	30	80	350	115±6	66±5	83±5	352±7
8	R28	120	30	90	350	131±10	73±4	93±6	348±8
1	A11	90	40	70	300	112±7	67±6	65±5	304±6
2	A12	90	40	90	300	101±5	66±6	84±5	306±7
3	A13	100	40	70	300	110±7	60±3	66±6	303±11
4	A14	100	40	90	300	109±7	66±4	89±4	309±8
5	A15	120	40	70	400	131±8	67±5	69±5	409±9
6	A16	120	40	90	400	128±6	66±7	91±6	408±10
1	A21	90	40	80	400	96±7	64±6	83±4	406±8
2	A22	90	40	100	400	107±8	67±5	82±2	413±7
3	A23	100	40	80	400	105±6	69±4	78±5	410±5
4	A24	100	40	100	400	102±5	61±5	105±6	409±9
5	A25	120	40	90	400	129±10	65±6	93±5	410±7
6	A26	120	40	100	400	120±7	66±5	102±7	406±9

Table 5.2: The geometric parameters of fabricated metasurfaces. Codes are given in the format 'Xmn'. The unit cell for R17 to R1A is a rectangle with the size of 250 nm × 300 nm, and the rests have square unit cells.

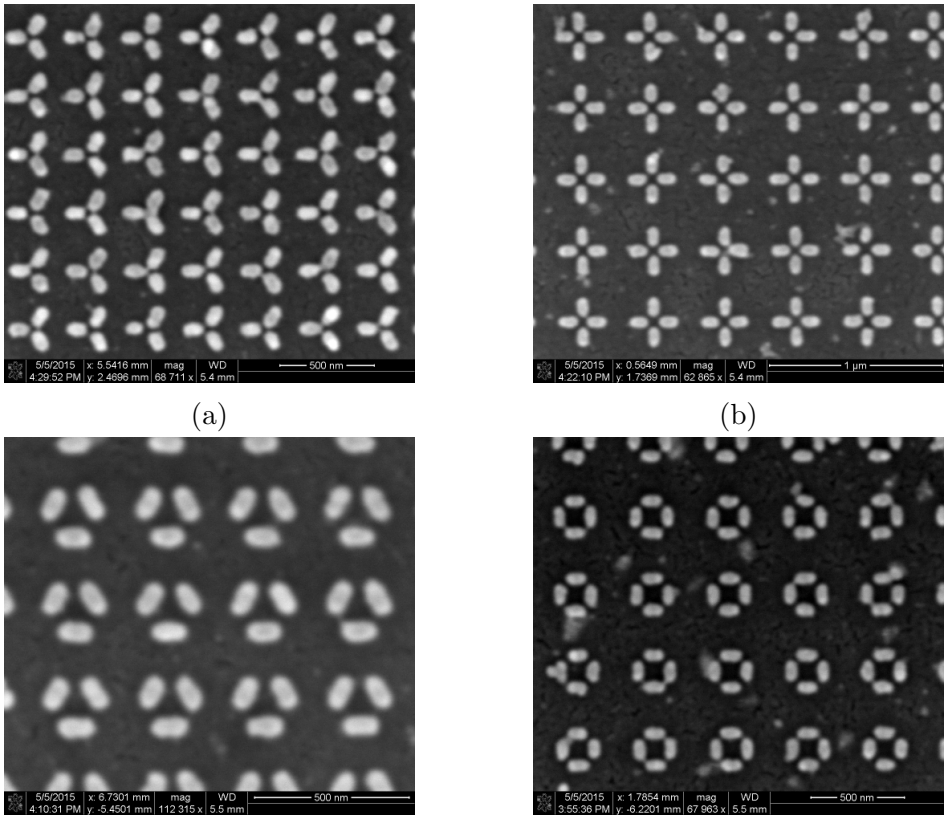

Figure 5.2: A few SEM images of the metasurfaces fabricated for experimental characterisation for (a) radial trimers (#R13), (b) radial tetramers (#R23), (c) azimuthal trimers (#A13), and (d) azimuthal tetramers (#A23).

5.2 Experimental Characterisation

When an antenna is illuminated with light, it will resonate at certain wavelengths depending on the modes being excited. The antenna absorbs as well as scatters some of the radiation. When identical antennas are assembled in an array, they will collectively absorb and/or scatter light. These properties can be characterised by measurements of the transmission through and/or the reflection of light from the array. In the transmission spectrum, various sections of the spectrum will be missing as a result of reflection and absorption. On the other hand, other regions of the spectrum will be preferentially reflected (or absorbed) as a result of the excitation of resonances of the antenna. By studying the maxima and minima in the reflection and transmission spectra, therefore, we can obtain useful information about the modes of the system.

The metasurfaces were characterised using two different set-ups to obtain either the transmission or reflection spectra. The resonant frequencies appear as valleys or minima in the transmission spectrum as the incident power is reflected or absorbed. The reflected light has intensity peaks or maxima corresponding to mode excitation. The experimental set-ups are shown in Figure 5.3 for transmission and Figure 5.4 for reflection. The details of the optical components used in these set-ups are provided in Table 5.3. More specifically, light sources and objective lenses used are listed in Table 5.4 and 5.5. The characterisation system was established on a bench-top using a 30 mm cage system from Thorlabs.

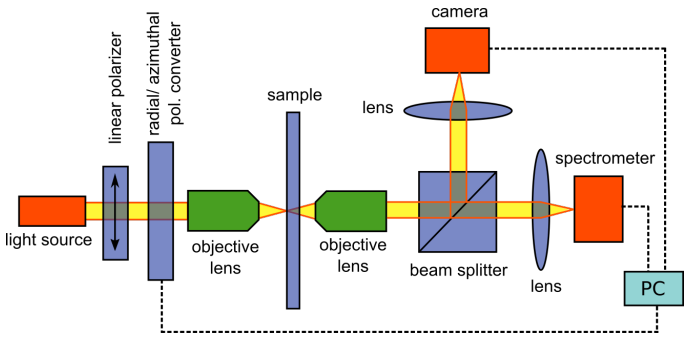

Figure 5.3: The experimental set-up for measuring transmission spectra.

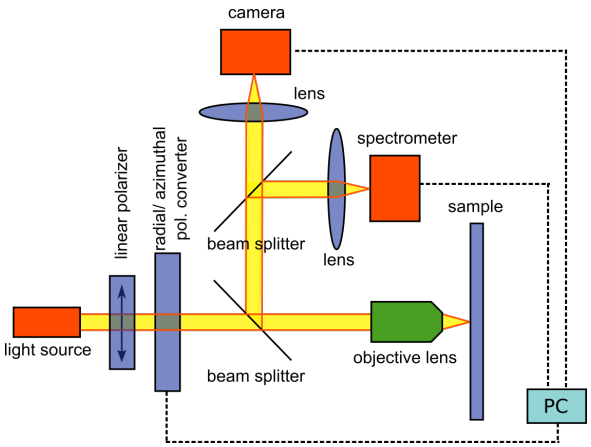

Figure 5.4: The experimental set-up for measuring reflection spectra.

There were two types of light source used in the experiment. One was a low-power light source, a tungsten-halogen lamp, for measuring spectra and the other was a high-power light source, a class-IV supercontinuum laser, for obtaining far-field beam patterns. The tungsten-halogen lamp was preferred for

Component	Brand	Type	Description(s)
linear polariser	Thorlabs	LPVIS050-MP	mounted linear polariser with range 550 nm–1.5 µm
radial/ azimuthal polarisation converter	Arcoptix	LC radial polarization converter	wavelength range 350–1700 nm with >75% transmission
beam splitter	Thorlabs	CM1-BS013	cubed beam splitter with range 400–700 nm
	Thorlabs	BSW26	plate beam splitter with range 350–1100 nm
thin lens	Thorlabs	AL250-B	aspheric lens with f=20.0 mm, focussing light into the fibre of spectrometer
	Thorlabs	LA1131-A-ML	plan-convex lens with f=50.0 mm, focussing light into the camera
mirror	Thorlabs	PF10-03-G01	protected aluminum mirror
camera	Thorlabs	DCC1645C-HQ	HQ colour camera
spectrometer	Ocean Optics	QE65000	range 200–1100 nm

Table 5.3: Optical components used in experiments.

Component	Brand	Type	Description(s)
tungsten-halogen lamp	Ocean Optics	HL2000-FHSA	broadband spectrum 360–2400 nm
optical fibre	Ocean Optics	727-733-2447	for directing the broadband light into the cage system
beam-collimator lens	Thorlabs	F810SMA-780	produces a collimated beam of light from the fibre optic, used with broadband light
laser	Fianium	SC-450-2	class-IV high-power super-continuum laser, <460 nm to >2000 nm
mono-chromator	Fianium	SuperChrome	tunable wavelength filter for the laser
optical fibre	Thorlabs	GIF625	multimode fibre, for directing the laser into the cage system
	Thorlabs	P1-630A-FC1	singlemode fibre, for directing the laser into the cage system
beam-collimator lens	Thorlabs	F280FC-A	produces a collimated beam of light from the fibre optic, used with laser

Table 5.4: Light sources used in experiments.

measuring the spectra because it has enough power to the excite the metasurfaces, and is safer, and simpler to use. The supercontinuum laser was used for measuring the far-field beam profiles at resonances because it needs to be spectrally bright.

The details of the two light sources are summarised in Table 5.4. The tungsten-halogen lamp was coupled into an optical fibre and the fibre was connected to a lens that collimates the outgoing light. Alternatively, the light produced by a supercontinuum laser was sent through a tunable monochromator with spectra bandwidth 10 nm to 100 nm. The light was then coupled into a multi-mode optical fibre with an objective lens. The multi-mode optical fibre was coupled to a single-mode optical fibre which also spatially filtered the light to create a clean beam. The light from the fibre then passed through a lens that collimates the beam as in the case of the tungsten-halogen light source.

The collimated beam is passed through a linear polariser to produce linearly polarised light. This polariser can be rotated 360°, with the polarisation direction indicated on the device. The transmitted light can then be converted

Code	Magnification	NA	Brand	Type	Description
O1	20X	0.40	Olympus	Plan N UIS-2	-
O2	40X	0.65	N/A	N/A	generic microscope objective lenses
O3	40X	0.75	Olympus	U Plan Fl	-
O4	40X	0.65	Olympus	Plan N UIS-2	-
O5	100X	0.90	Nikon	NCG	-

Table 5.5: Objective lens used.

into either radially or azimuthally polarised light if required. The polarisation converter used in this in experiment (see Table 5.3) contains liquid crystals. It is composed of two alignment layers, one is uniform and another is circularly rubbed. The local twist angle between the alignment layers defines the polarisation twist locally so that linearly polarised light can be converted into either radial or azimuthal polarisation. The device is designed to produce a beam that has a continuous radial or azimuthal polarisation distribution that is stable in time. This device can be included or removed as needed. The toggle switch between radial and azimuthal polarisation was controlled computationally with PC software.

The light then passed through an objective lens which focussed the light beam onto the metasurface. Several objective lenses with different numerical apertures (NAs) were used to investigate the effect of focussed light on radiant and sub-radiant mode excitation. The objective lenses are listed in Table 5.5 and the photo of these objectives is shown in Figure 5.5. Once the light illuminates the antenna structures, the light is partially transmitted and partially reflected. With either of the systems of Figure 5.3 and 5.4, both transmission and reflection cannot be measured simultaneously so several changes were required to switch between the two set-ups.

To obtain transmission measurements, another objective lens was placed after the sample to collect the transmitted light (Figure 5.3). The objective lens with the same or a larger NA is preferred to be able to collect all transmitted angles. In this study, the transmission measurements were performed with two identical objectives. If the two objective lenses were confocal, the output light beam is collimated. The beam then passed through a beam splitter that divides the beam into two paths; with 50% of the incident power to the

Figure 5.5: The photograph of objective lenses used in the spectra measurements. From left to right: 'O1' to 'O5' as in Table 5.5.

spectrometer and 50% to the camera. Each path had a lens to either image the metasurface onto the camera or couple the light into the fibre connected to the spectrometer. The spectrometer was used for determining the spectrum and the camera for finding and aligning the antenna structures. The sample was placed on a three-dimensional translation stage that was able to move the sample.

In the reflection set-up (Figure 5.4), a beam splitter was placed before the first objective lens. This beam splitter transmits 50% of the incident light onto the objective lens. The beam was focussed onto the sample and the reflected beam was collected by the same objective lens. The beam passed through the same beam splitter, reflecting 50% of the beam into the detector arm and was then split between the camera and spectrometer by another beam splitter.

Two types of beam-splitter are listed in Table 5.3. One is a cube-mounted beam splitter that was used in initial experiments. All measurements with objective lenses #O1 and #O2 were performed with this type of beam splitter. The other type used was a plate beam-splitter which was used in the latter experiments. All measurements with #O3, #O4 and #O5 were performed using this type of beam splitter. Both types are non-polarising and the choice does not affect the accuracy of the spectral measurements as the spectra were normalised with the reference beam passing through the respective beam splitters. For far-field imaging measurements, however, the plate beam splitter has an advantage over the cube beam splitter because it has a broader range of operating wavelengths (350–1100 nm vs 400–700 nm), preventing background or 'ghost' reflection at

near-infrared wavelengths. The plate beam splitters, however, produce a beam off-set in the set-up and further adjustments of alignment must be carefully addressed.

Figure 5.6 and 5.7 show the photographs of the transmission and reflection set-ups respectively used for the measurements.

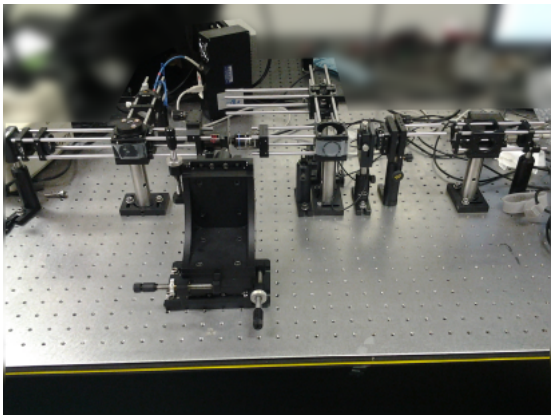

Figure 5.6: Photograph of experimental set-up for measuring transmission.

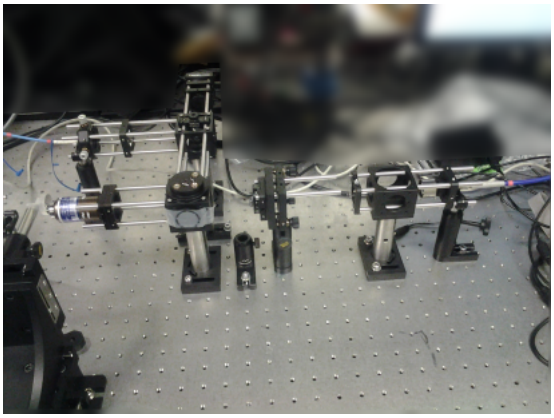

Figure 5.7: Photograph of experimental set-up for measuring reflection.

5.3 Transmission and Reflection Spectra

Sub-radiant modes of the metasurfaces are sensitive to the angular spectrum components of the beam. This means that highly focussed beams excite sub-radiant modes more strongly than only weakly converging beams as seen in Figure 4.69.

Several different objectives with different NAs were used for measuring the transmission and reflection spectra. With different NAs, the effects of different angular spectrum components on sub-radiant mode excitations can be studied. The sub-radiant modes are also sensitive to the polarisation of the incident light. These effects were discussed in Chapter 4, Section 4.3.3.

In this section, the polarisation axis of linearly polarised light is described by the coordinate system defined for each metasurface design. The coordinates are defined in Figure 5.8 for each design. In the measurements, the polarisation axis is set to be parallel to the x-axis, y-axis, or at 45° from the x-axis (diagonal).

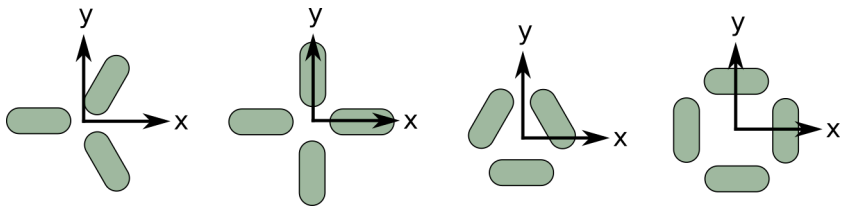

Figure 5.8: The coordinate systems defined for each metasurface design. Left to right: radial trimer, radial tetramer, azimuthal trimer, and azimuthal tetramer antennas composing the metasurfaces.

All measured spectra shown here are the normalised spectra of the transmission and reflection. The raw transmitted signal through the metasurface was normalised by dividing it to the transmitted signal through the substrate where the structures are absent, to obtain the normalised transmission spectra. On the other hand, the raw reflected signal from the metasurface was normalised to the reflection signal from the substrate, to obtain the reflection spectra.

5.3.1 Radial Trimer Metasurfaces

5.3.1.1 The Effects of Various Illumination and Nanorod Lengths

Consider the metasurface with radial trimer antennas with nanorod nominal lengths of $L = 100$ nm, widths and heights[3] $w = h = 40$ nm , and off-set distance $s = 70$ nm (Table 5.2, #R13). The periodicity of the structures is p =300 nm. Illumination was performed with various objective lenses with

[3]All optical antennas discussed here have the thickness (or height) of $h = 40$ nm

different NAs. Figure 5.9 and 5.10 shows the transmission through this radial trimer metasurface with linearly polarised light (parallel to the y-axis) and radially polarised light illumination, respectively. The objective lenses used in these figures have NAs of 0.4, 0.65, and 0.75 (#O1, #O2, and #O3).

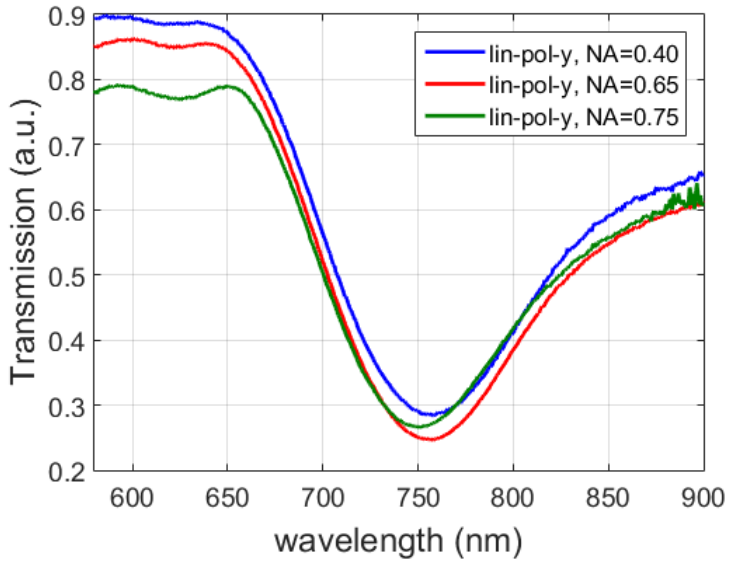

Figure 5.9: The transmission through the radial trimer metasurface with L = 100 nm, w = 40 nm, s = 70 nm, and p = 300 nm (#R13) with linearly polarised light illumination through objective lenses with different NA.

In both Figures 5.9 and 5.10, the dipole mode centred on 750 nm can be clearly seen. This mode has a strong and broad resonance as expected of a radiant mode. There is a slight difference on the spectral location of the dipole modes when the metasurface is illuminated with linearly x- and y-polarised light. This is shown in Figure 5.11a in which the dipole mode resonance is centred at 725 nm with x-polarised illumination, compared to 750 nm with y-polarised illumination. This happens due to asymmetric coupling between neighbouring antennas. The radial trimer array is not symmetric with respect to 90° rotation, so that the dipole mode excited along the x- and y-axis (refer to Figure 4.7) would have slightly different resonances. This shift is not seen with radially or azimuthally polarised beam as the bulk effect of the metasurface produce both components of dipole modes along the x- and y-axes.

In Figure 5.9, it can be seen that with linearly polarised illumination, the excitation of the radial mode at 620 nm is found to be weak, but the strength

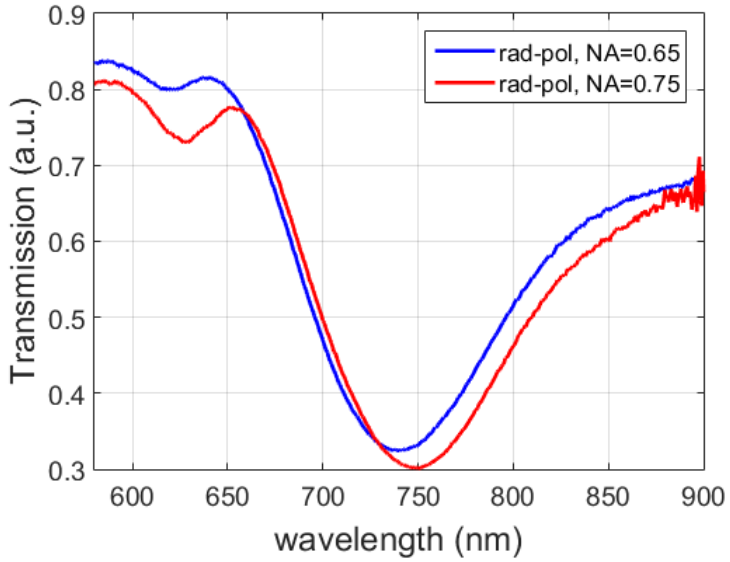

Figure 5.10: The transmission through the radial trimer metasurface with L = 100 nm, w = 40 nm, s = 70 nm, and p = 300 nm (#R13) with radially polarised light illumination through objective lenses with different NA.

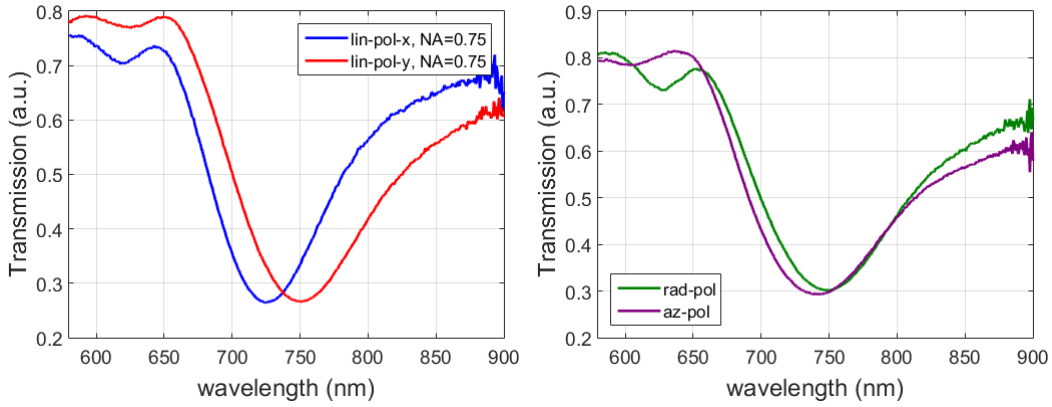

(a) (b)

Figure 5.11: The transmission through the radial trimer metasurface with L = 100 nm, w = 40 nm, s = 70 nm, and p = 300 nm (#R13) with (a) linearly x- and y-polarised light and (b) radially and azimuthally polarised light illumination, using objective lens with NA=0.75.

increases with higher NA objectives. The resonance is also slightly red-shifted to 630 nm when a higher NA is used.

If the metasurface is illuminated with radially polarised light, the excitation of the radial mode is stronger. This can be seen in Figure 5.10. Again, a higher NA objective can be seen to excite the radial mode more strongly. On the

other hand, as shown in Figure 5.11b, azimuthally polarised light suppress the radial mode excitation as the resonance at 630 nm weakens. The signature of the radial mode appear to be excited due to imperfection in the polarisation of the beam as partly linearly polarised light is still present.

These properties of radial and dipole modes with various illuminations found in the above experimental data are supported by the simulation results of the previous chapter. Recall that plane wave components with p-polarisation excite radial modes while those with s-polarisation do not. A focussed linearly polarised beam has a combination of both p- and s-polarised plane wave components. On the other hand, a focussed radially polarised beam is composed of predominantly p-polarised plane wave components. As a result, radially polarised beams excite the radial mode more strongly than the linearly polarised beams. The strength of the radial mode excitation depends also on the angles of incidence. In line with the experimental results, the radial mode is excited more strongly with higher NA objective as it produces components with larger angles of incidence.

The same transmission measurements were performed for a radial trimer metasurface with different nanorod nominal lengths $L = 120$ nm (#R15) which are shown in Figure 5.12 for various objective NAs. Note that this metasurface, consisting of radial trimers with $L = 120$ nm, has a larger periodicity $p = 400$ nm to fit the larger antenna elements in a unit cell. It has similar spectra to that with $L = 100$ nm with the main difference being the red-shifting of resonances due to the longer nanorod size. It also has a clearer spectral separation between the two resonances, making the radial mode appear stronger than that of the antenna with $L = 100$ nm.

The illumination of this metasurface with linearly x- and y-polarised focussed beams as well as radially and azimuthally polarised light are shown in Figure 5.13. Linearly x-polarised light gives a slightly blue-shifted dipole resonance compared to y-polarisation, suggesting a small asymmetry in the antennas. As expected, azimuthally polarised light gives no radial mode excitation.

One more variation of the nanorod length investigated has $L = 90$ nm (#R11). Other than length, all parameters of device #R11 are the same as device #R13 discussed above. The measurements of this metasurface are summarised in Figure 5.14 and 5.15. As the nanorods are shorter, the metasurface with

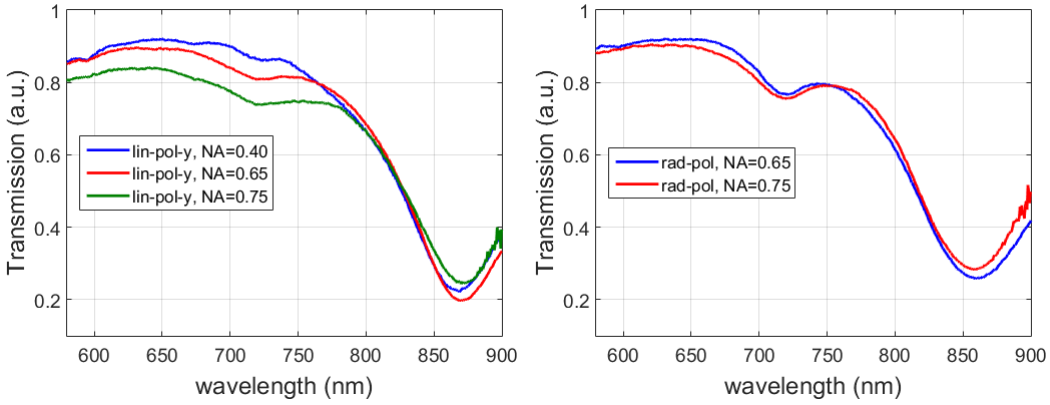

(a) (b)

Figure 5.12: The transmission through the radial trimer metasurface with L = 120 nm, w = 40 nm, s = 85 nm, and p = 400 nm (#R15) with (a) linearly and (b) radially polarised light illumination through the objective lens with different NA.

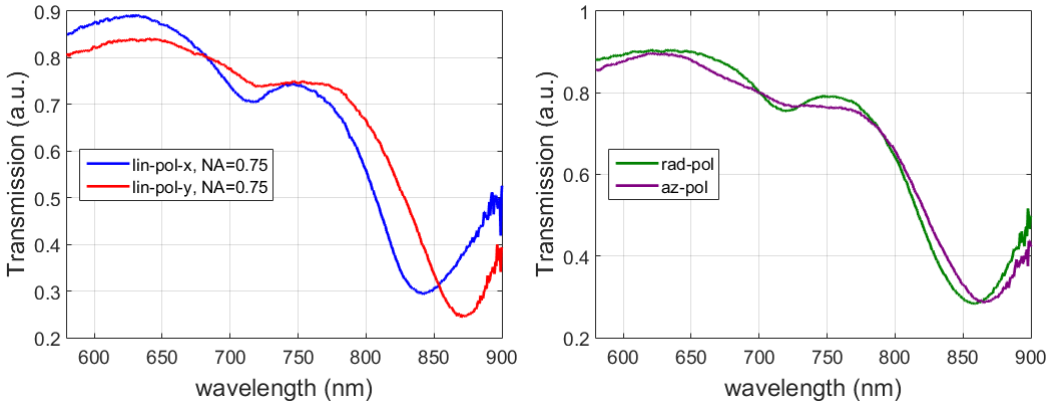

(a) (b)

Figure 5.13: The transmission through the radial trimer metasurface with L = 120 nm, w = 40 nm, s = 85 nm, and p = 400 nm (#R15) with (a) linearly x- and y-polarised light and (b) radially and azimuthally polarised light illumination using objective lens with NA=0.75.

L = 90 nm is responsive to shorter wavelengths, giving blue-shifted spectra compared to that with L = 100 nm. The dipole mode appears clearly on all measurements at 710 nm and the radial mode at 610 nm appears stronger with higher NA objectives and radially polarised illumination.

All compiled results for radially polarised excitation for radial trimer metasurfaces are summarised in Figure 5.16. As the nanorod lengths increase, the resonance wavelengths of both radial and dipole modes are red-shifted.

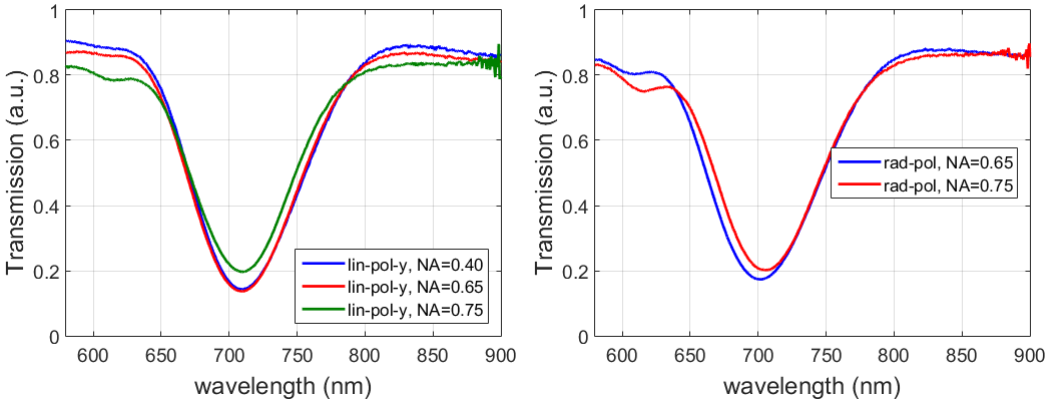

(a) (b)

Figure 5.14: The transmission through the radial trimer metasurface with L = 90 nm, w = 40 nm, s = 70 nm, and p = 300 nm (#R11) with (a) linearly and (b) radially polarised light illumination through the objective lens with different NA.

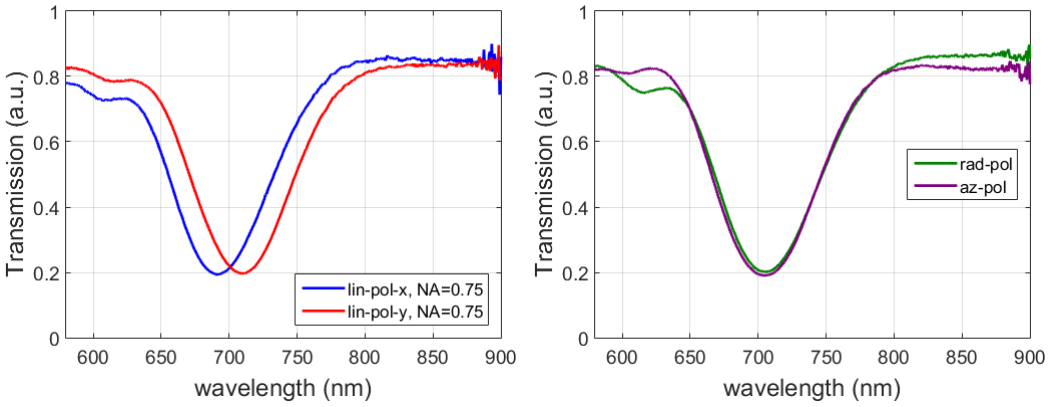

(a) (b)

Figure 5.15: The transmission through the radial trimer metasurface with L = 90 nm, w = 40 nm, s = 70 nm, and p = 300 nm (#R11) with (a) linearly x- and y-polarised light and (b) radially and azimuthally polarised light illumination,using objective lens with NA=0.75.

The metasurfaces were also characterised by measuring their reflectance. As it has been previously shown that a high NA objective lens is needed for exciting sub-radiant modes, only objective lenses with NA 0.65 and 0.90 were used.

Figure 5.17, 5.18, and 5.19 show the reflectance from the same radial metasurfaces with L = 90 nm (#R11), L = 100 nm (#R13), and L = 120 nm (#R15) respectively. Metasurfaces were illuminated with linearly x-polarised light and radially polarised light with two different objective lenses with different NA

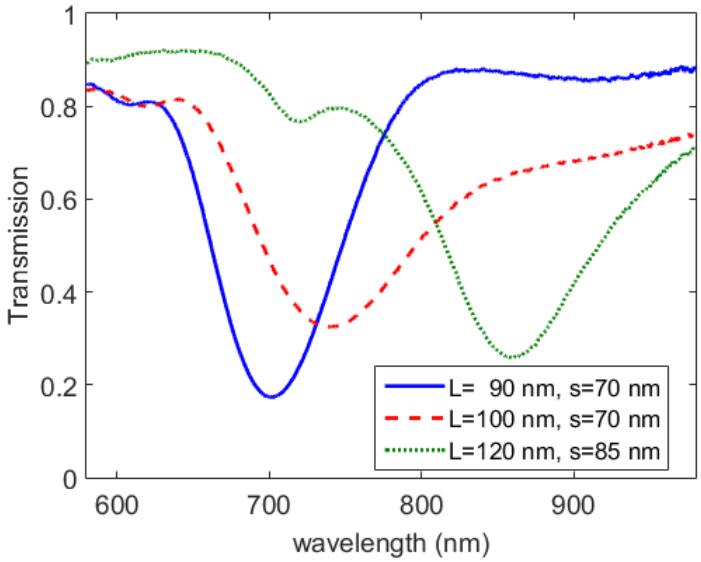

Figure 5.16: The transmission of light through the radial trimer antennas of different L and s with radially polarised light focussed by the objective lens of NA=0.65.

(#O4 and #O5).

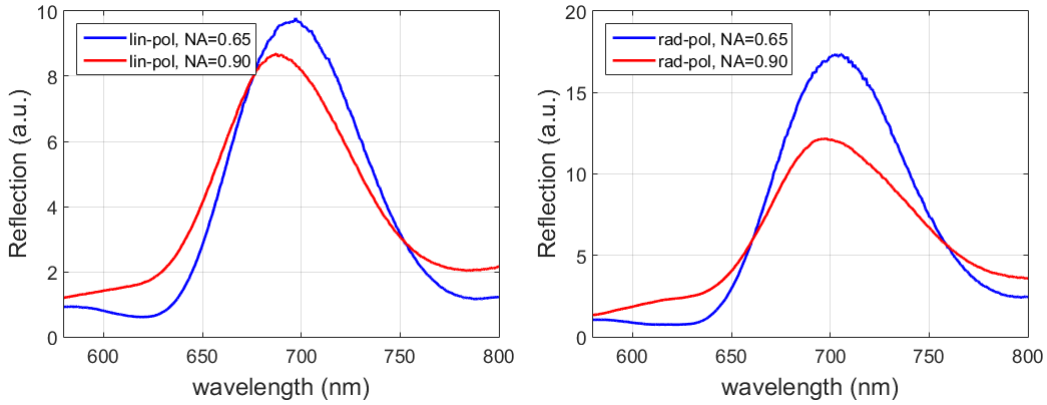

(a) (b)

Figure 5.17: The reflection from the radial trimer metasurface with $L = 90$ nm, $w = 40$ nm, $s = 70$ nm, and $p = 300$ nm (#R11) with (a) linearly and (b) radially polarised light illumination through the objective lens with different NA.

Using the NA 0.90 objective, the signatures of radial modes appear clearly with both linearly polarised and radially polarised illumination on metasurfaces #R13 and #R15, shown in Figures 5.18 and 5.19. The radial mode strength is weaker on metasurface #R11, shown in Figure 5.17. As previously discussed, this happens as a result of larger incident angle components being produced by

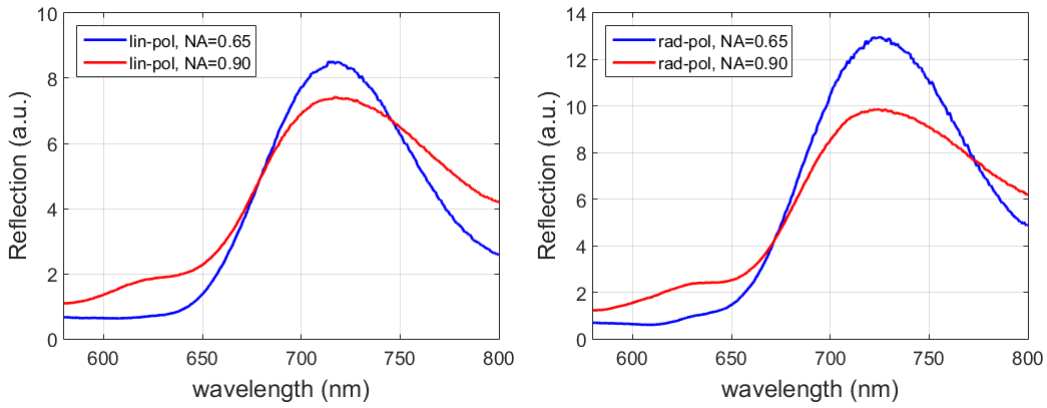

(a) (b)

Figure 5.18: The reflection from the radial trimer metasurface with $L = 100$ nm, $w = 40$ nm, $s = 70$ nm, and $p = 300$ nm (#R13) with (a) linearly and (b) radially polarised light illumination through the objective lens with different NA.

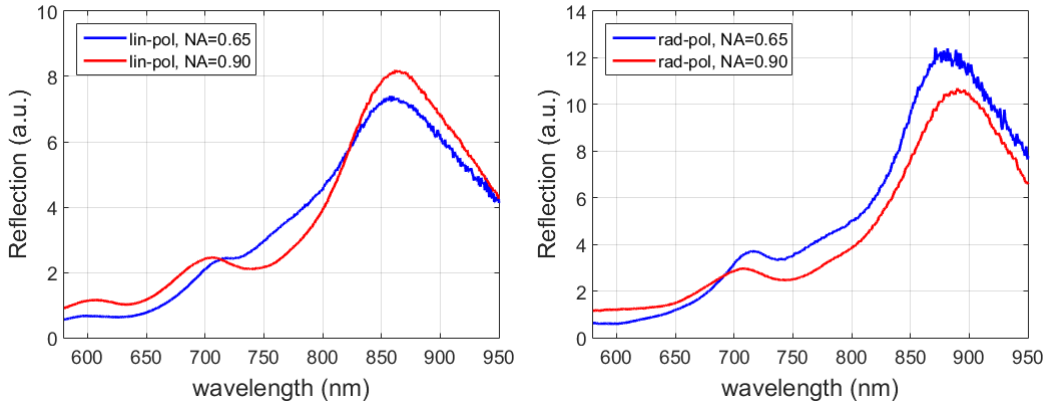

(a) (b)

Figure 5.19: The reflection from the radial trimer metasurface with $L = 120$ nm, $w = 40$ nm, $s = 85$ nm, and $p = 400$ nm (#R15) with (a) linearly and (b) radially polarised light illumination through the objective lens with different NA.

a higher NA objective. With this objective, linearly polarised light is sufficient to produce a distinct reflection peak corresponding to radial mode excitation.

The signature of radial mode excitation in the device #R11 (Figure 5.17) cannot be clearly identified by its reflection spectra. This is due to the small spectral separation of radial and dipole resonances for this geometry. There is a weak radial mode peak at 610 nm with NA 0.90 although this is not distinct. The radial mode resonance is seen more clearly in its transmission spectra, shown in Figure 5.14. This happened because a sub-radiant mode,

in this case a radial mode, has a longer lifetime than the dipole mode [104, 105]. At a radial mode resonance, antennas exhibit large absorption and weak scattering compared to those at dipole mode resonance, causing a stronger drop in transmission compared to the enhancement in reflection.

In devices #R13 and #R15, the spectral locations of the radial and dipole mode resonances are better separated. This leads to clearer signatures of the radial mode excitation at 620 nm and 720 nm for devices #R13 and #R15 respectively, shown in Figures 5.18 and 5.19.

The reflectance from radial trimer metasurfaces with various nanorod lengths with radially polarised light illumination is summarised in Figure 5.20. The objective lens used was NA 0.90 (#O5). The spectral locations of the radial and dipole mode resonances are consistent to those found in the transmittance measurements in Figure 5.16.

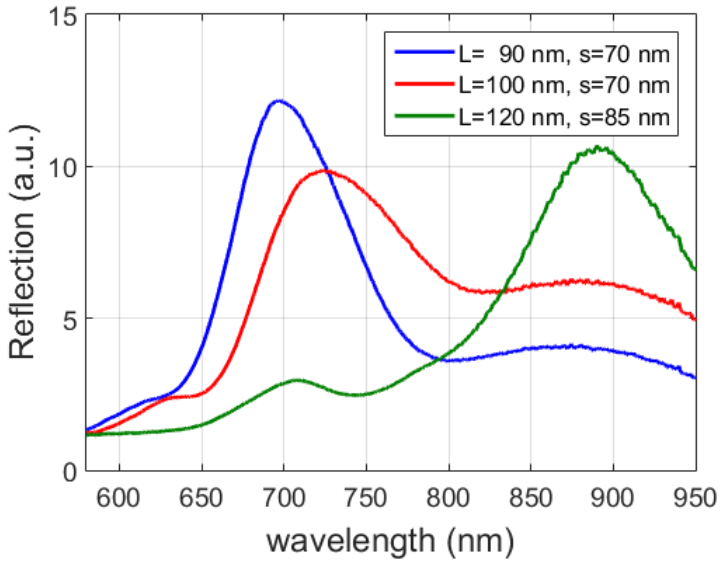

Figure 5.20: The reflection from the radial trimer metasurface with different L and s (#R11, #R13, #R15) illuminated with focussed radially polarised light with NA=0.75.

5.3.1.2 Comparison with Simulation Results

The experimentally obtained spectra are compared with those from the simulations in previous chapter. Figure 5.21 shows the transmission and reflection

spectra of the radial trimer metasurface with $L = 100$ nm, $w = 40$ nm, and $s = 70$ nm (#R13). The simulations were performed with the FDTD method in which the metasurface was illuminated with a p-polarised plane wave. The angle of incidence is 20° inside the medium with a refractive index of $n = 1.5$, which is that of the glass substrate and the PMMA encapsulating the whole metasurface. This angle corresponds to 31° in air, before the plane wave enters the PMMA layer. The comparison is also shown for $L = 120$ nm, $w = 40$ nm, and $s = 85$ nm (#R15) in Figure 5.22, with an angle of incidence of 30°, corresponding to 49° inside air[4].

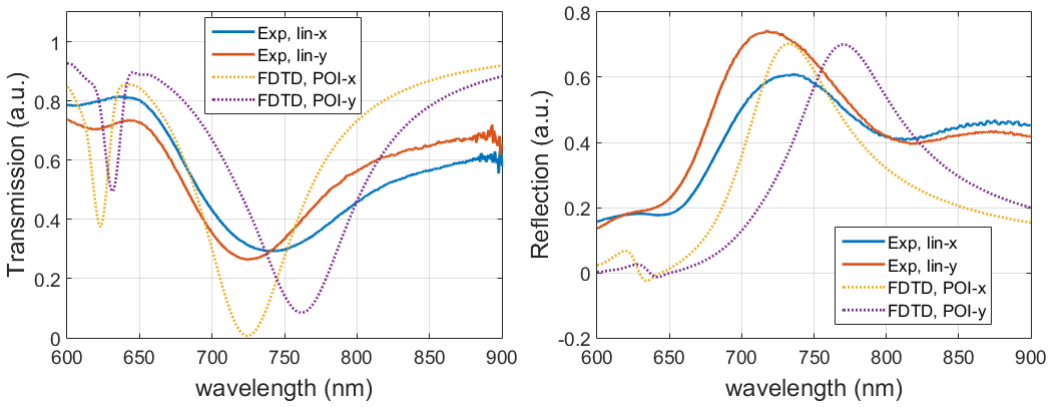

(a) (b)

Figure 5.21: The (a) transmission though and (b) reflection from radial trimer metasurface with $L = 100$ nm, $s = 70$ nm (#R13) with linearly x- and y-polarised illumination compared with the FDTD simulation results, performed with p-polarised plane wave illumination (at 20°)and plane of incidence (POI) parallel either to the x- or y-axis. The experimental data were taken with NA 0.75 (#O3) and 0.90 (#O5) for the transmission and reflection respectively.

In both Figures 5.21 and 5.22, simulations were performed with two different planes of incidence, parallel to the x- and y-axis. This results in two slightly different central wavelengths of the dipole resonances with those arising from illumination in the yz-plane having a slightly longer resonance wavelength. This means that the resonant energies of radiant modes are affected by orientation. The resonance of radial modes are also affected by this asymmetry. This shifting of resonances might be introduced by the asymmetry in the metasurfaces due to fabrication process. In simulation, the asymmetry was introduced

[4]This angle of incidence for $L = 120$ nm was chosen to be larger to minimise the effect of numerical errors produced by the FDTD meshes

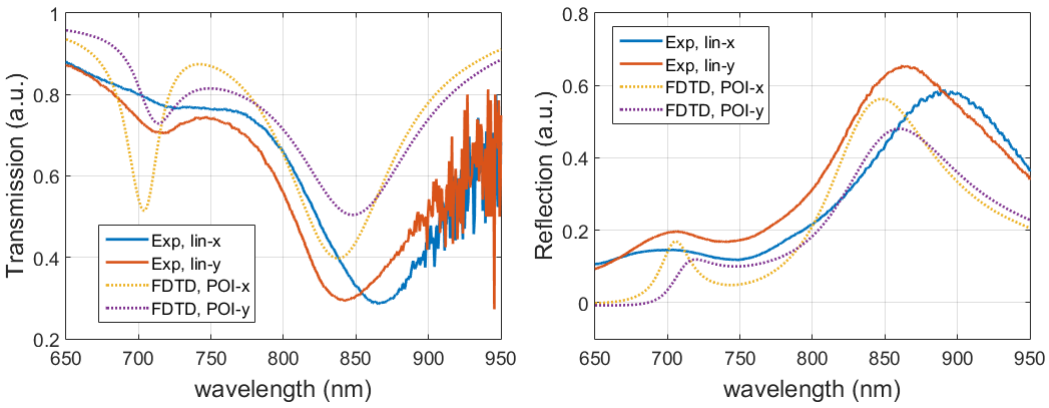

(a) (b)

Figure 5.22: The (a) transmission though and (b) reflection from radial trimer metasurface with $L = 120$ nm, $s = 85$ nm (#R15) with linearly x- and y-polarised illumination compared with the FDTD simulation results, performed with p-polarised plane wave illumination (at 30°) and plane of incidence (POI) parallel either to the x- or y-axis. The experimental data were taken with NA 0.75 (#O3) and 0.90 (#O5) for the transmission and reflection respectively.

by the FDTD meshing as two nanorods in a unit cell making an angle to the square grids of the mesh.

As discussed in Section 3.4, a focussed, linearly x-polarised beam has dominant p-polarised components near the σ_x-axis in spatial frequency coordinates. This means that the simulation results with p-polarised plane wave illumination incident in xz-plane should be a better fit to the experimental results obtained with a linearly x-polarised beam. The same argument applies to plane simulation with a incident in the yz-plane and experiments with a linearly y-polarised beam. The experimental data with radially polarised beam illumination have dipole mode resonances located in between those orthogonally polarised illumination.

The fabricated samples do not have the precise size of the nominal designs, as summarised in Table 5.2. These parameters could have been used in the FDTD simulation to reproduce the experimental results more accurately. The nanorod shapes on the fabricated samples, however, also deviate from the modelled shapes in the simulation and this could also compromise the accuracy of produced spectra. An example is shown in Figure 5.23 for metasurfaces #R13 and #R15, simulated with the FDTD using the fabricated geometric parameters, as obtained from the SEM images. The spectral location of the

resonances produced by this simulation are still shifted from the actual experimental data. The modelling could be further modified by altering the radius of the corner rounding but the results produced by those with the nominal sizes are reasonably accurate, so further modifications were not performed.

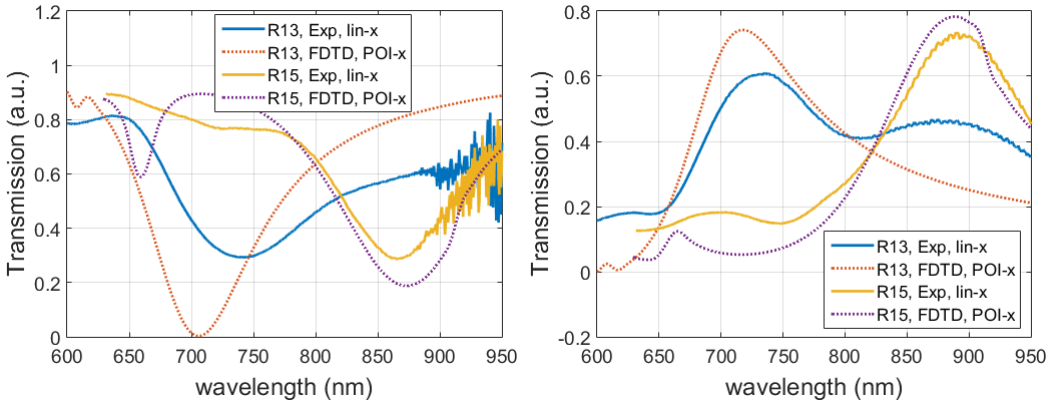

Figure 5.23: The (a) transmission through and (b) reflection from the metasurfaces #R13 and #R15 compared with the FDTD results with the geometric parameters taken from the SEM images.The experimental data were taken with NA 0.75 (#O3) and 0.90 (#O5) for the transmission and reflection respectively.

Another experimental data fitting can be provided by the EEM method. This method has a much shorter calculation time and can be used for fitting experimental results by tuning parameters, such as coupling constants. The comparison of the reflectance from the experiments with the scattering calculated by the EEM is shown in Figure 5.24 for metasurface #R13 and #R15 ($L = 100$ nm and $L = 120$ nm). The EEM parameters used are provided in Table 5.6.

Parameters (Units)	Values	
	#R13	#R15
λ_i (nm)	700	835
A (rad/s)	1×10^{14}	1×10^{14}
Γ (rad/s)	3.6×10^{14}	3.3×10^{14}
G	-1.3	-1.7

Table 5.6: The fitting parameters of the EEM for experimental data of metasurfaces #R13 and #R15, for comparison shown in Figure 5.24.

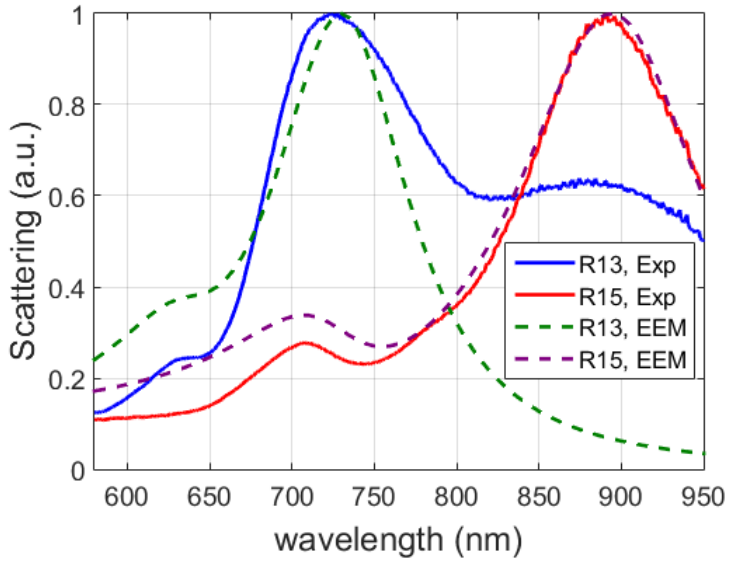

Figure 5.24: The comparison between the experimental data of metasurfaces #R13 and #R15 with radially polarised illumination and the simulation results with the EEM. The experimental data were taken with NA 0.90 (#O5).

5.3.1.3 The Effects of Separation Distances and Nanorod Widths

As it has been shown in simulations that increasing the distance between nanoparticles leads to weaker coupling and results in a weaker splitting of the resonances. In other words, the dipole and radial mode resonance wavelengths come closer and approach the resonance wavelength of a single particle as the interparticle distance is increased.

Consider two metasurfaces consisting of radial trimer antennas with nominal nanorod lengths $L = 90$ nm and widths $w = 40$ nm, but with different off-set distances, $s = 70$ nm to $s = 85$ nm (#R11 and #R12). Figure 5.25 shows the measurements obtained from these metasurfaces. The dipole mode always shows the characteristic strong peak and a broad spectrum. As the off-set distance s is increased, the radial mode is red-shifted and the dipole mode is blue-shifted so they become closer as expected. For $s = 85$ nm, the radial mode resonance is closer to the tail of the dipole mode, making it harder to observe compared to that of $s = 70$ nm.

The effect of a variation in off-set distances was also investigated for metasurfaces with $L = 100$ nm and $L = 120$ nm. For $L = 100$ nm, the off-set distances are $s = 70$ nm and $s = 85$ nm (#R13 & #R14), and for $L = 100$ nm, the

off-set distances studied are $s = 85$ nm and $s = 100$ nm (#R15 & #R16). The transmittance and reflectance measurements for these devices are shown in Figure 5.26 and 5.27. The results of this variation in interparticle distance lead to the same trend found in $L = 90$ nm. Note that in Figures 5.25 and 5.26, the periodicity of the structures is 300 nm and in Figure 5.27, the periodicity is 400 nm, but this is not expected to affect major conclusions.

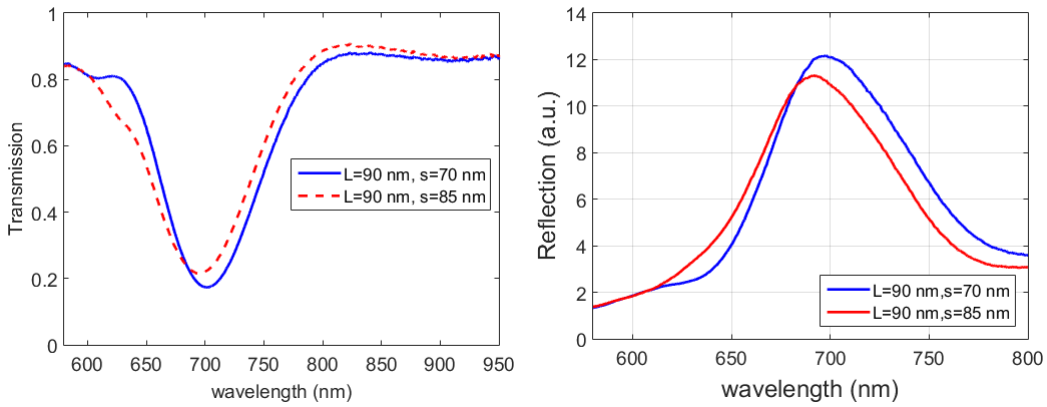

(a) (b)

Figure 5.25: The (a) transmission through and (b) reflection from the radial trimer metasurfaces with $L = 90$ nm and different off-set distance s with radially polarised light. Code: #R11; #R12

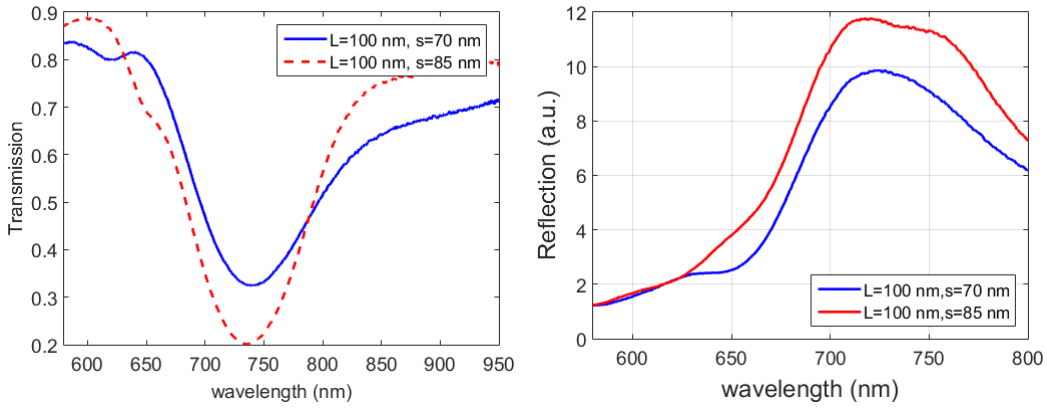

(a) (b)

Figure 5.26: The (a) transmission through and (b) reflection from the radial trimer metasurfaces with $L = 100$ nm and different off-set distance s with radially polarised light. Code: #R13; #R14

The effect of variation in nanorod lengths L and off-set distances s have been presented. The aspect ratio of the nanorod can also be changed by changing

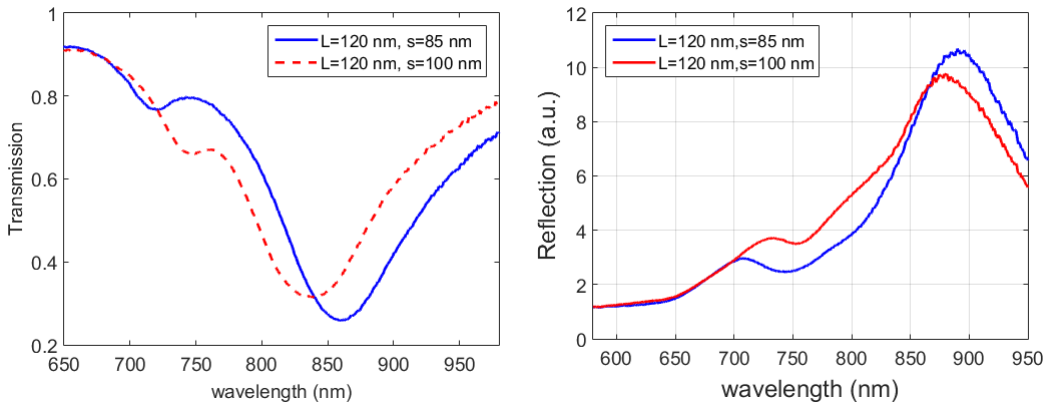

(a) (b)

Figure 5.27: The (a) transmission through and (b) reflection from the radial trimer metasurfaces with $L = 120$ nm and different off-set distance s with radially polarised light. Code: #R13; #R14

the nanorod width w while keeping the length fixed. Increasing the aspect ratio of nanorods while keeping one parameter fixed red-shifts their resonances [106]. In antennas with smaller nanorod widths, the corners of the nanorods become further away. As in the case with increasing s, this leads to weaker coupling and brings the two resonances (dipole and radial modes) closer. However, because the nanorod is narrower, the whole spectrum is red-shifted, consistent with previous reports in the literature. Figure 5.28 shows the effect of changing the width of the rods for metasurfaces composed of radial trimmers with $L =$ 100 nm and $s = 70$ nm (#R13, #R17, #R18). It should be noted that the resonances of antennas with $w = 30$ nm and $w = 20$ nm are more closely spaced than those with $w = 40$ nm. Their periodicity is 250 nm $\times$ 300 nm, where the smaller value describes their periodicity along the x-axis. The periodicity was kept as small as practical to minimise the effects of diffraction.

The same measurements were also performed for metasurfaces with radial trimers with $L = 120$ nm and $s = 80$ nm (#R19 & #R1A). The nanorod widths investigated were $w = 30$ nm and $w = 20$ nm. The transmission and reflection results are shown in Figure 5.29. Again, reducing the nanorod widths slightly red-shifts the entire spectrum.

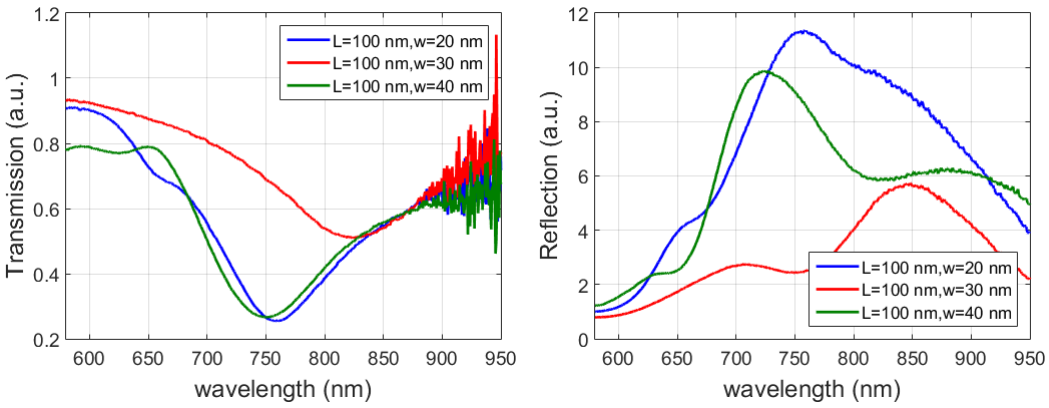

(a) (b)

Figure 5.28: The (a) transmission through and (b) reflection from radial trimer metasurfaces with $L = 100$ nm, $s = 70$ nm, and different nanorod width w (#R13, #R17, #R18).

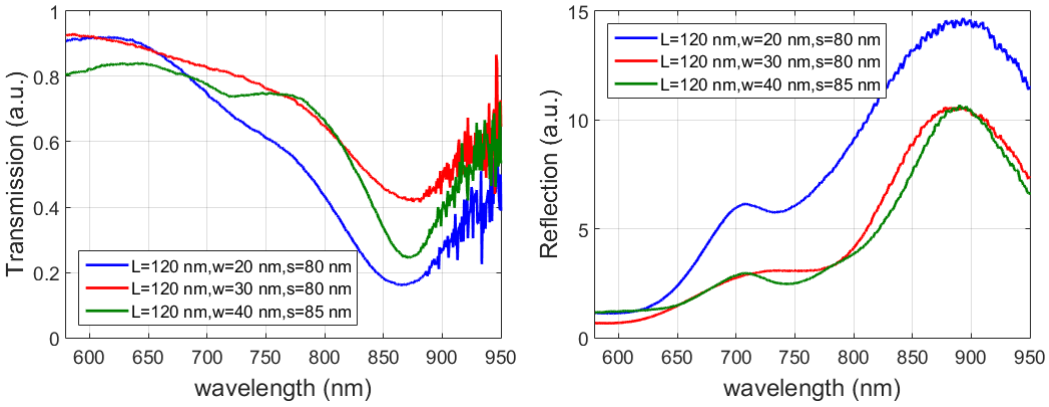

(a) (b)

Figure 5.29: The (a) transmission through and (b) reflection from radial trimer metasurfaces with $L = 120$ nm and different nanorod width w (#R15, #R19, #R1A). Off-set distance is $s = 85$ nm for $w = 40$ nm, and $s = 80$ nm for the other two.

5.3.2 Radial Tetramer Metasurfaces

5.3.2.1 Variation of Illumination and Comparison with Simulations

Another type of metasurface supporting radial modes that was investigated in this study is one consisting of radial tetramer antennas. It involves four nanorods and, as discussed in Chapter 4, Section 4.1, in additional to a radial mode similar to that of the trimers, supports an additional dark, breathing,

mode. In order of increasing resonance wavelength, the modes are radial, dipole, and breathing modes.

Consider the radial tetramer metasurface with $L = 120$ nm, $w = h = 40$ nm, $s = 90$ nm, and periodicity is $p = 400$ nm (#R25). As performed for radial trimer metasurfaces, the transmittance through, and reflectance from, this device were also measured using various objective lenses with different NA as well as for various input polarisations. For transmission spectra, the objective lenses used were #O1, #O2, and #O3 with NA 0.40, 0.65, and 0.75 respectively. Reflection spectra were measured using #O4 and #O5 objective lenses with NA 0.65 and 0.90 respectively. The input polarisation of the beam is either linearly, radially, or azimuthally polarised.

Figure 5.30 shows the transmission and reflection spectra with linearly x-polarised beam illumination through different NA objectives. As expected, a higher NA produces a stronger resonance of the radial mode. The radial mode resonance occurs at 670 nm.

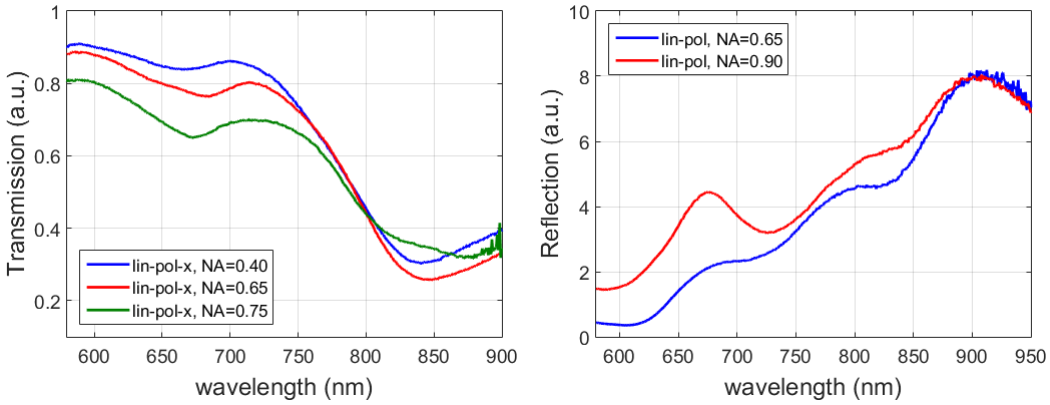

(a) (b)

Figure 5.30: The (a) transmission through and (b) reflection from the radial tetramer metasurface with $L = 120$ nm, $w = 40$ nm, $s = 90$ nm, and $p = 400$ nm (#R25) with linearly polarised light illumination through the objective lens with different NA.

The dipole resonance of this metasurface occurs at ∼840 nm as can be seen in the transmission spectra (Figure 5.30a). The resonance, however, shows the broadening effect at that wavelength, and the peak is shifted to a longer wavelength for NA= 0.75. In the reflection spectra (Figure 5.30b), the effect is even stronger, producing two resonance peaks at 800 nm and 900 nm. This

phenomenon is due to the presence of another dark mode, (the breathing mode, which has the longest resonance wavelength of the antenna), altering the line shape of the dipole mode.

Figure 5.31 shows the transmission and reflection spectra with radially polarised illumination with various NA objectives. Higher-NA illumination also produces a stronger excitation of the radial mode. The use of a radially polarised beam, however, does not produce a significant difference in the spectra from those produced with linearly polarised illumination shown in Figure 5.30.

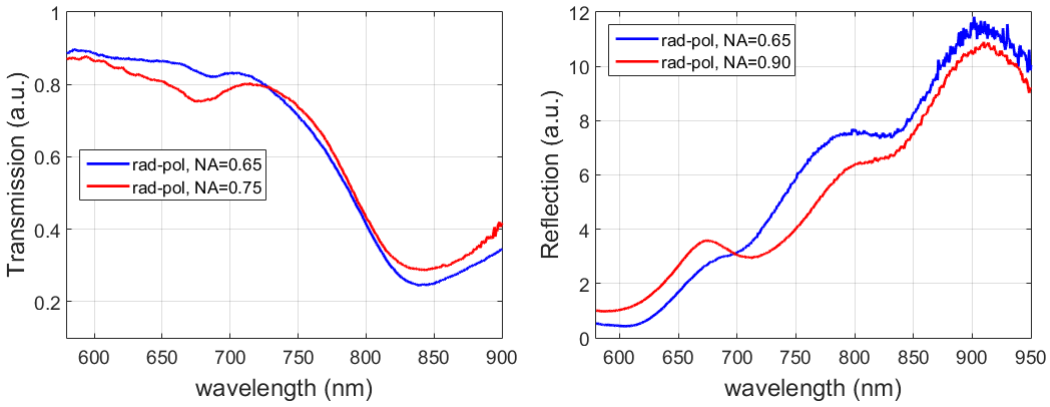

(a) (b)

Figure 5.31: The (a) transmission through and (b) reflection from the radial tetramer metasurface with $L = 120$ nm, $w = 40$ nm, $s = 90$ nm, and $p = 400$ nm (#R25) with radially polarised light illumination through the objective lens with different NA.

The metasurface is symmetric with respect to rotation by 90° about the normal (x and y axes are interchangeable) so that linear polarisation parallel to either of the main axis should give similar results. Another variation was performed by aligning the polarisation diagonally (labelled 'lin-d'), at 45° with respect to the x-axis. The purpose was to see the changes in breathing mode strength, as observed in the simulation for various orientations of the plane of incidence (Section 4.3.1). Figure 5.32 shows the dependence on the direction of linear polarisation. The results, however, do not indicate any sensitivity to linear polarisation.

Figure 5.33 shows the transmission and reflection spectra from #R25 when illuminated with radially and azimuthally polarised light. When the device

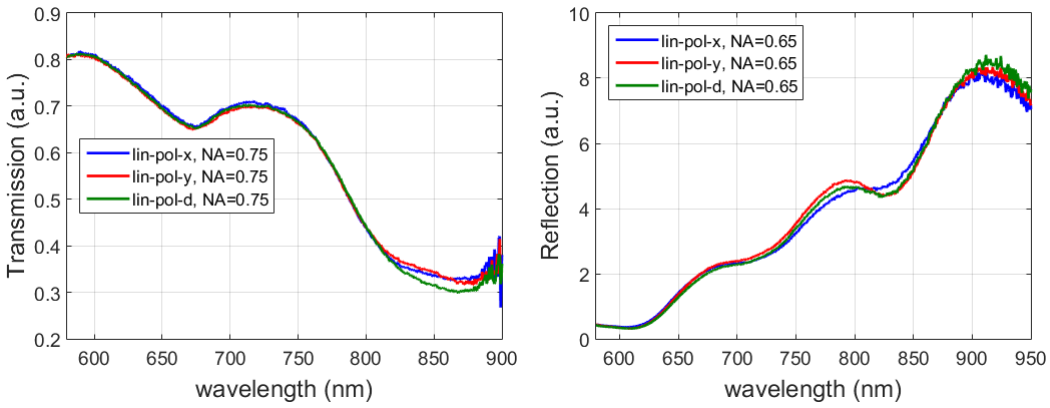

(a) (b)

Figure 5.32: The (a) transmission through and (b) reflection from the radial tetramer metasurfaces with $L = 120$ nm, $w = 40$ nm, $s = 90$ nm, and $p = 400$ nm (#R25) with linearly x- and diagonal-polarised light illumination, using objective lens with NA=0.75 for Fig.(a) and NA=0.90 for Fig.(b). Diagonal polarisation makes an angle 45° from the x-axis.

is illuminated with either a radially or azimuthally polarised beam, both give two peaks at 670 nm. These peaks, however, correspond to the excitation of different modes. When a radially polarised beam is used, this excites the radial and dipole modes, as previously discussed. On the other hand, the peak produced with azimuthal polarisation correspond to a different mode and this is discussed in the following sub-section.

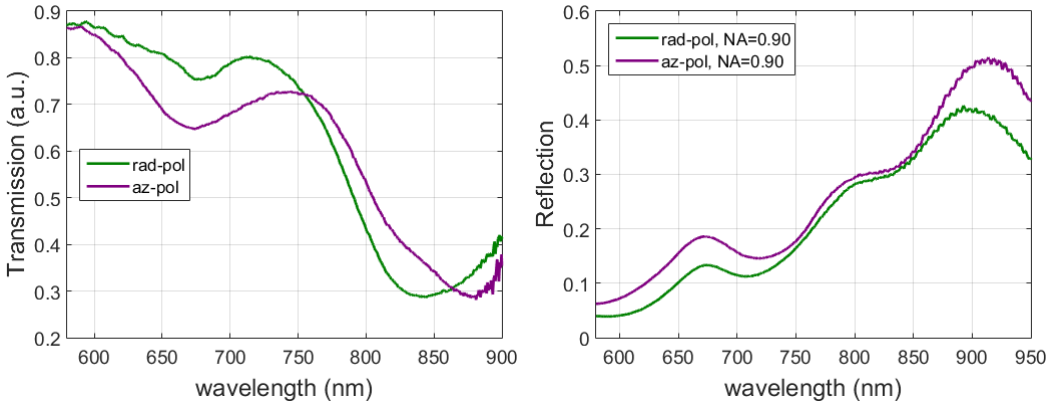

(a) (b)

Figure 5.33: The (a) transmission through and (b) reflection from the radial tetramer metasurfaces with $L = 120$ nm, $w = 40$ nm, $s = 90$ nm, and $p = 400$ nm (#R25) with radially and azimuthally polarised light illumination, using objective lens with NA=0.75 for Fig.(a) and NA=0.90 for Fig.(b).

5.3.2.2 Comparison with Simulations

Figure 5.34 shows the comparison between the experimental data obtained from metasurface #R25 with FDTD simulations. The experimental data shown are those obtained with radially polarised illumination. The simulation was performed with p-polarised plane wave illumination, giving three distinct resonances which correspond to radial, dipole, and breathing mode resonances at 670 nm, 820 nm, and 860 nm respectively. The spectral locations of dipole and breathing modes are adjacent and they interfere with each other. In the experimental data these two modes form a broad resonance in the transmission spectrum and two distinct peaks in the reflection spectrum.

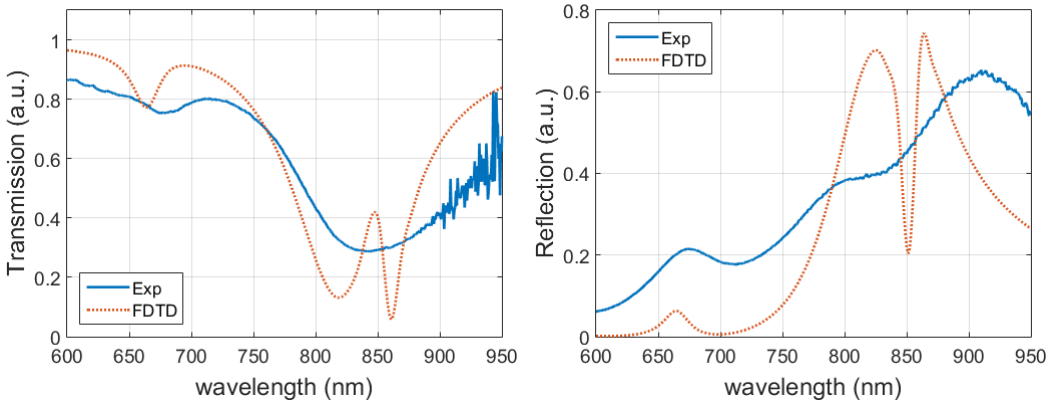

(a) (b)

Figure 5.34: The comparison between the experimental data of metasurface #R25 and the FDTD simulation results of the (a) transmission through and (b) reflection from the metasurface. The experimental data were taken with NA 0.75 (#O3) and 0.90 (#O5) for the transmission and reflection respectively.

To explain the modes excited with radial and azimuthal polarisation, in Figure 5.33, the FDTD simulation was performed with off-normal p- and s-polarised plane wave illumination. This was already discussed in Section 4.2.3.1 for a radial tetramer metasurface in Figure 4.19. The figure is reproduced here along with the surface charges associated with each mode, shown in Figure 5.35. The plane wave with p-polarisation produces the radial mode but the plane wave with s-polarisation produces a Fano resonance at about the same wavelength and the surface charges do not have radial symmetry.

The EEM method can also be used for fitting the mode excitation of the radial

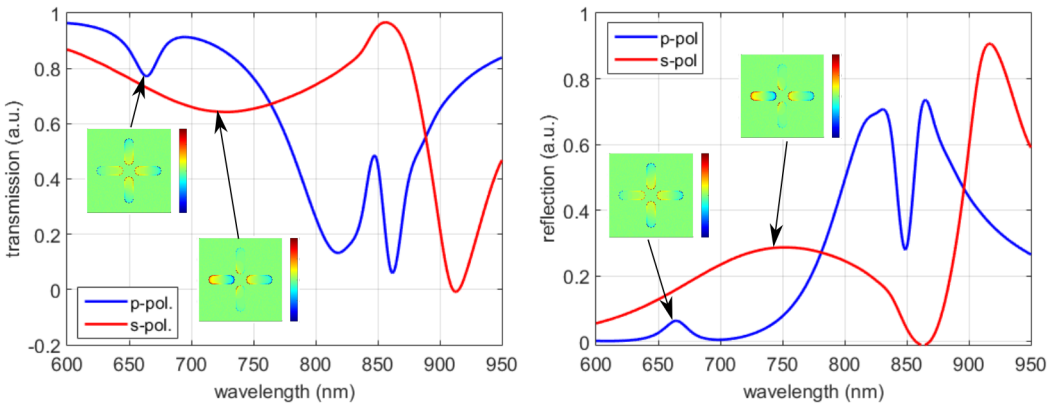

(a) (b)

Figure 5.35: The (a) transmission trough and (b) reflection from metasurface #R25 modelled by the FDTD with p- and s-polarisation, with surface charges at indicated wavelength on the spectra.

tetramer metasurfaces and results are shown in Figure 5.36. The scattering obtained in the experiment is given by the reflection R which is scaled to have a maximum value of 1. Using this method, however, the breathing mode appears to be much weaker compared to the dipole mode and has a minimal effect on either broadening or shifting the dominant resonance.

The first EEM result (labelled 'EEM(1)') was calculated for a radially polarised beam which was a superposition of plane wave components with a uniform amplitude spectrum, up to NA= 0.90. This was able to reproduce the radial and dipole resonances at 670 nm and 840 nm respectively. Further analysis (labelled as 'EEM(2)') was performed by decreasing the linewidth Γ significantly to 0.5×10^14 rad/s to be able to observe the modes more clearly. The calculation was performed with a p-polarised incident plane wave with a normalised wavevector $(\sigma_x, \sigma_y) = (0.6, 0)$. The spectral locations of all modes the agree well with experimental data although the lineshape is different.

5.3.2.3 Variation of Nanorod Sizes and Separation Distances

Other metasurfaces consisting of radial tetramers composed of nanorods with different lengths L follow the same behaviour as discussed previously for $L =$ 120 nm (#R25) in the response to various types of illumination. The only difference is the shifting of the spectral location of the resonances. Complete data

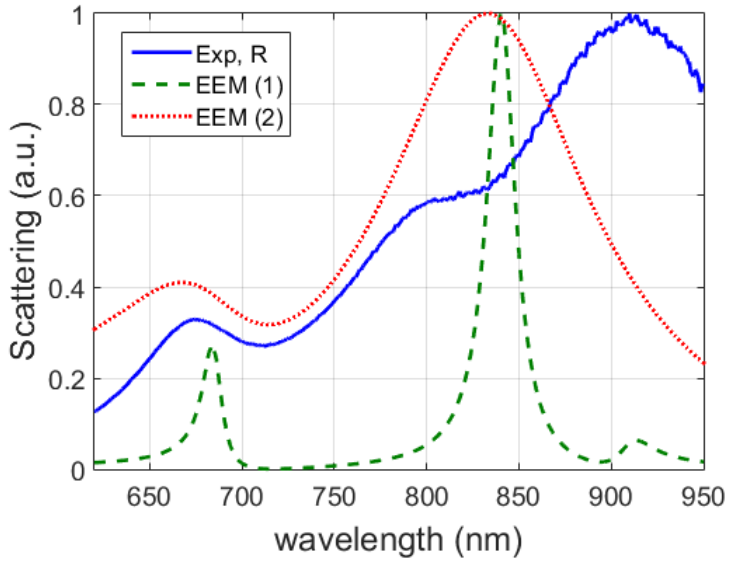

Figure 5.36: The comparison between the experimental data of metasurfaces #R25 under radially polarised illumination and the simulation results with the EEM. The experimental data were taken with NA 0.90 (#O5).

Parameters (Units)	Values	
	EEM(1)	EEM(2)
λ_i (nm)	810	810
A (rad/s)	1×10^{14}	1×10^{14}
Γ (rad/s)	3.6×10^{14}	0.5×10^{14}
G_A	-1.7	-1.7
G_B	-0.85	-0.85

Table 5.7: Best fit parameters for the EEM for experimental data of metasurface #R25, for comparison shown in Figure 5.36.

are available in Appendix A. A summary of the metasurfaces with different nanorod lengths is shown in Figure 5.37.

Figure 5.37 shows the transmission and reflection spectra for radial tetramer metasuraces with $L = 90$ nm, $L = 100$ nm, and $L = 120$ nm (#R11, #R13, #R15) with radially polarised illumination. In this set of devices, the gap sizes are fixed. Shorter nanorod lengths have blue-shifted resonances as expected. The breathing modes can be seen more strongly in the reflection spectra compared to those in the transmission spectra.

The effect of coupling between nanorods in radial tetramers can be investigated by varying the distance between them with the same size. Figures 5.38, 5.39,

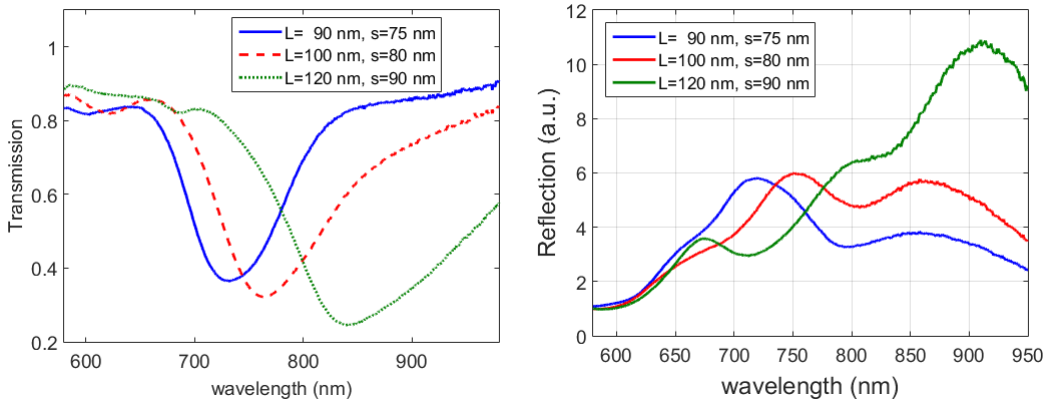

(a) (b)

Figure 5.37: The (a) transmission through and (b) reflection from the radial tetramer metasurfaces with various L (#R21,#R23,#R25) with radially polarised light illumination, using objective lens with NA=0.75 for Fig.(a) and NA=0.90 for Fig.(b).

and 5.40 show the effect of the variation in off-set distances s for devices with $L = 90$ nm, $L = 100$ nm, and $L = 120$ nm respectively. In all cases, increasing the distance s will red-shift the radial mode and blue-shift the dipole mode.

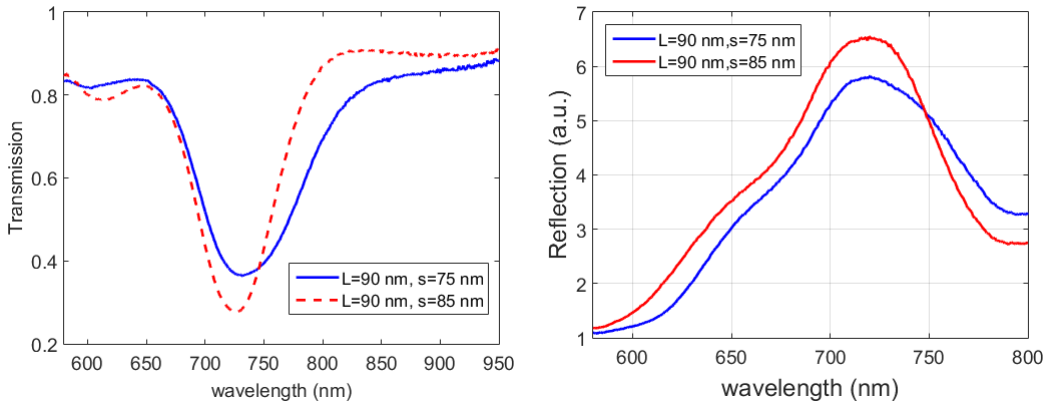

(a) (b)

Figure 5.38: The (a) transmission through and (b) reflection from the radial tetramer metasurfaces with $L = 90$ nm and different off-set distance s (#R21 & #R22) with radially polarised light, using objective lens with NA=0.75 for Fig.(a) and NA=0.90 for Fig.(b).

A variation in width changes the aspect ratio of the nanorods. Figure 5.41 and 5.42 show the transmission and reflection spectra of metasurfaces with varying nanorod widths where the length L and distance s are kept fixed. For $L = 100$ nm (#R27 & #R23), shown in Figure 5.41, the smaller width brings the radial

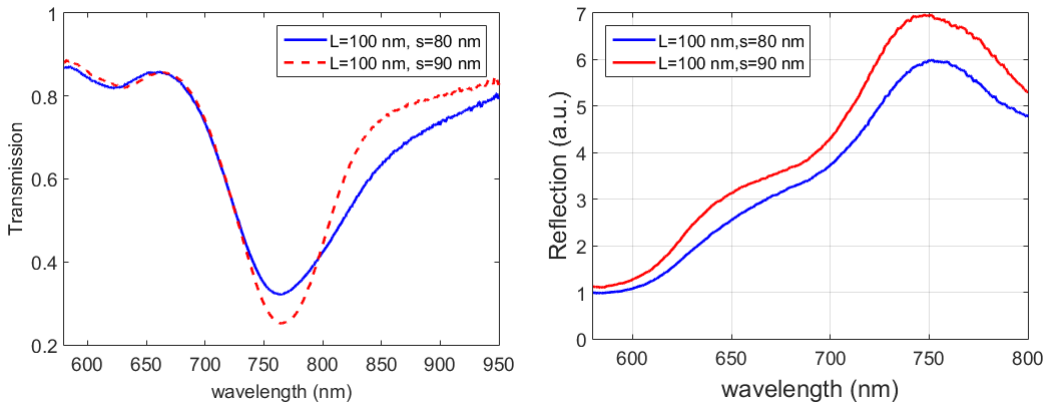

(a) (b)

Figure 5.39: The (a) transmission through and (b) reflection from the radial tetramer metasurfaces with $L = 100$ nm and different off-set distance s (#R23 & #R24) with radially polarised light, using objective lens with NA=0.75 for Fig.(a) and NA=0.90 for Fig.(b).

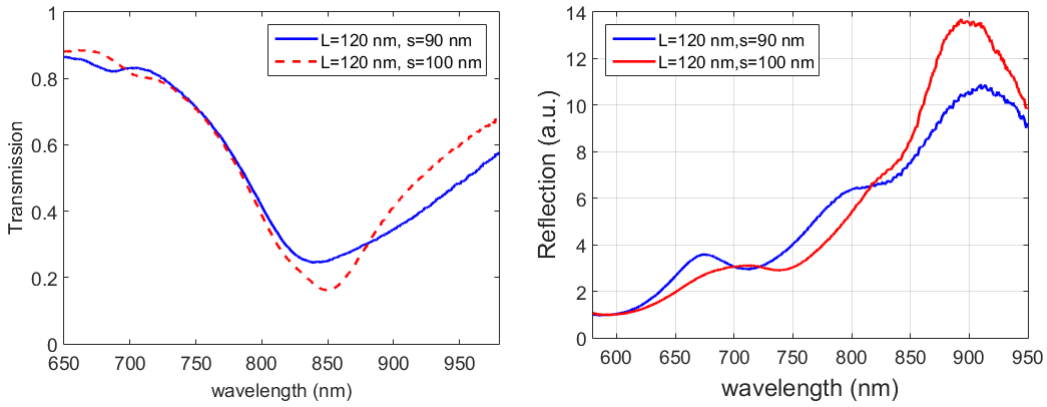

(a) (b)

Figure 5.40: The (a) transmission through and (b) reflection from the radial tetramer metasurfaces with $L = 120$ nm and different off-set distance s (#R25 & #R26) with radially polarised light, using objective lens with NA=0.75 for Fig.(a) and NA=0.90 for Fig.(b).

and dipole modes closer. This is due to slightly weaker coupling associated with smaller widths making nanorod ends slightly further apart. For $L = 120$ nm, however, the radial mode on the metasurface with a smaller width is not apparent in the spectra, due to the weaker coupling between nanorods as the gap size increases.

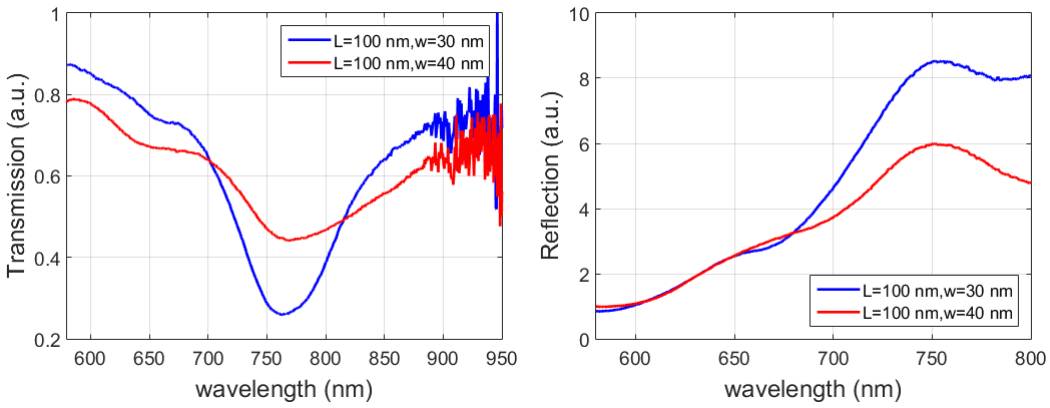

(a) (b)

Figure 5.41: The (a) transmission through and (b) reflection from the radial tetramer metasurfaces with various width for L =100 nm (#R27 & #R23) with radially polarised light illumination using objective lens with NA=0.75.

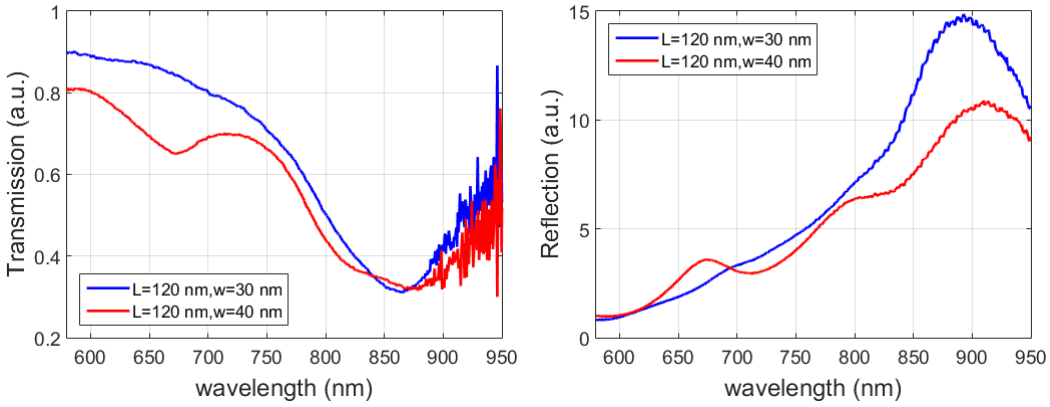

(a) (b)

Figure 5.42: The (a) transmission through and (b) reflection from the radial tetramer metasurfaces with various width for L = 120 nm (#R28 & #R25) with radially polarised light illumination using objective lens with NA=0.75. Device code:

5.3.3 Azimuthal Trimer Metasurfaces

The excitation of sub-radiant modes of metasurfaces consisting of azimuthal antennas is more challenging. Recalling the simulation results from Chapter 4, azimuthal modes appear at a longer wavelength than the dipole mode and the strength of azimuthal modes is weaker compared to radial modes.

Consider the metasurface consisting of azimuthal trimers with L = 120 nm, w = 40 nm, s = 70 nm, and p = 400 nm (#A15). This metasurface was

measured with various objectives with different NAs and various polarisations of the input beam.

Figures 5.43 and 5.44 show the transmission and reflection spectra of azimuthal metasurface #A15 with linearly and azimuthally polarised light. Various objectives with different NAs were used and the spectra produced by those with a higher NA are expected to exhibit an azimuthal mode resonance. The dipole mode is strong and located at 760 nm but there is no signature of the azimuthal mode resonance in the transmission spectra. In the reflectance measurements, there are peaks at 850 nm, suggesting the excitation of the azimuthal modes.

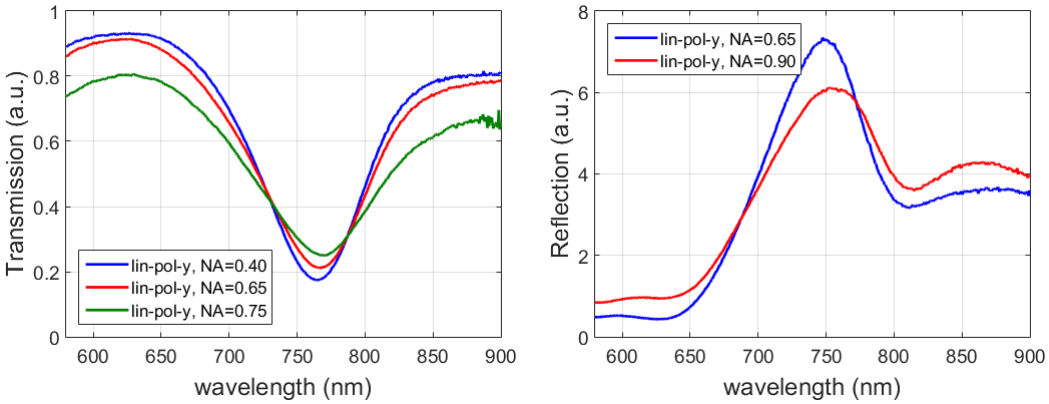

(a) (b)

Figure 5.43: The (a) transmission through and (b) reflection from the azimuthal trimer metasurface with $L = 120$ nm, $w = 40$ nm, $s = 70$ nm, and $p = 400$ nm (#A15) with linearly polarised light illumination through the objective lens with different NA.

The results of varying the polarisation direction of linearly polarised light with polarisation axis parallel to either the x- and y-axis are given in Figure 5.45. Again, there is no azimuthal mode appearing in the transmission spectra. The shape of the reflection spectrum is sensitive to the direction of polarisation of the incident light. The azimuthal mode peak at 870 nm becomes weaker and the dominant mode shifted to 780 nm when the polarisation changes from x to y. In Figure 5.46, the use of a radially polarised beam did not change the transmission spectrum but the resulting reflection spectrum has a similar lineshape to that found using a linearly x-polarised beam.

Stronger evidence of the azimuthal mode excitation appears looking at metasurfaces with $L = 90$ nm and $L = 100$ nm, both with $s = 90$ nm (#A12

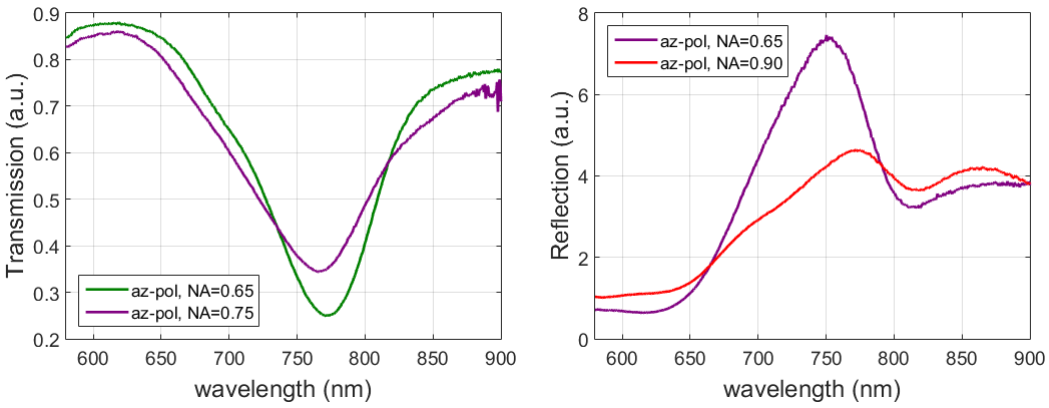

(a) (b)

Figure 5.44: The (a) transmission through and (b) reflection from the azimuthal trimer metasurface with $L = 120$ nm, $w = 40$ nm, $s = 70$ nm, and $p = 400$ nm (#A15) with azimuthally polarised light illumination through the objective lens with different NA.

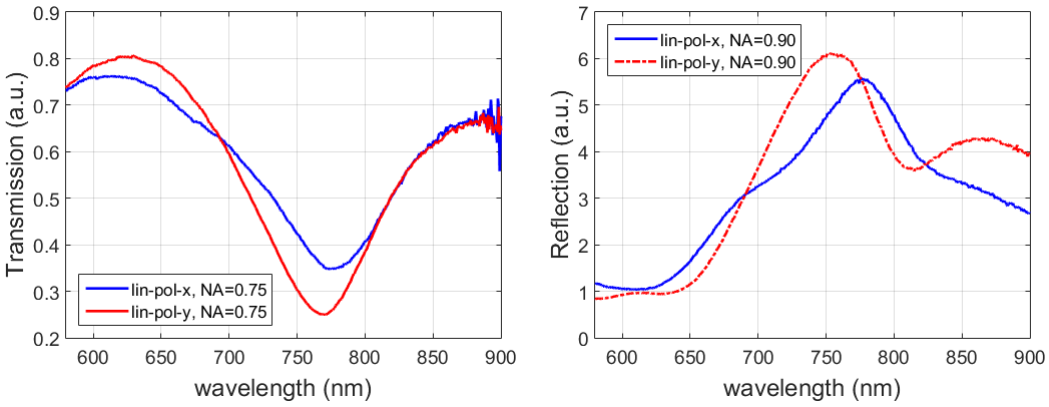

(a) (b)

Figure 5.45: The(a) transmission through and (b) reflection from the azimuthal trimer metasurfaces with $L = 120$ nm, $w = 40$ nm, $s = 70$ nm, and $p = 400$ nm (#A15) with linearly x- and y-polarised light polarised light illumination, using objective lens with NA=0.75 for Fig.(a) and NA=0.90 for Fig.(b).

and #A14). In the spectra shown in Figure 5.47, by using linearly x-polarised illumination, the azimuthal modes appear at 720 nm and 750 nm in metasurface #A12 and #A14 respectively. The azimuthal modes appear weakly in both transmission and reflection. Changing the illumination to an azimuthally polarised beam, however, surprisingly reduces the strength of the azimuthal mode peak, as shown in Figure 5.48. Hence, further and closer investigation of the azimuthal modes are needed to explain this finding. The metasurface

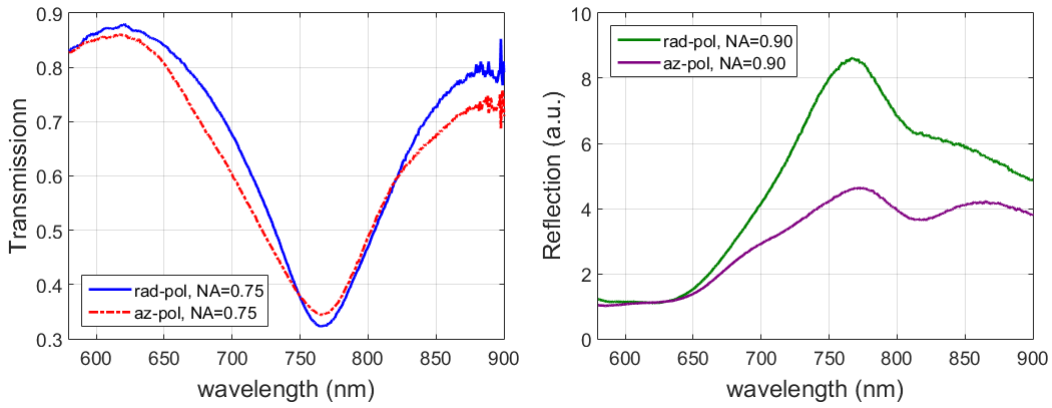

(a) (b)

Figure 5.46: The(a) transmission through and (b) reflection from the azimuthal trimer metasurfaces with $L = 120$ nm, $w = 40$ nm, $s = 70$ nm, and $p = 400$ nm (#A15) with radially and azimuthally light polarised light illumination, using objective lens with NA=0.75 for Fig.(a) and NA=0.90 for Fig.(b).

with $L = 120$ nm did not, however, produce similar result.

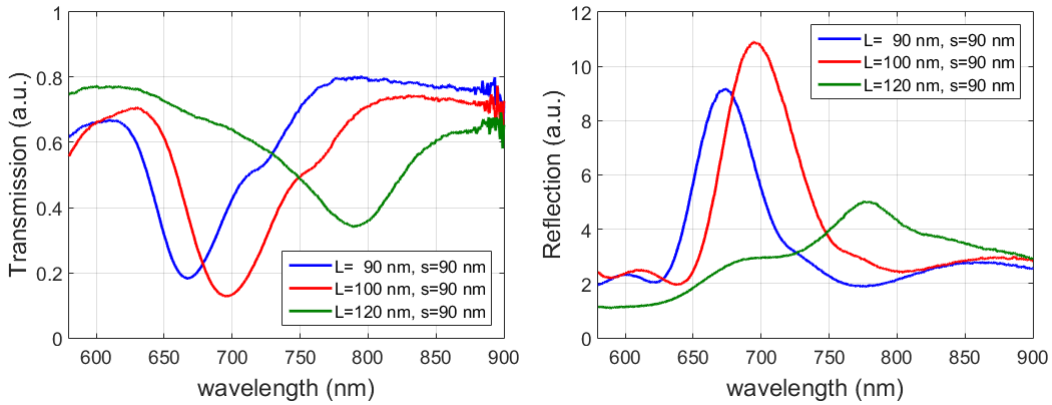

(a) (b)

Figure 5.47: The(a) transmission through and (b) reflection from the azimuthal trimer metasurfaces with code #A12, #A14, and #A16 with linearly x-polarised light polarised light illumination, using objective lens with NA=0.75 for Fig.(a) and NA=0.90 for Fig.(b).

The azimuthal mode resonances for azimuthal trimer metasurfaces were predicted using FDTD simulation when s-polarised light is used. Figure 5.49 shows the transmission and reflection spectra of metasurface #A14 with s-polarised illumination and a plane of incidence parallel to the y-axis calculated by the FDTD method. The angle of incidence is 20°.

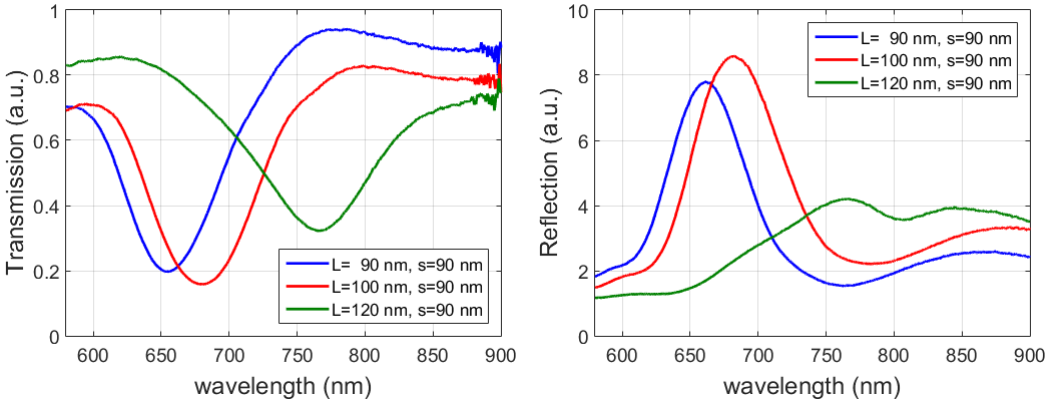

(a) (b)

Figure 5.48: The(a) transmission through and (b) reflection from the azimuthal trimer metasurfaces with code #A12, #A14, and #A16 with azimuthally polarised light polarised light illumination, using objective lens with NA=0.75 for Fig.(a) and NA=0.90 for Fig.(b).

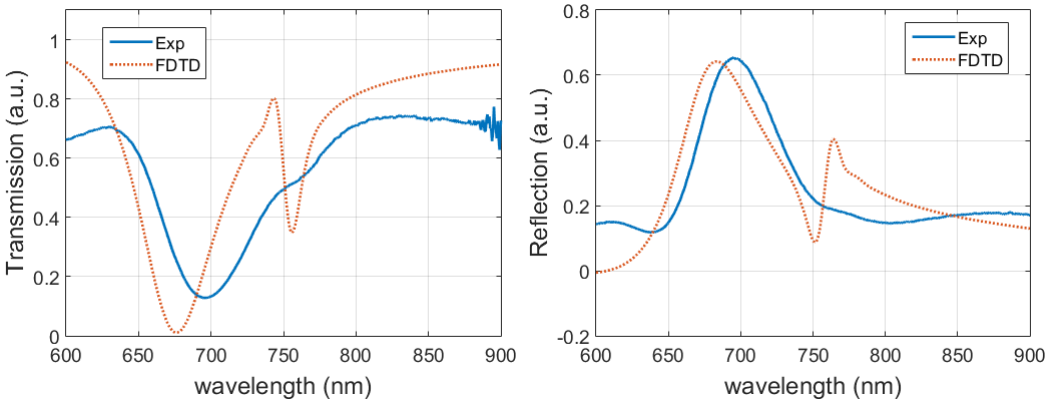

(a) (b)

Figure 5.49: Comparison between experimental results and FDTD simulation for the (a) transmission through and (b) reflection from the azimuthal trimer metasurfaces. The experimental data were taken with NA 0.75 (#O3) and 0.90 (#O5) for the transmission and reflection respectively.

In addition to the FDTD, the EEM can also reproduce the dipole and azimuthal peaks of the resonances from the experiment. For comparison, scattering was assumed to be equivalent to the reflection R. As shown in Figure 5.50, the lineshape calculated using the EEM fits the spectrum calculated from the transmission. The EEM parameters are provided in Table 5.8.

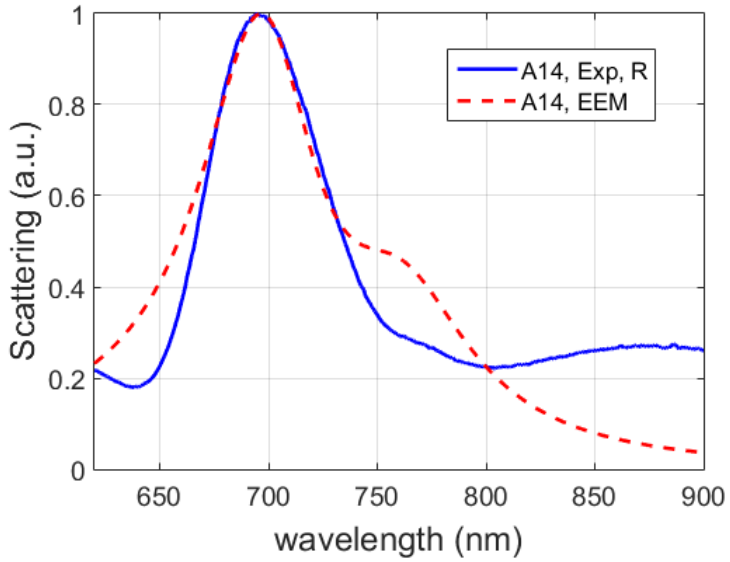

Figure 5.50: Comparison between the experimental data of metasurfaces #A15 with radially polarised illumination and the simulation results with the EEM. The experimental data were taken with NA 0.90 (#O5).

Parameters (Units)	Values
λ_i (nm)	720
A (rad/s)	1×10^{14}
Γ (rad/s)	2.5×10^{14}
G	0.7

Table 5.8: The fitting parameters of the EEM for experimental data of metasurfaces #R13 and #R15, for comparison shown in Figure 5.50.

5.3.4 Azimuthal Tetramer Metasurfaces

The experimental results for azimuthal tetramer metasurfaces are similar to those found in azimuthal trimer metasurfaces. There are no convincing azimuthal mode resonances appearing in the spectra . Only one example is considered here – that with $L = 120$ nm, $w = 40$ nm, $s = 90$ nm, and $p = 400$ nm (#A25). The results for other sizes can be seen in Appendix A.

Figure 5.51 and 5.52 show the transmission and the reflection spectra of this azimuthal tetramer device obtained using linearly and azimuthally polarised illumination. These were obtained using objectives with various NAs. In all measurements, the dipole mode has a resonance centred on 750 nm.

In the transmission spectra, the dominant mode resonance shows a broadened

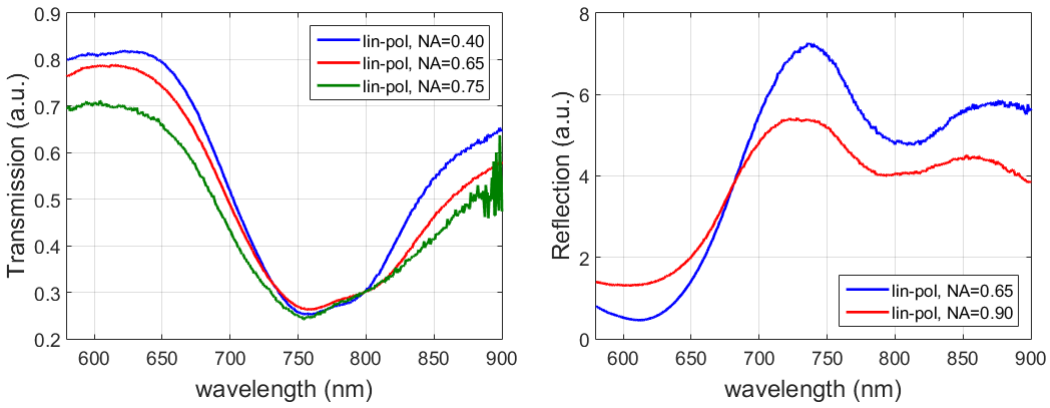

(a) (b)

Figure 5.51: The (a) transmission through and (b) reflection from the azimuthal tetramer metasurface with $L = 120$ nm, $w = 40$ nm, $s = 90$ nm, and $p = 400$ nm (#A25) with linearly polarised light illumination through the objective lens with different NA.

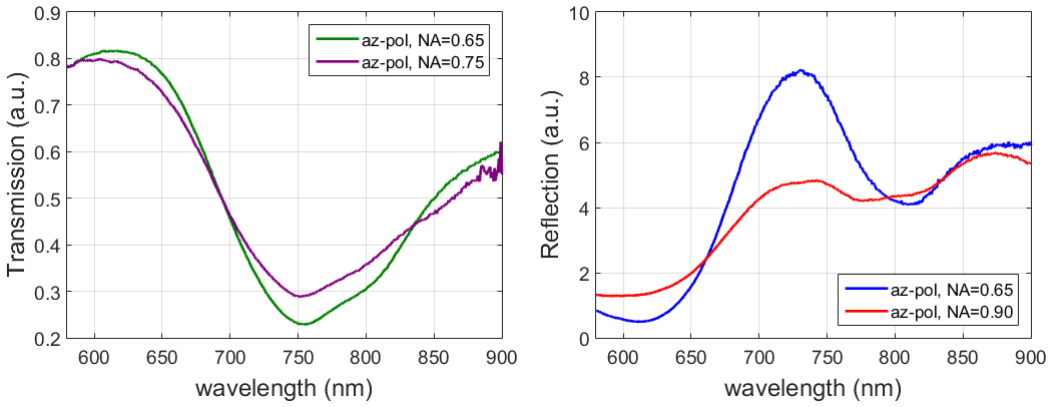

(a) (b)

Figure 5.52: The (a) transmission through and (b) reflection from the azimuthal tetramer metasurface with $L = 120$ nm, $w = 40$ nm, $s = 90$ nm, and $p = 400$ nm (#A25) with azimuthally polarised light illumination through the objective lens with different NA.

spectrum which is a result of mode interference between the dipole and azimuthal modes. This is similar to the observation of the breathing mode of the radial tetramer metasurface which does not appear clearly in the transmission spectra but influences the width of the dipole mode resonance. In the reflection spectra, however, there is another peak at 870 nm which suggests the excitation of azimuthal modes.

Figure 5.53 show the comparison between the experimental data of metasur-

face #A25 and simulation results obtained using the FDTD. No quadrupole mode[5] is observed. Note that the spectral location of the resonances from the simulation agree with the experimental data.

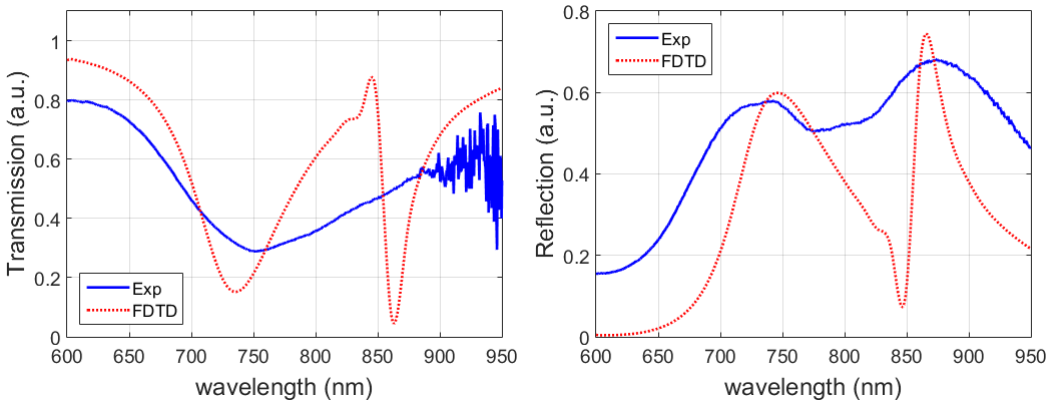

(a) (b)

Figure 5.53: The (a) transmission through and (b) reflection from the metasurface #R25 from the experiment compared with the FDTD simulation. The experimental data were taken with NA 0.75 (#O3) and 0.90 (#O5) for the transmission and reflection respectively.

The EEM was also used for simulating spectra from #A25, shown in Figure 5.54. The first calculation, labelled 'EEM (1)' does not produce other peaks other than the dominant resonance at 750 nm. Further analysis, labelled 'EEM (2)' was performed with a decreased value of Γ. This shows that a quadrupole mode is excited at 720 nm and an azimuthal mode at 880 nm but both are weak. The strength of azimuthal mode is significantly weaker when calculated using the EEM compared to that with the FDTD method.

Parameters (Units)	Values	
	EEM(1)	EEM(2)
λ_i (nm)	780	780
A (rad/s)	1×10^{14}	1×10^{14}
Γ (rad/s)	3.6×10^{14}	1×10^{14}
G_A	1.2	1.2
G_B	0.5	0.5

Table 5.9: Best fit parameters for the EEM for experimental data of metasurface #A25, for comparison shown in Figure 5.54.

[5]If present, the quadruple mode is expected to have a resonance at a shorter wavelength than the dipole mode.

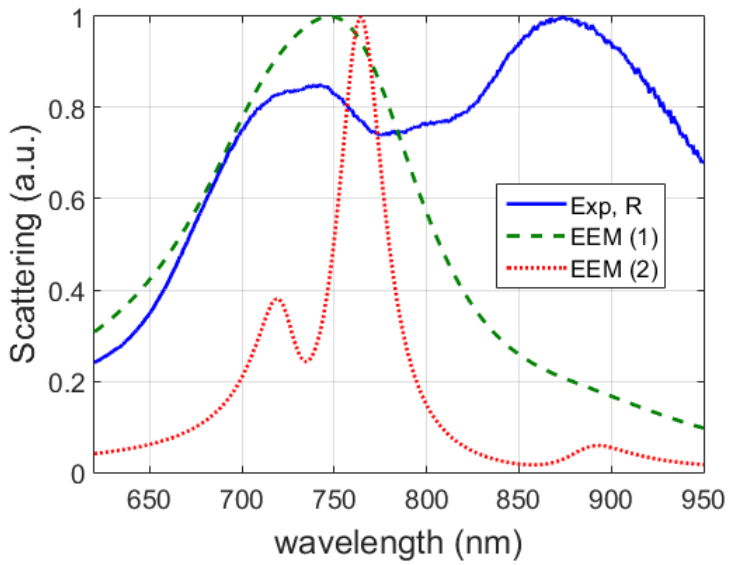

Figure 5.54: Comparison between the experimental data of metasurface #A25 with azimuthally polarised illumination and the simulation results with the EEM. The experimental data were taken with NA 0.90 (#O5).

Metasurfaces consisting of azimuthal tetramers with other sizes do not provide convincing results either. The peaks in the reflection spectra are present but the dominant modes in transmission do not show any indication of another resonance and those dominant modes are not broadened as in metasurface #A25 discussed previously. This suggests that further optimisation of geometric parameters are needed to see evidence of azimuthal mode excitation. This could be the subject of future work.

The spectra of other metasurfaces with different nanorod lengths L are summarised in Figure 5.55 for azimuthally polarised light illumination. For smaller values of L, the dipole modes are blue-shifted as expected. The dipole resonances are at 660 nm, 700 nm for devices #A21 and #A23 respectively and the peaks for azimuthal modes appear in the reflection spectra at both ∼850 nm.

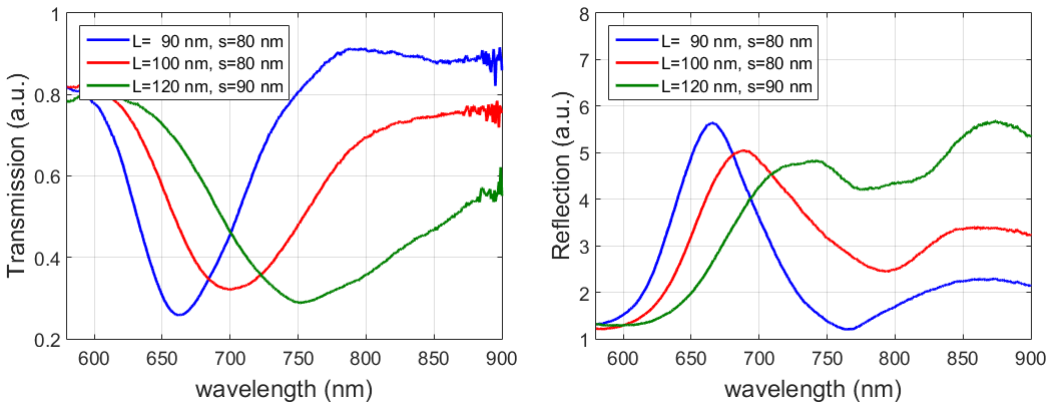

(a) (b)

Figure 5.55: The (a) transmission through and (b) reflection from the azimuthal tetramer metasurfaces with various L (#A21,#A23,#A25) with azimuthally polarised light illumination, using objective lens with NA=0.75 for Fig.(a) and NA=0.90 for Fig.(b).

5.4 Fourier Plane (Far-Field) Images of Reflected Beams at Resonances

The excitation of radial modes was studied using focussed light and modes have been identified in the transmission and reflection spectra. An objective lens with a high numerical aperture (NA) was needed to observe this excitation. If the lens has an NA of 0.90, both radially and linearly polarised light were capable of exciting radial modes. However, if the lens has an NA of only 0.65, radially polarised light is needed to ensure that radial mode excitation was strong enough to be observed using this approach.

On the other hand, azimuthal modes were more difficult to observe. The evidence that azimuthal modes were excited is not as strong as that for radial modes. The existence of features in the reflection and transmission spectra at frequencies predicted by modelling provides evidence for the excitation of subradiant modes. More compelling evidence, however, should be seen in the far-field of the scattered beams as discussed in Section 4.3.3. The far-field intensity (Fourier plane images) of reflected beams at the resonance wavelengths of radial and dipole modes is discussed in this section.

Recall the angular spectrum distribution of polarisation of a focussed light

beam shown in Figure 3.11. If the input light is linearly polarised, spatial frequencies along the polarisation axis are predominantly p-polarised. Recall also that radial modes are excited by p-polarised, rather than s-polarised light, so if the wavelength is tuned to the resonance of a radial mode and the reflected or transmitted beam is imaged in the Fourier plane, there will be an asymmetry in the intensity distribution. Spatial frequencies corresponding to p-polarised light will have a higher intensity. Furthermore, low spatial frequencies, corresponding to near-normal incidence illumination, will not strongly excite radial modes. Hence, the Fourier plane image would be expected to have a minimum in the centre in contrast to the dipole mode.

The EEM can be used to predict Fourier plane image patterns of scattered beams[6]. For example, if the radial trimer with resonance wavelength $\lambda_p = 700$ nm, $G = -3$, $\Gamma = 2 \times 10^{14}$ s^{-1} and $s = 70$ nm is illuminated at a wavelength of 570 nm (corresponding to the radial mode resonance) with linearly x-polarised light, we would expect to see a Fourier plane image pattern of the form shown in Figure 5.56a. If, on the other hand, the illumination is at 785 nm, corresponding to the dipole mode resonance, we would see an image similar to Figure 5.56b.

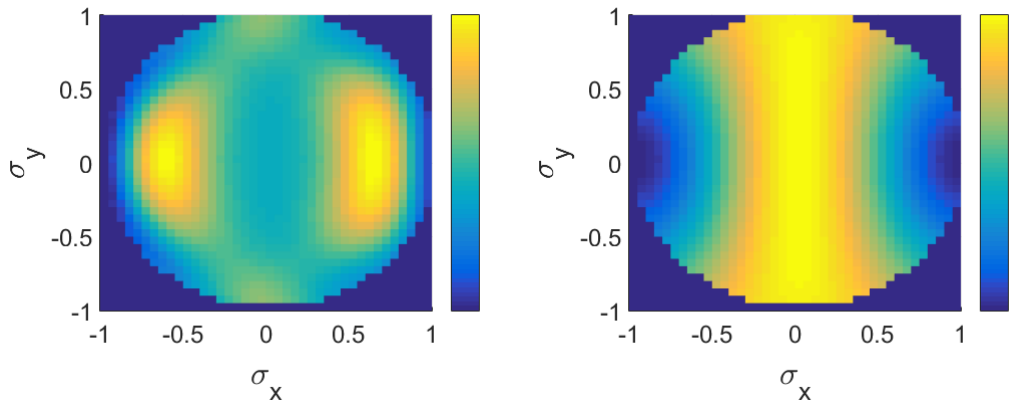

Figure 5.56: The scattered light intensity from radial trimer antennas at (a) radial and (b) dipole mode, under illumination of focussed light with linearly x-polarisation, where $\sigma_x = k_x/k_0$ and $\sigma_y = k_y/k_0$ are x- and y-components unit spatial frequencies.

[6]Recall that the EEM is an approximate method and the wavelengths mentioned here do not represent the actual measured resonance wavelengths. The key properties of intensity profiles however can be seen more clearly using these parameters.

If a focussed radially polarised beam is used, the beam is purely p-polarised. This leads to a higher intensity at larger angle of incidence symmetric about the origin on k-space. Hence, by examining the Fourier plane images at specific wavelenghts, we can obtain further information about the nature of the antenna resonance. The EEM modelling result for radially polarised beam illumination is shown in Figure 5.57.

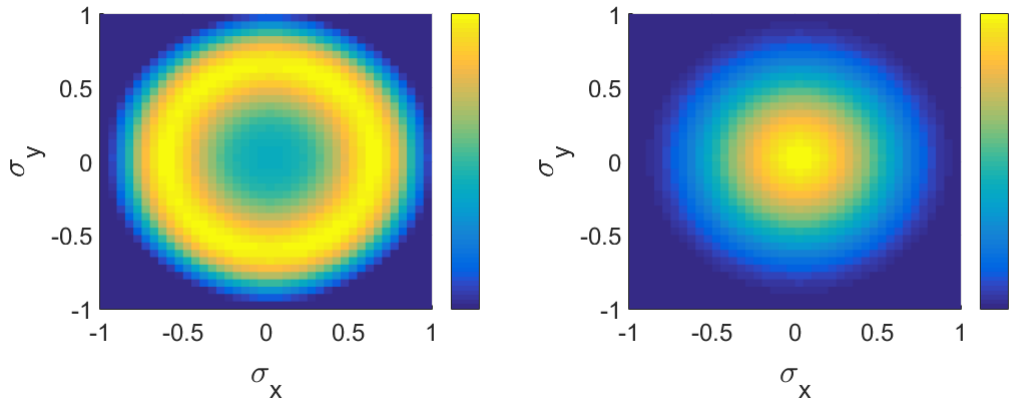

Figure 5.57: The reflected light intensity from radial trimer antennas at (a) radial and (b) dipole mode, under illumination of focussed light with radial polarisation, where $\sigma_x = k_x/k_0$ and $\sigma_y = k_y/k_0$ are x- and y-components unit spatial frequencies.

In the experiment presented here, a focussed beam illuminates the metasurfaces consisting arrays of nanoantennas. To analyse the far-field (Fourier plane) intensity pattern, the focussed beam can be viewed as a superposition of plane waves with various propagation vectors and polarisations. A single antenna in a unit cell interacts with an incident plane wave at a particular propagation vector k_x and k_y and with a defined polarisation. If the reflected beam is imaged at a radial mode resonance, spatial frequencies with dominant p-polarised light will have a higher intensity compared to spatial frequencies with dominant s-polarised as they scatter more light. On the other hand, the transmitted light will have lower intensity at these spatial frequencies.

The set-up of Figure 5.58 was used to obtain the Fourier plane images of reflected beam at the radial and dipole resonances. The differences between this and the set-up of Figure 5.4 are the removal of the second beam-splitter (which divides the beam between the camera and the spectrometer) and changing the light source to a spectrally filtered broadband laser. The beam splitter was

removed to produce undisturbed images at the camera. Before the camera, a lens, referred as Bertrand lens, was placed to convert real-space image to Fourier plane images. If a spectral measurement was needed (to find, for example, the sample distance from the objective where the signal is maximised), a mirror is added to the path to reflect the beam into the spectrometer and was removed afterwards. The light source was a supercontinuum laser source (listed in Table 5.4) that can be filtered with a tunable monochromator to select only a narrow bandwidth of wavelengths from 5 nm to more than 100 nm over a range below 400 nm to greater than 850 nm.

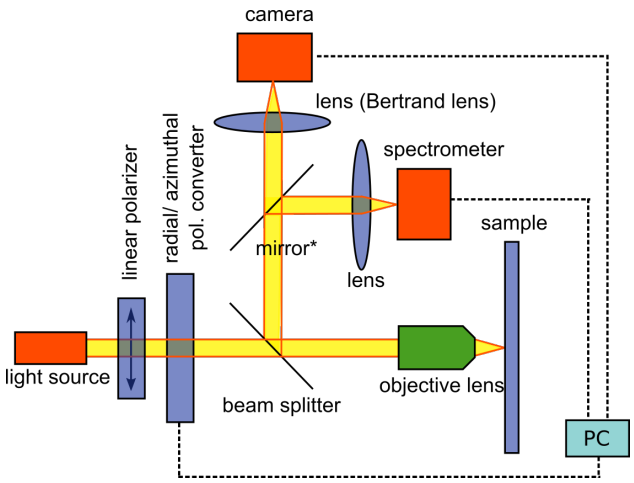

Figure 5.58: The experimental set-up for imaging the Fourier-plane reflected beams from the metasurfaces. *Mirror was only placed when needed.

The filter was set to produce an incident spectrum with 10 nm bandwidth. A few examples of the measured filtered laser spectrum are shown in Figure 5.59 for various central wavelengths, from 550 nm to 820 nm. A high-NA objective lens was used, with NA 0.90 (#O5). The input light is linearly polarised, along either the x- or y-axis. The x-axis is aligned to one of the nanorods in the radial trimer antenna metasurfaces. In the images, the x-axis is the horizontal axis.

In the data shown in this section, the Fourier plane image of the beam reflected from the sample was obtained, as well as the reflection from the glass substrate (where there is no structure). The illumination was performed from the PMMA side (top side) of the sample. The glass reflection was taken on the area next to the structures, maintaining all the measurement conditions, including the

distance between the sample and the objective lens. The normalised reflected beam was obtained by dividing the raw reflected beam from the metasurface by the reflected beam from the glass. This is consistent with the data of reflection spectra in previous section which were normalised by the reflection of the beam from the glass substrate and highlights the role played by the metasurface.

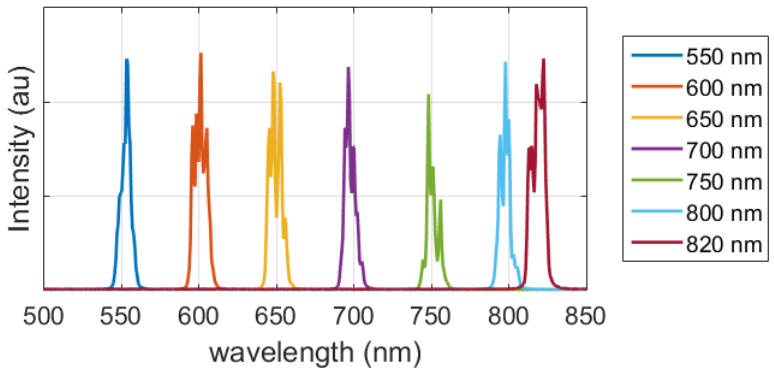

Figure 5.59: The spectrum of the laser, filtered with monochromator, centred at various wavelengths. The spectrum bandwidths were all 10 nm.

Key properties of the Fourier-plane beams reflected from the metasurfaces consisting of radial antennas are discussed here for metasurface #R13, #R18, and #R25. More Fourier plane images data characterised in this project are provided in Appendix B.

Figures 5.60 and 5.61 show the Fourier-plane intensity of the beam reflected from the metasurface of radial trimers with $L = 100$ nm, $w = 40$ nm, and $s = 70$ nm (#R13), with both x- and y-linearly polarised input. Figure (a) is an unnormalised reflected beam from the metasurface and Figure (b) is the reference beam reflected from the glass substrate. The reflected beam in Figure (a) is then normalised by dividing it by Figure (b) to obtain a normalised reflected beam in Figure (c). The x- and y-axis of the images correspond to the normalised spatial frequencies $\sigma_x = k_x/k_0$ and $\sigma_y = k_y/k_0$. All data discussed in this section were measured using an objective lens with NA=0.90 (#O5).

The radial mode resonance of this metasurface occurs at 620 nm, as shown previously in Figures 5.11 and 5.18. It is apparent that there are anomalies in these Fourier plane images. In both Figures 5.60a and 5.61a, there is a ring-shaped darker area on the image around the centre of the origin. This

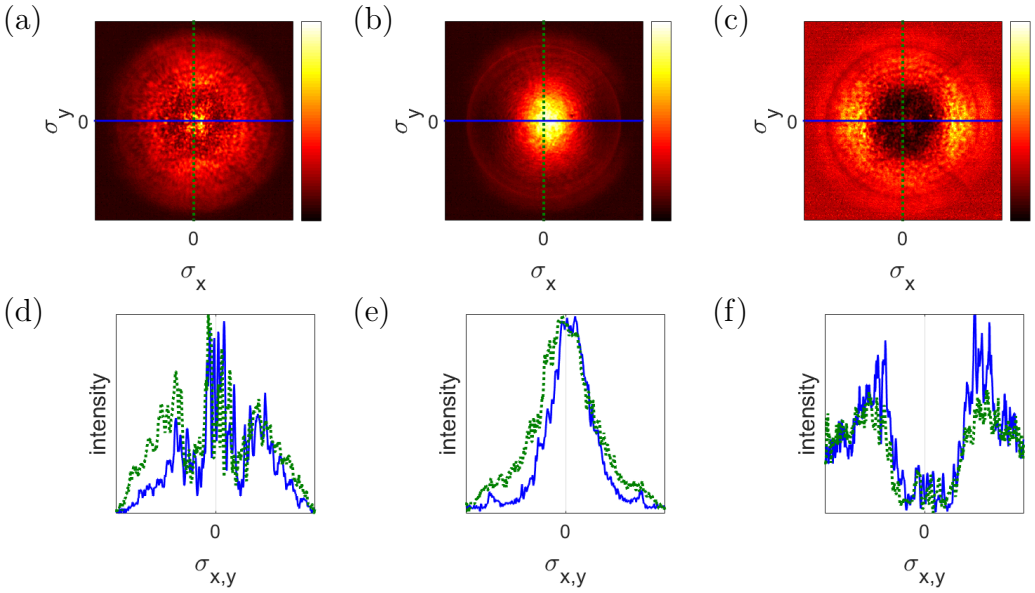

Figure 5.60: The Fourier plane images of (a) unnormalised, (b) reference, and (c) normalised beams, reflected from metasurface **#R13** with **linearly** x**-polarised** illumination, at **radial mode** resonance (620 nm), and (d,e,f) the intensity along the blue-solid and green-dotted lines in Fig. (a,b,c) respectively.

suggests low reflection at near-normal incidence.

In Figures 5.60c and 5.61c, two things are apparent. Firstly, there is a minimum at the centre of the normalised image consistent with near-normal incidence waves not exciting the radial mode and, hence, not being strongly reflected. Secondly, two bright lobes appear along the σ_x-axis at larger spatial frequencies. Again, this is consistent with expectations and the EEM results shown in Figure 5.56. In Figure 5.61, the polarisation was rotated by 90° so that the bright lobes were also rotated since the direction of p-polarisation was rotated.

The images are accompanied by plots of the intensity through the centre of the beam, along lines parallel to the σ_x- and σ_y-axis. These are plotted below their respective Fourier plane images in Figures 5.60 and 5.61 (Figures d, e, and f). The blue-solid line corresponds to the slice along $\sigma_y = 0$ and the green-dotted line to the slice along $\sigma_x = 0$.

It is interesting to see that the beam reflected from the unpatterned glass is asymmetric. The beam is not circular but is rather narrower along a direction perpendicular to the polarisation axis. A simple explanation for this

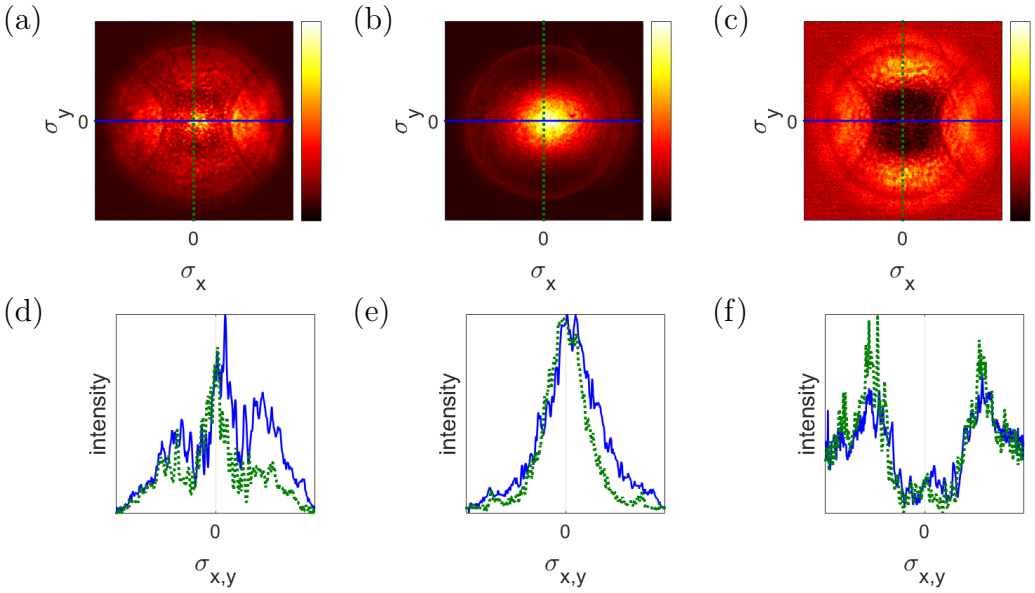

Figure 5.61: The Fourier plane images of (a) unnormalised, (b) reference, and (c) normalised beams, reflected from metasurface **#R13** with **linearly y-polarised** illumination, at **radial mode** resonance (620 nm), and (d,e,f) the intensity along the blue-solid and green-dotted lines in Fig. (a,b,c) respectively.

phenomenon can be understood by looking at the reflection coefficients for p- and s-polarised plane waves, calculated using the Fresnel equations, as shown in Figure 5.62 [107]. The waves propagate in the air ($n = 1$) and are reflected from a glass surface ($n = 1.5$). For each polarisation, the reflection approaches the same values at 0° and 90° angles of incidence and they have similar values for small angles, $\theta < 10°$. At other angles, the s-polarised plane wave has a higher reflectance compared the the p-polarised plane wave. Relating this to the focussed beam, the s-polarised components have a higher reflectance compared to the p-polarised components. In Figure 5.60b, the area near σ_x-axis corresponding to the dominant p-polarised components, which a slightly lower reflectance compared to the area near the σ_y-axis, corresponding to the dominant s-polarised components. The beam profile is rotated by 90° in Figure 5.61b. There are also thin dark lines appearing in the images due to Wood anomalies arising from diffraction which is not included in the EEM.

The wavelength was then changed to the dipole mode resonance centred on a wavelength of 750 nm. Figure 5.63 and 5.64 show the reflected beam at the dipole resonance for both linear polarisation inputs. At near-normal angles, the dipole mode is excited more strongly and the result is that the far-field has

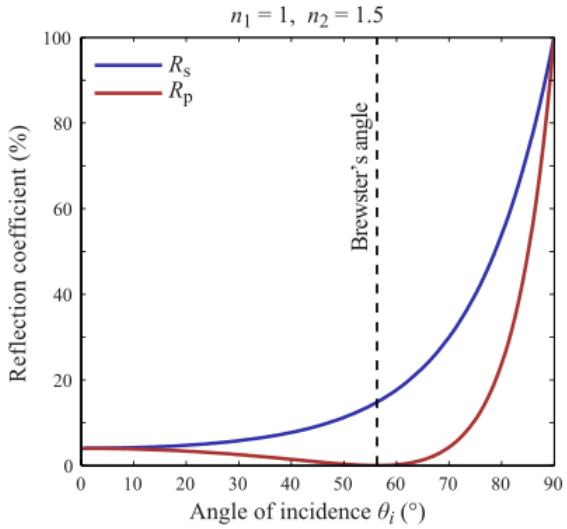

Figure 5.62: The reflection coefficient of the plane waves with p-polarised (R_p) and s-polarised (R_s) plane waves propagating in the air ($n_1 = 1$) and being reflected by an interface of the glass ($n = 1.5$) surface, calculated with Fresnel equations [108].

a maximum at the centre of the beam. This is in contrast to the behaviour seen with the radial mode.

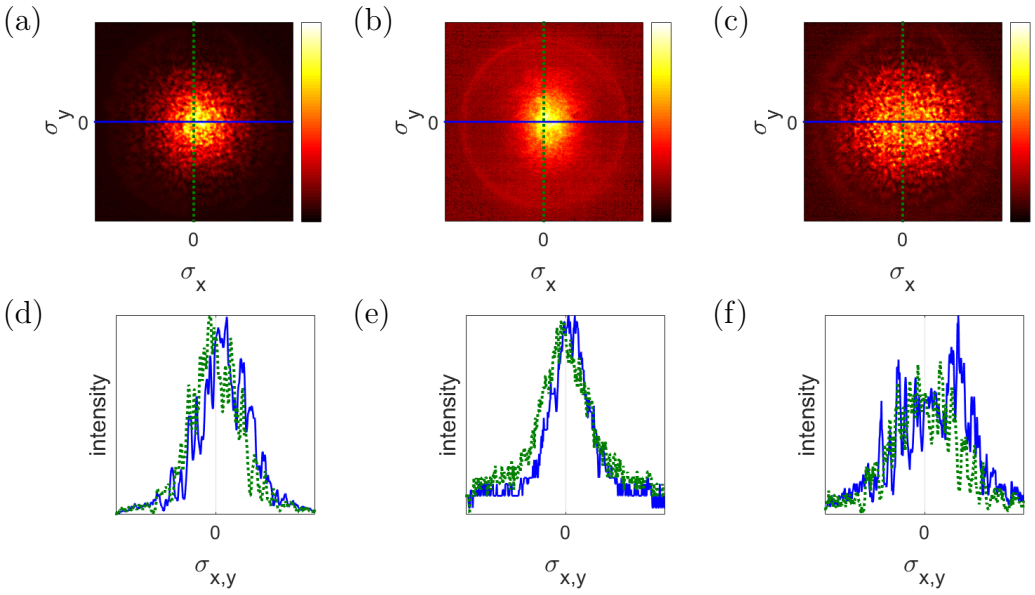

Figure 5.63: The Fourier plane images of (a) unnormalised, (b) reference, and (c) normalised beams, reflected from metasurface **#R13** with **linearly** x**-polarised** illumination, at **dipole mode** resonance (750 nm), and (d,e,f) the intensity along the blue-solid and green-dotted lines in Fig. (a,b,c) respectively.

Further investigation was performed by changing the illumination to a ra-

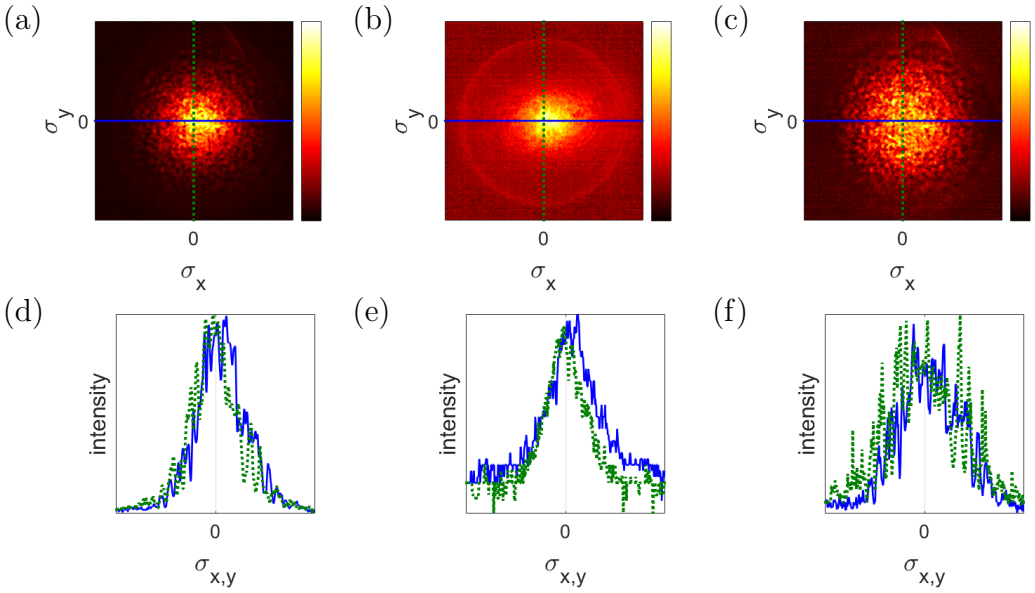

Figure 5.64: The Fourier plane images of (a) unnormalised, (b) reference, and (c) normalised beams, reflected from metasurface **#R13** with **linearly** y**-polarised** illumination, at **dipole mode** resonance (750 nm), and (d,e,f) the intensity along the blue-solid and green-dotted lines in Fig. (a,b,c) respectively.

dially polarised beam. With this polarisation, incident field is composed of p-polarised components across the beam. Figure 5.65 shows the Fourier-plane images of reflected beam from the metasurface #R13 with a radially polarised illumination at its radial resonance, $\lambda = 620$ nm.

Since illumination with radially polarised light was used, the beam profile is symmetric, producing a circular shape, unlike the case with linearly polarised illumination. In the reflected beam (Figure (a)), a lower intensity region is observed in the form of a circle. At the centre, the intensity is slightly lower and the plot of the intensity along lines through the centre of the beam can be seen in the plot below it (Figure (d)). This suggests that the near-normal incidence components were not strongly reflected. This is a property of the radial mode where higher spatial frequencies excite the radial mode more strongly.

The observation of the effect can be seen more clearly with normalisation where the near normal incidence component is reflected with a lower intensity compared to components with higher angles of incidence. The overall effect is a the doughnut-shaped beam. This result is consistent with those found with linearly polarised illumination.

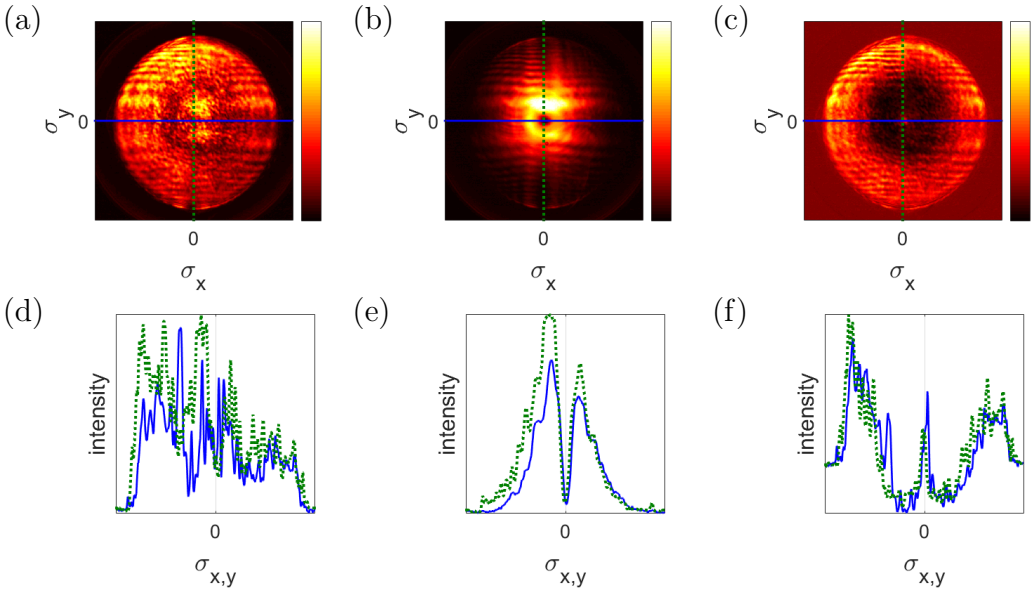

Figure 5.65: The Fourier plane images of (a) unnormalised, (b) reference, and (c) normalised beams, reflected from metasurface **#R13** with **radially polarised** illumination, at **radial mode** resonance (620 nm), and (d,e,f) the intensity along the blue-solid and green-dotted lines in Fig. (a,b,c) respectively.

Figure 5.66 shows the same measurement for metasurface #R13 but where the wavelength was changed to the resonance of the dipole mode (λ = 750 nm). The dipole mode, as discussed earlier, is excited with normal incidence components. The reflected beam at this wavelength is almost flat since the dipole mode is relatively insensitive to angles of incidence.

To see changes in the beam profile from the radial mode to the dipole mode resonances, the wavelength of the incident light is changed gradually from 600 nm to 750 nm. The results are shown in Figure 5.67 for illumination with radially polarised light. The figures shown are the normalised beams. The complete results including the unnormalised beams and the intensity profiles across the blue and green lines are provided in Appendix B.

At 600 nm, the metasurface is slightly off-resonance and the lower intensity region on the reflected beam becomes larger. At 650 nm, the metasurface is also slightly off-resonance but the wavelength is closer to the dipole mode resonance. At this wavelength, the tail of the dipole mode starts to disturb the beam profile produced by the radial mode resonance and the intensity at the centre of the beam becomes higher. As the wavelength increases, the lower intensity region at the centre of the beam disappears. The dipole mode

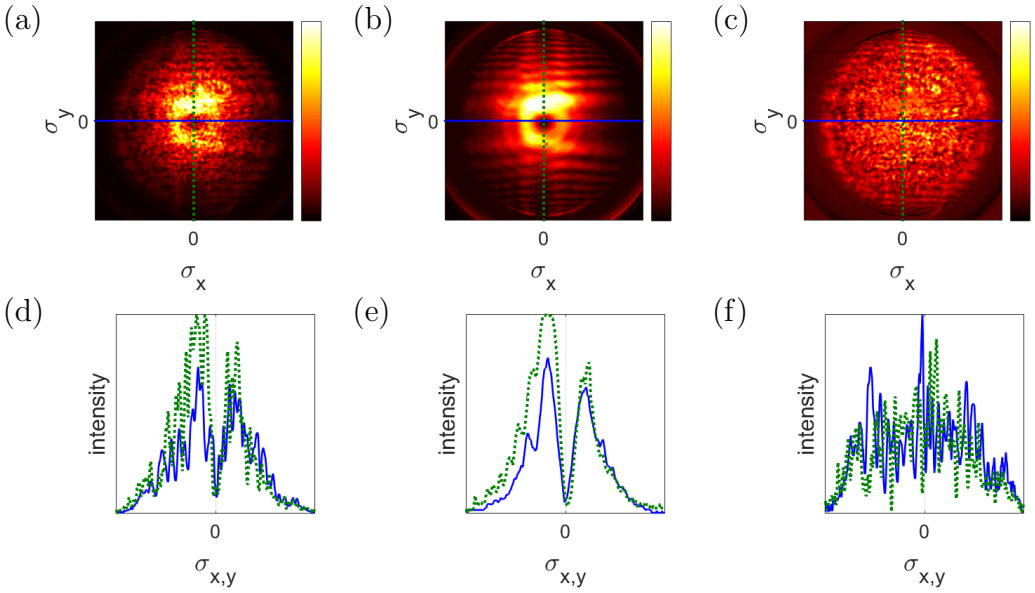

Figure 5.66: The Fourier plane images of (a) unnormalised, (b) reference, and (c) normalised beams, reflected from metasurface **#R13** with **radially polarised** illumination, at **dipole mode** resonance (750 nm), and (d,e,f) the intensity along the blue-solid and green-dotted lines in Fig. (a,b,c) respectively.

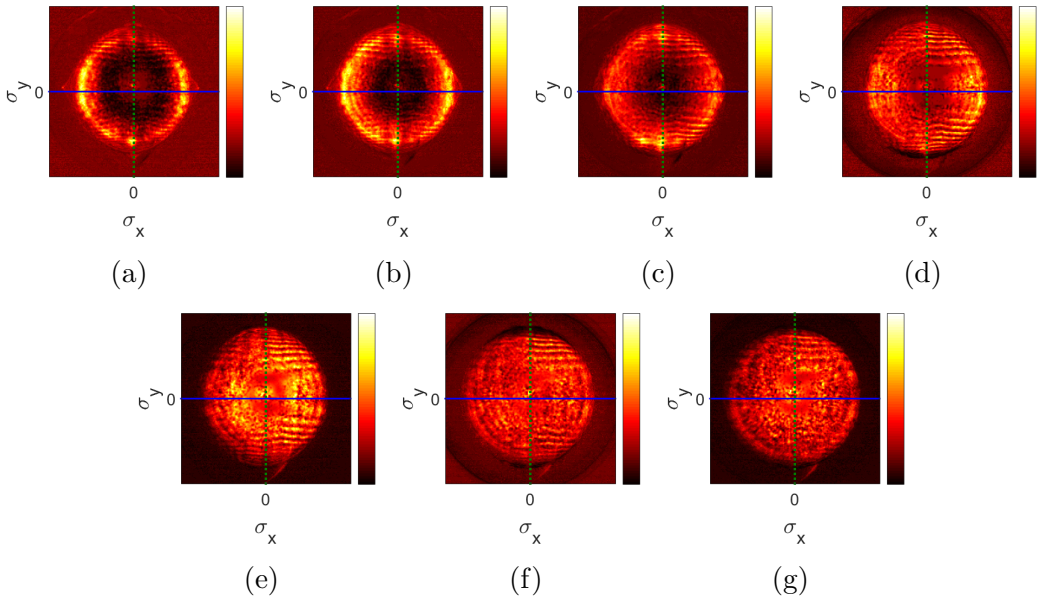

Figure 5.67: The normalised reflected beams from metasurface #R13 with radially polarised beam illumination at various wavelengths, (a) 600 nm, (b) 620 nm, (c) 650 nm, (d) 675 nm, (e) 700 nm, (f) 725 nm, and (g) 750 nm.

dominates the radial mode and the beam becomes brighter at the centre.

Similar measurements with linearly x-polarised light were also performed. The

results are also consistent to those obtained with a radially polarised beam, but with spatial frequencies along the σ_x-axis having a higher intensity than along the σ_y axis. At 600 nm, the bright lobes are pushed to higher spatial frequencies, corresponding to a large angle of incidence. At 650 nm, the interference from the dipole mode starts to change the beam profile, with the intensity at the centre of the beam increasing as the wavelength increases.

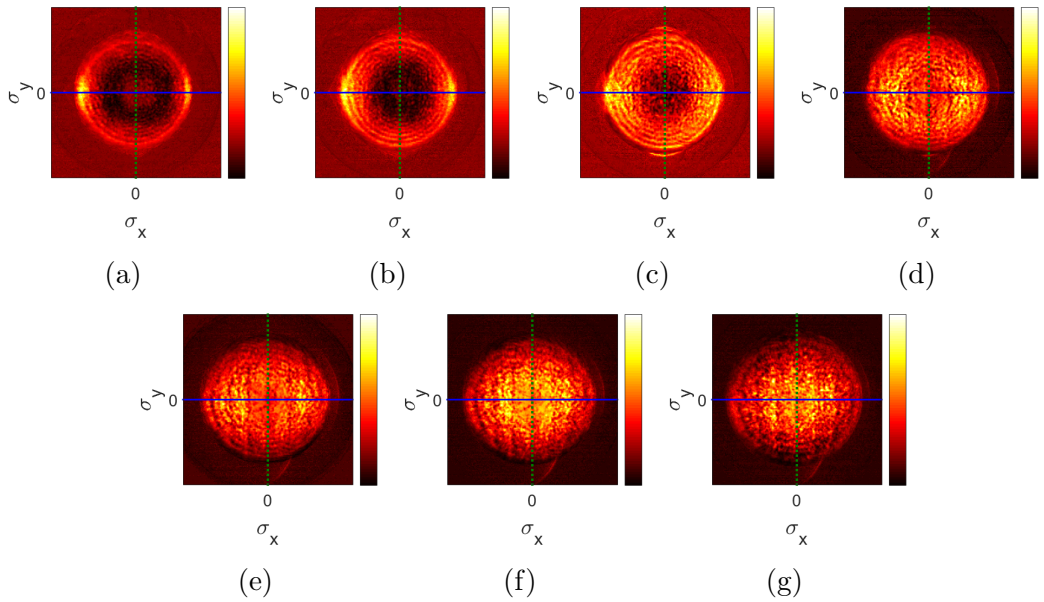

Figure 5.68: The normalised reflected beams from metasurface #R13 with linearly x-polarised beam illumination at various wavelengths, (a) 600 nm, (b) 620 nm, (c) 650 nm, (d) 675 nm, (e) 700 nm, (f) 725 nm, and (g) 750 nm.

The same measurements were undertaken for another metasurface consisting of radial trimer antennas with different sizes. Figure 5.69 shows the (normalised) far-field reflected beams from the metasurface #R18 at the radial mode resonance ($\lambda = 650$ nm). This metasurface has nominal nanorod widths $w = 30$ nm, lengths $L = 100$ nm, and off-set distances $s = 70$ nm. In this case, the periodicity is decreased to 250×300 nm to prevent the appearance of diffraction lines. The illumination is either radially (Fig. a) or linearly (Fig. b and c) polarised light. As expected, radially polarised illumination produces a doughnut-shaped profile as p-polarisation components are dominant throughout the beam. Linearly polarised light produces two bright lobes along the axis parallel to its polarisation, e.g x-polarisation produces two lobes along the σ_x axis of the image.

The images of the normalised reflected beams from metasurface #R18 at the

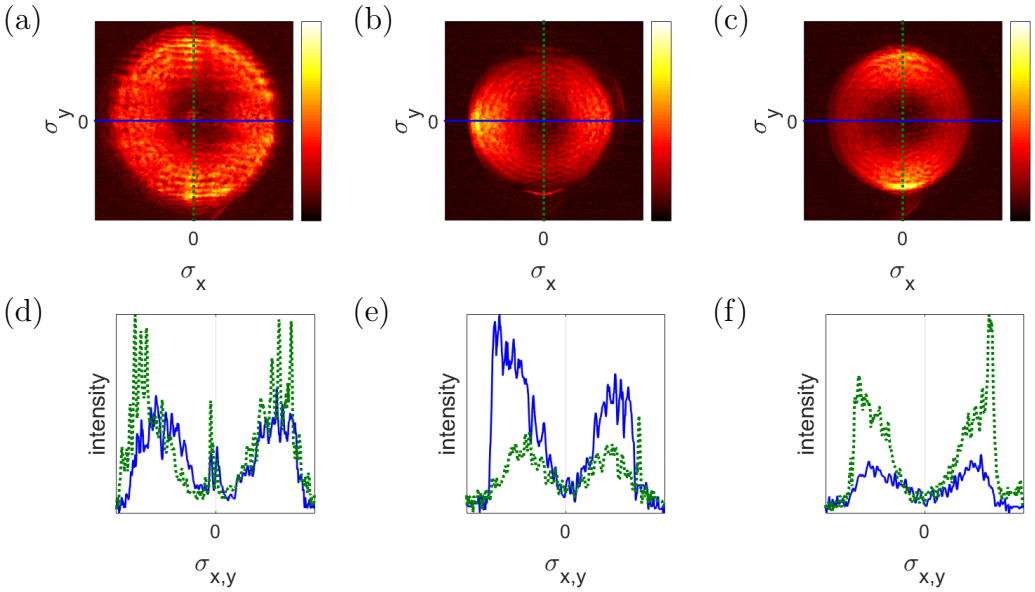

Figure 5.69: The Fourier plane images of normalised beams reflected from metasurface **#R18** with (a) radially, (b) linearly x-, and (c) linearly y-polarised illumination, at **radial mode** resonance (650 nm), and (d,e,f) the intensity along the blue-solid and green-dotted lines in Fig. (a,b,c) respectively.

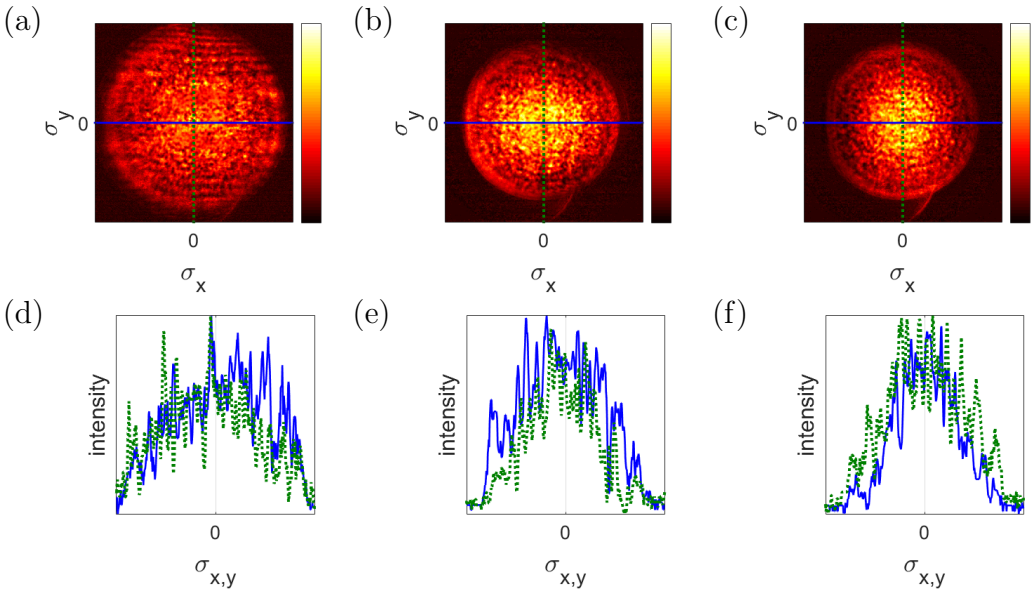

Figure 5.70: The Fourier plane images of normalised beams reflected from metasurface **#R18** with (a) radially, (b) linearly x-, and (c) linearly y-polarised illumination, at **dipole mode** resonance (750 nm), and (d,e,f) the intensity along the blue-solid and green-dotted lines in Fig. (a,b,c) respectively.

dipole mode resonance ($\lambda = 750$) are shown in Figure 5.70. All polarisations produced a bright intensity at near-normal angles of incidence components of

the beam.

Another design supporting radial modes is the metasurface consisting of radial tetramer antennas. The spectra are however more complex due to the presence of the breathing modes. These modes, however, do not affect the excitation of the radial modes because they are located in the infrared region of the spectrum. The reflected beams produce profiles through the intensity distribution consistent with metasurfaces of radial trimers. The normalised far-field beams reflected from the radial tetramer metasurface #R25 with various polarisations are shown in Figures 5.71 and 5.72 for illumination at its radial and dipole mode resonances respectively. In these Fourier plane images, the diffractive lines due to Wood anomalies become more solid and noticeable as the periodicity of the structure is significantly larger (400 nm) compared to those previously discussed (300 nm).

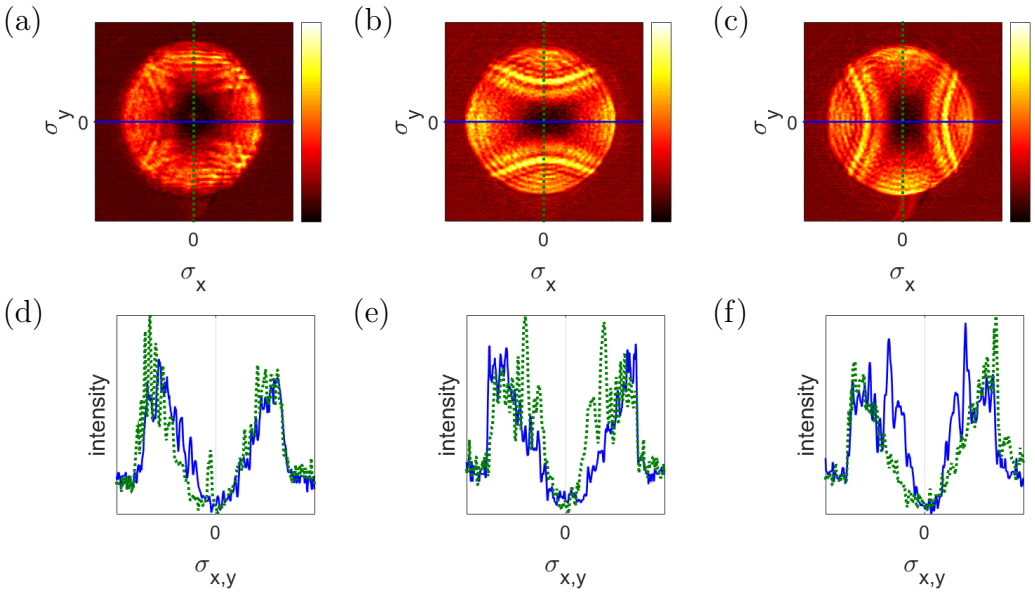

Figure 5.71: The Fourier plane images of normalised beams reflected from metasurface **#R25** with (a) radially, (b) linearly x-, and (c) linearly y-polarised illumination, at **radial mode** resonance (675 nm), and (d,e,f) the intensity along the blue-solid and green-dotted lines in Fig. (a,b,c) respectively.

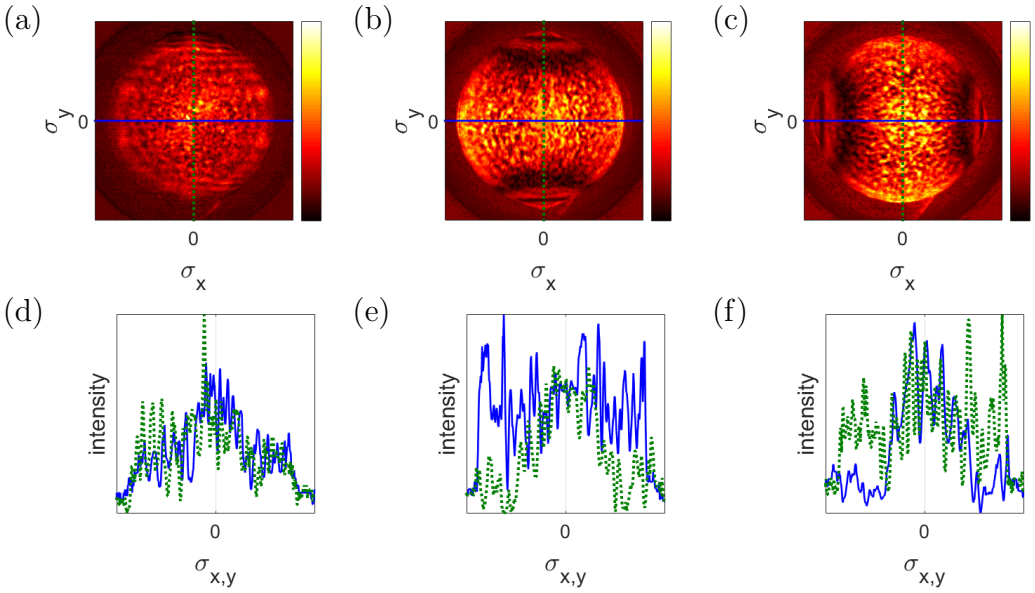

Figure 5.72: The Fourier plane images of normalised beams reflected from metasurface **#R25** with (a) radially, (b) linearly x-, and (c) linearly y-polarised illumination, at 820 nm (near **dipole mode** resonance), and (d,e,f) the intensity along the blue-solid and green-dotted lines in Fig. (a,b,c) respectively.

5.5 Chapter Conclusion

This chapter describes the key experimental findings of this thesis. Devices were fabricated using electron beam lithography based on design principles discussed in Chapter 4. The devices were characterised using a reconfigurable optical set-up that could determine the reflection and transmission spectra for illumination with linearly, radially and azimuthally polarised light. Furthermore, it could be adapted to image the far-field (Fourier) plane of the reflected beam over a narrow spectral bandwidth centred on wavelengths associated with different resonances of the antenna elements.

It was found that the reflection and transmission spectra exhibited features that could be associated with either radiant or sub-radiant modes. It was shown that the strength of the sub-radiant mode excitation depended on the numerical aperture of the microscope used to illuminate the metasurfaces. It was inferred that the presence of large angle components in the incident field led to more efficient excitation of the dark modes. Radial modes could also be observed when metasurfaces were illuminated with radially polarised light, but not with azimuthally polarised light. Furthermore, the use of this vector

beam partly suppressed excitation of the dipole mode, making the radial mode more visible.

Azimuthal modes, on the other hand, are more difficult to excite in a metasurface with the set-ups described here and geometries considered. The azimuthal modes are significantly weaker than the dipole modes so that the spectra produced in the simulations are less likely to be reproduced in experiment. The azimuthal modes tend to produce identifiable peaks in the reflection spectra but only appeared to broaden the resonance in the transmission spectra.

To further test the attribution of spectral features to dark and dipole mode excitation, Fourier plane (far-field) images of the reflected beams were found. At wavelengths where radial mode excitation was hypothesised, a normalised far-field pattern with a low intensity at the centre and bright lobes at large values of the component of the spatial frequency parallel to the direction of the incident electric field were observed for linearly polarised excitations. At wavelengths corresponding to bright mode excitation, on the other hand, the far-field images appeared quite different. These results are consistent with simulations performed using the electrostatic eigenmode method (EEM).

Chapter 6

Conclusion

Charge oscillations on the metallic antennas making up a metasurface support a variety of modes. Some of them are bright, or radiant modes, and the others are dark, or sub-radiant modes. While the radiant modes are relatively easy to couple to propagating electromagnetic fields, the sub-radiant modes are more complex to excite and observe. Furthermore, the spectral location of the resonances of these modes are sometimes very close, leading to interference and making observation more difficult.

Sub-radiant modes can be excited in the far-field with off-normally incident plane waves with appropriate polarisation. In this project, the specific focus was on sub-radiant modes with radial or azimuthal surface charge distributions. It was shown that radial modes can be excited with off-normally incident p-polarised plane waves while azimuthal modes can be excited with s-polarised plane waves. In metasurfaces consisting of array of antennas composed of four nanorods, another sub-radiant mode is present near the spectral location of the dipole modes. Since focussed beams consist of an angular spectrum of plane waves travelling in different directions with different polarisations, these can also excite dark modes. Higher numerical aperture lenses produce higher incident angle plane wave components and these will more strongly excite dark modes.

The main focus of this study was radial modes on metasurfaces consisting of antennas composed of radially-oriented nanorods. The radial modes of these antennas had higher energy resonances (occurring at a shorter wavelength)

than the corresponding dipole modes. These modes could be observed in the transmission and the reflection spectra of the metasurfaces. Beside radial modes, azimuthal modes were also studied and some evidence of these modes was seen on metasurfaces consisting of antennas composed of azimuthally-oriented nanorods. The azimuthal mode has a longer resonance wavelength than the dipole mode.

The theory behind mode excitation on the metasurfaces was investigated using two methods, the finite-difference time-domain (FDTD) method and the electrostatic eigenmode method (EEM). The characterisation of the metasurfaces was also performed experimentally using beams with various polarisations focussed by lenses with varying numerical apertures (NAs). It was seen that the strength of the sub-radiant mode excitation increased with the NA of the lens.

To further support evidence of radial mode excitation and investigate their angular behaviour, reflected far-field images on resonance were observed. According to modelling, the radial modes are excited at higher angles of incidence, producing different far-field patterns from those at dipole mode resonances which can be excited at normal incidence. The results of far-field measurements were consistent with the earlier attribution of modes based on spectral measurements and simulations.

Based on the work presented in this thesis, the radial mode is the most reliable sub-radiant mode to be utilised for future work as it is relatively strong, easier to excite, and lies in the visible range. Nevertheless, investigation of other sub-radiant modes, such as the azimuthal and breathing modes would also be very interesting, particularly if they can be brought into the visible part of the spectrum and their intensity increased. Furthermore, the spatial variation of the metasurfaces discussed here is also potential aspect to be explored.

During the process, it is found that studying metasurfaces with focussed optical fields is interesting, yet very complex. It is rich area for further work. Firstly, the use of a focussed beam reduces the size required for the metasurface. Secondly, the sub-radiant modes which are sensitive to angle of incidence can be used for angular spectrum filtering with no requirement for additional optics as in conventional spatial filtering. Using various designs as well as tuning the metasurface parameters, the desired spatial frequency filtering could be tailored and applied to producing ultra-compact spatial filters, with a thick-

ness of only tens of nanometers. Other potential applications of the sub-radiant modes of metasurfaces are for imaging and light enhancement devices.

For imaging applications, a wavelength-tunable phase imaging device may be constructed based on metasurfaces possesing sub-radiant modes. The metasurface senses phase gradients in the incident field, potentially introducing contrast into imaged object based on sub-radiant mode resonances. Phase sensing with with sub-radiant modes has already been demonstrated in [109] and there is scope for extending this concept to the surfaces discussed in this thesis.

For light enhancement devices, a metasurface, through sub-radiant modes, could show strong coupling with quantum emitters such as quantum dots or fluorescent molecules. Due to their longer lifetimes, sub-radiant modes couple more strongly with emitters compared to radiant modes, increasing their emission rate as well as potentially directivity with an appropriate design of the metasurface. The enhancement of quantum emitters with plasmonic nanostructures has been demonstrated in the literature [110–113]. The coupling between quantum emitters and nanowire antennas through sub-radiant modes was specifically investigated in [114].

The narrow linewidth of the resonances of sub-radiant modes can also be utilised for sensing application with higher accuracy than sensing devices relying on radiant modes [115, 116].

Bibliography

[1] E. Hecht, *Optics*. Addison-Wesley, 2002.

[2] N. Engheta and R. W. Ziolkowski, *Metamaterials: physics and engineering explorations*. John Wiley & Sons, 2006.

[3] A. Sihvola, "Metamaterials in electromagnetics," *Metamaterials*, vol. 1, no. 1, pp. 2–11, 2007.

[4] C. M. Soukoulis and M. Wegener, "Past achievements and future challenges in the development of three-dimensional photonic metamaterials," *Nature Photonics*, vol. 5, no. 9, pp. 523–530, 2011.

[5] D. R. Smith, J. B. Pendry, and M. C. Wiltshire, "Metamaterials and negative refractive index," *Science*, vol. 305, no. 5685, pp. 788–792, 2004.

[6] M. Vollmer and U. Kreibig, "Optical properties of metal clusters," *Springer Ser. Mat. Sci*, vol. 25, 1995.

[7] G. V. Hartland, "Optical studies of dynamics in noble metal nanostructures," *Chemical Reviews*, vol. 111, no. 6, pp. 3858–3887, 2011.

[8] S. A. Maier, *Plasmonics: fundamentals and applications*. Springer Science & Business Media, 2007.

[9] J. B. Pendry, "Negative refraction makes a perfect lens," *Physical Review Letters*, vol. 85, no. 18, p. 3966, 2000.

[10] N. Yu and F. Capasso, "Flat optics with designer metasurfaces," *Nature Materials*, vol. 13, no. 2, pp. 139–150, 2014.

[11] R. C. Johnson and H. Jasik, "Antenna engineering handbook," *New York, McGraw-Hill Book Company, 1984, 1356 p. No individual items are abstracted in this volume.*, vol. 1, 1984.

[12] G. Raju, *Antennas and wave propagation.* Pearson Education India, 2006.

[13] M. Pelton, J. Aizpurua, and G. Bryant, "Metal-nanoparticle plasmonics," *Laser & Photonics Reviews*, vol. 2, no. 3, pp. 136–159, 2008.

[14] P. Bharadwaj, B. Deutsch, and L. Novotny, "Optical antennas," *Advances in Optics and Photonics*, vol. 1, no. 3, pp. 438–483, 2009.

[15] J. J. Cadusch, E. Panchenko, N. Kirkwood, T. D. James, B. C. Gibson, K. J. Webb, P. Mulvaney, and A. Roberts, "Emission enhancement and polarization of semiconductor quantum dots with nanoimprinted plasmonic cavities: towards scalable fabrication of plasmon-exciton displays," *Nanoscale*, vol. 7, no. 33, pp. 13 816–13 821, 2015.

[16] M. A. Kats, D. Sharma, J. Lin, P. Genevet, R. Blanchard, Z. Yang, M. M. Qazilbash, D. Basov, S. Ramanathan, and F. Capasso, "Ultra-thin perfect absorber employing a tunable phase change material," *Applied Physics Letters*, vol. 101, no. 22, p. 221101, 2012.

[17] M. A. Kats, R. Blanchard, P. Genevet, and F. Capasso, "Nanometre optical coatings based on strong interference effects in highly absorbing media," *Nature Materials*, vol. 12, no. 1, pp. 20–24, 2013.

[18] J. B. Pendry, D. Schurig, and D. R. Smith, "Controlling electromagnetic fields," *Science*, vol. 312, no. 5781, pp. 1780–1782, 2006.

[19] T. Davis, K. Vernon, and D. Gomez, "A plasmonic AC wheatstone bridge circuit for high-sensitivity phase measurement and single-molecule detection," *Journal of Applied Physics*, vol. 106, no. 4, p. 043502, 2009.

[20] N. E. Omaghali, V. Tkachenko, A. Andreone, and G. Abbate, "Optical sensing using dark mode excitation in an asymmetric dimer metamaterial," *Sensors*, vol. 14, no. 1, pp. 272–282, 2013.

[21] D. Gómez, Z. Teo, M. Altissimo, T. Davis, S. Earl, and A. Roberts, "The dark side of plasmonics," *Nano Letters*, vol. 13, no. 8, pp. 3722–3728, 2013.

[22] A. V. Kildishev, A. Boltasseva, and V. M. Shalaev, "Planar photonics with metasurfaces," *Science*, vol. 339, no. 6125, p. 1232009, 2013.

[23] C. L. Holloway, E. F. Kuester, J. A. Gordon, J. O'Hara, J. Booth, and D. R. Smith, "An overview of the theory and applications of metasurfaces: The two-dimensional equivalents of metamaterials," *IEEE Antennas and Propagation Magazine*, vol. 54, no. 2, pp. 10–35, 2012.

[24] Y. Xu, K. Yao, and H. Chen, "Generalized laws of reflection and refraction from transformation optics," *EPL (Europhysics Letters)*, vol. 99, no. 4, p. 44002, 2012.

[25] F. Aieta, P. Genevet, M. A. Kats, N. Yu, R. Blanchard, Z. Gaburro, and F. Capasso, "Aberration-free ultrathin flat lenses and axicons at telecom wavelengths based on plasmonic metasurfaces," *Nano Letters*, vol. 12, no. 9, pp. 4932–4936, 2012.

[26] C. Pfeiffer and A. Grbic, "Metamaterial huygens surfaces: tailoring wave fronts with reflectionless sheets," *Physical Review Letters*, vol. 110, no. 19, p. 197401, 2013.

[27] N. Yu, F. Aieta, P. Genevet, M. A. Kats, Z. Gaburro, and F. Capasso, "A broadband, background-free quarter-wave plate based on plasmonic metasurfaces," *Nano Letters*, vol. 12, no. 12, pp. 6328–6333, 2012.

[28] J. J. Cadusch, T. D. James, and A. Roberts, "Experimental demonstration of a wave plate utilizing localized plasmonic resonances in nanoapertures," *Optics Express*, vol. 21, no. 23, pp. 28 450–28 455, 2013.

[29] X. Yi, X. Ling, Z. Zhang, Y. Li, X. Zhou, Y. Liu, S. Chen, H. Luo, and S. Wen, "Generation of cylindrical vector vortex beams by two cascaded metasurfaces," *Optics Express*, vol. 22, no. 14, pp. 17 207–17 215, 2014.

[30] J. Lin, P. Genevet, M. A. Kats, N. Antoniou, and F. Capasso, "Nanostructured holograms for broadband manipulation of vector beams," *Nano Letters*, vol. 13, no. 9, pp. 4269–4274, 2013.

[31] J. J. Cadusch, T. D. James, A. Djalalian-Assl, T. J. Davis, and A. Roberts, "A chiral plasmonic metasurface circular polarization filter," *IEEE Photonics Technology Letters*, vol. 23, no. 26, pp. 2357–2360, 2014.

[32] B. Walther, C. Helgert, C. Rockstuhl, F. Setzpfandt, F. Eilenberger, E.-B. Kley, F. Lederer, A. Tünnermann, and T. Pertsch, "Spatial and spectral light shaping with metamaterials," *Advanced Materials*, vol. 24, no. 47, pp. 6300–6304, 2012.

[33] M. Padgett, J. Courtial, and L. Allen, "Light's orbital angular momentum," *Physics Today*, vol. 57, no. 5, pp. 35–40, 2004.

[34] M. Kang, J. Chen, X.-L. Wang, and H.-T. Wang, "Twisted vector field from an inhomogeneous and anisotropic metamaterial," *JOSA B*, vol. 29, no. 4, pp. 572–576, 2012.

[35] M. Kang, T. Feng, H.-T. Wang, and J. Li, "Wave front engineering from an array of thin aperture antennas," *Optics Express*, vol. 20, no. 14, pp. 15 882–15 890, 2012.

[36] X. Chen, L. Huang, H. Mühlenbernd, G. Li, B. Bai, Q. Tan, G. Jin, C.-W. Qiu, S. Zhang, and T. Zentgraf, "Dual-polarity plasmonic metalens for visible light," *Nature Communications*, vol. 3, p. 1198, 2012.

[37] L. Huang, X. Chen, H. Muhlenbernd, G. Li, B. Bai, Q. Tan, G. Jin, T. Zentgraf, and S. Zhang, "Dispersionless phase discontinuities for controlling light propagation," *Nano Letters*, vol. 12, no. 11, pp. 5750–5755, 2012.

[38] F. Eftekhari, D. E. Gómez, and T. J. Davis, "Measuring subwavelength phase differences with a plasmonic circuitan example of nanoscale optical signal processing," *Optics Letters*, vol. 39, no. 10, pp. 2994–2997, 2014.

[39] Y. Hwang and T. J. Davis, "Optical metasurfaces for subwavelength difference operations," *Applied Physics Letters*, vol. 109, no. 18, p. 181101, 2016.

[40] F. Hao, E. M. Larsson, T. A. Ali, D. S. Sutherland, and P. Nordlander, "Shedding light on dark plasmons in gold nanorings," *Chemical Physics*

Letters, vol. 458, no. 4, pp. 262–266, 2008.

[41] L. Novotny and B. Hecht, *Principles of nano-optics*. Cambridge University Press, 2012.

[42] P. B. Johnson and R.-W. Christy, "Optical constants of the noble metals," *Physical Review B*, vol. 6, no. 12, p. 4370, 1972.

[43] E. D. Palik, *Handbook of optical constants of solids*. Academic Press, 1998, vol. 3.

[44] E. Kretschmann and H. Raether, "Notizen: Radiative decay of non radiative surface plasmons excited by light," *Zeitschrift für Naturforschung A*, vol. 23, no. 12, pp. 2135–2136, 1968.

[45] A. Otto, "Excitation of nonradiative surface plasma waves in silver by the method of frustrated total reflection," *Zeitschrift für Physik*, vol. 216, no. 4, pp. 398–410, 1968.

[46] J. Mock, M. Barbic, D. Smith, D. Schultz, and S. Schultz, "Shape effects in plasmon resonance of individual colloidal silver nanoparticles," *The Journal of Chemical Physics*, vol. 116, no. 15, pp. 6755–6759, 2002.

[47] H. Kuwata, H. Tamaru, K. Esumi, and K. Miyano, "Resonant light scattering from metal nanoparticles: Practical analysis beyond rayleigh approximation," *Applied Physics Letters*, vol. 83, no. 22, pp. 4625–4627, 2003.

[48] W. L. Barnes, A. Dereux, and T. W. Ebbesen, "Surface plasmon subwavelength optics," *Nature*, vol. 424, no. 6950, pp. 824–830, 2003.

[49] A. V. Zayats and I. I. Smolyaninov, "Near-field photonics: surface plasmon polaritons and localized surface plasmons," *Journal of Optics A: Pure and Applied Optics*, vol. 5, no. 4, p. S16, 2003.

[50] E. Hutter and J. H. Fendler, "Exploitation of localized surface plasmon resonance," *Advanced Materials*, vol. 16, no. 19, pp. 1685–1706, 2004.

[51] L. Novotny and N. Van Hulst, "Antennas for light," *Nature Photonics*, vol. 5, no. 2, pp. 83–90, 2011.

[52] K. A. Willets and R. P. Van Duyne, "Localized surface plasmon resonance spectroscopy and sensing," *Annu. Rev. Phys. Chem.*, vol. 58, pp. 267–297, 2007.

[53] C. Sönnichsen, T. Franzl, T. Wilk, G. Von Plessen, and J. Feldmann, "Plasmon resonances in large noble-metal clusters," *New Journal of Physics*, vol. 4, no. 1, p. 93, 2002.

[54] L. J. Sherry, S.-H. Chang, G. C. Schatz, R. P. Van Duyne, B. J. Wiley, and Y. Xia, "Localized surface plasmon resonance spectroscopy of single silver nanocubes," *Nano Letters*, vol. 5, no. 10, pp. 2034–2038, 2005.

[55] W. Wang, D. He, J. Duan, M. Fu, X. Zhang, H. Wu, Y. Hu, and Y. Wang, "Modulated photoluminescence of graphene quantum dots in the vicinity of an individual silver nano-octahedron," *Phys. Chem. Chem. Phys.*, vol. 16, no. 10, pp. 4504–4509, 2014.

[56] R. Filter, K. Słowik, J. Straubel, F. Lederer, and C. Rockstuhl, "Nanoantennas for ultrabright single photon sources," *Optics Letters*, vol. 39, no. 5, pp. 1246–1249, 2014.

[57] S. V. Boriskina and L. Dal Negro, "Multiple-wavelength plasmonic nanoantennas," *Optics Letters*, vol. 35, no. 4, pp. 538–540, 2010.

[58] A. Sundaramurthy, P. J. Schuck, N. R. Conley, D. P. Fromm, G. S. Kino, and W. Moerner, "Toward nanometer-scale optical photolithography: utilizing the near-field of bowtie optical nanoantennas," *Nano Letters*, vol. 6, no. 3, pp. 355–360, 2006.

[59] P. Biagioni, J. Huang, L. Duò, M. Finazzi, and B. Hecht, "Cross resonant optical antenna," *Physical Review Letters*, vol. 102, no. 25, p. 256801, 2009.

[60] A. P. Edwards and A. M. Adawi, "Plasmonic nanogaps for broadband and large spontaneous emission rate enhancement," *Journal of Applied Physics*, vol. 115, no. 5, p. 053101, 2014.

[61] P. Anger, P. Bharadwaj, and L. Novotny, "Enhancement and quenching of single-molecule fluorescence," *Physical Review Letters*, vol. 96, no. 11, p. 113002, 2006.

[62] H. Wang, Y. Wu, B. Lassiter, C. L. Nehl, J. H. Hafner, P. Nordlander, and N. J. Halas, "Symmetry breaking in individual plasmonic nanoparticles," *Proceedings of the National Academy of Sciences*, vol. 103, no. 29, pp. 10 856–10 860, 2006.

[63] J. P. Kottmann and O. J. Martin, "Retardation-induced plasmon resonances in coupled nanoparticles," *Optics Letters*, vol. 26, no. 14, pp. 1096–1098, 2001.

[64] S.-C. Yang, H. Kobori, C.-L. He, M.-H. Lin, H.-Y. Chen, C. Li, M. Kanehara, T. Teranishi, and S. Gwo, "Plasmon hybridization in individual gold nanocrystal dimers: direct observation of bright and dark modes," *Nano Letters*, vol. 10, no. 2, pp. 632–637, 2010.

[65] J. Alegret, T. Rindzevicius, T. Pakizeh, Y. Alaverdyan, L. Gunnarsson, and M. Kall, "Plasmonic properties of silver trimers with trigonal symmetry fabricated by electron-beam lithography," *The Journal of Physical Chemistry C*, vol. 112, no. 37, pp. 14 313–14 317, 2008.

[66] Y. Bao, X. Zhu, and Z. Fang, "Plasmonic toroidal dipolar response under radially polarized excitation," *Scientific Reports*, vol. 5, 2015.

[67] F. Hao, P. Nordlander, Y. Sonnefraud, P. V. Dorpe, and S. A. Maier, "Tunability of subradiant dipolar and fano-type plasmon resonances in metallic ring/disk cavities: implications for nanoscale optical sensing," *ACS Nano*, vol. 3, no. 3, pp. 643–652, 2009.

[68] A. Yanai, M. Grajower, G. M. Lerman, M. Hentschel, H. Giessen, and U. Levy, "Near-and far-field properties of plasmonic oligomers under radially and azimuthally polarized light excitation," *ACS Nano*, vol. 8, no. 5, pp. 4969–4974, 2014.

[69] B. Luk'yanchuk, N. I. Zheludev, S. A. Maier, N. J. Halas, P. Nordlander, H. Giessen, and C. T. Chong, "The fano resonance in plasmonic nanostructures and metamaterials," *Nature Materials*, vol. 9, no. 9, pp. 707–715, 2010.

[70] C. F. Bohren and D. R. Huffman, *Absorption and scattering of light by small particles*. John Wiley & Sons, 2008.

[71] T. Davis and N. Hauppauge, "Evanescent coupling between resonant plasmonic nanoparticles and the design of nanoparticle systems," *Plasmons: Theory and Applications], Helsey, KN, ed*, pp. 111–141, 2011.

[72] D. E. Gómez, T. J. Davis, and A. M. Funston, "Plasmonics by design: design principles to structure–function relationships with assemblies of metal nanoparticles," *Journal of Materials Chemistry C*, vol. 2, no. 17, pp. 3077–3087, 2014.

[73] M. A. Yurkin and A. G. Hoekstra, "The discrete dipole approximation: an overview and recent developments," *Journal of Quantitative Spectroscopy and Radiative Transfer*, vol. 106, no. 1, pp. 558–589, 2007.

[74] W. S. Hall, *Boundary element method*. Springer, 1994.

[75] A. Taflove and S. C. Hagness, *Computational electrodynamics*. Artech House, 2005.

[76] J. B. Schneider, "Understanding the finite-difference time-domain method," *School of Electrical Engineering and Computer Science Washington State University.–URL: http://www.eecs.wsu.edu/˜schneidj/ufdtd/*, 2011.

[77] G. Dhatt, E. Lefrançois, and G. Touzot, *Finite element method*. John Wiley & Sons, 2012.

[78] K.-J. Bathe, *Finite element method*. Wiley Online Library, 2008.

[79] A. Farjadpour, D. Roundy, A. Rodriguez, M. Ibanescu, P. Bermel, J. Joannopoulos, S. G. Johnson, and G. Burr, "Improving accuracy by subpixel smoothing in the finite-difference time domain," *Optics Letters*, vol. 31, no. 20, pp. 2972–2974, 2006.

[80] A. Deinega and I. Valuev, "Subpixel smoothing for conductive and dispersive media in the finite-difference time-domain method," *Optics Letters*, vol. 32, no. 23, pp. 3429–3431, 2007.

[81] K. S. Yee *et al.*, "Numerical solution of initial boundary value problems involving maxwells equations in isotropic media," *IEEE Trans. Antennas Propag*, vol. 14, no. 3, pp. 302–307, 1966.

[82] J.-P. Berenger, "A perfectly matched layer for the absorption of electromagnetic waves," *Journal of Computational Physics*, vol. 114, no. 2, pp. 185–200, 1994.

[83] W. Pernice, F. Payne, and D. Gallagher, "An fdtd method for the simulation of dispersive metallic structures," *Optical and Quantum Electronics*, vol. 38, no. 9-11, pp. 843–856, 2006.

[84] J. Shibayama, R. Ando, A. Nomura, J. Yamauchi, and H. Nakano, "Simple trapezoidal recursive convolution technique for the frequency-dependent fdtd analysis of a drude–lorentz model," *IEEE Photonics Technology Letters*, vol. 21, no. 2, pp. 100–102, 2009.

[85] A. Vial, "Implementation of the critical points model in the recursive convolution method for modelling dispersive media with the finite-difference time domain method," *Journal of Optics A: Pure and Applied Optics*, vol. 9, no. 7, p. 745, 2007.

[86] J. Shibayama, K. Watanabe, R. Ando, J. Yamauchi, and H. Nakano, "Simple frequency-dependent fdtd algorithm for a drude-critical points model," in *Microwave Conference Proceedings (APMC), 2010 Asia-Pacific*. IEEE, 2010, pp. 73–75.

[87] J. Shibayama, K. Watanabe, J. Yamauchi, and H. Nakano, "Frequency-dependent formulations of a drude-critical points model for explicit and implicit fdtd methods using the trapezoidal rc technique," *IEICE Transactions on Electronics*, vol. 95, no. 4, pp. 725–732, 2012.

[88] A. Vial and T. Laroche, "Comparison of gold and silver dispersion laws suitable for fdtd simulations," *Applied Physics B*, vol. 93, no. 1, pp. 139–143, 2008.

[89] T. J. Davis, K. C. Vernon, and D. E. Gómez, "Effect of retardation on localized surface plasmon resonances in a metallic nanorod," *Optics Express*, vol. 17, no. 26, pp. 23 655–23 663, 2009.

[90] T. Davis and D. Gómez, "Colloquium: An algebraic model of localized surface plasmons and their interactions," *Reviews of Modern Physics*, vol. 89, no. 1, p. 011003, 2017.

[91] J. D. Jackson, *Classical electrodynamics*. Wiley, 1999.

[92] T. J. Davis, "An analysis of the plasmonic dark mode response of a rectangular arrangement of metal nanorods," Personal communication.

[93] Q. Zhan, "Cylindrical vector beams: from mathematical concepts to applications," *Advances in Optics and Photonics*, vol. 1, no. 1, pp. 1–57, 2009.

[94] A. Roberts, "Beam transmission through hole arrays," *Optics Express*, vol. 18, no. 3, pp. 2528–2533, 2010.

[95] M. Mansuripur, "Distribution of light at and near the focus of high-numerical-aperture objectives," *JOSA A*, vol. 3, no. 12, pp. 2086–2093, 1986.

[96] ——, "Certain computational aspects of vector diffraction problems," *JOSA A*, vol. 6, no. 6, pp. 786–805, 1989.

[97] M. Liu, T.-W. Lee, S. K. Gray, P. Guyot-Sionnest, M. Pelton *et al.*, "Excitation of dark plasmons in metal nanoparticles by a localized emitter," *Physical Review Letters*, vol. 102, no. 10, p. 107401, 2009.

[98] L. Mandel and E. Wolf, *Optical coherence and quantum optics*. Cambridge University Press, 1995.

[99] G. Fletcher, M. D. Arnold, T. Pedersen, V. J. Keast, and M. B. Cortie, "Multipolar and dark-mode plasmon resonances on drilled silver nanotriangles," *Optics Express*, vol. 23, no. 14, pp. 18 002–18 013, 2015.

[100] E. Prodan, C. Radloff, N. J. Halas, and P. Nordlander, "A hybridization model for the plasmon response of complex nanostructures," *Science*, vol. 302, no. 5644, pp. 419–422, 2003.

[101] [Online]. Available: http://refractiveindex.info/?shelf=glass&book=fused_silica&page=Malitson

[102] [Online]. Available: http://www.klayout.de/

[103] [Online]. Available: http://refractiveindex.info/?shelf=other&book=pmma_resists&page=Microchem495

[104] C. Ropers, D. Park, G. Stibenz, G. Steinmeyer, J. Kim, D. Kim, and C. Lienau, "Femtosecond light transmission and subradiant damping in plasmonic crystals," *Physical review letters*, vol. 94, no. 11, p. 113901, 2005.

[105] A. Christ, O. J. Martin, Y. Ekinci, N. A. Gippius, and S. G. Tikhodeev, "Symmetry breaking in a plasmonic metamaterial at optical wavelength," *Nano Letters*, vol. 8, no. 8, pp. 2171–2175, 2008.

[106] J. Pérez-Juste, I. Pastoriza-Santos, L. M. Liz-Marzán, and P. Mulvaney, "Gold nanorods: synthesis, characterization and applications," *Coordination Chemistry Reviews*, vol. 249, no. 17, pp. 1870–1901, 2005.

[107] M. Mansuripur, "Effects of high-numerical-aperture focusing on the state of polarization in optical and magneto-optic data storage systems," *Applied Optics*, vol. 30, no. 22, pp. 3154–3162, 1991.

[108] [Online]. Available: https://en.wikipedia.org/wiki/Fresnel_equations

[109] F. Hao, Y. Sonnefraud, P. V. Dorpe, S. A. Maier, N. J. Halas, and P. Nordlander, "Symmetry breaking in plasmonic nanocavities: subradiant lspr sensing and a tunable fano resonance," *Nano letters*, vol. 8, no. 11, pp. 3983–3988, 2008.

[110] A. Kinkhabwala, Z. Yu, S. Fan, Y. Avlasevich, K. Müllen, and W. Moerner, "Large single-molecule fluorescence enhancements produced by a bowtie nanoantenna," *Nature Photonics*, vol. 3, no. 11, pp. 654–657, 2009.

[111] M. L. Andersen, S. Stobbe, A. S. Sørensen, and P. Lodahl, "Strongly modified plasmon-matter interaction with mesoscopic quantum emitters," *Nature Physics*, vol. 7, no. 3, pp. 215–218, 2011.

[112] S. Pillai, K. Catchpole, T. Trupke, G. Zhang, J. Zhao, and M. Green, "Enhanced emission from si-based light-emitting diodes using surface plasmons," *Applied Physics Letters*, vol. 88, no. 16, p. 161102, 2006.

[113] D. Chang, A. S. Sørensen, P. Hemmer, and M. Lukin, "Quantum optics with surface plasmons," *Physical Review Letters*, vol. 97, no. 5, p. 053002, 2006.

[114] A. G. Curto, T. H. Taminiau, G. Volpe, M. P. Kreuzer, R. Quidant, and N. F. Van Hulst, "Multipolar radiation of quantum emitters with nanowire optical antennas," *Nature Communications*, vol. 4, p. 1750, 2013.

[115] B. Gallinet and O. J. Martin, "Refractive index sensing with subradiant modes: A framework to reduce losses in plasmonic nanostructures," *ACS Nano*, vol. 7, no. 8, pp. 6978–6987, 2013.

[116] J. Butet, I. Russier-Antoine, C. Jonin, N. Lascoux, E. Benichou, and P.-F. Brevet, "Sensing with multipolar second harmonic generation from spherical metallic nanoparticles," *Nano Letters*, vol. 12, no. 3, pp. 1697–1701, 2012.

Appendix A

The Experimental Data of Transmission and Reflection Spectra

A.1 Transmission Spectra

Code	Radial/ Azimuthal Pol.	Linear Polarisation
#R11-O1	N/A	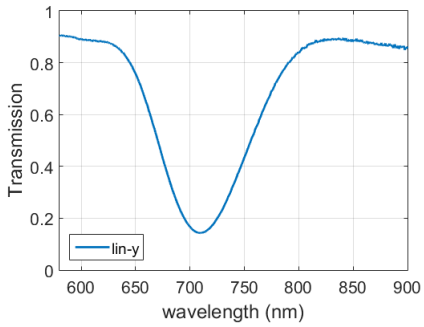
#R12-O1	N/A	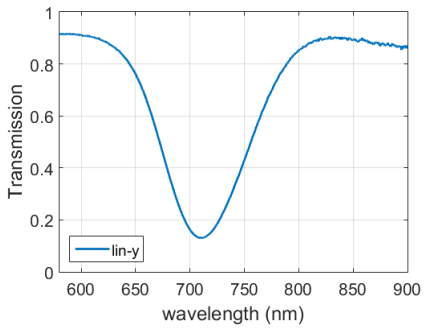

#R13-O1	N/A	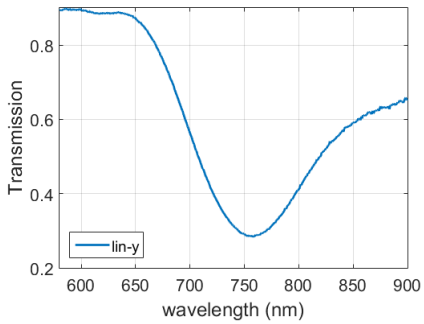
#R14-O1	N/A	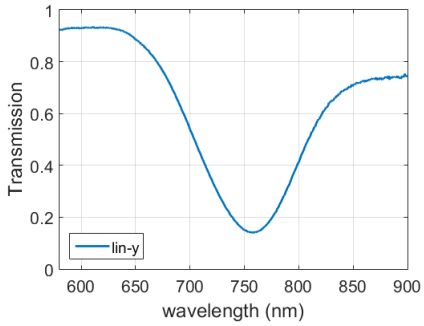
#R15-O1	N/A	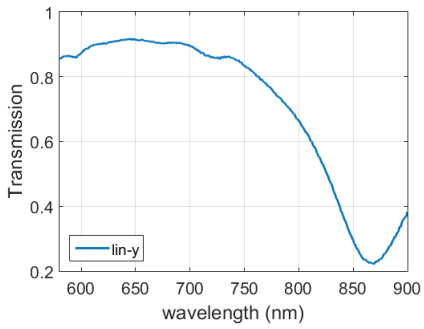
#R16-O1	N/A	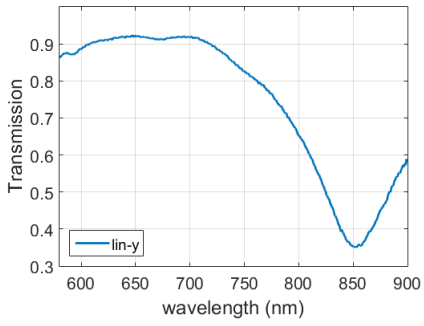

#R21-O1	N/A	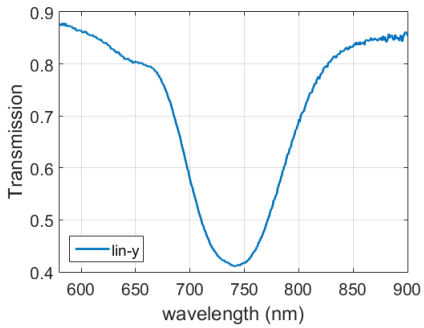
#R22-O1	N/A	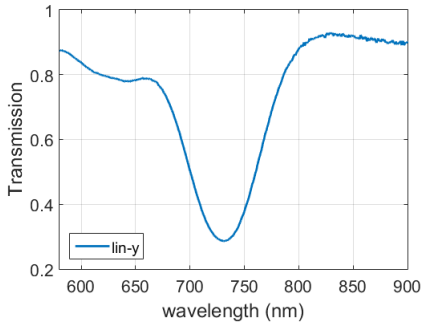
#R23-O1	N/A	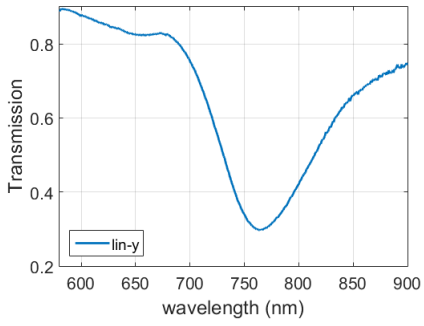
#R24-O1	N/A	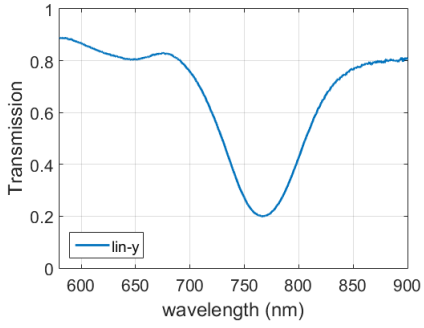

#R25-O1	N/A	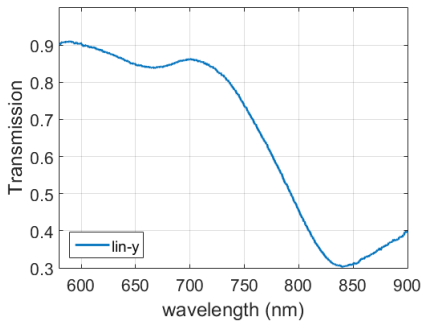
#R26-O1	N/A	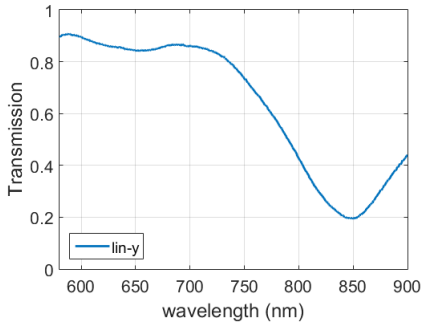
#A11-O1	N/A	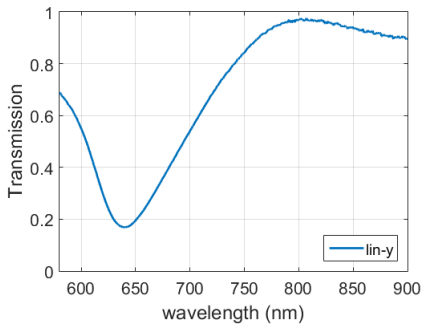
#A12-O1	N/A	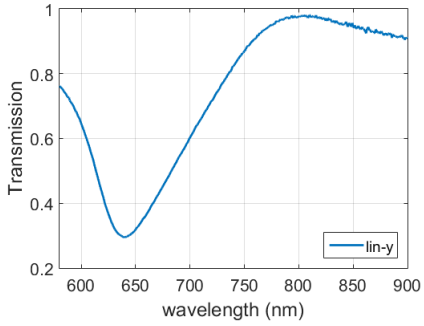

#A13-O1	N/A	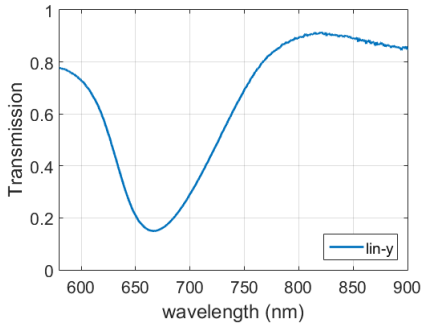
#A14-O1	N/A	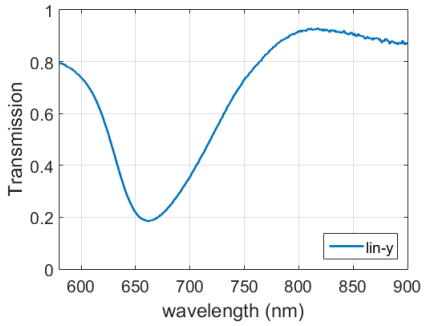
#A15-O1	N/A	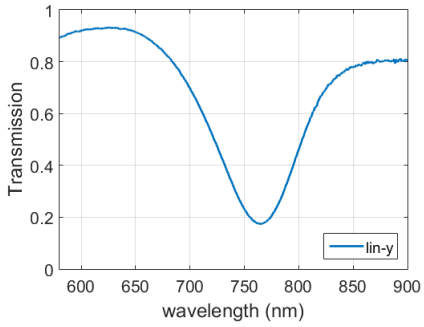
#A16-O1	N/A	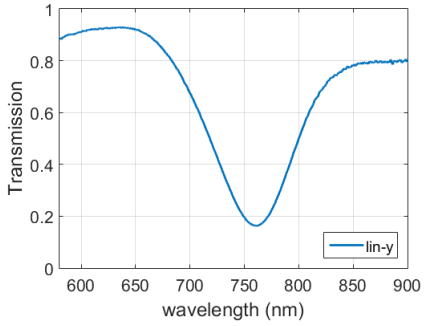

#A21-O1	N/A	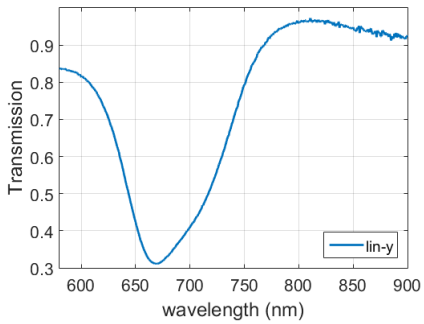
#A22-O1	N/A	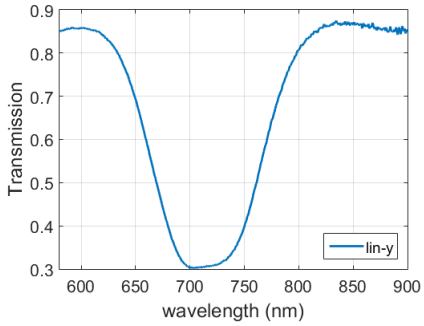
#A23-O1	N/A	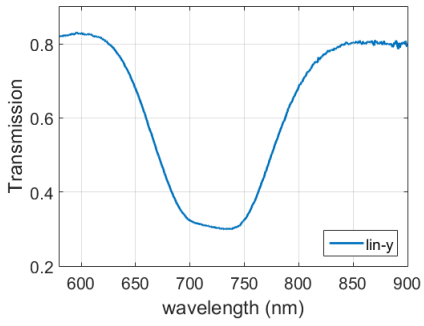
#A24-O1	N/A	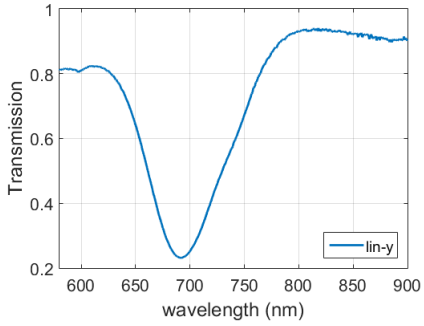

#A25-O1	N/A	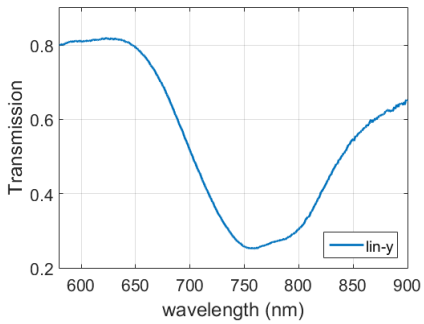
#A26-O1	N/A	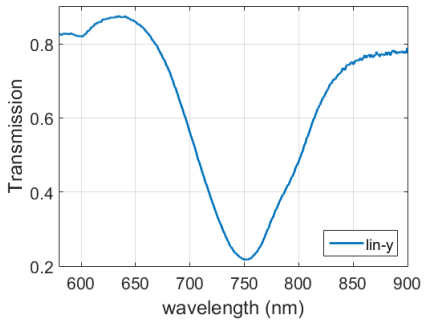
#R11-O2	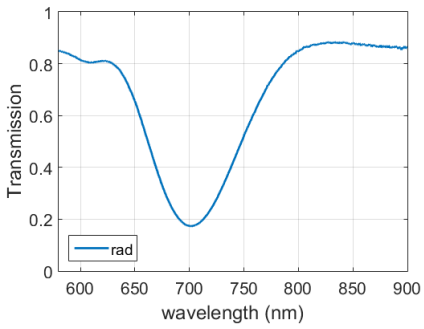	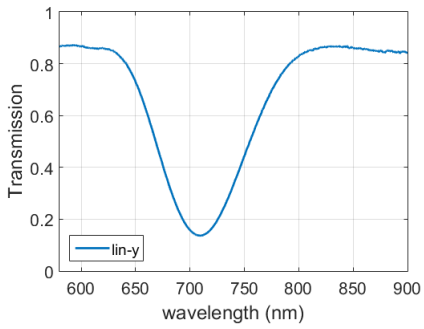
#R12-O2	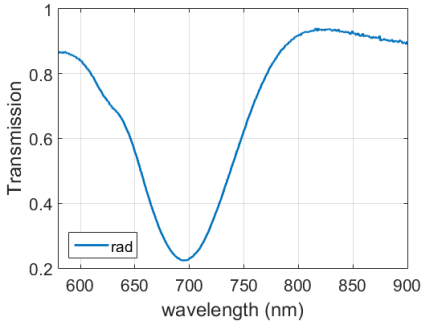	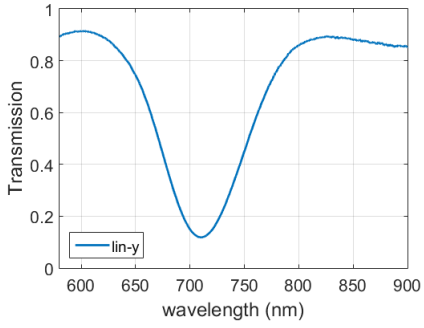

#R13-O2	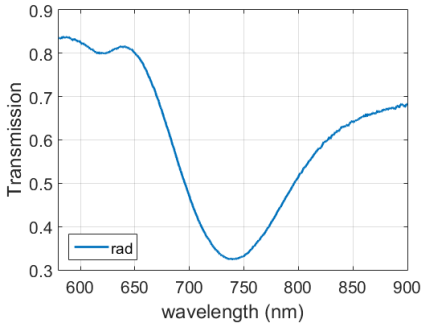	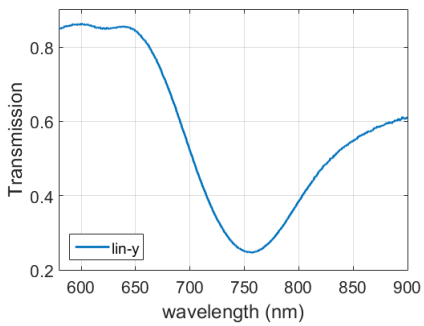
#R14-O2	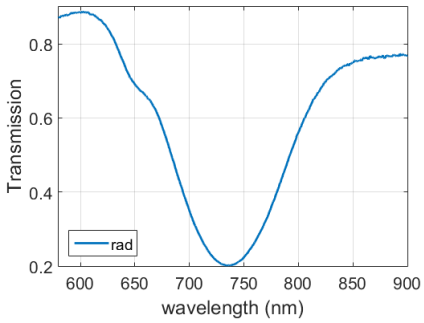	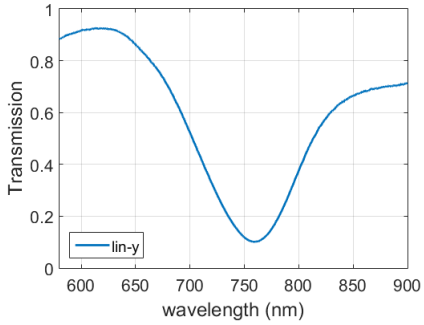
#R15-O2	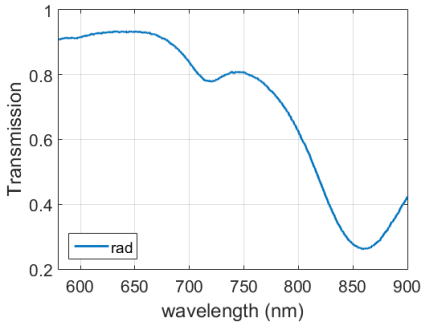	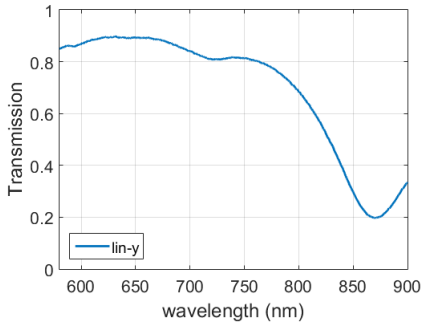
#R16-O2	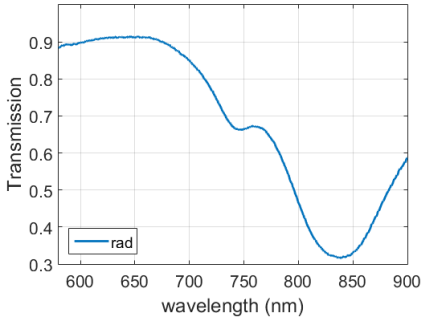	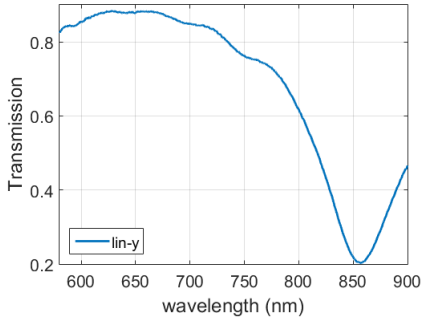

#R21-O2	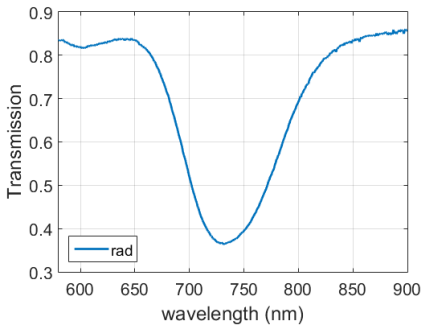	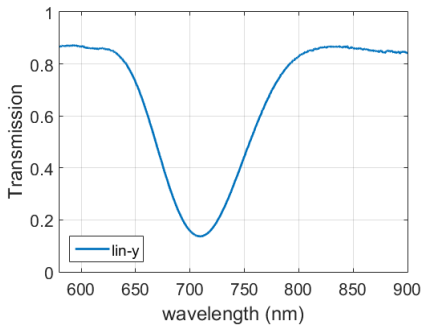
#R22-O2	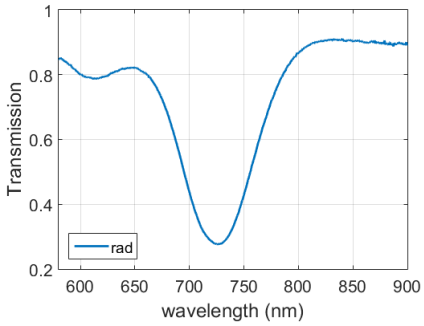	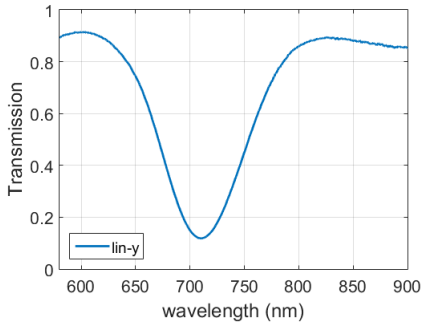
#R23-O2	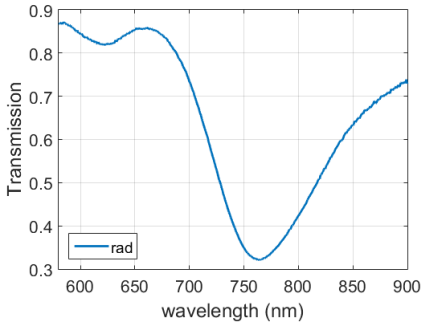	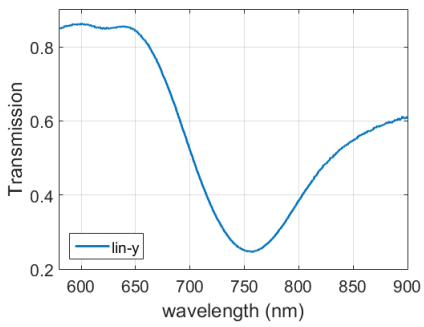
#R24-O2	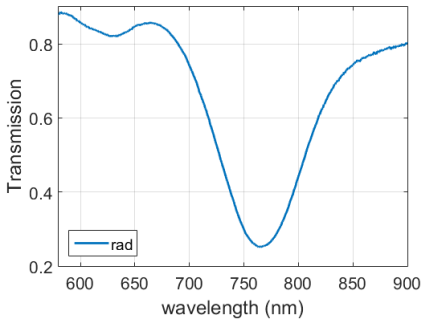	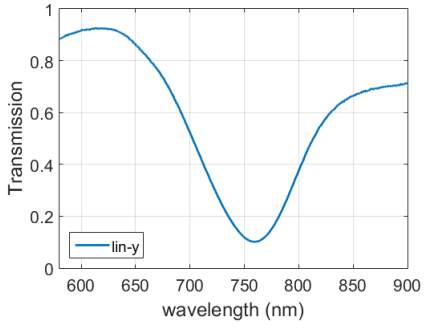

#R25-O2	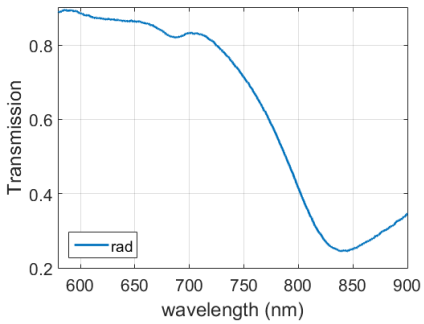	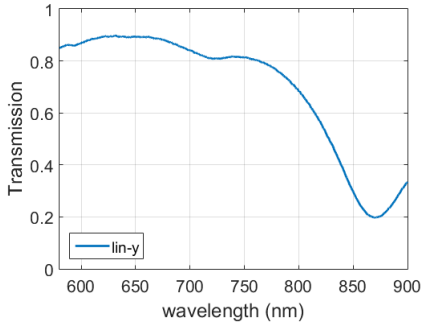
#R26-O2	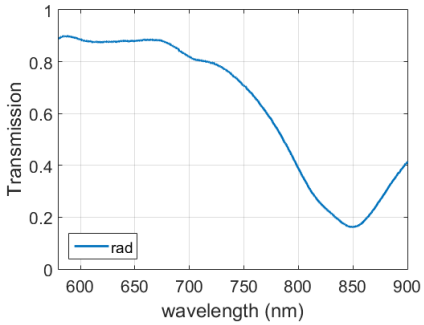	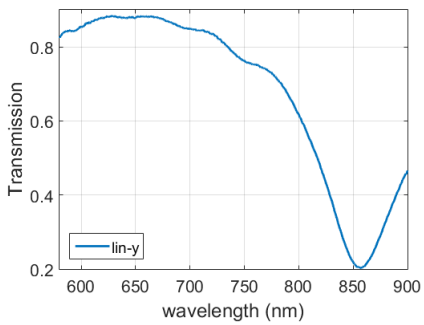
#A11-O2	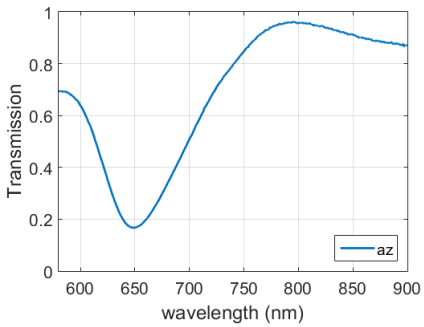	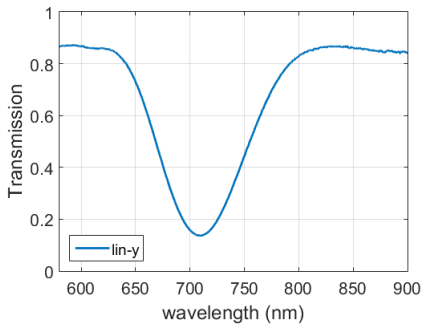
#A12-O2	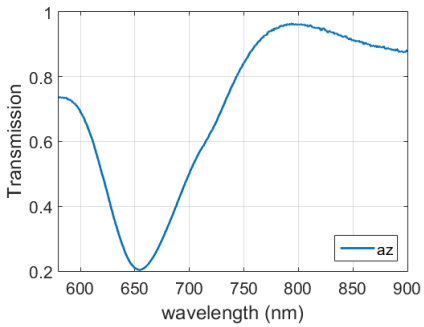	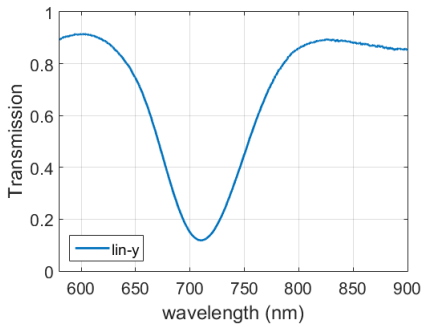

#A13-O2	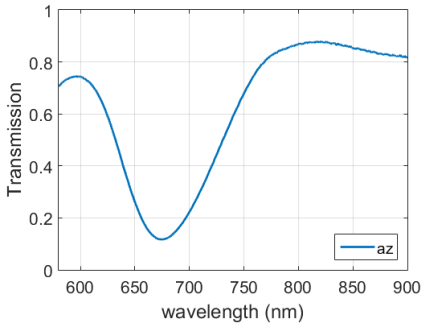	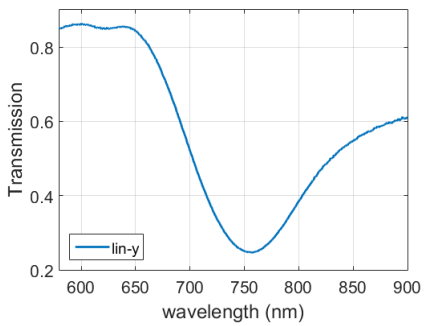
#A14-O2	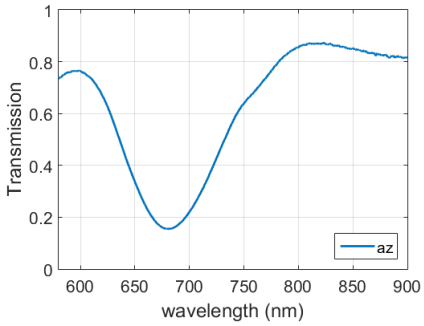	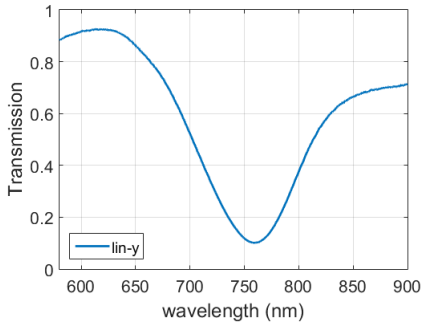
#A15-O2	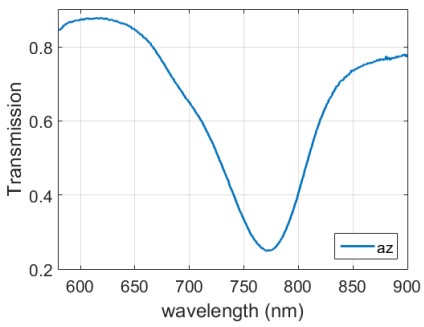	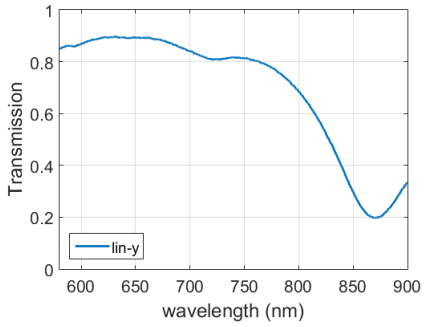
#A16-O2	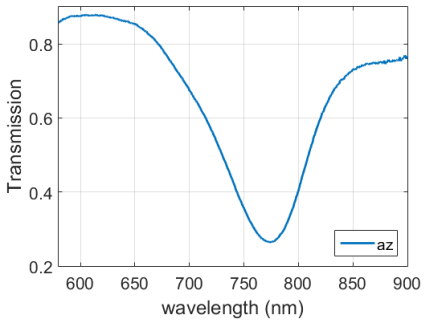	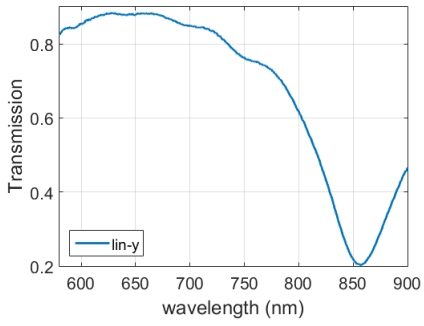

#A21-O2	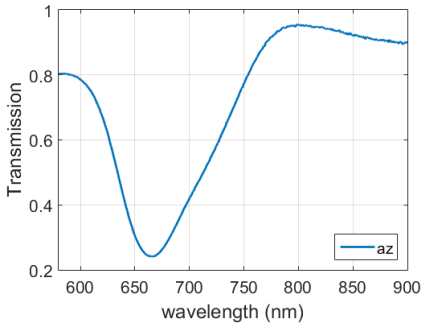	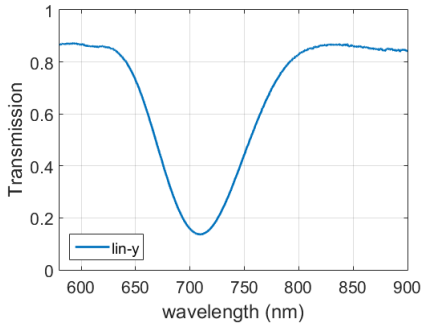
#A22-O2	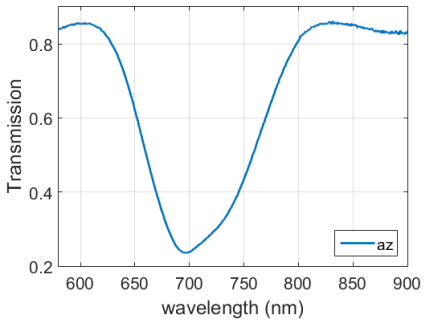	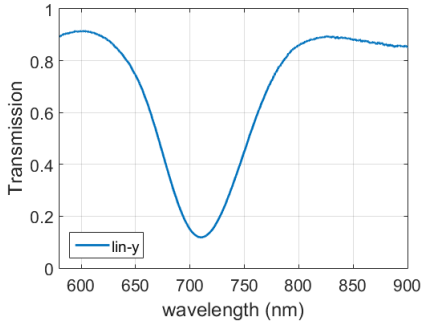
#A23-O2	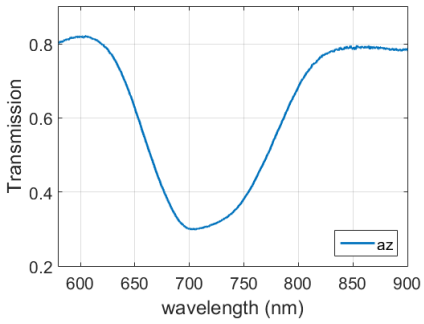	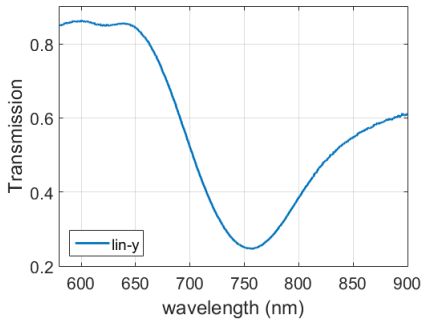
#A24-O2	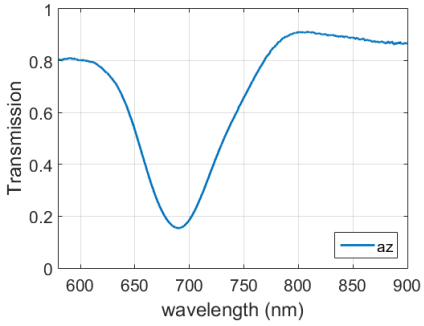	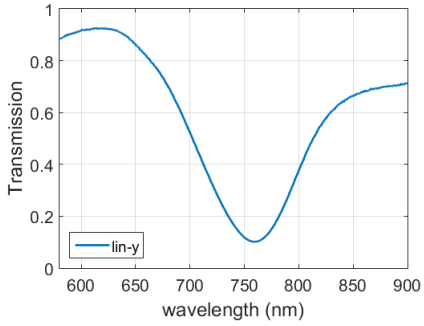

#A25-O2	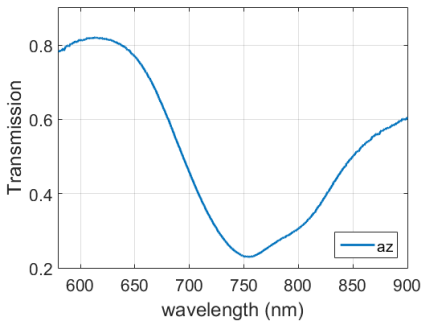	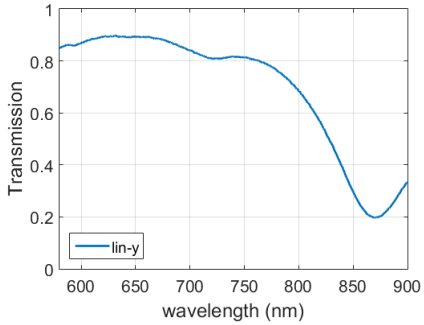
#A26-O2	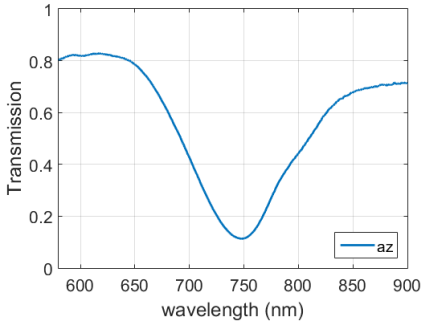	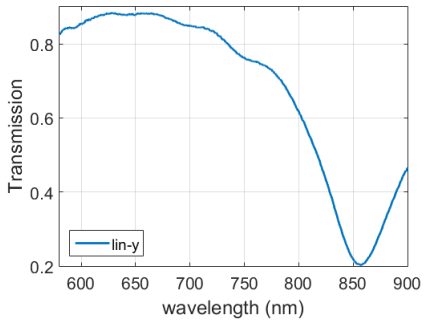
#R11-O3	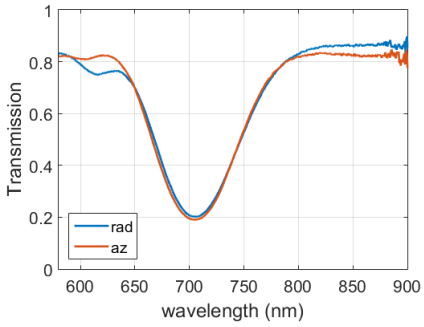	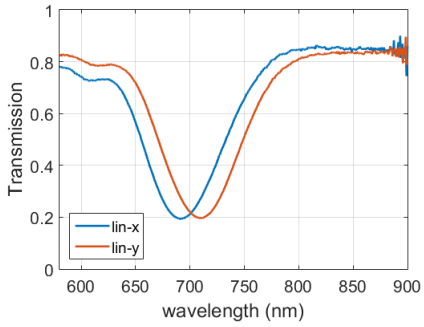
#R12-O3	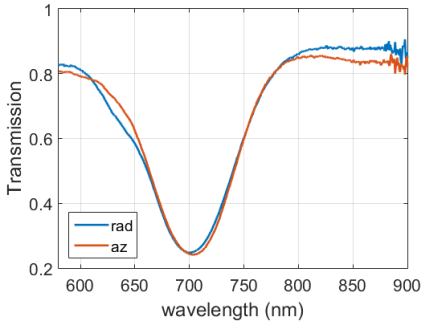	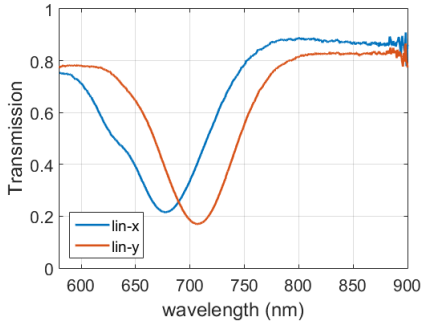

#R13-O3	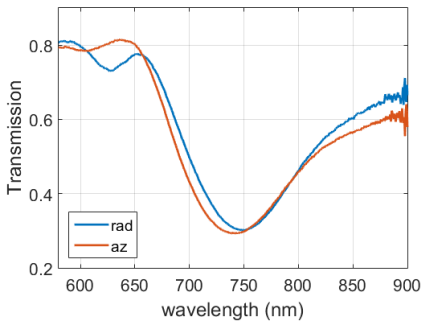	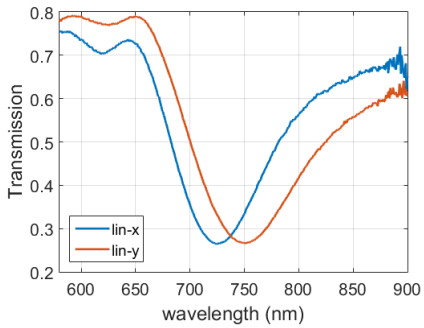
#R14-O3	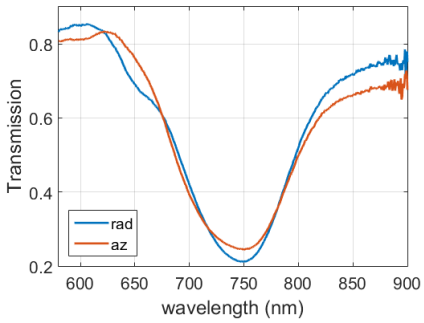	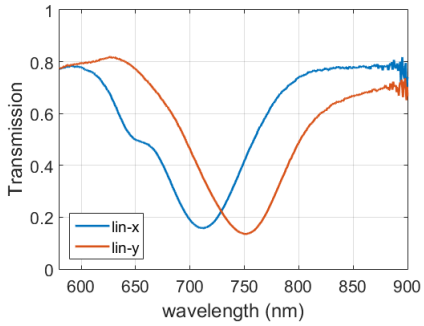
#R15-O3	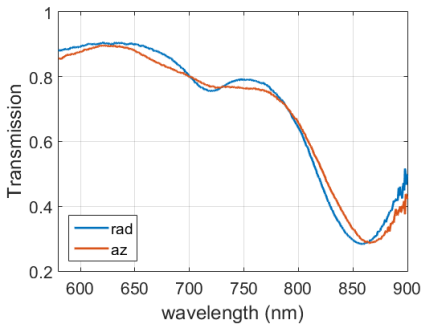	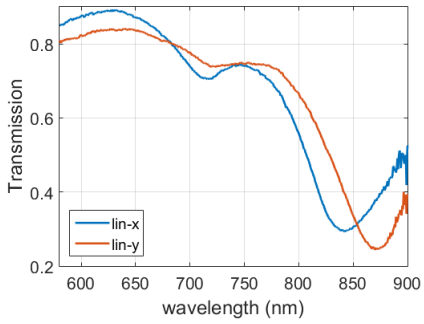
#R16-O3	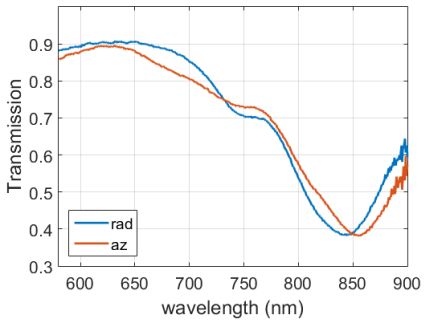	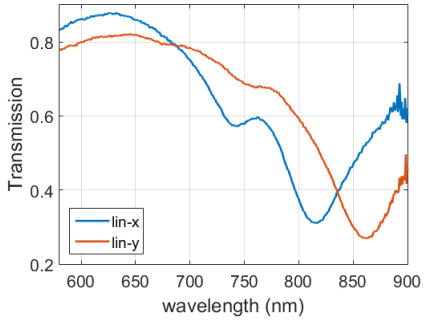

#R17-O3	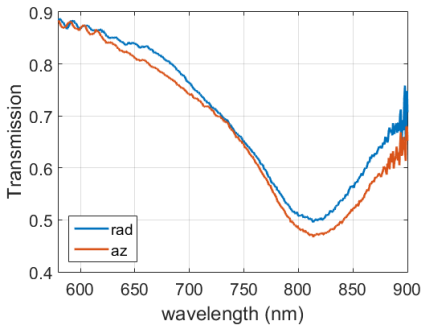	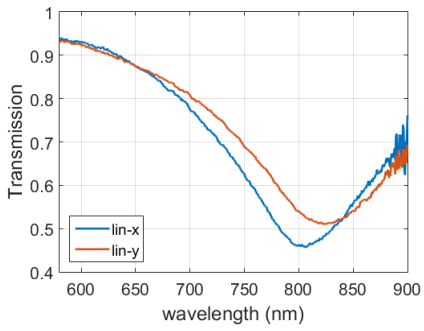
#R18-O3	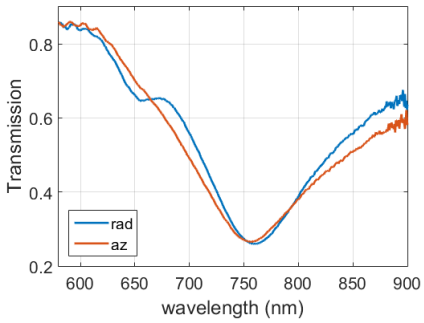	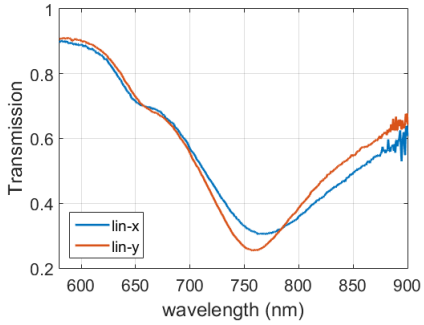
#R19-O3	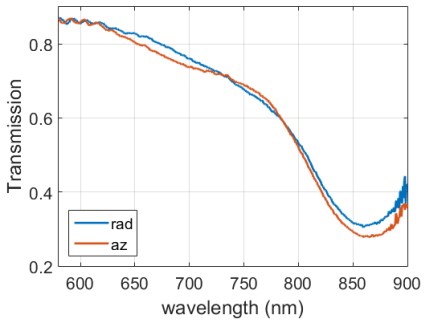	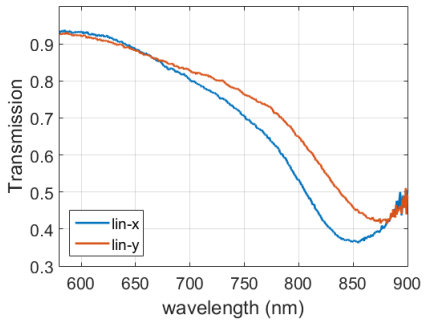
#R1A-O3	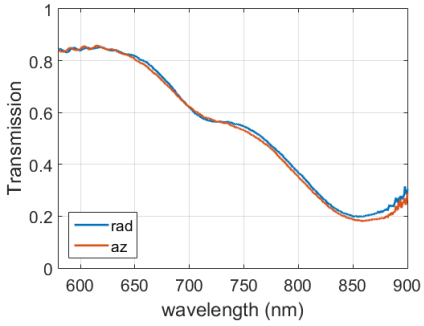	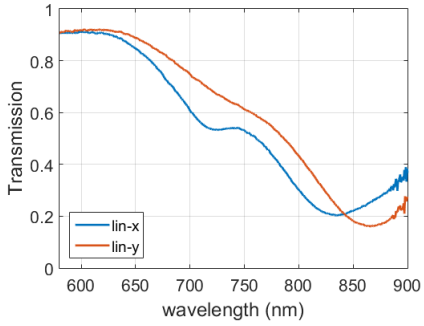

#R1B-O3	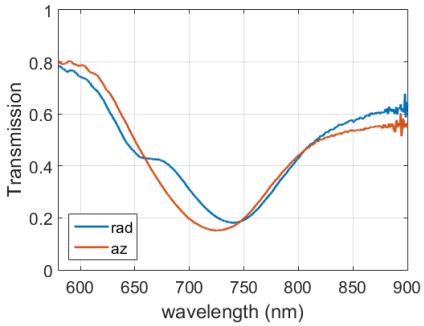	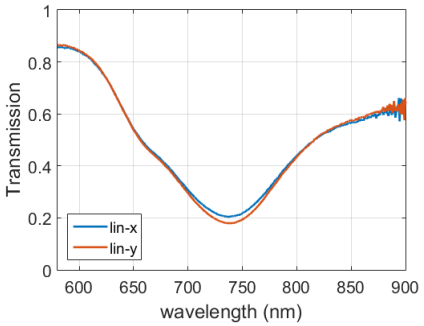
#R1C-O3	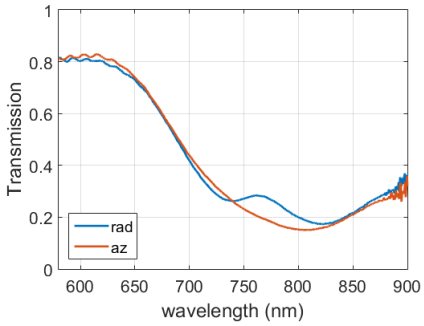	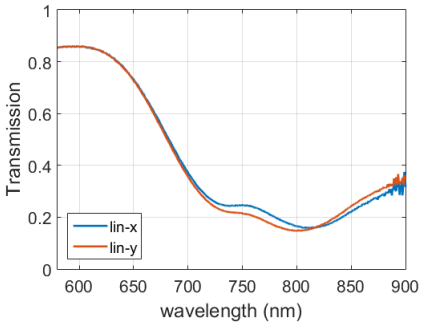
#R21-O3	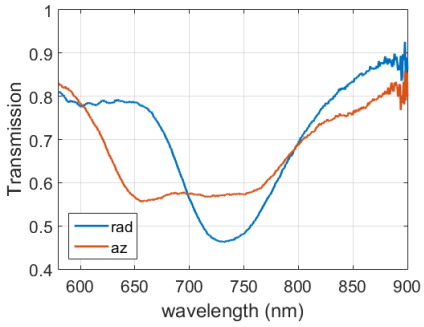	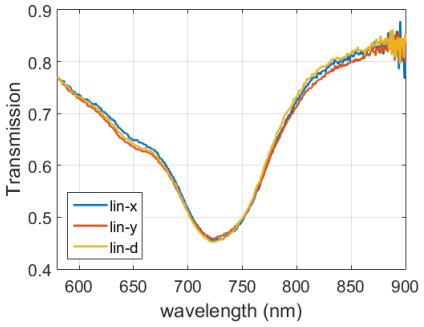
#R22-O3	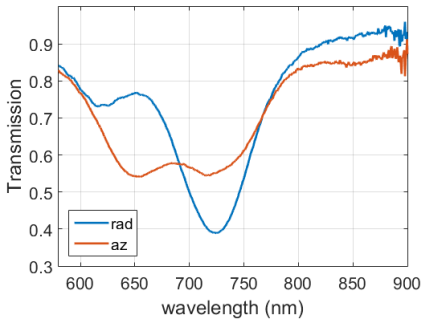	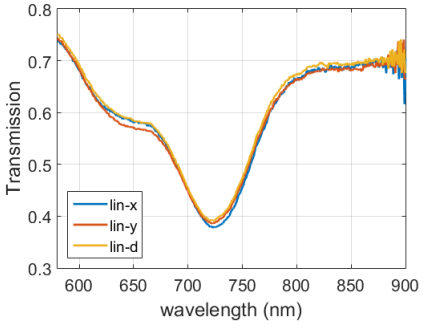

#R23-O3	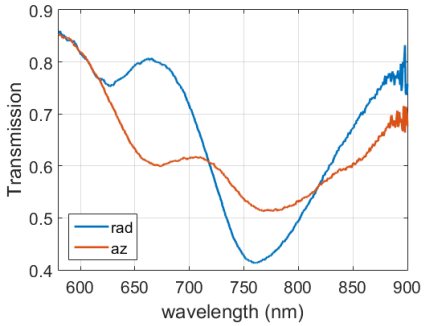	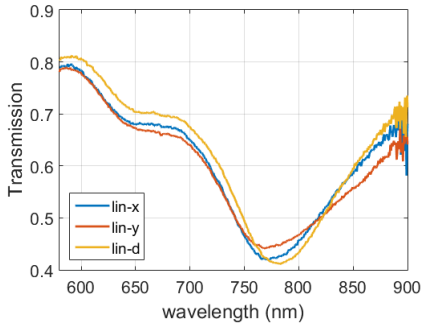
#R24-O3	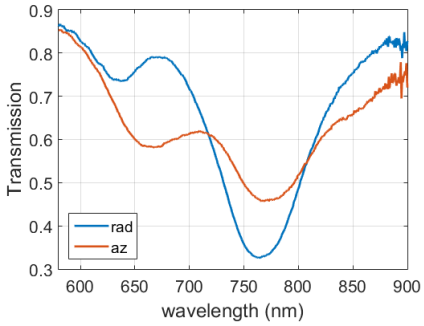	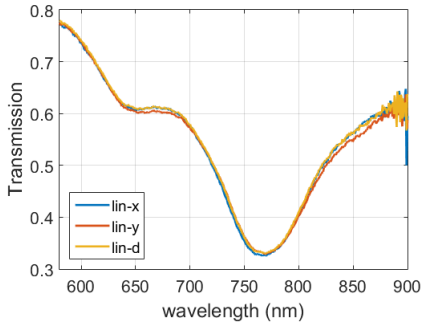
#R25-O3	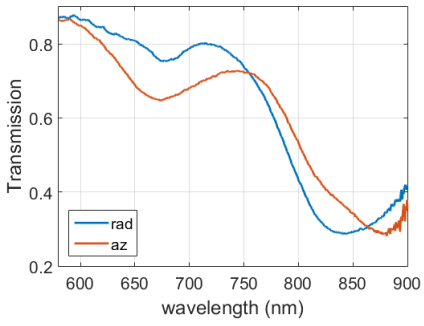	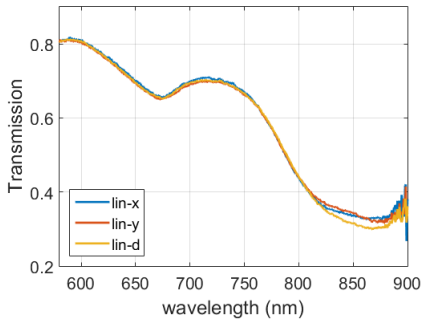
#R26-O3	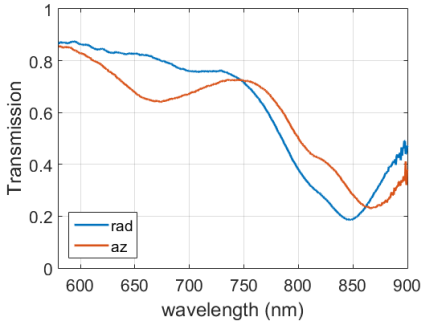	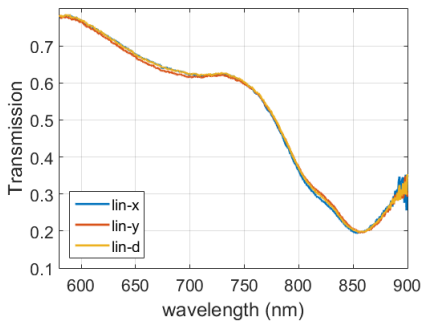

#R27-O3	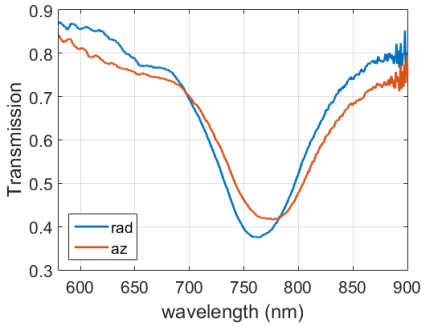	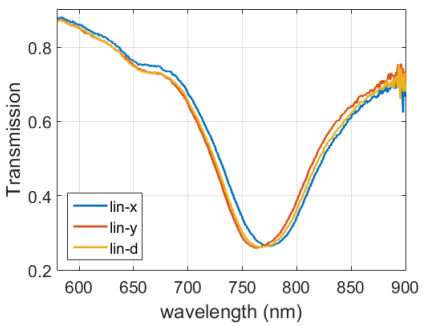
#R28-O3	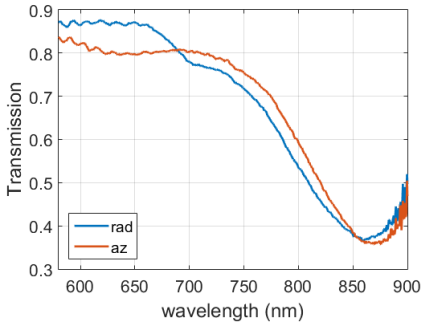	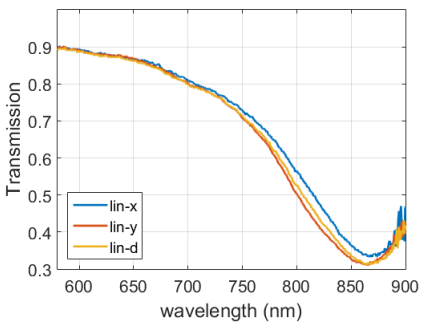
#A11-O3	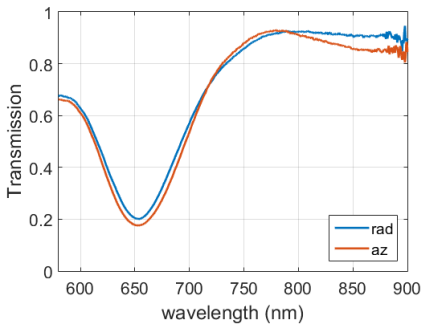	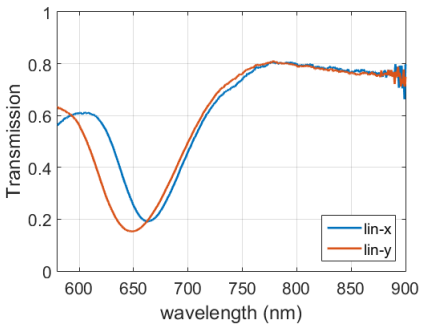
#A12-O3	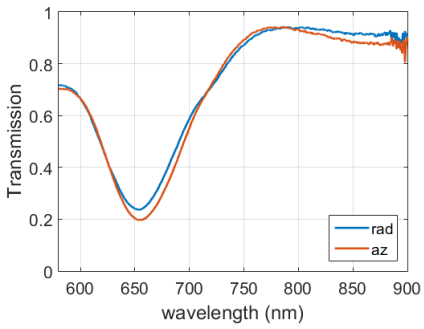	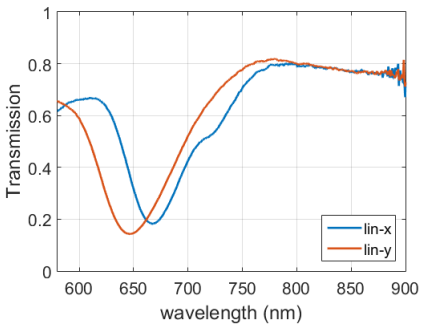

#A13-O3	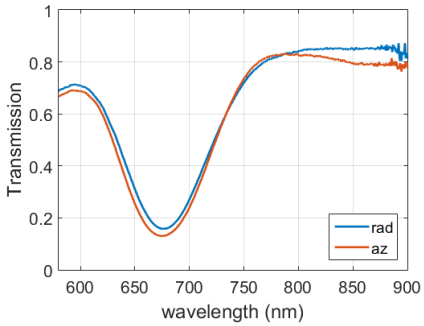	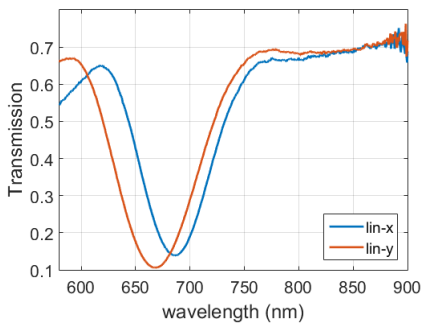
#A14-O3	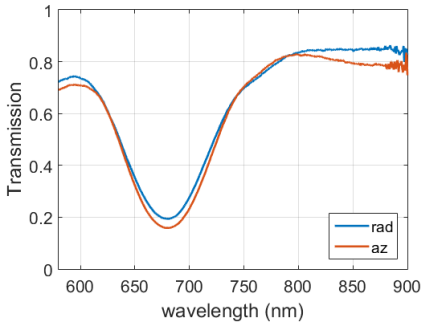	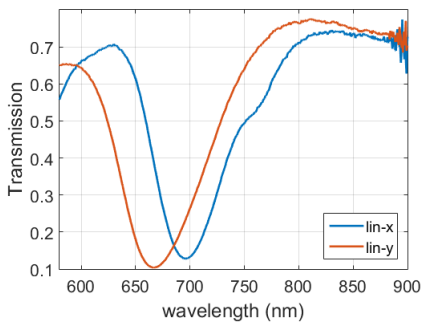
#A15-O3	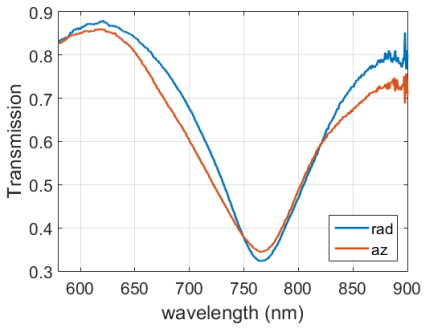	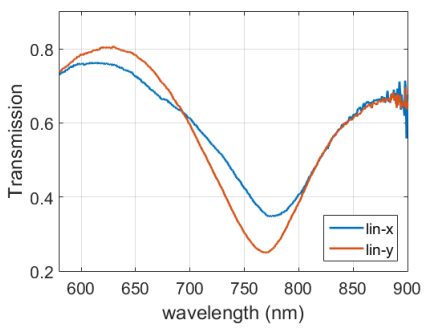
#A16-O3	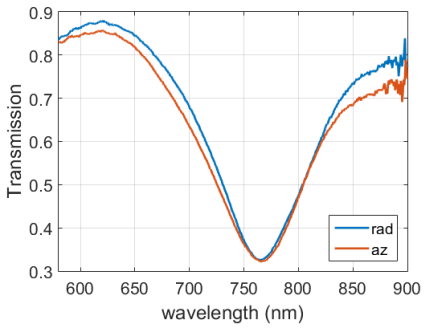	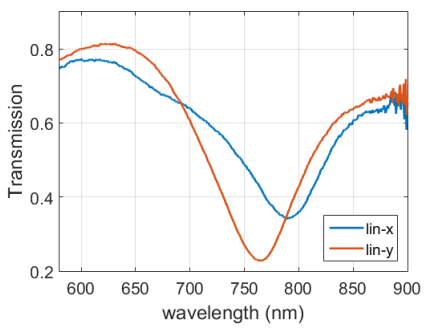

#A21-O3	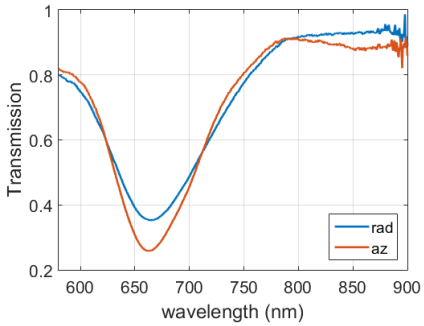	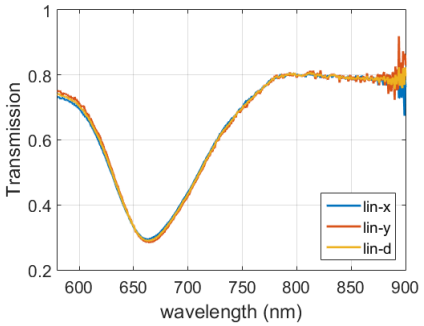
#A22-O3	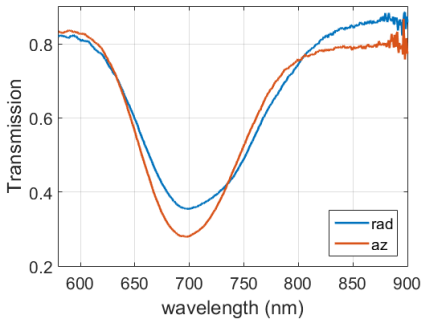	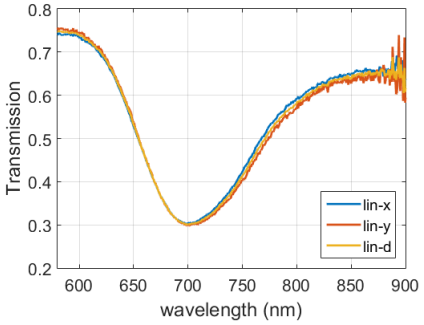
#A23-O3	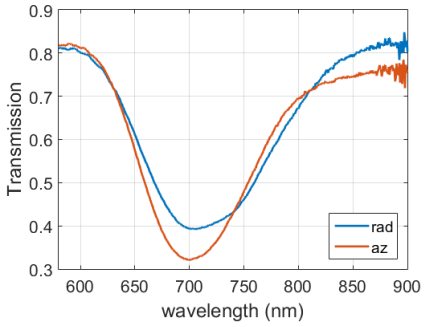	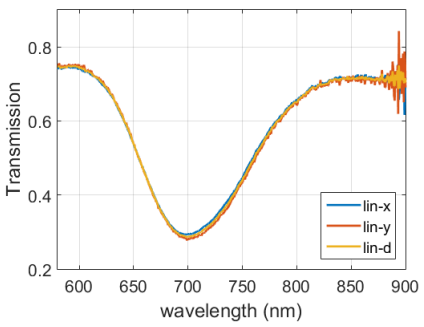
#A24-O3	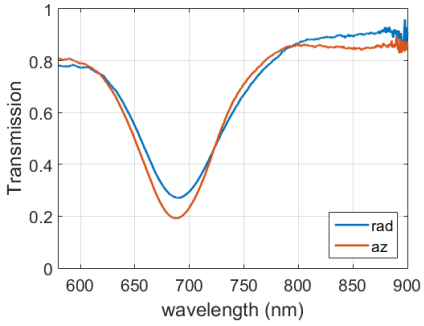	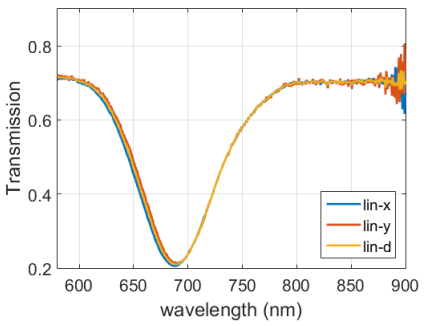

#A25-O3	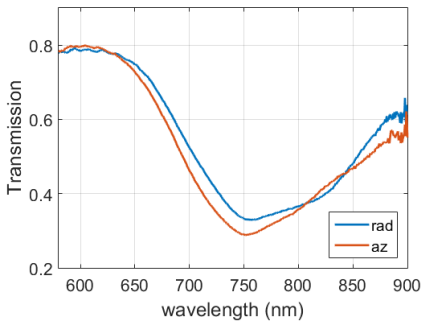	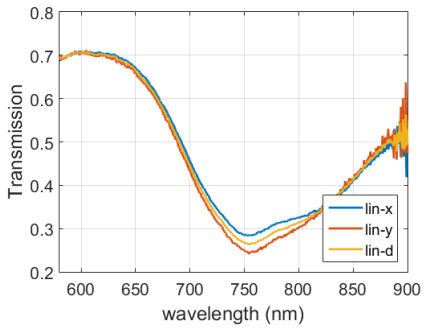
#A26-O3	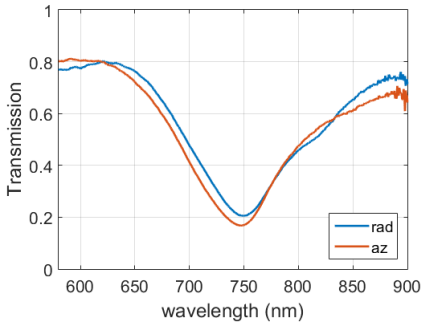	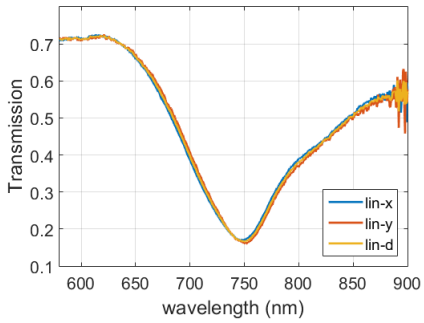

A.2 Reflection Spectra

Code	Radial/ Azimuthal Pol.	Linear Polarisation
#R11-O4	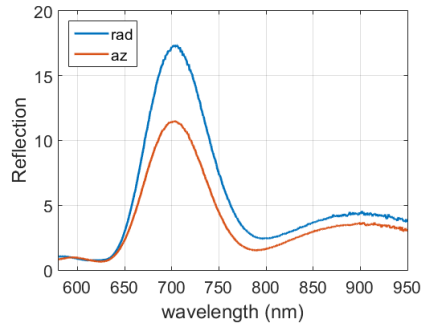	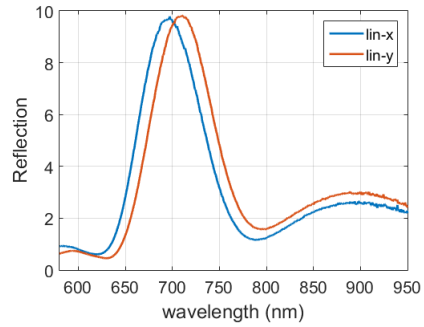
#R12-O4	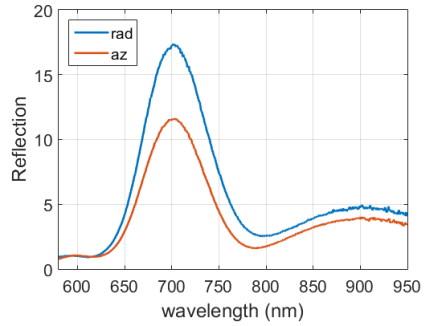	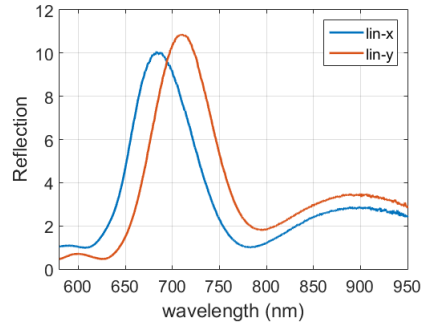

#R13-O4	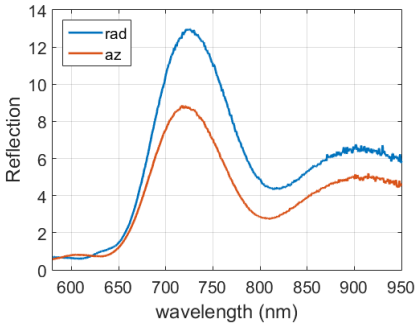	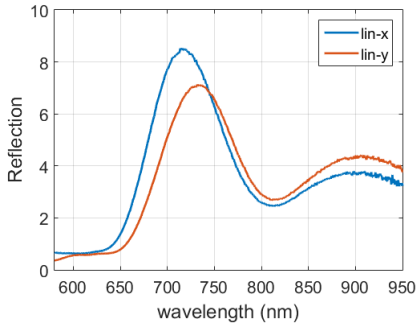
#R14-O4	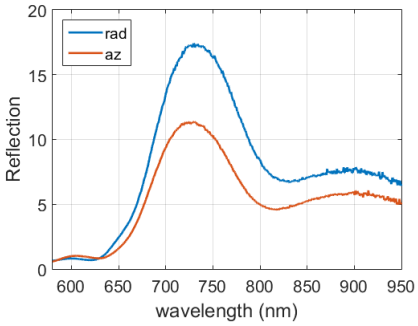	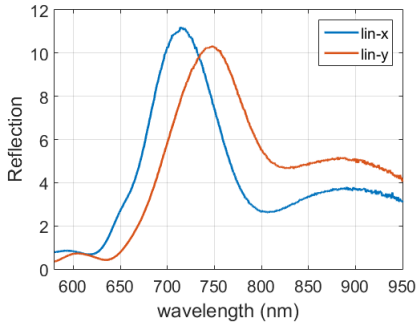
#R15-O4	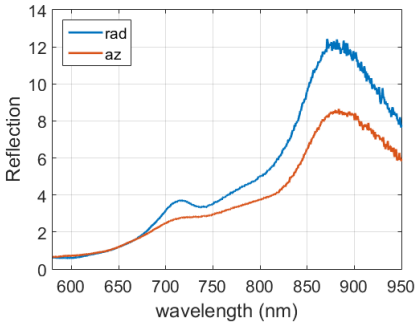	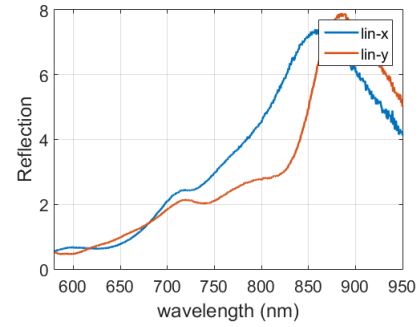
#R16-O4	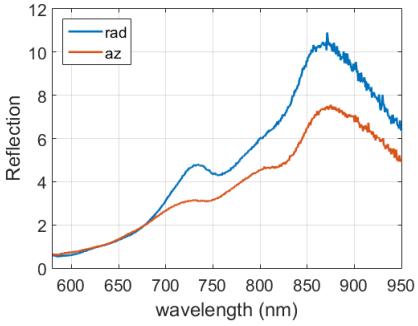	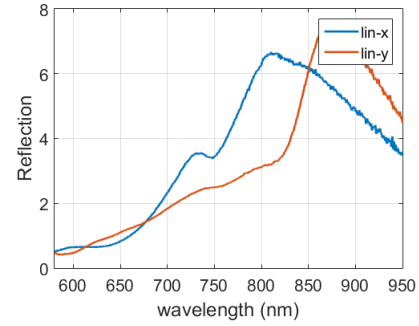

#R17-O4	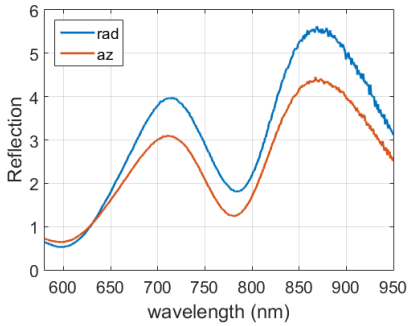	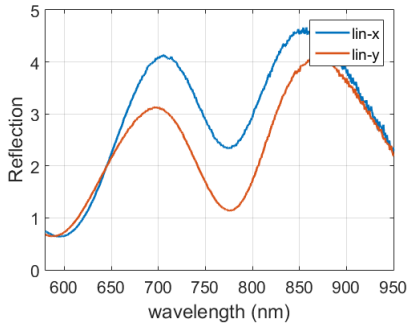
#R18-O4	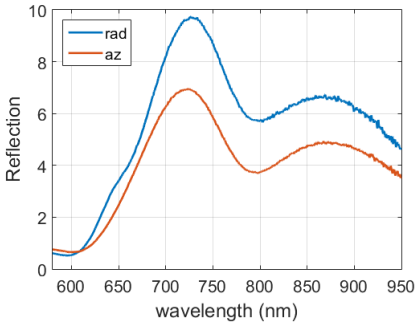	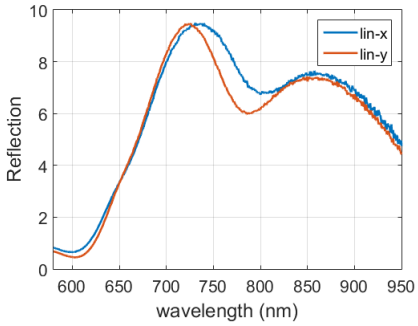
#R19-O4	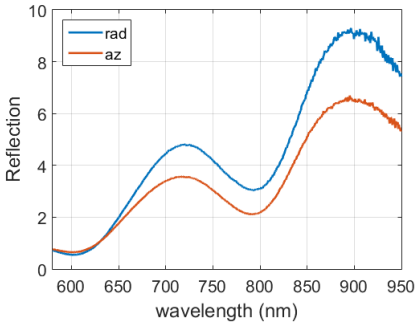	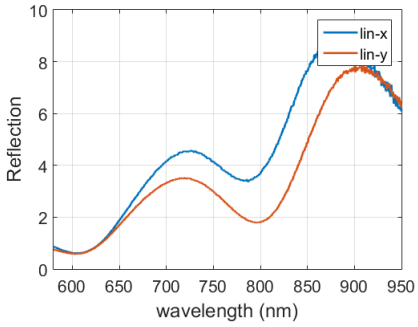
#R1A-O4	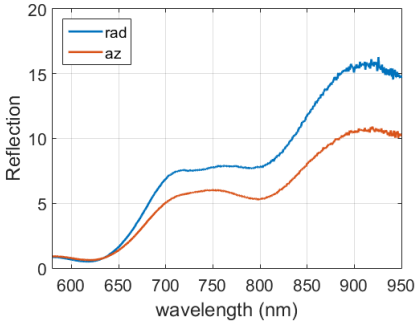	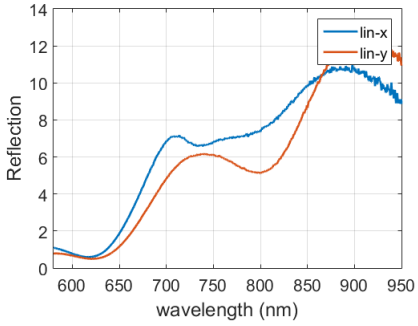

#R1B-O4	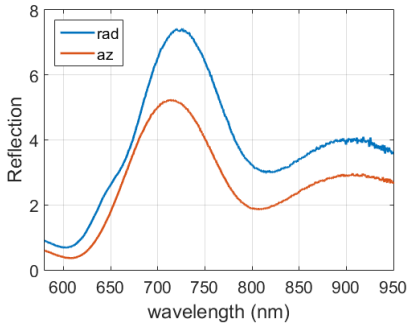	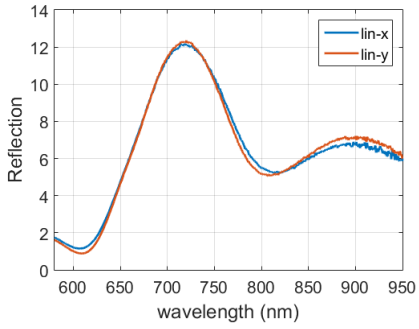
#R1C-O4	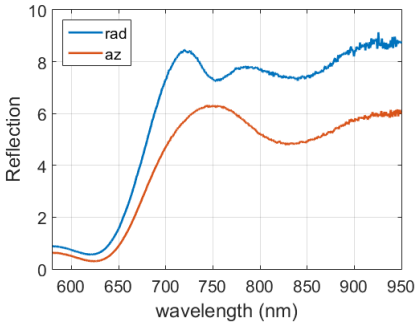	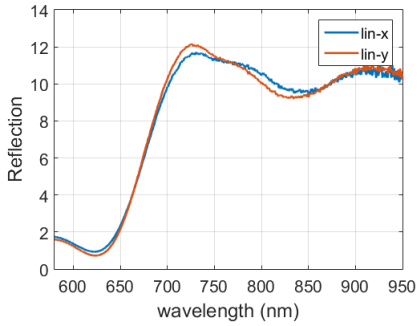
#R21-O4	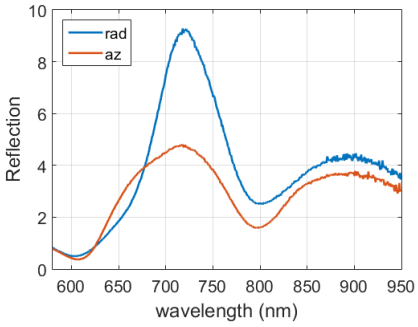	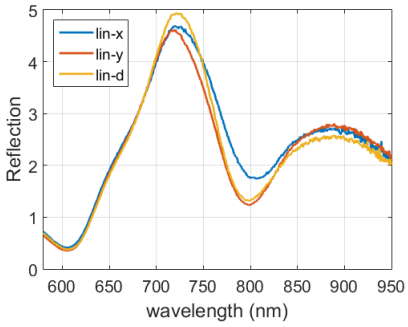
#R22-O4	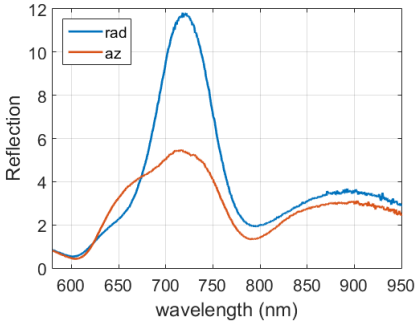	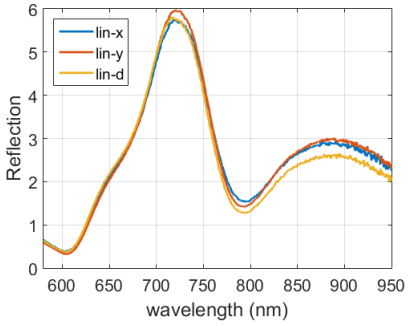

#R23-O4	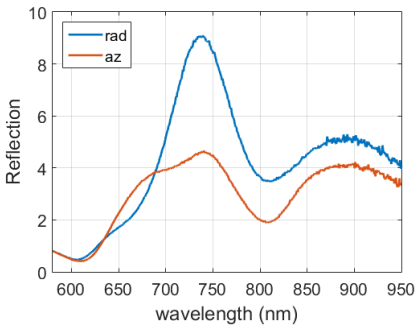	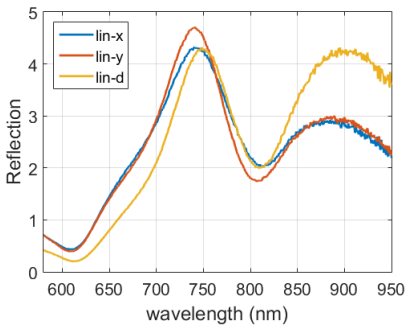
#R24-O4	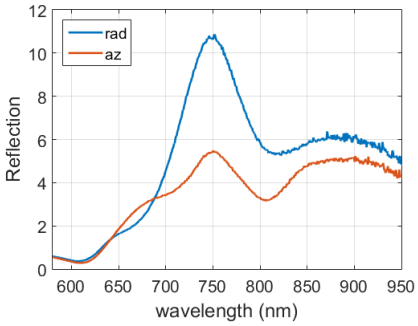	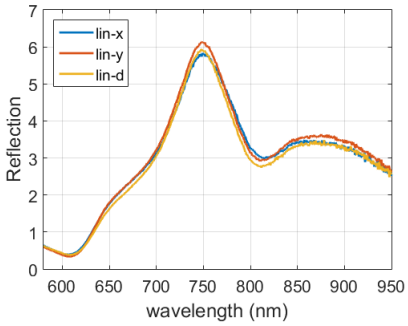
#R25-O4	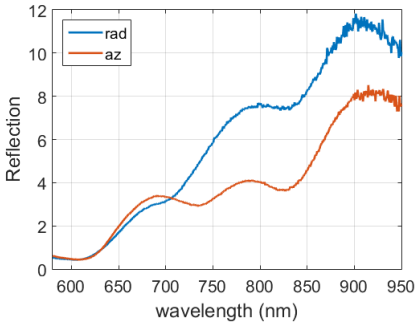	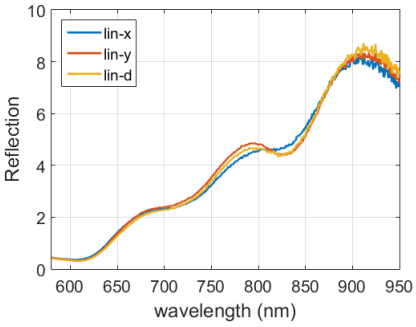
#R26-O4	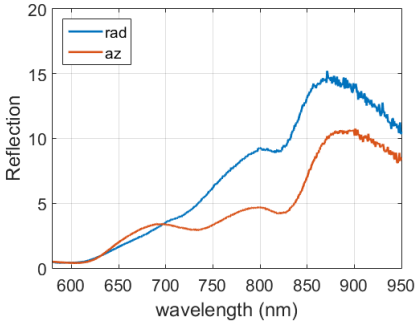	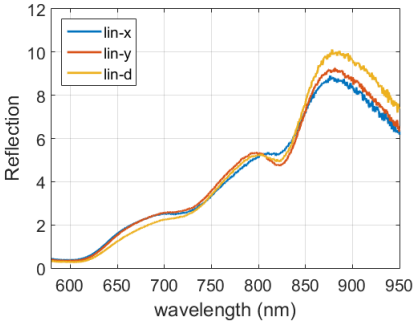

#R27-O4	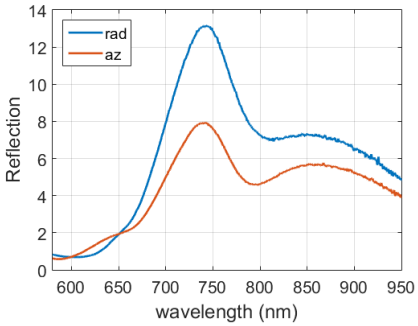	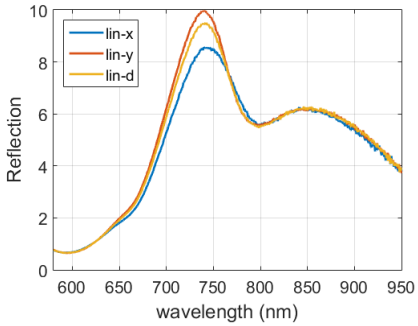
#R28-O4	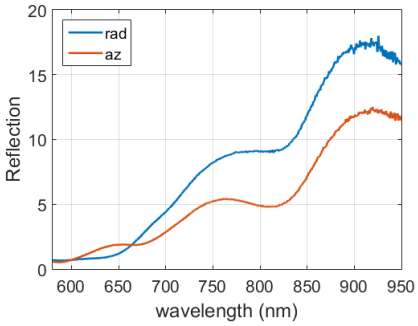	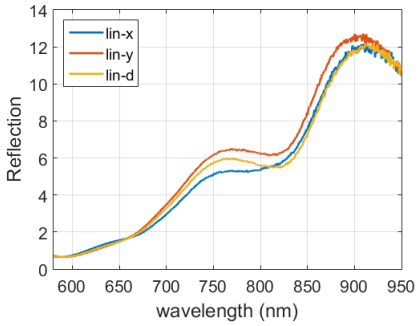
#A11-O4	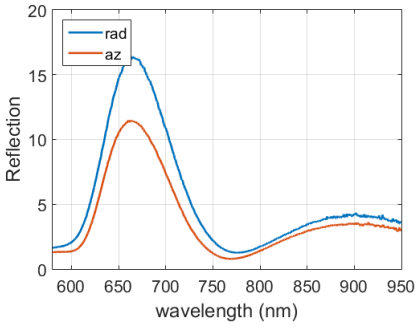	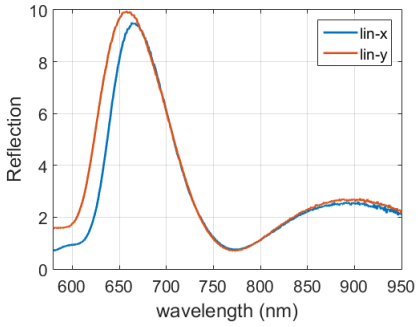
#A12-O4	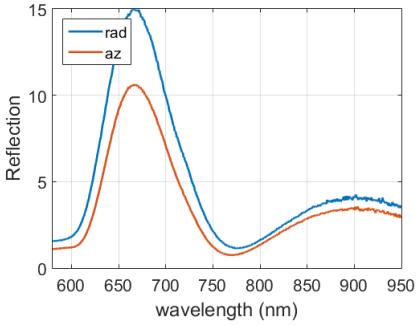	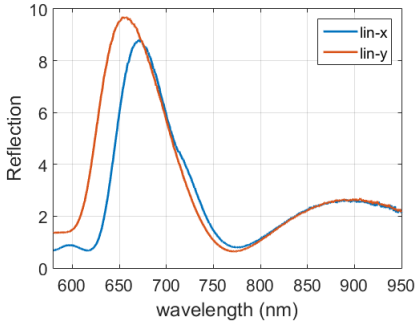

#A13-O4	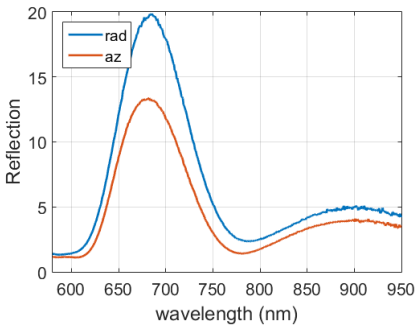	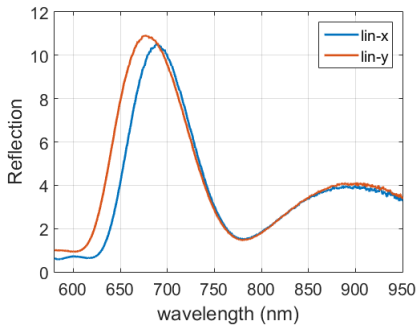
#A14-O4	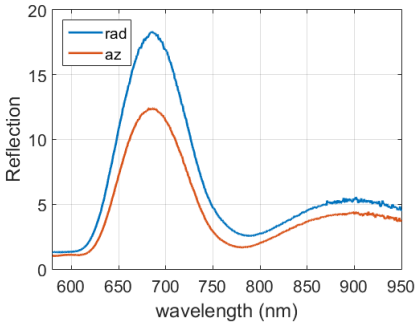	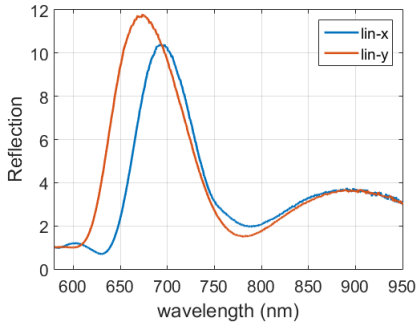
#A15-O4	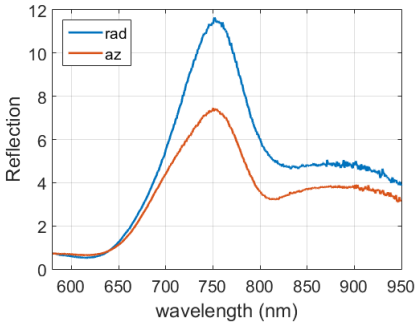	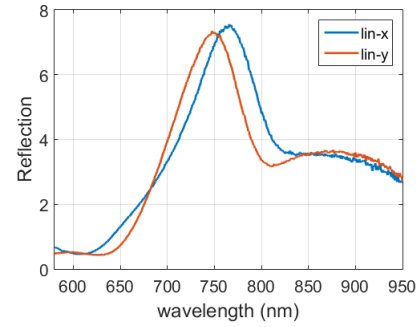
#A16-O4	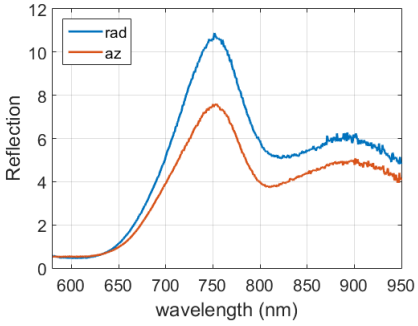	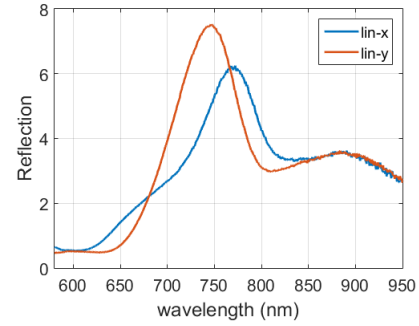

#A21-O4	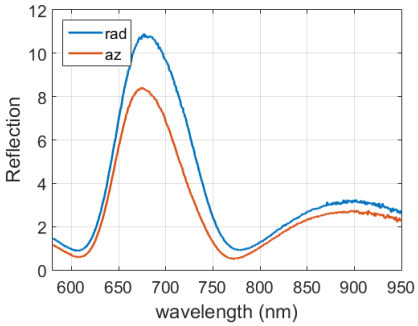	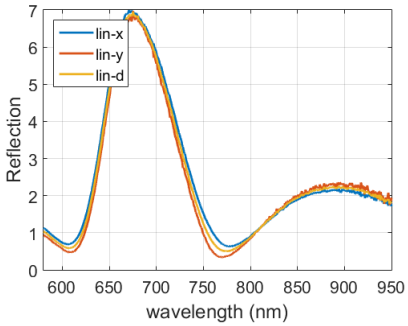
#A22-O4	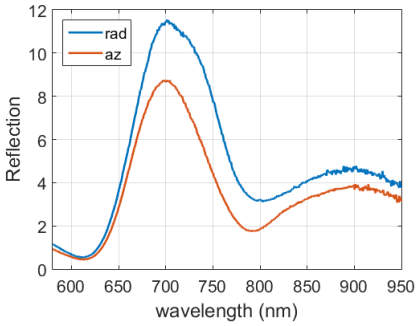	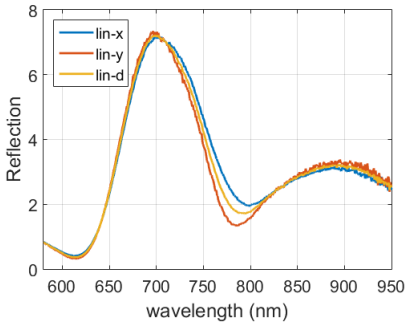
#A23-O4	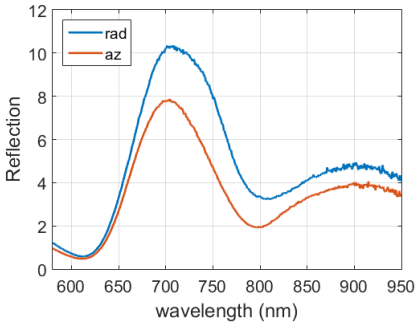	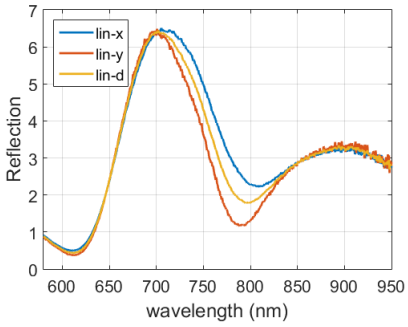
#A24-O4	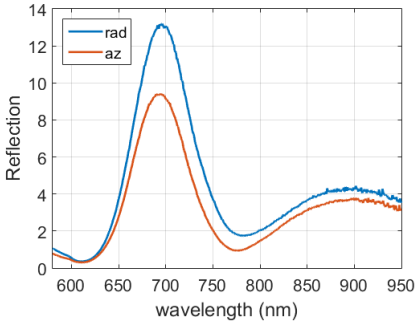	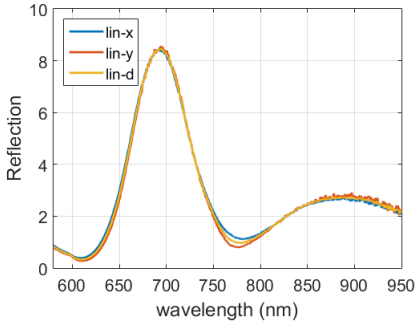

#A25-O4	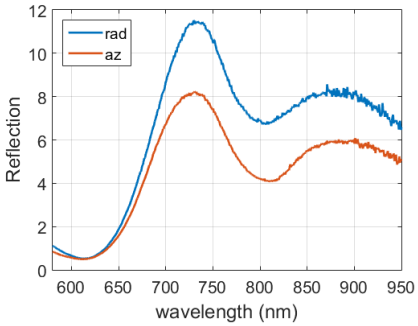	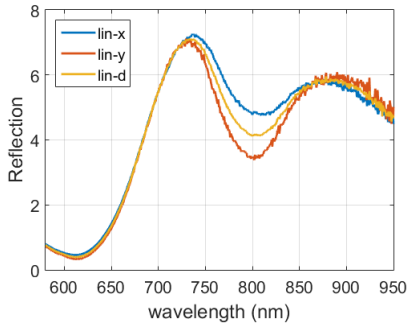
#A26-O4	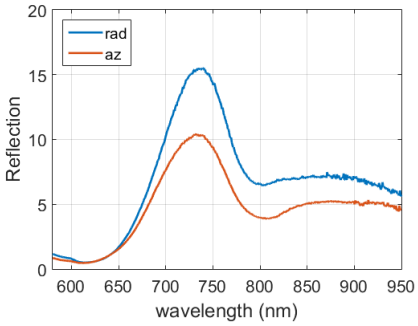	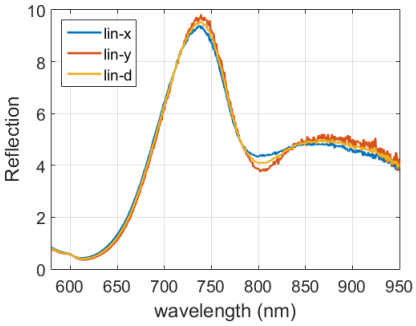
#R11-O5	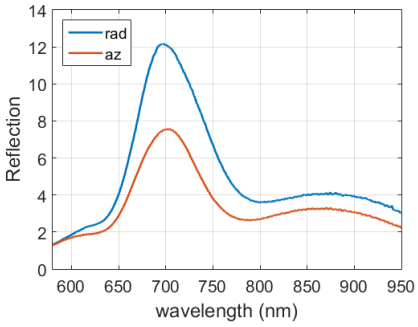	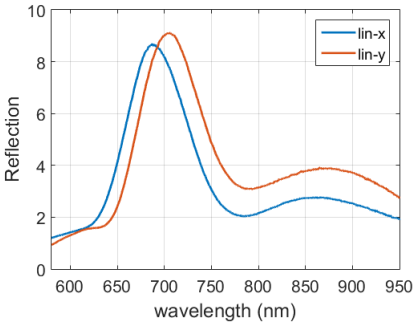
#R12-O5	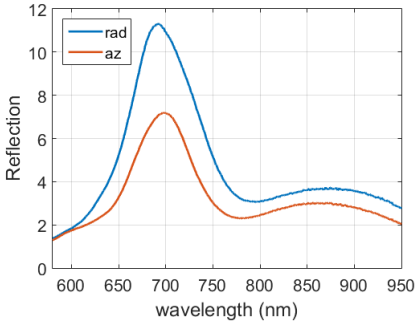	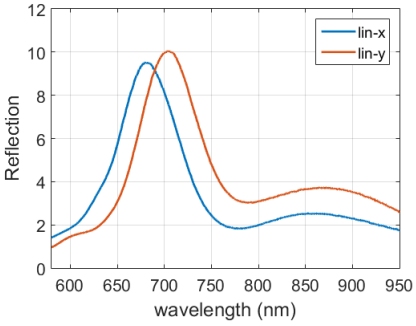

#R13-O5	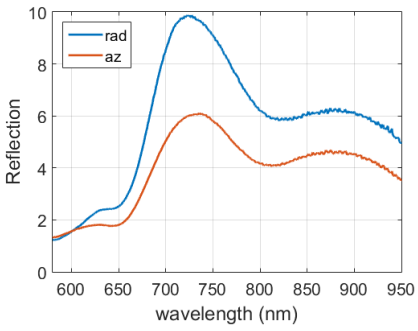	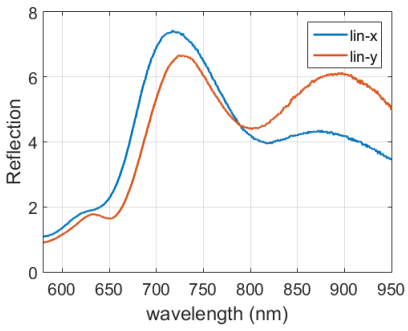
#R14-O5	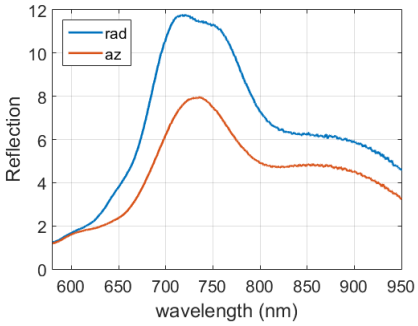	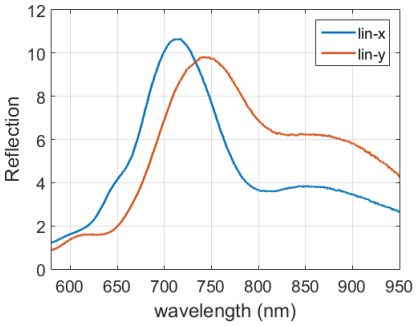
#R15-O5	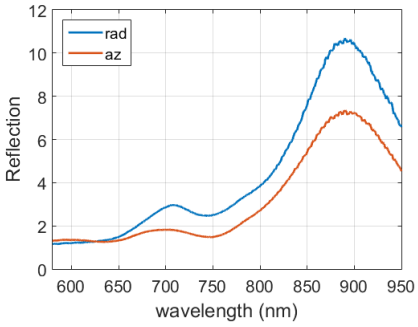	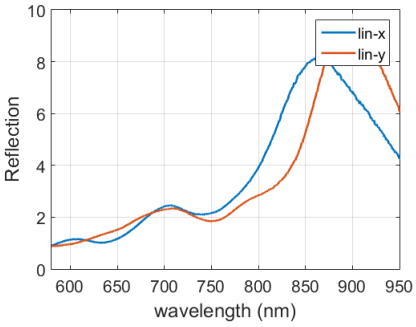
#R16-O5	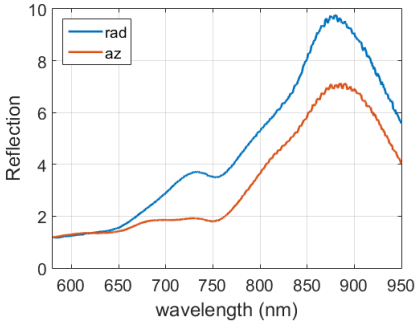	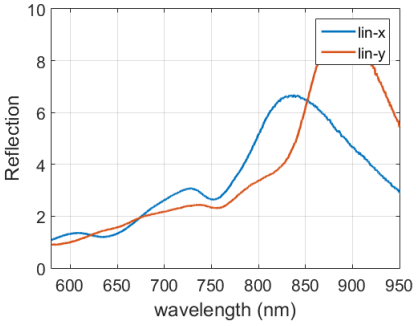

#R17-O5	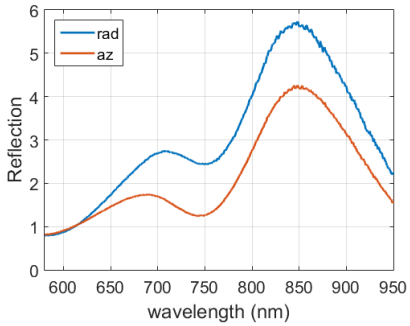	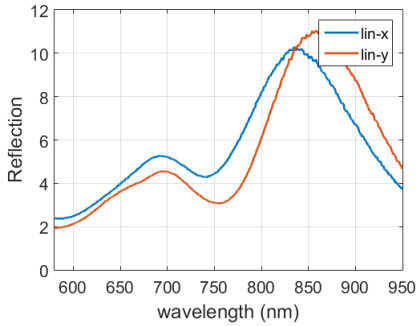
#R18-O5	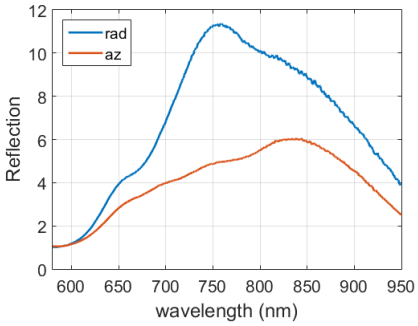	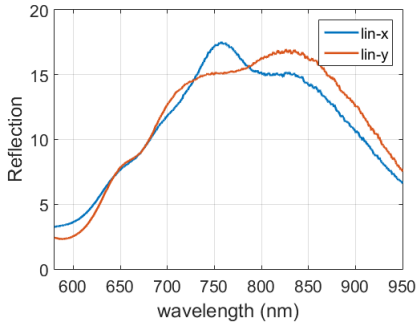
#R19-O5	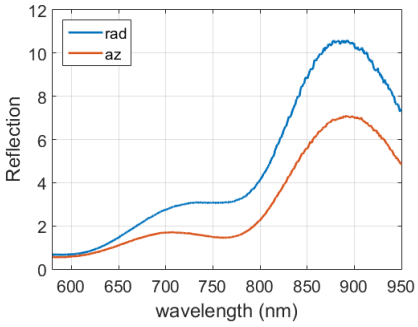	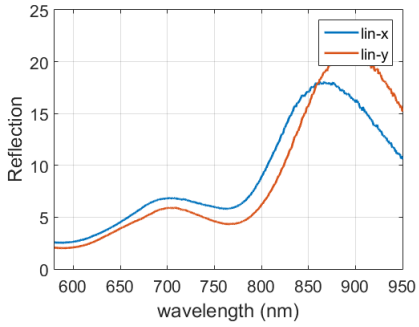
#R1A-O5	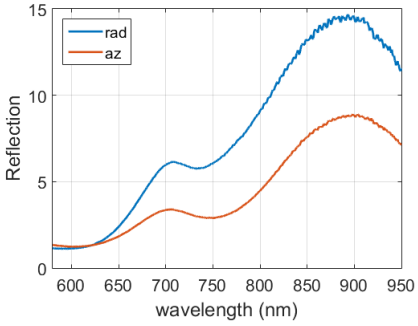	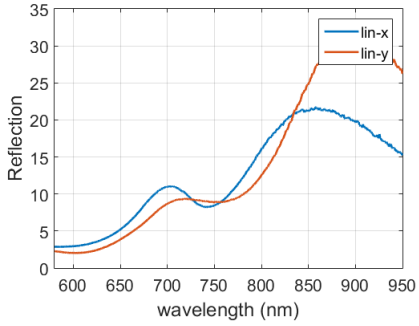

#R1B-O5	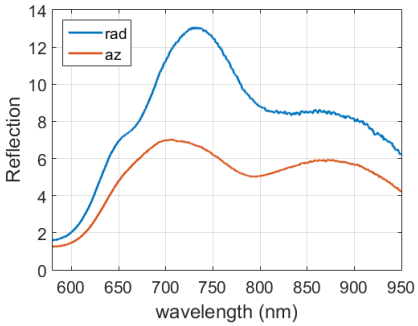	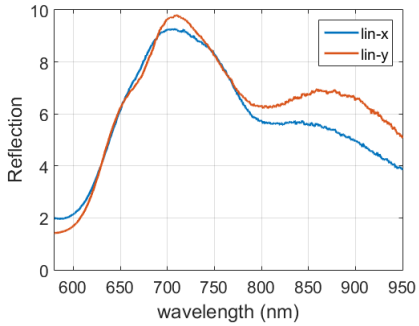
#R1C-O5	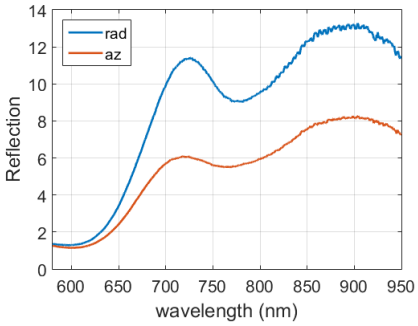	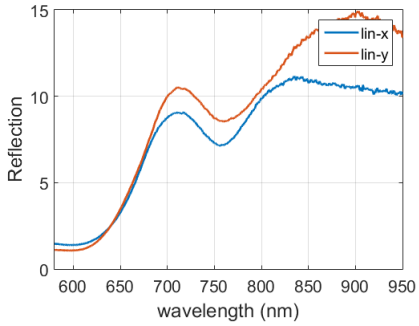
#R21-O5	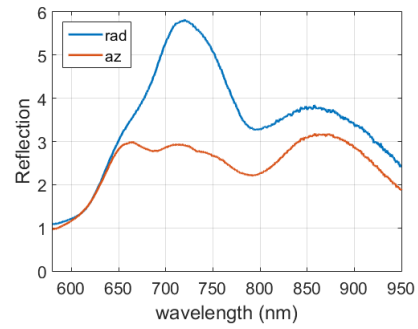	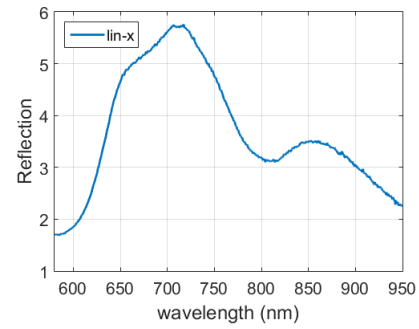
#R22-O5	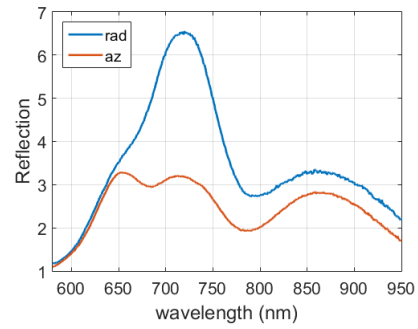	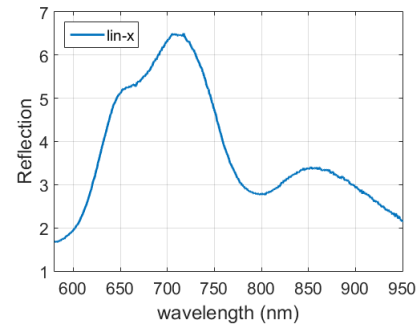

#R23-O5	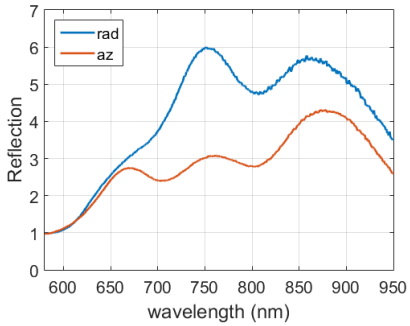	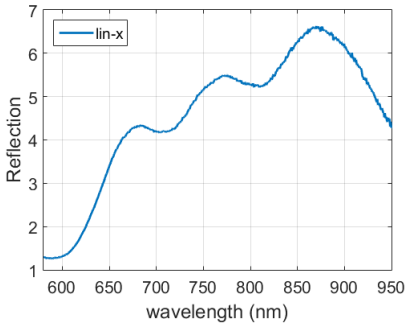
#R24-O5	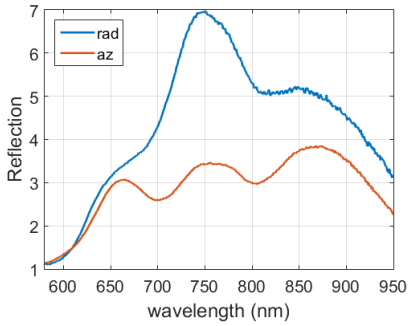	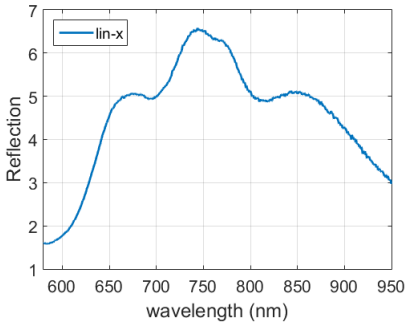
#R25-O5	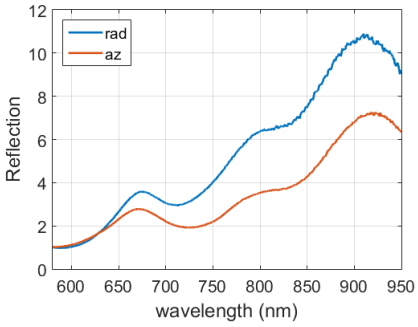	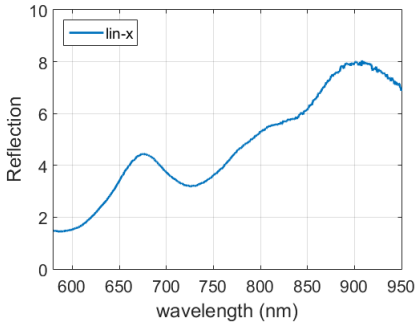
#R26-O5	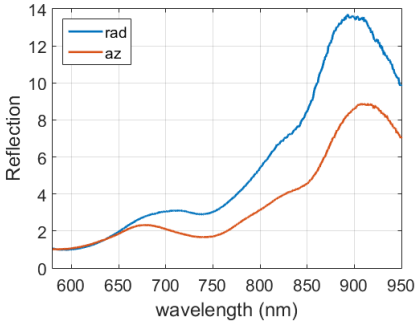	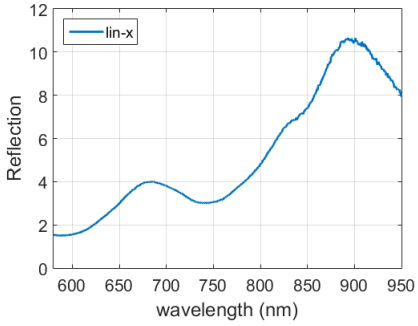

#R27-O5	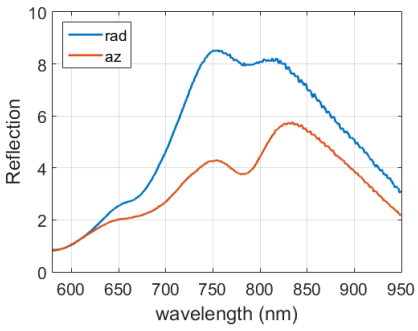	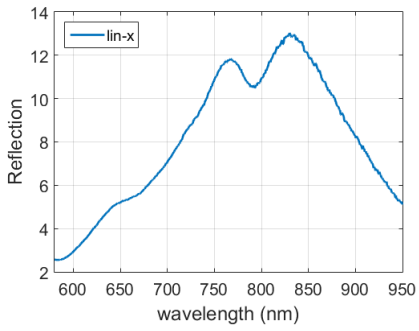
#R28-O5	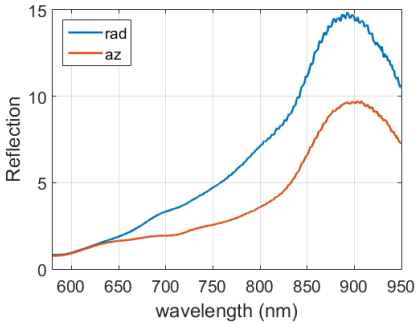	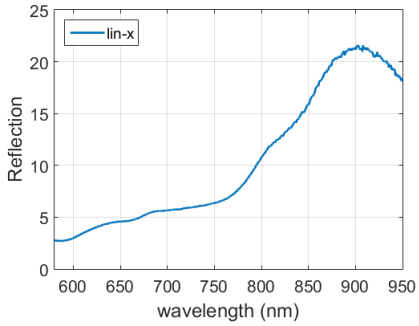
#A11-O5	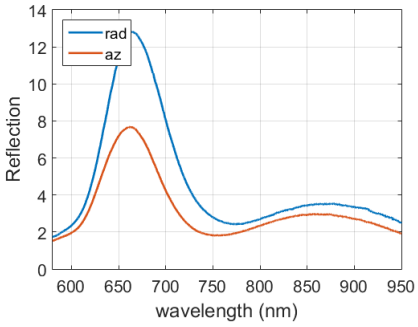	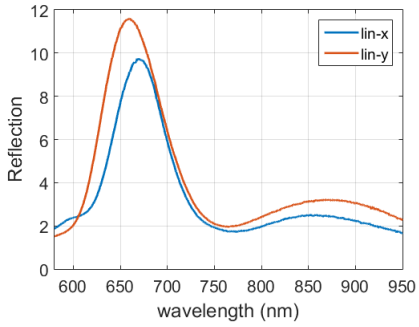
#A12-O5	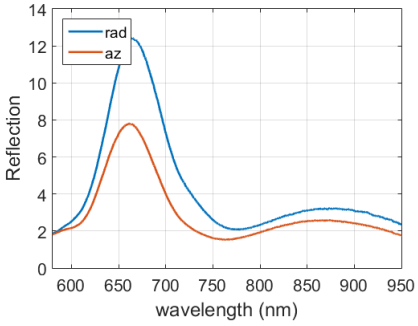	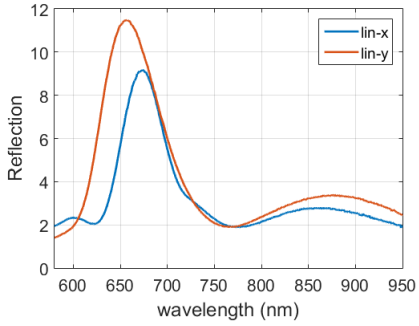

#A13-O5	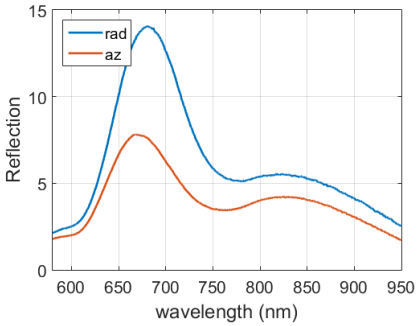	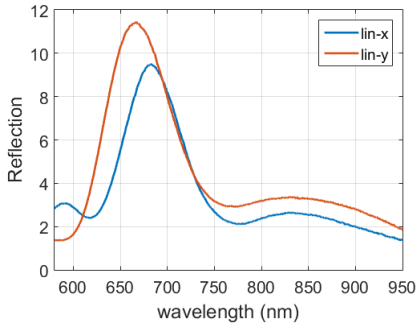
#A14-O5	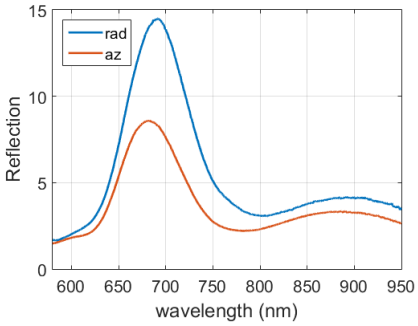	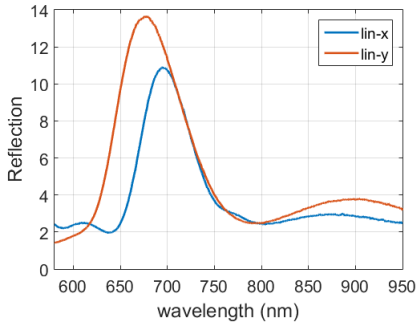
#A15-O5	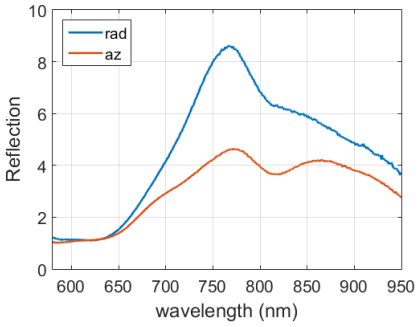	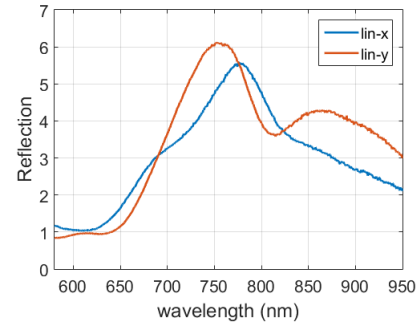
#A16-O5	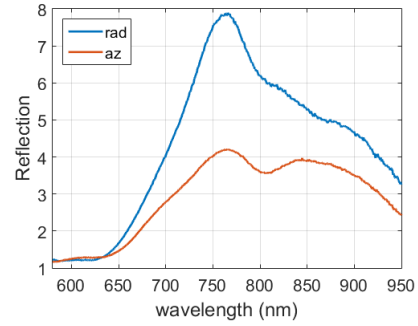	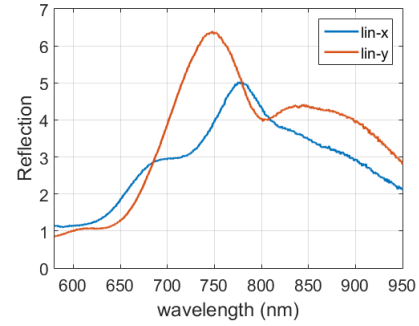

#A21-O5	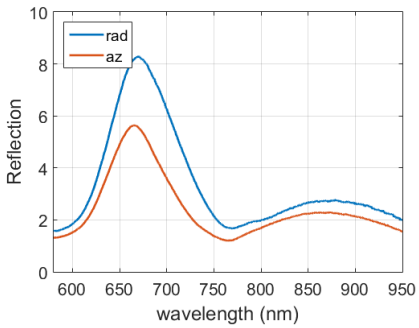	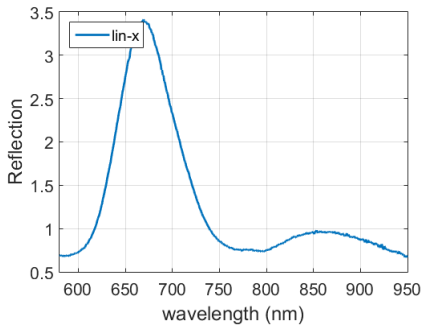
#A22-O5	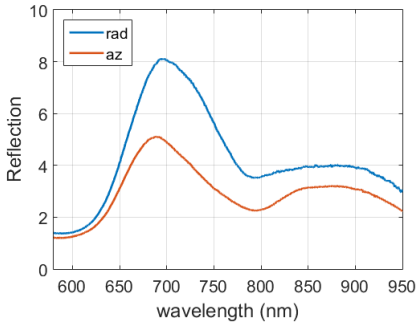	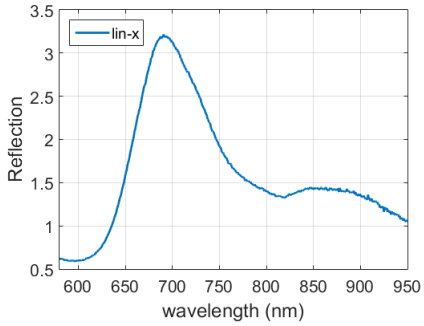
#A23-O5	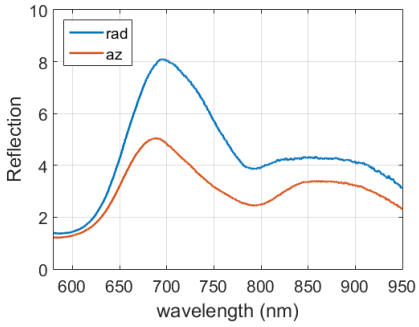	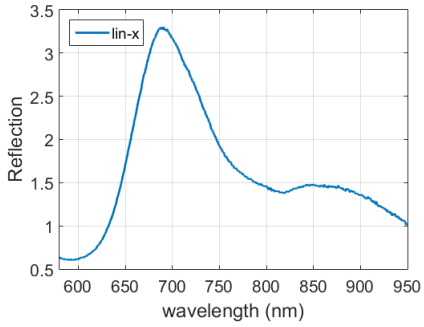
#A24-O5	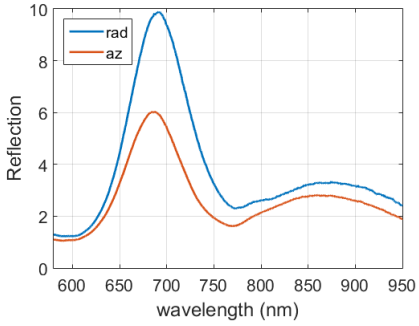	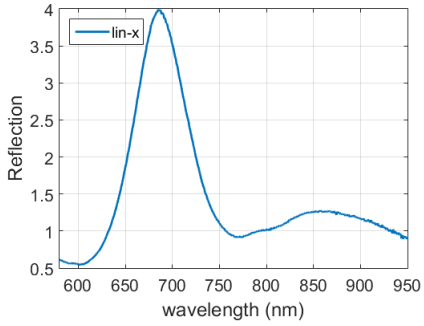

#A25-O5	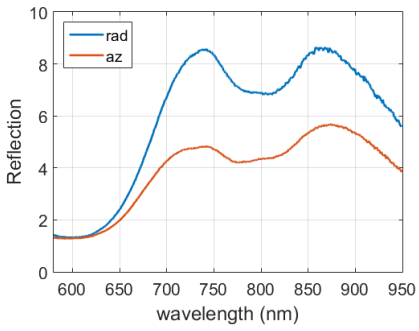 rad az Reflection wavelength (nm)	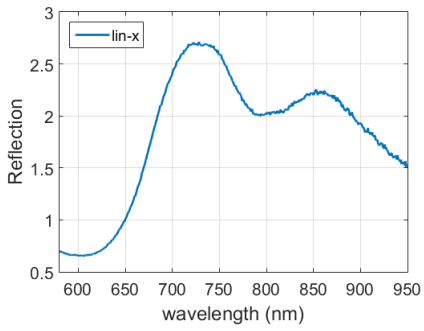 lin-x Reflection wavelength (nm)
#A26-O5	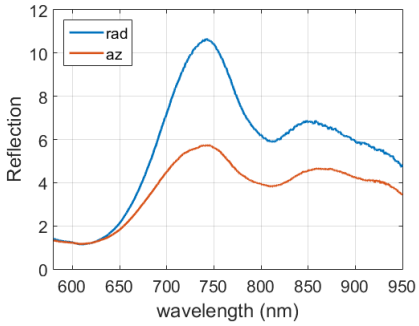 rad az Reflection wavelength (nm)	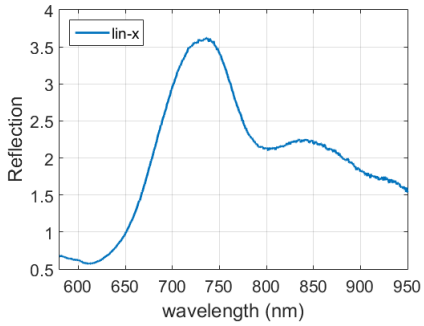 lin-x Reflection wavelength (nm)

Appendix B

Far-Field Images of the Reflected Beams from the Metasurfaces

B.1 Beam Profiles at Resonances of Radial and Dipole Modes

1. #R11, $\lambda_{rad} = 610$ nm, $\lambda_{dip} = 700$ nm

Code/ λ	Polarisation	Reflected Beam	Reference Beam	Normalised Reflected Beam
#R11/ 610 nm	linear-x	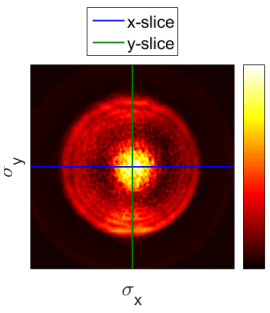	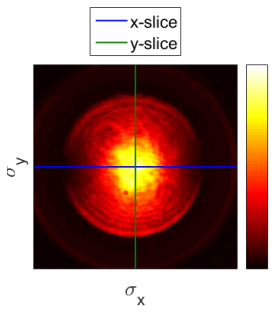	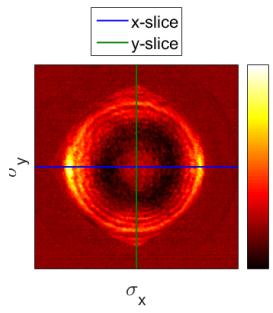

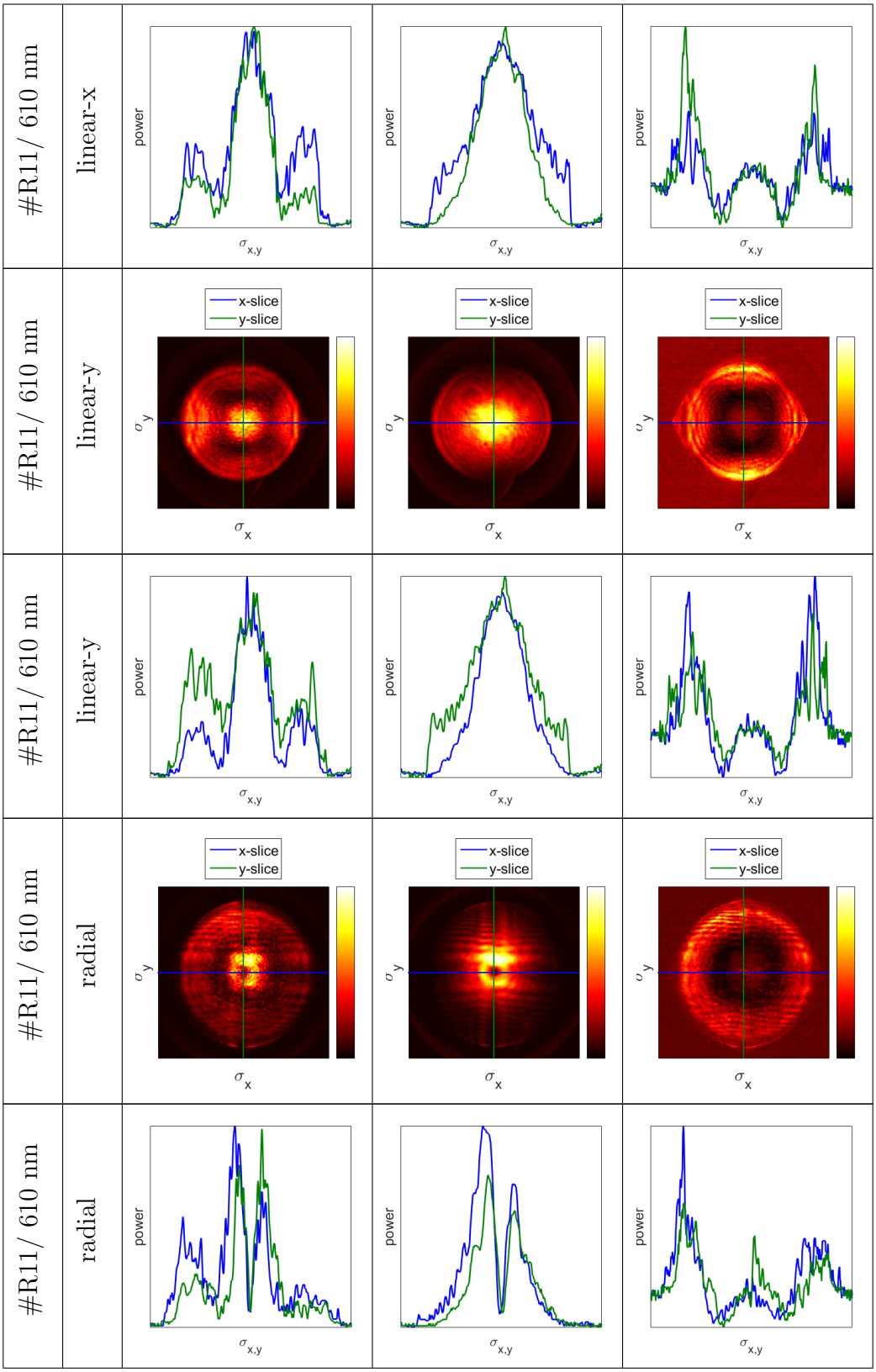
#R11/ 610 nm
linear-x
power
σx,y
#R11/ 610 nm
linear-y
x-slice
y-slice
σy
σx
#R11/ 610 nm
linear-y
power
σx,y
#R11/ 610 nm
radial
x-slice
y-slice
σy
σx
#R11/ 610 nm
radial
power
σx,y

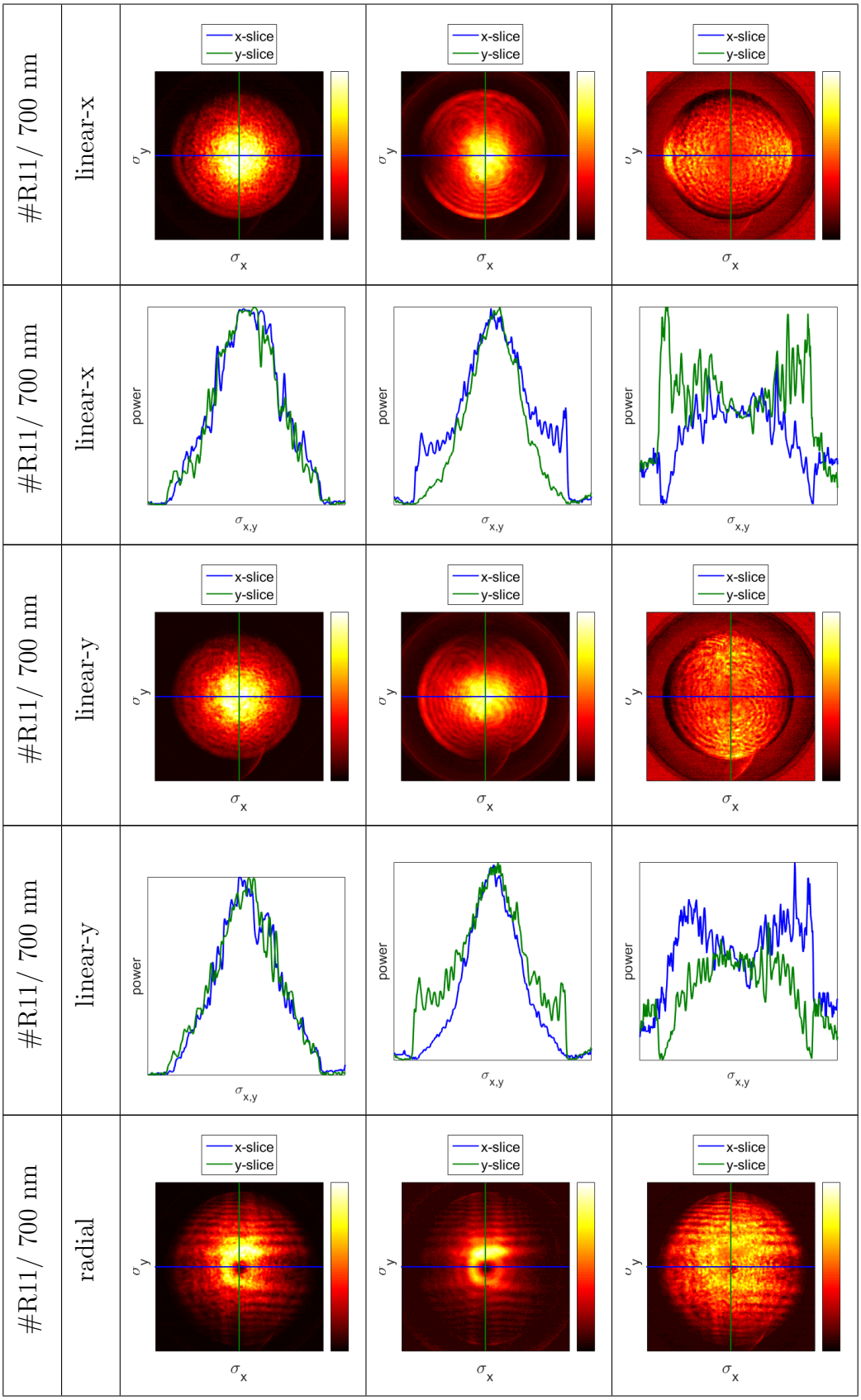
#R11/ 700 nm
linear-x
x-slice
y-slice
σ y
σ x
#R11/ 700 nm
linear-x
power
σ x,y
#R11/ 700 nm
linear-y
x-slice
y-slice
σ y
σ x
#R11/ 700 nm
linear-y
power
σ x,y
#R11/ 700 nm
radial
x-slice
y-slice
σ y
σ x

#R11/ 700 nm	radial	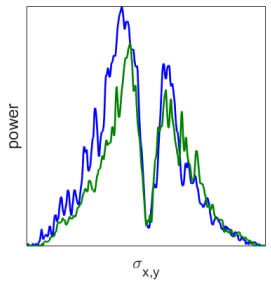	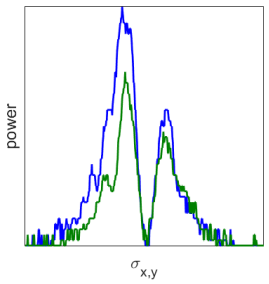	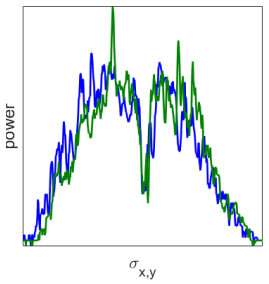

2. #R13, $\lambda_{rad} = 620$ nm, $\lambda_{dip} = 750$ nm

Code/ λ	Polarisation	Reflected Beam	Reference Beam	Normalised Reflected Beam
#R13/ 620 nm	linear-x	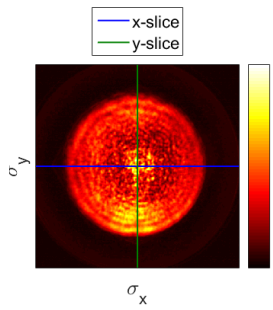	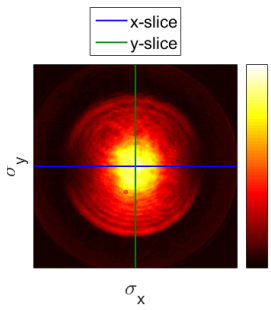	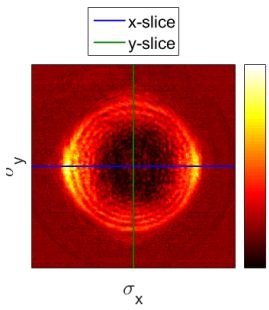
#R13/ 620 nm	linear-x	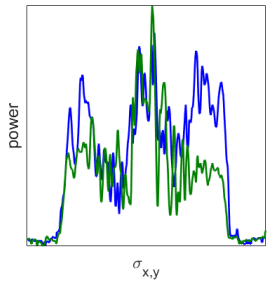	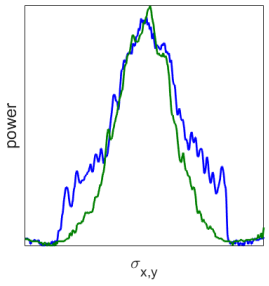	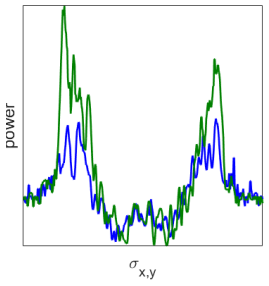
#R13/ 620 nm	linear-y	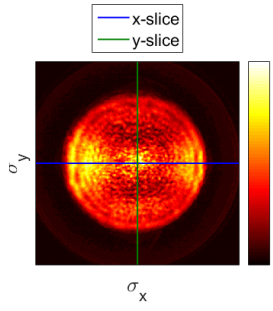	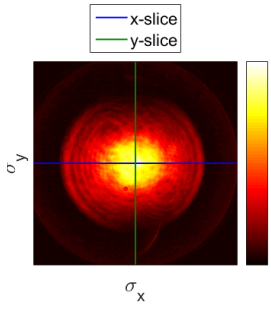	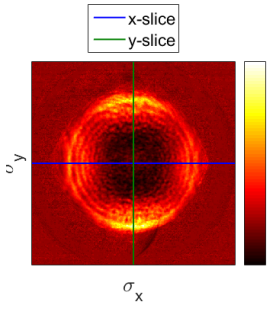

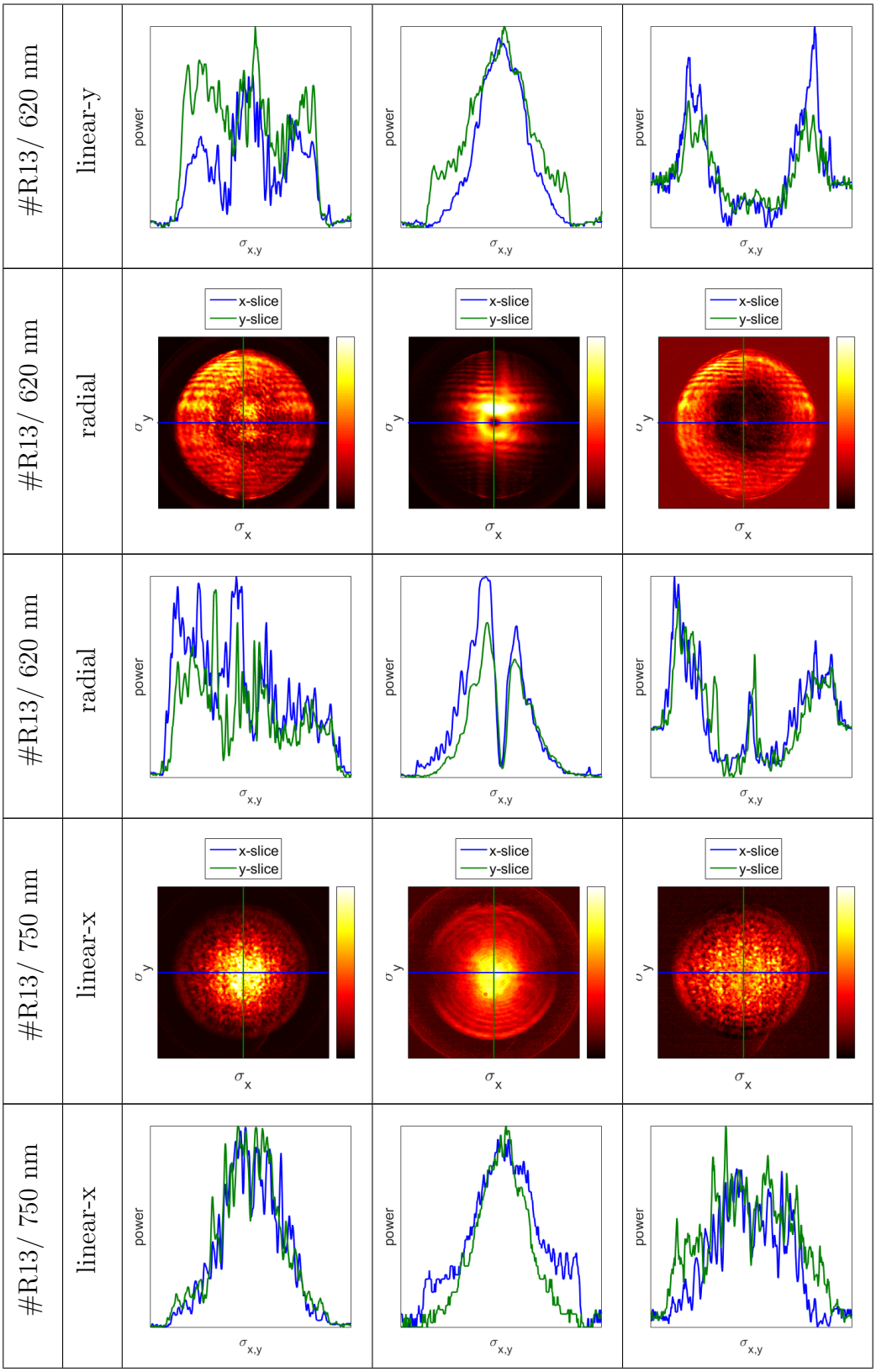
#R13/ 620 nm
linear-y
power
σx,y
#R13/ 620 nm
radial
x-slice
y-slice
σy
σx
#R13/ 620 nm
radial
power
σx,y
#R13/ 750 nm
linear-x
x-slice
y-slice
σy
σx
#R13/ 750 nm
linear-x
power
σx,y

#R13/ 750 nm	radial	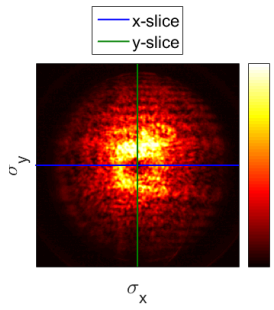	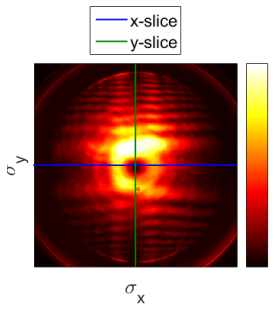	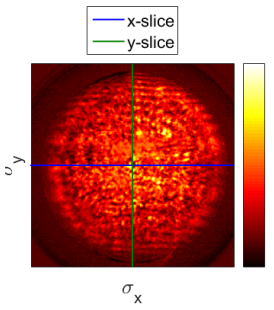
#R13/ 750 nm	radial	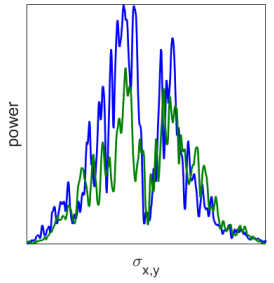	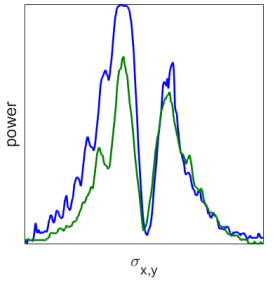	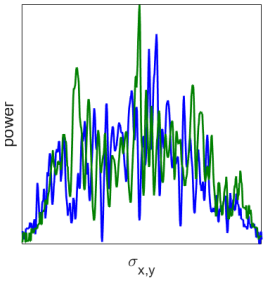

3. #R15, $\lambda_{rad} = 720$ nm, $\lambda_{dip} = 880$ nm

Code/ λ	Polarisation	Reflected Beam	Reference Beam	Normalised Reflected Beam
#R15/ 720 nm	radial	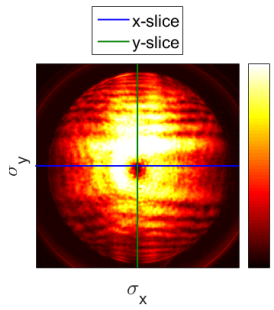	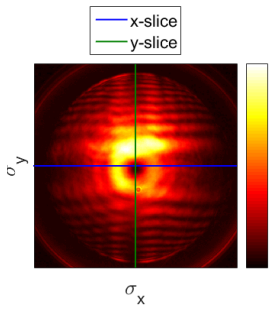	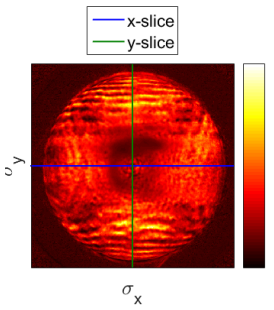
#R15/ 720 nm	radial	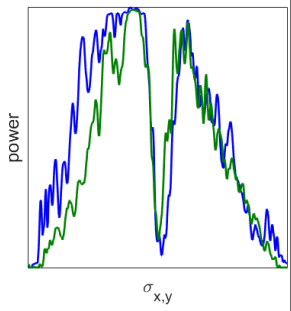	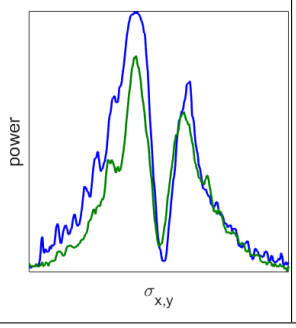	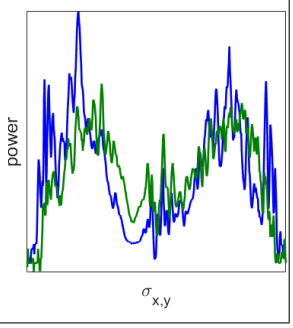

#R15/ 820 nm	radial	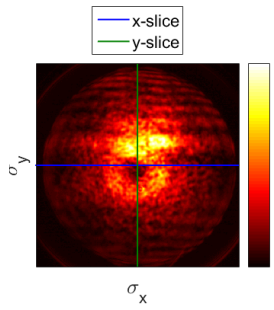	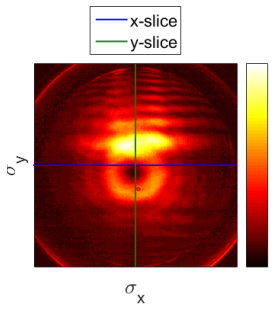	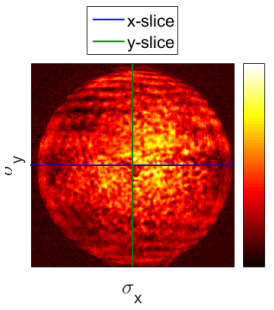
#R15/ 820 nm	radial	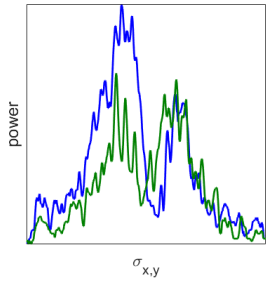	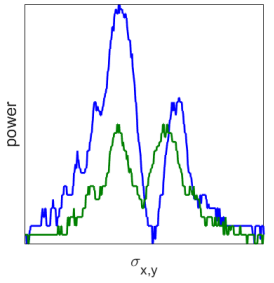	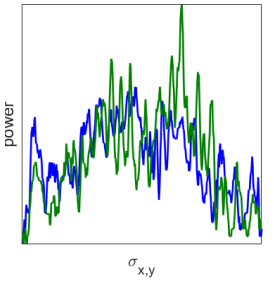

4. #R18, $\lambda_{rad} = 650$ nm, $\lambda_{dip} = 750$ nm

Code/ λ	Polarisation	Reflected Beam	Reference Beam	Normalised Reflected Beam
#R18/ 650 nm	linear-x	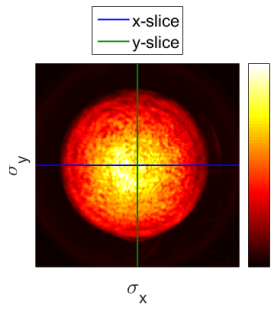	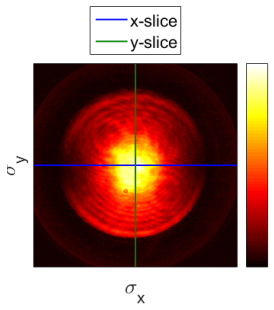	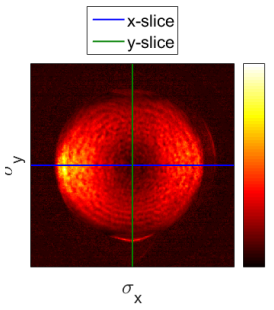
#R18/ 650 nm	linear-x	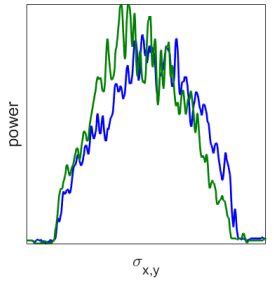	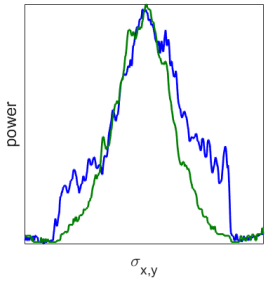	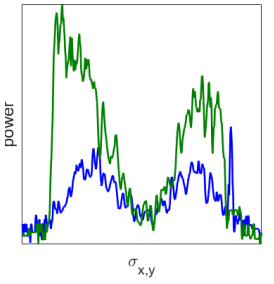

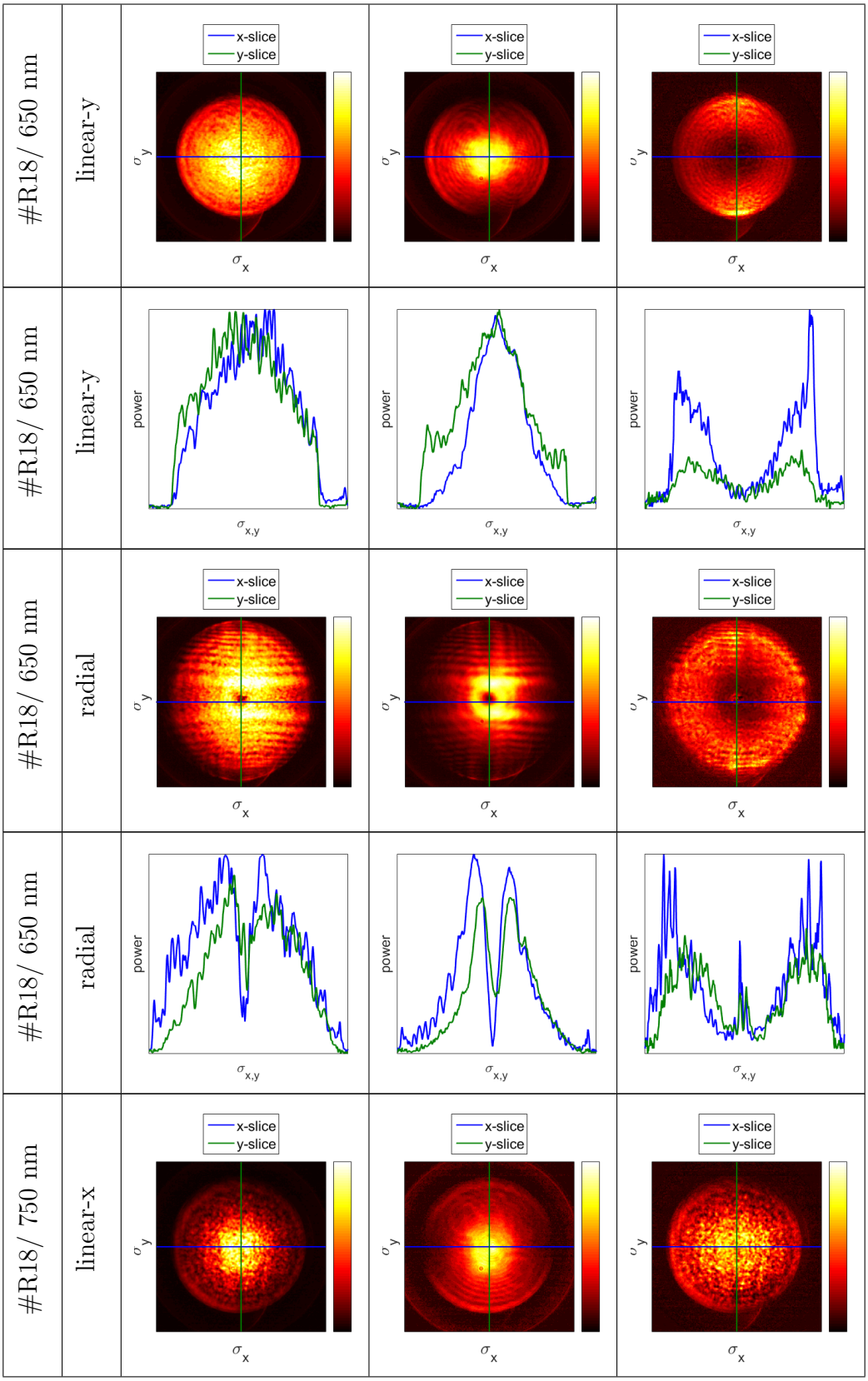
#R18/ 650 nm
linear-y
x-slice
y-slice
σ y
σ x
power
σ x,y
#R18/ 650 nm
linear-y
#R18/ 650 nm
radial
#R18/ 650 nm
radial
#R18/ 750 nm
linear-x

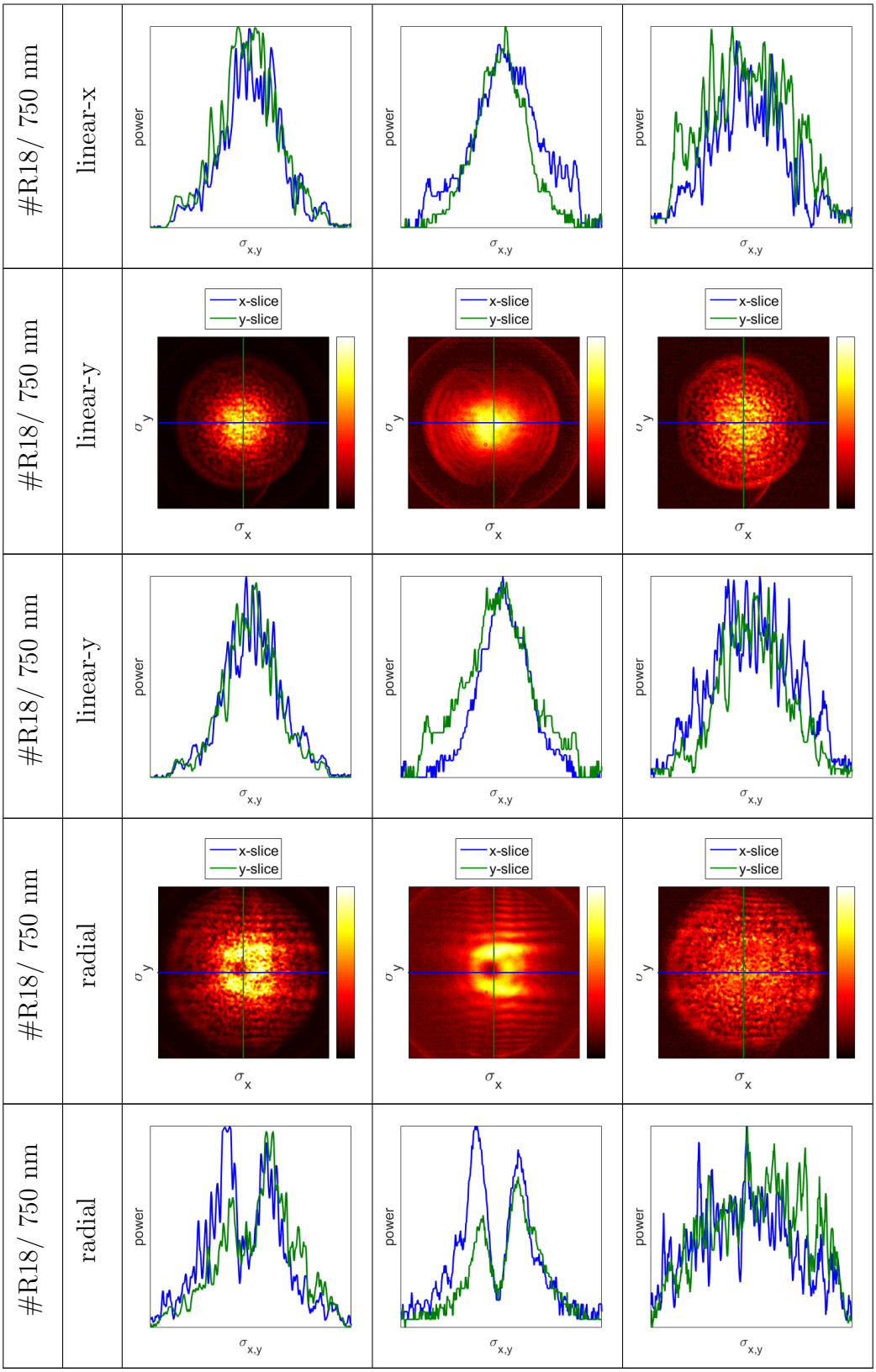
#R18/ 750 nm
linear-x
#R18/ 750 nm
linear-y
#R18/ 750 nm
linear-y
#R18/ 750 nm
radial
#R18/ 750 nm
radial
power
σx,y
x-slice
y-slice
σy
σx

5. #R25, $\lambda_{rad} = 675$ nm, $\lambda_{dip} = 830$ nm

Code/ λ	Polarisation	Reflected Beam	Reference Beam	Normalised Reflected Beam
#R25/ 675 nm	linear-x	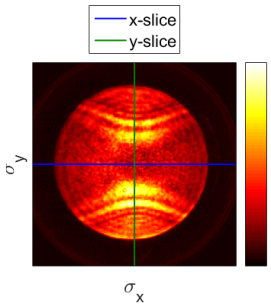	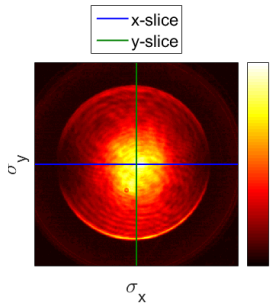	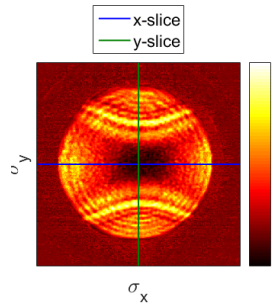
#R25/ 675 nm	linear-x	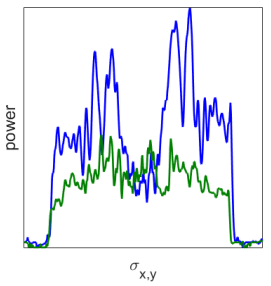	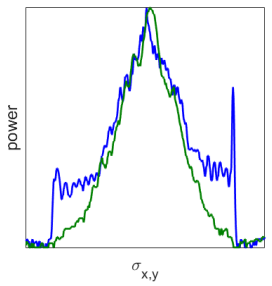	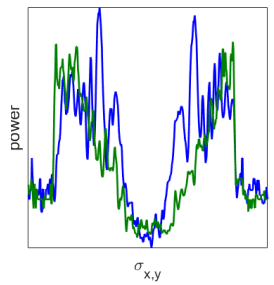
#R25/ 675 nm	linear-y	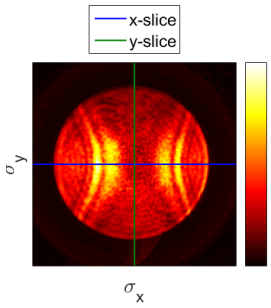	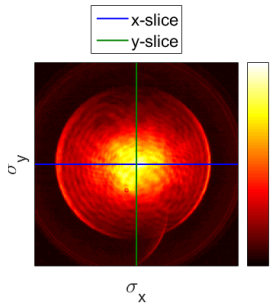	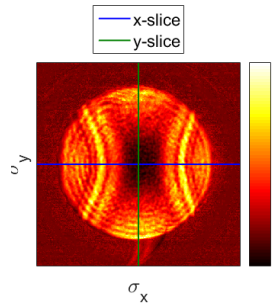
#R25/ 675 nm	linear-y	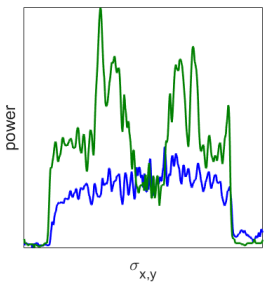	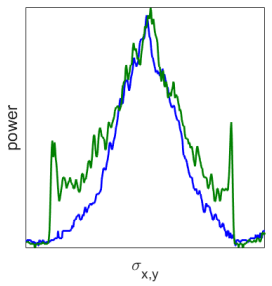	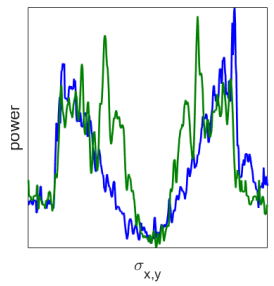

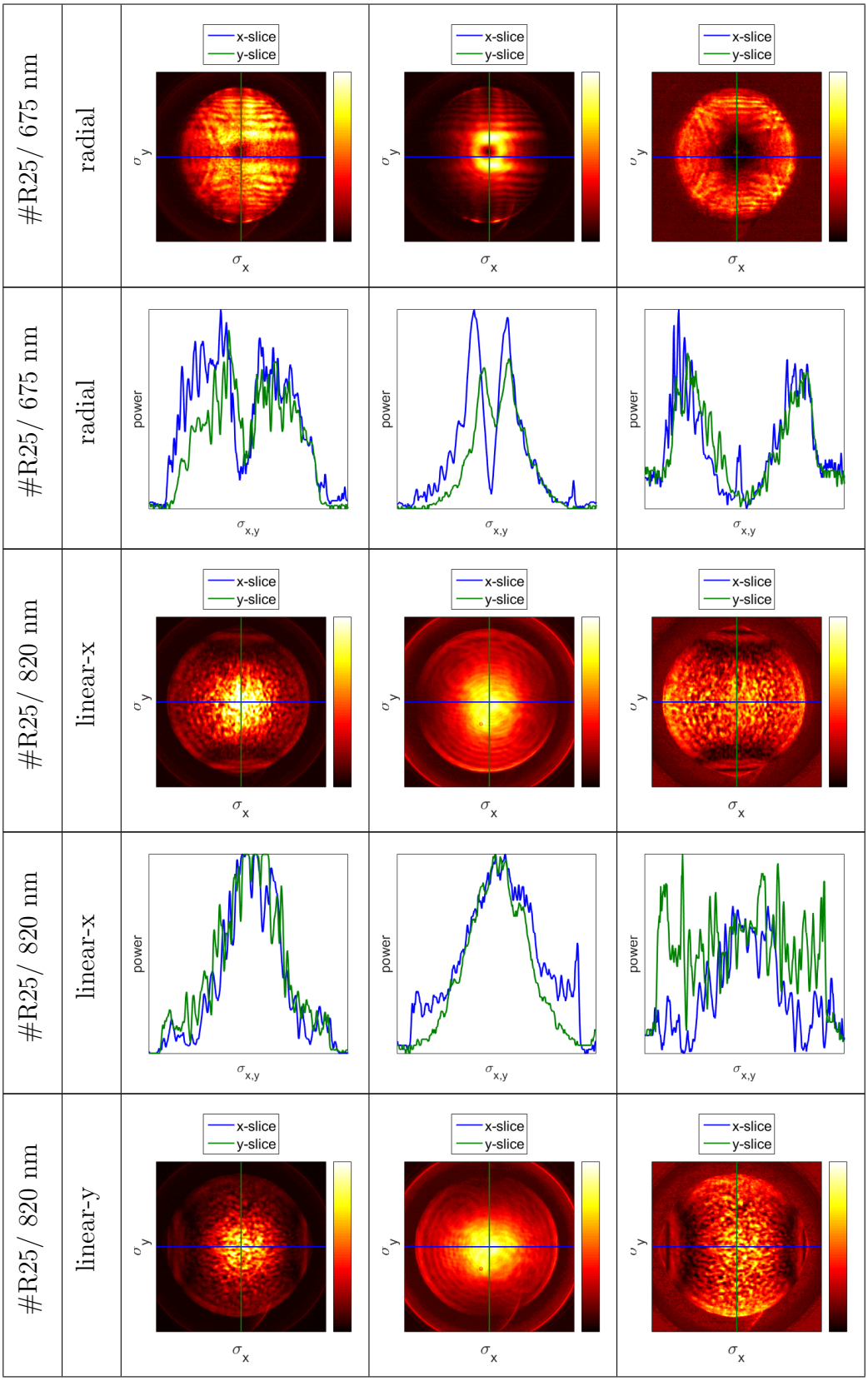
#R25/ 675 nm
radial
#R25/ 675 nm
radial
#R25/ 820 nm
linear-x
#R25/ 820 nm
linear-x
#R25/ 820 nm
linear-y
x-slice
y-slice
power
σx
σy
σx,y

#R25/ 820 nm	linear-y	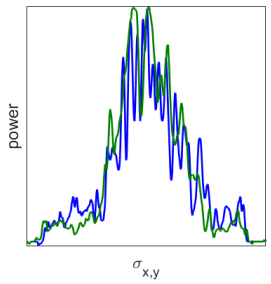	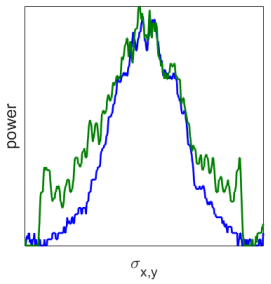	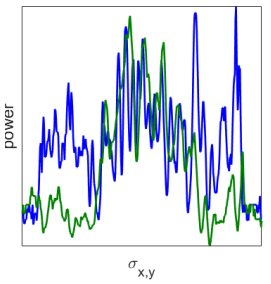
#R25/ 820 nm	radial	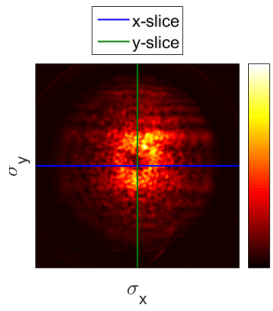	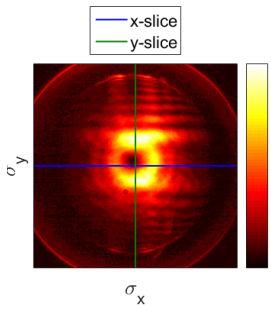	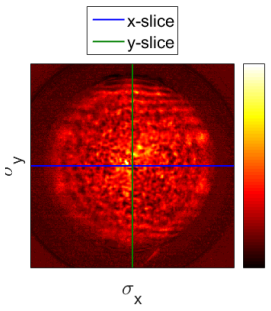
#R25/ 820 nm	radial	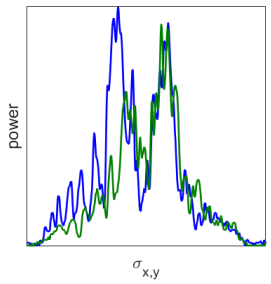	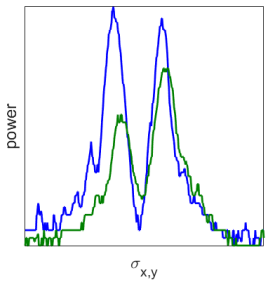	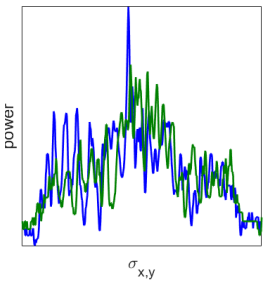

6. #R27, $\lambda_{rad} = 650$ nm, $\lambda_{dip} = 750$ nm

Code/ λ	Polarisation	Reflected Beam	Reference Beam	Normalised Reflected Beam
#R27/ 650 nm	linear-x	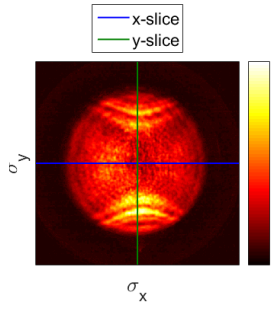	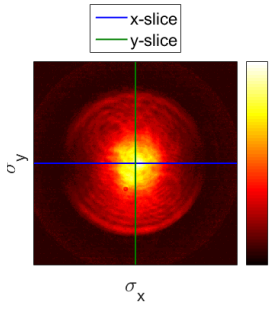	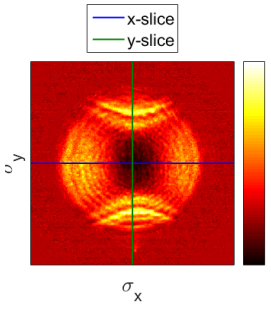

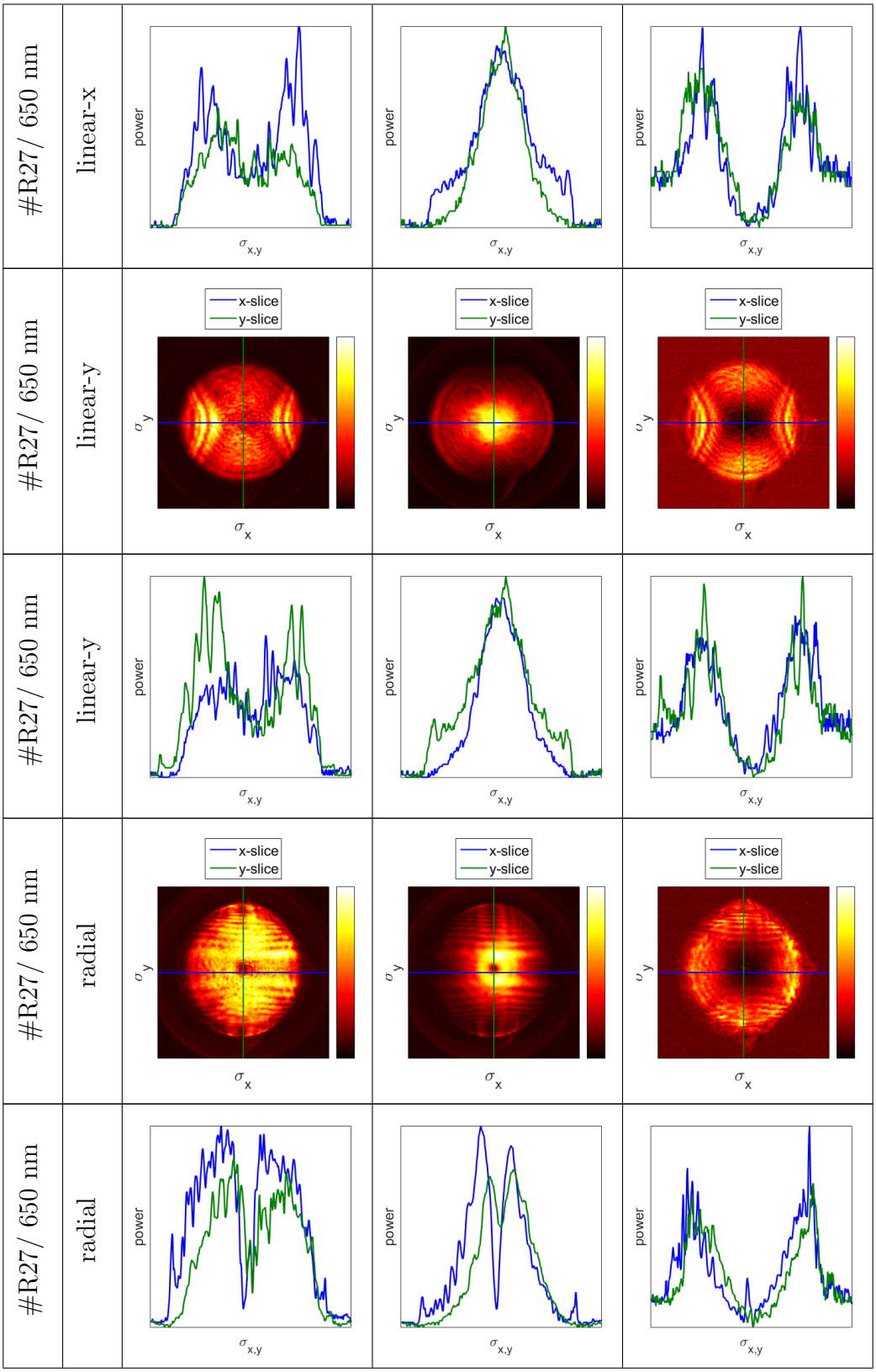
#R27/ 650 nm
linear-x
power
$\sigma_{x,y}$
#R27/ 650 nm
linear-y
x-slice
y-slice
σ_y
σ_x
#R27/ 650 nm
linear-y
power
$\sigma_{x,y}$
#R27/ 650 nm
radial
x-slice
y-slice
σ_y
σ_x
#R27/ 650 nm
radial
power
$\sigma_{x,y}$

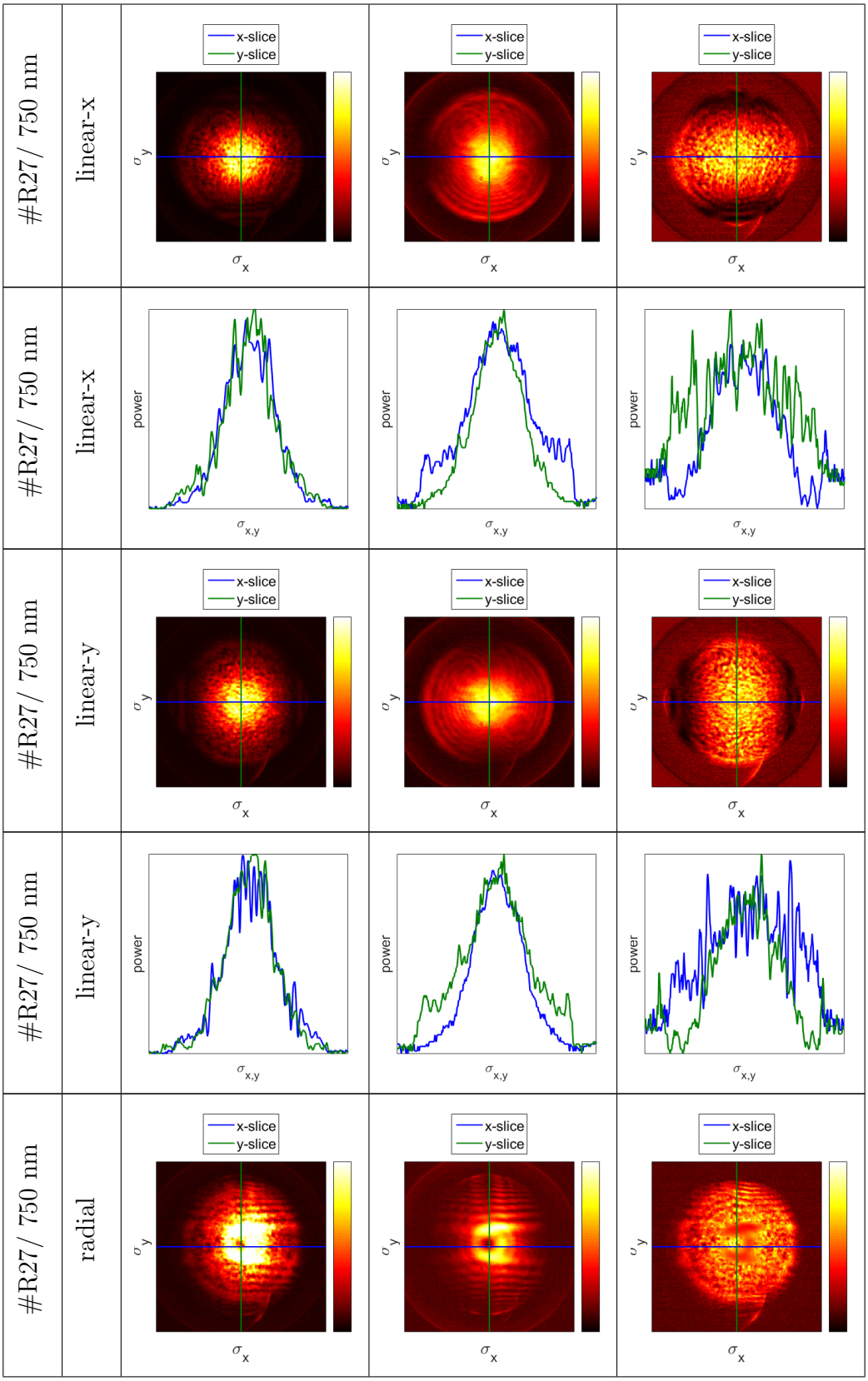
#R27/ 750 nm
linear-x
x-slice
y-slice
σ y
σ x
power
σ x,y
#R27/ 750 nm
linear-x
#R27/ 750 nm
linear-y
#R27/ 750 nm
linear-y
#R27/ 750 nm
radial

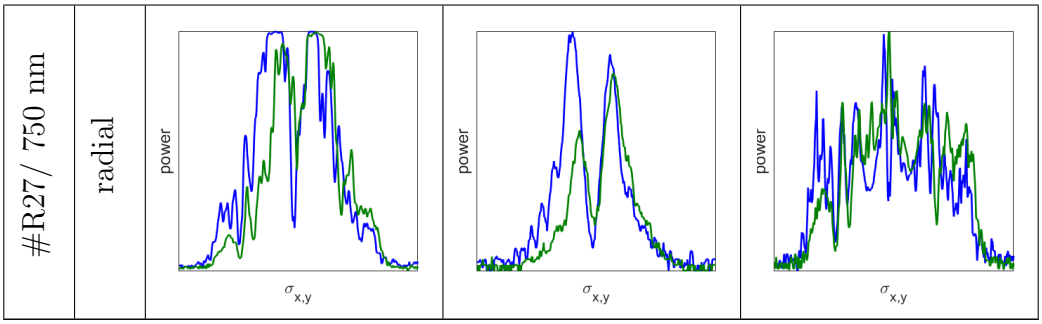

B.2 Beam Profiles at Various Wavelengths

1. #R13 with linearly polarised beam, $\lambda_{rad} = 620$ nm, $\lambda_{dip} = 750$ nm

a. Unnormalised reflection

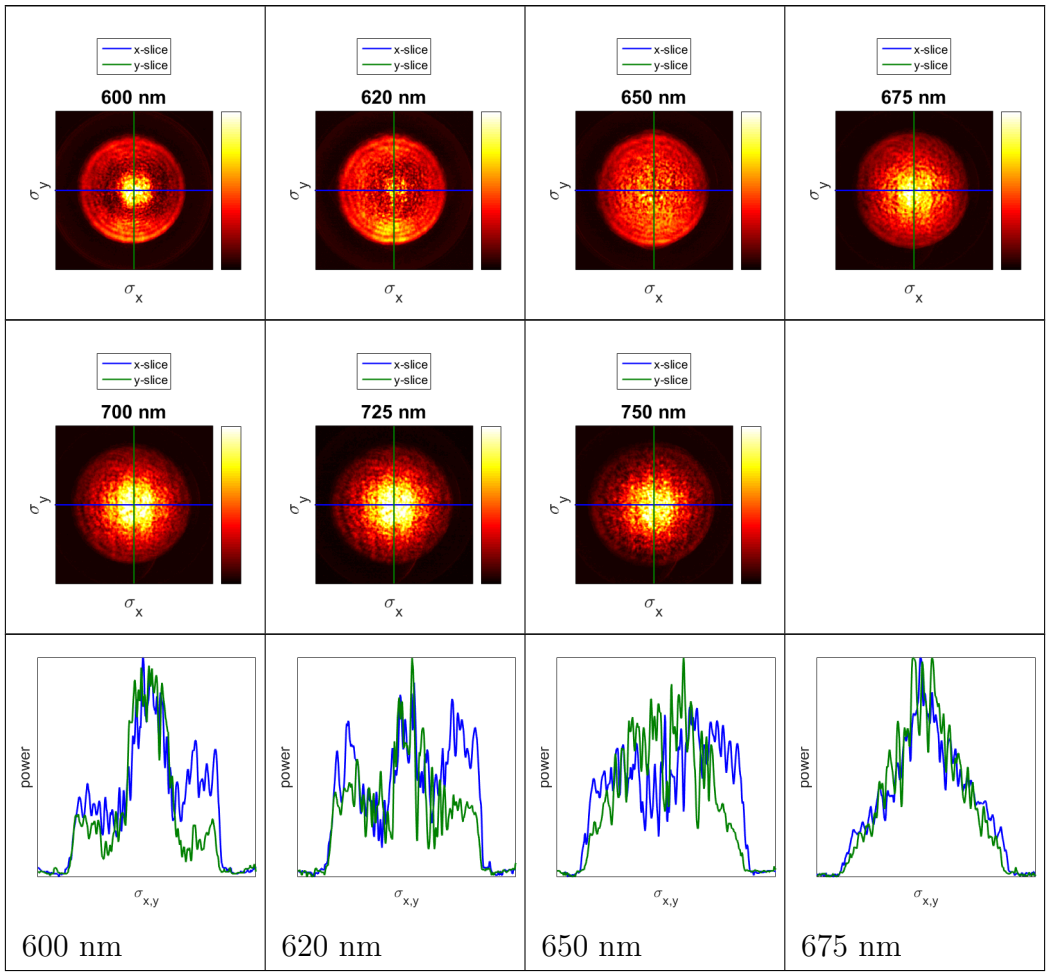

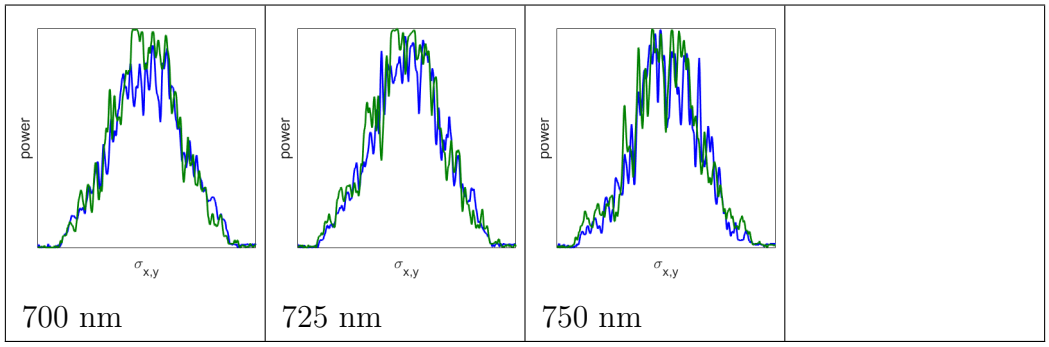

b. Normalised reflection

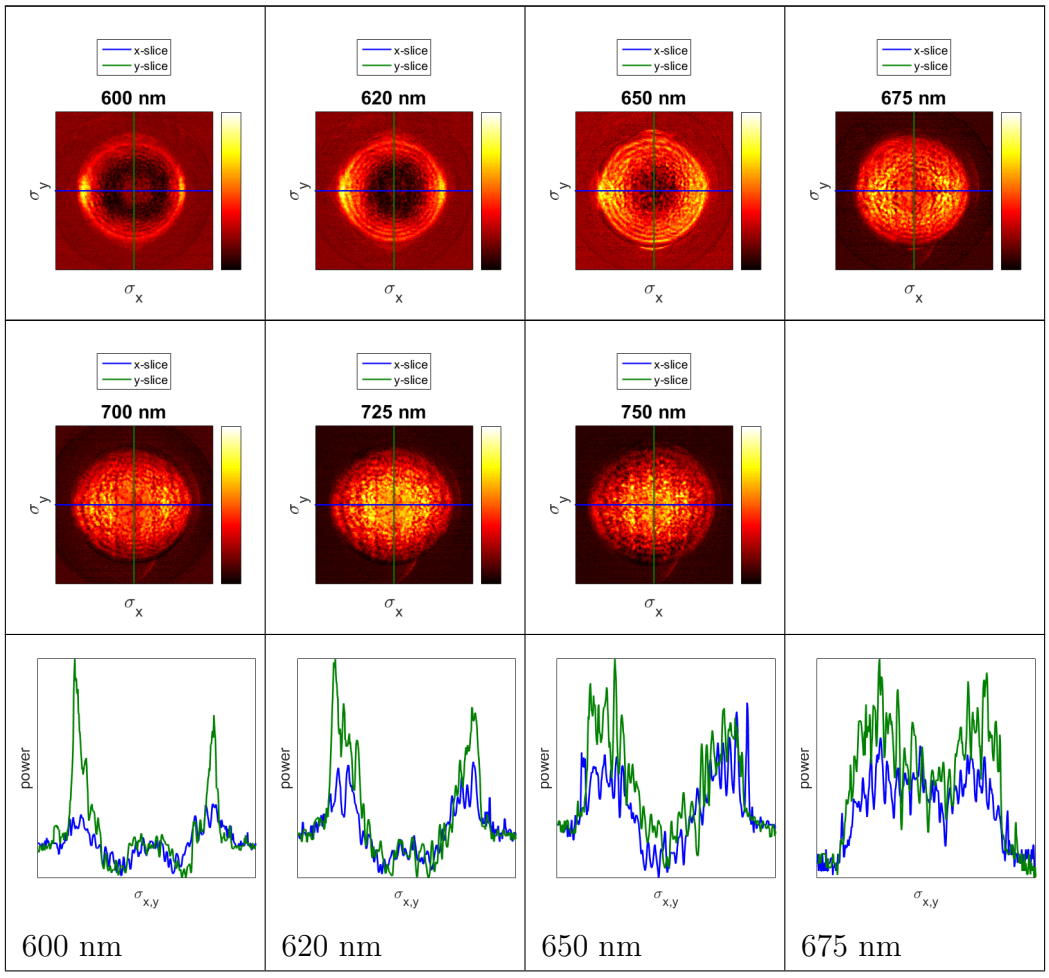

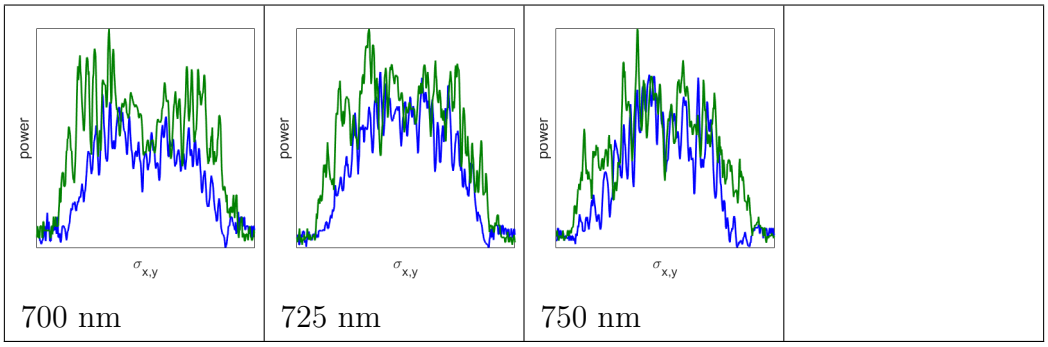

2. #R13 with radially polarised beam

a. Unnormalised reflection

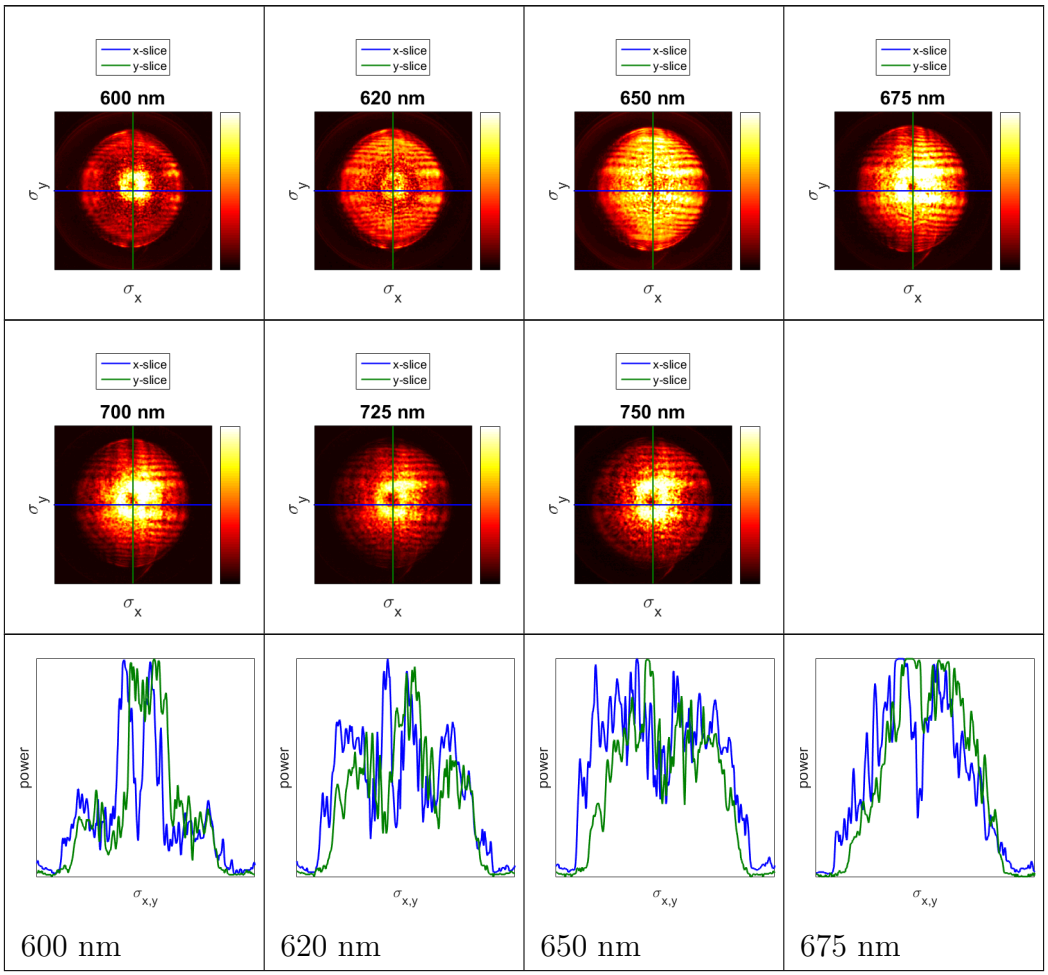

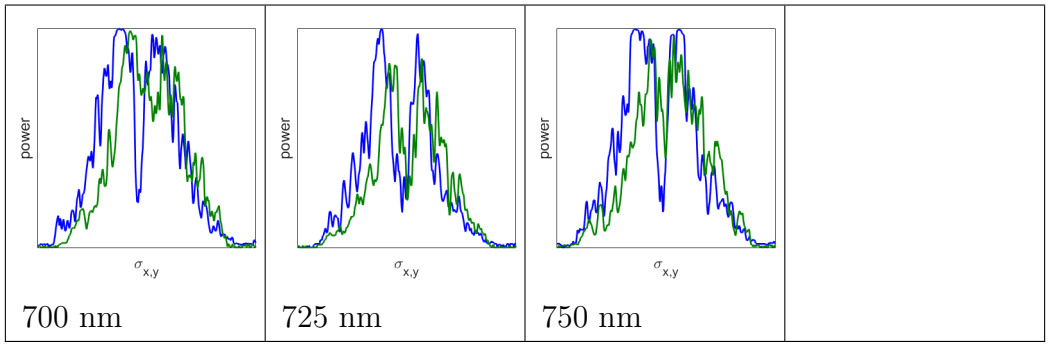

b. Normalised reflection

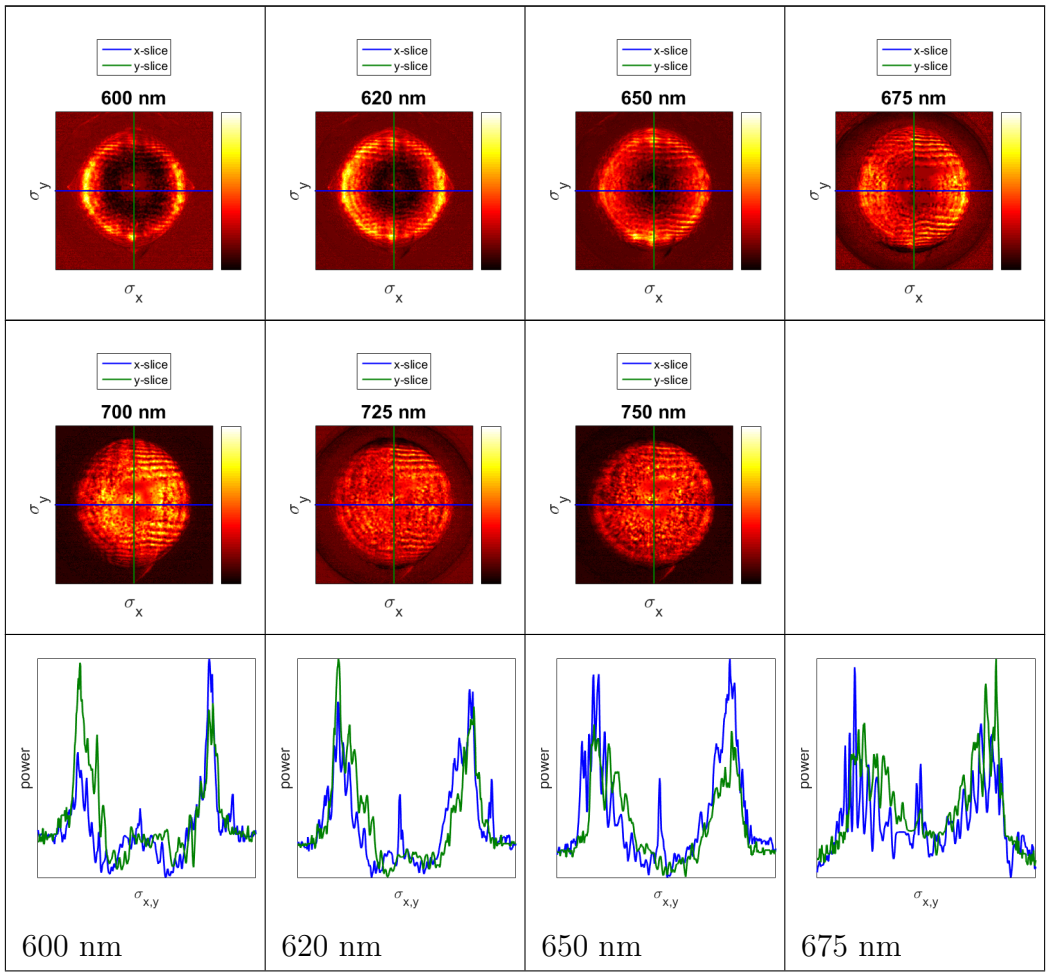

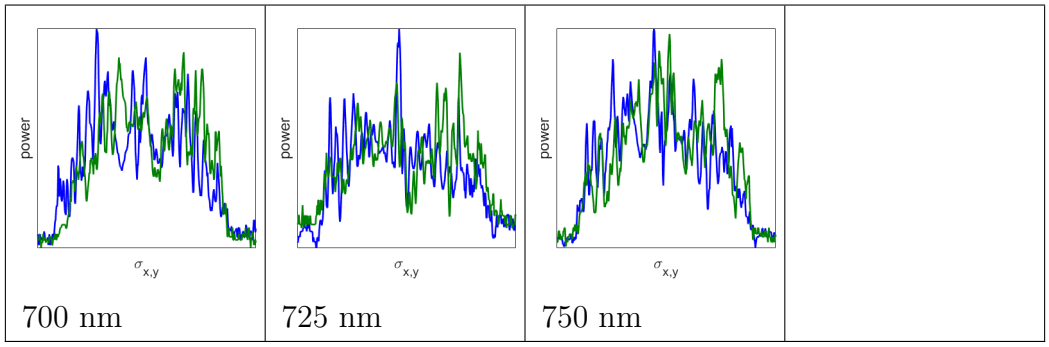

3. #R18 with linearly polarised beam

a. Unnormalised reflection

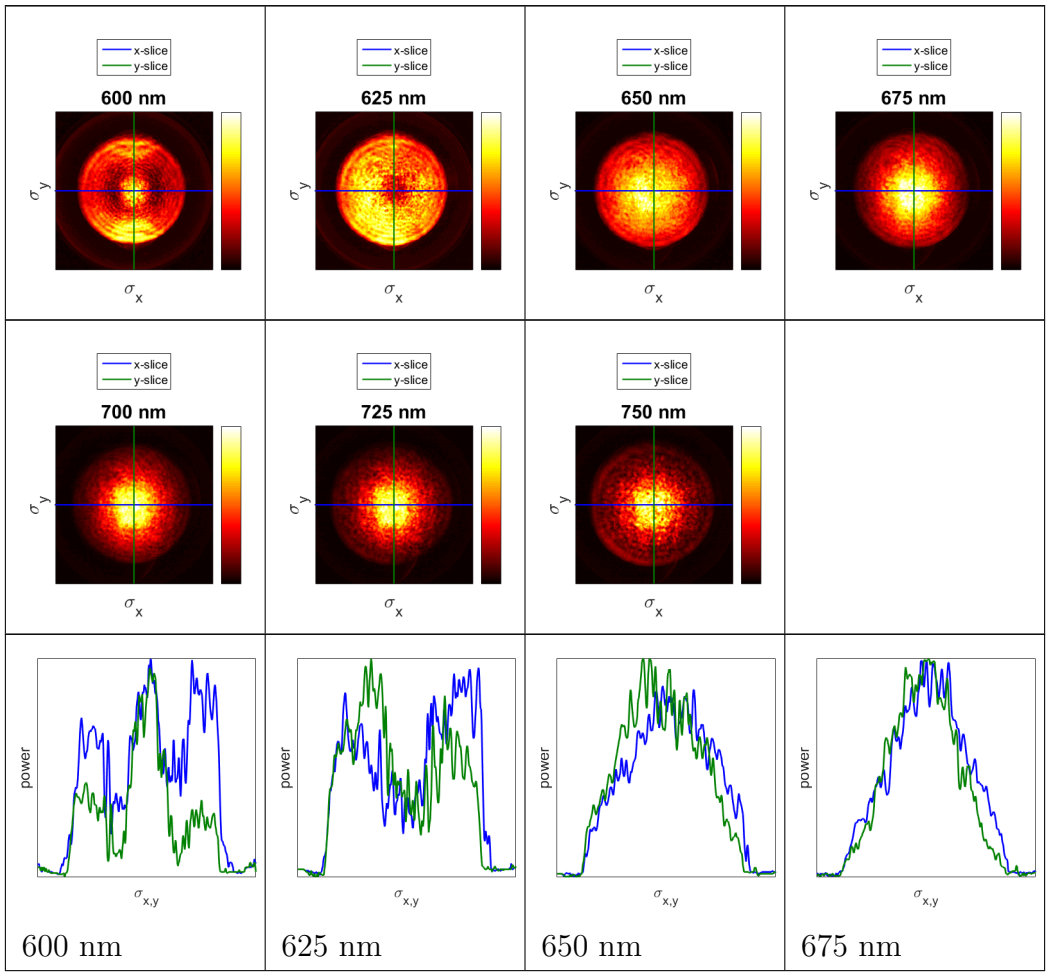

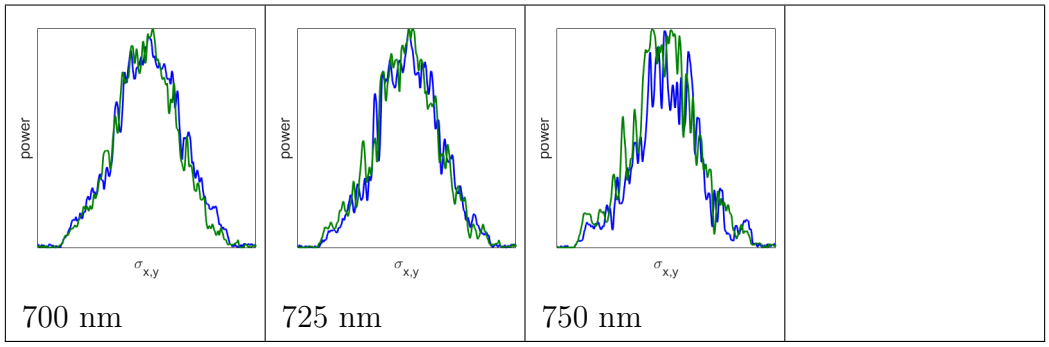

b. Normalised reflection

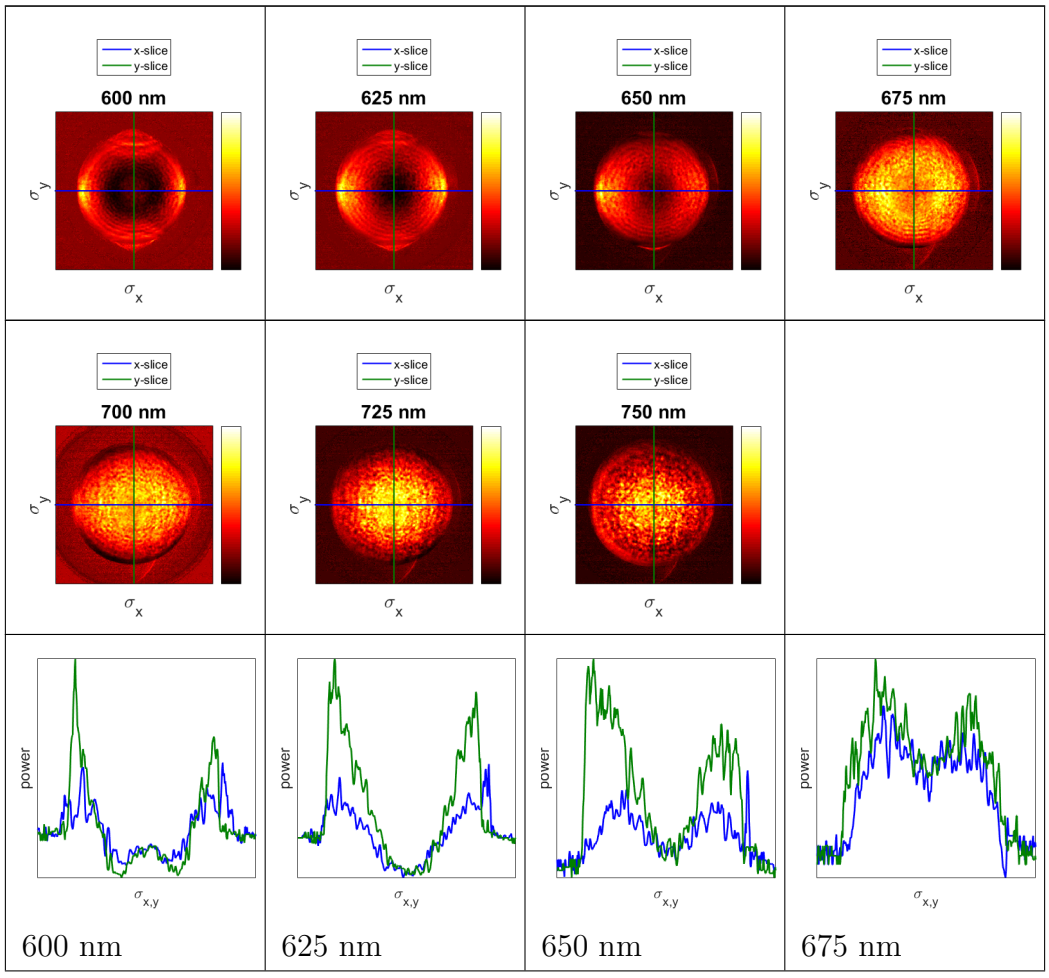

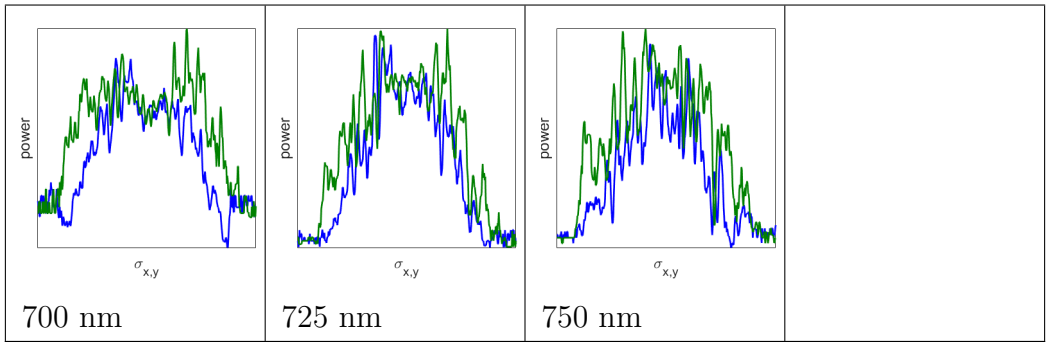

4. #R18 with radially polarised beam

a. Unnormalised reflection

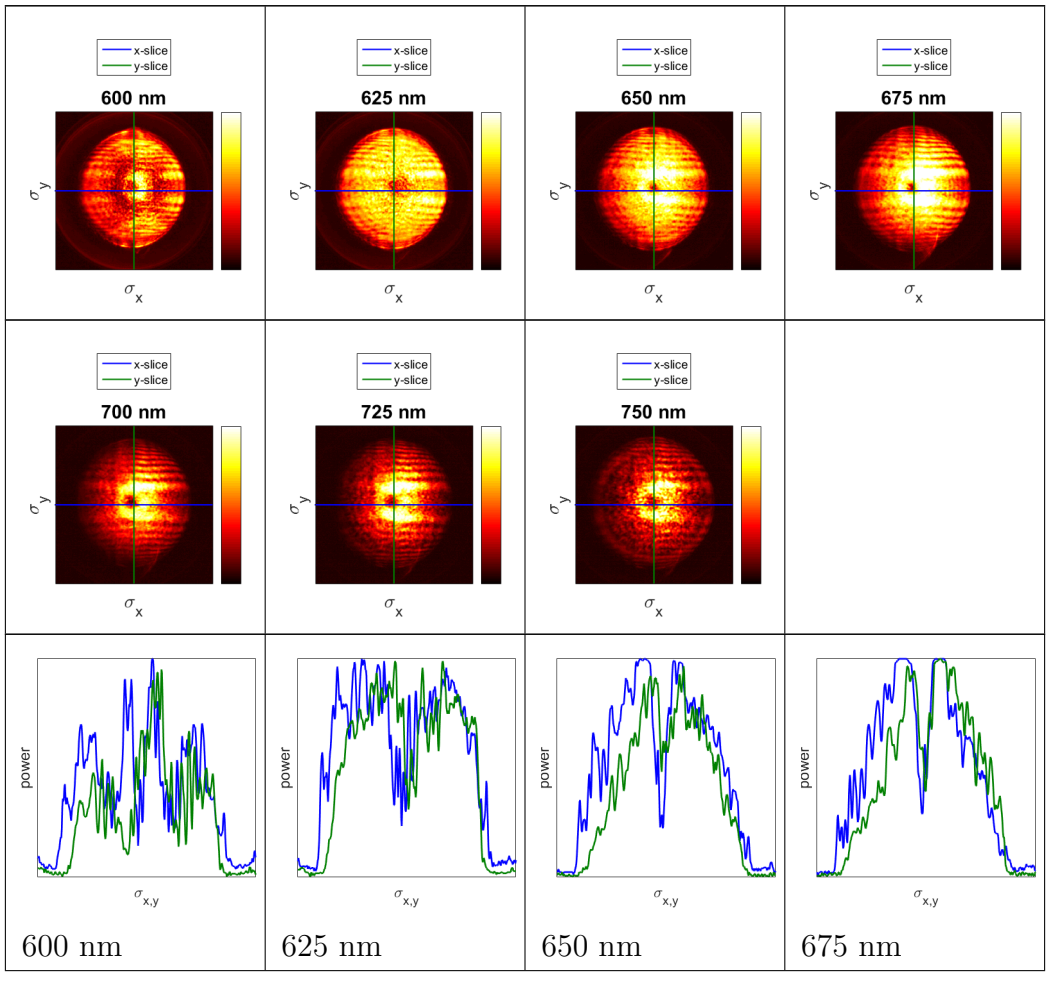

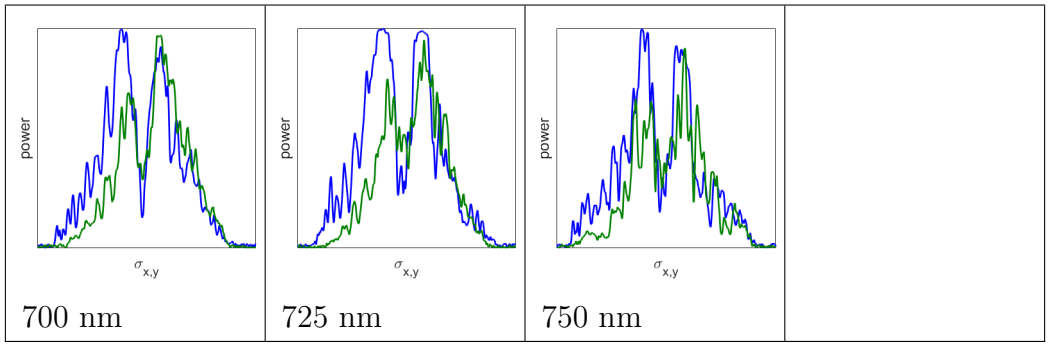

b. Normalised reflection

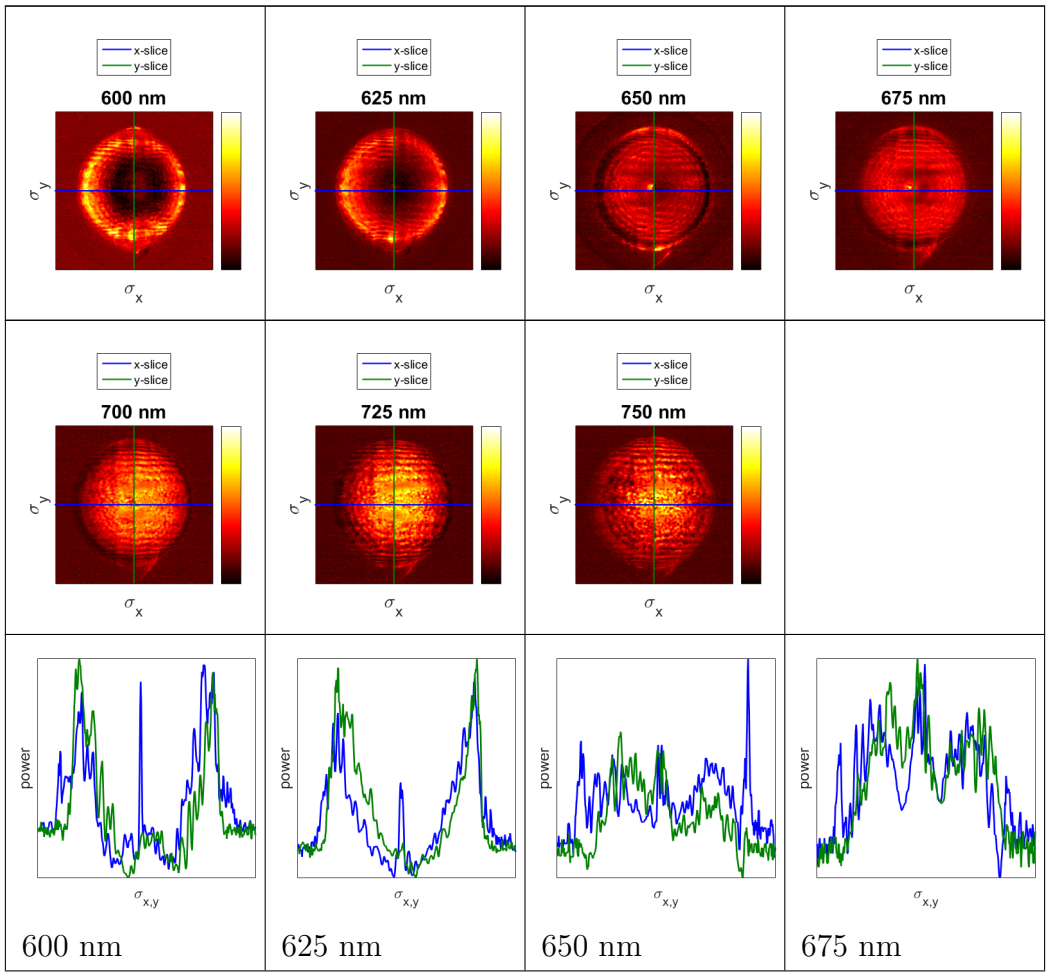

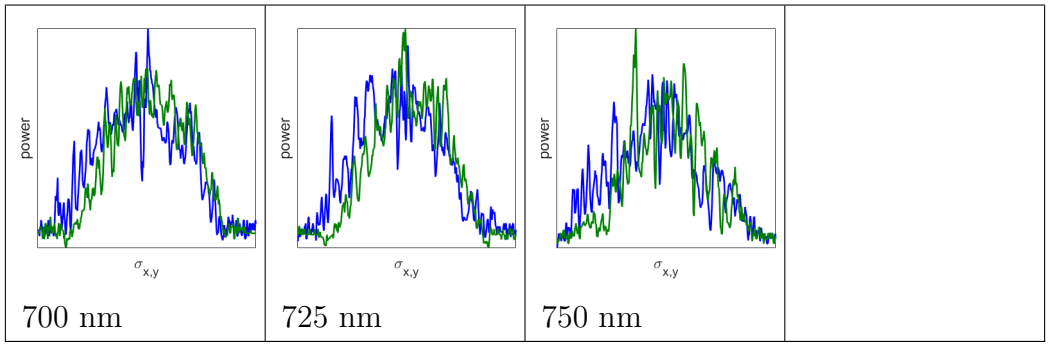

5. #R25 with linearly polarised beam

a. Unnormalised reflection

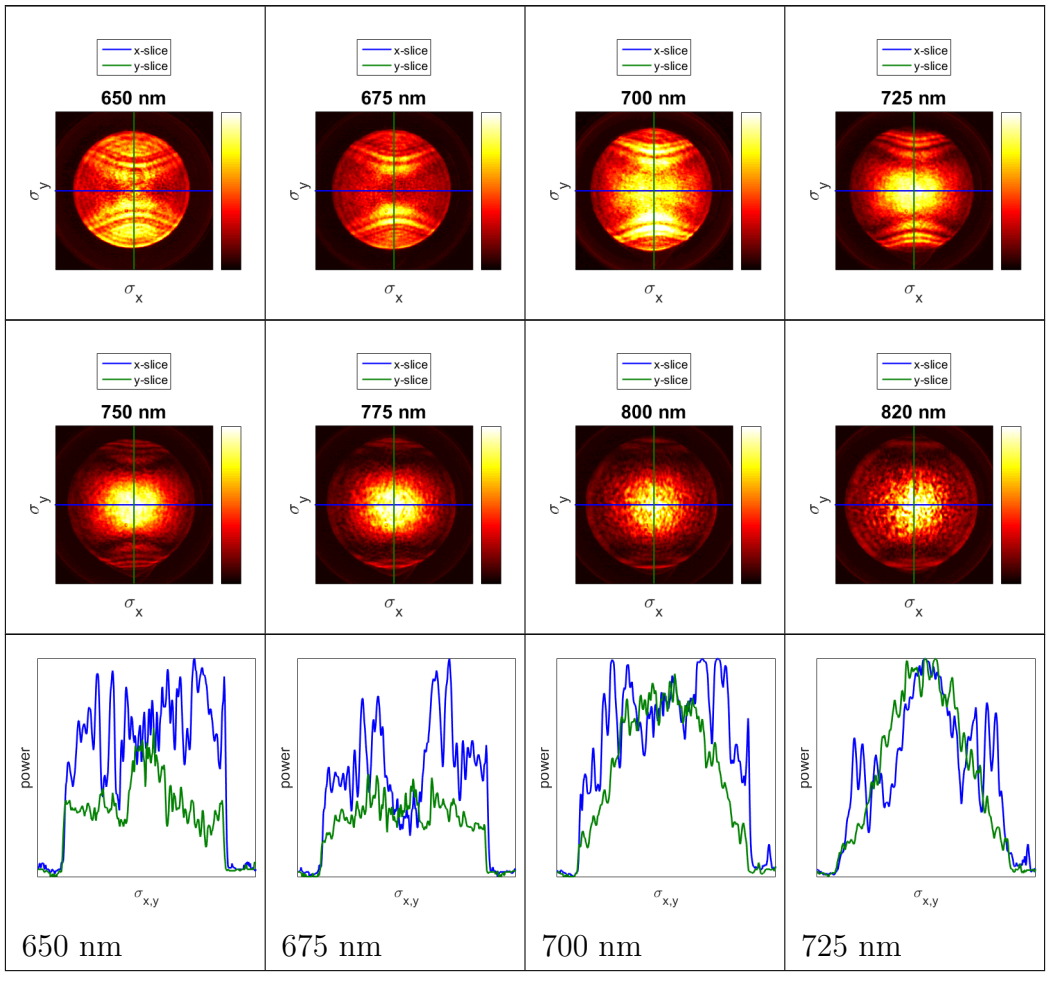

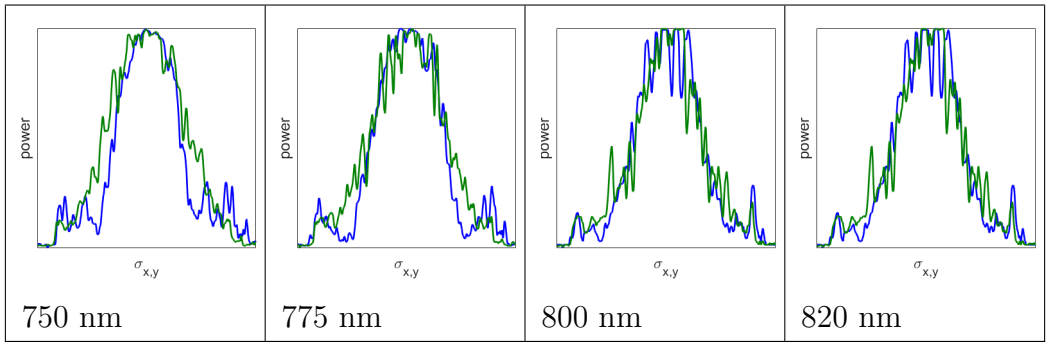

b. Normalised reflection

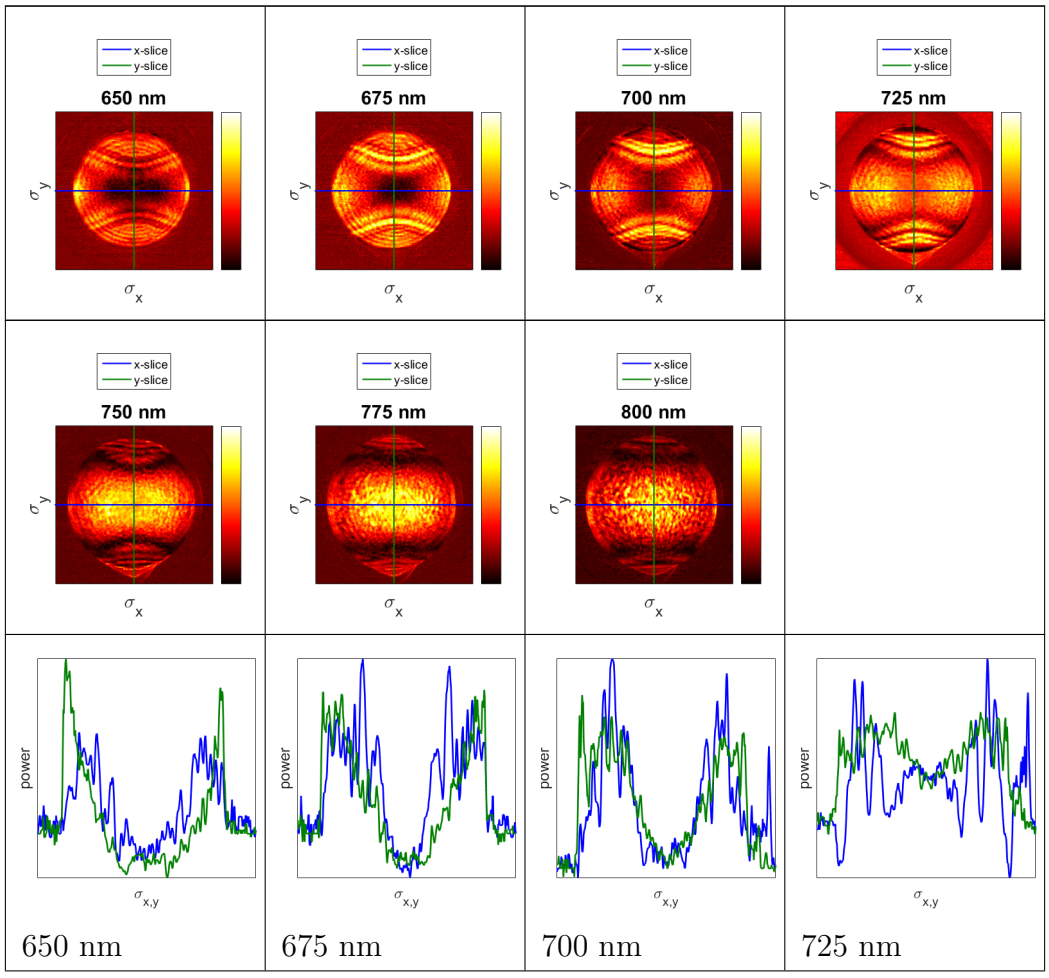

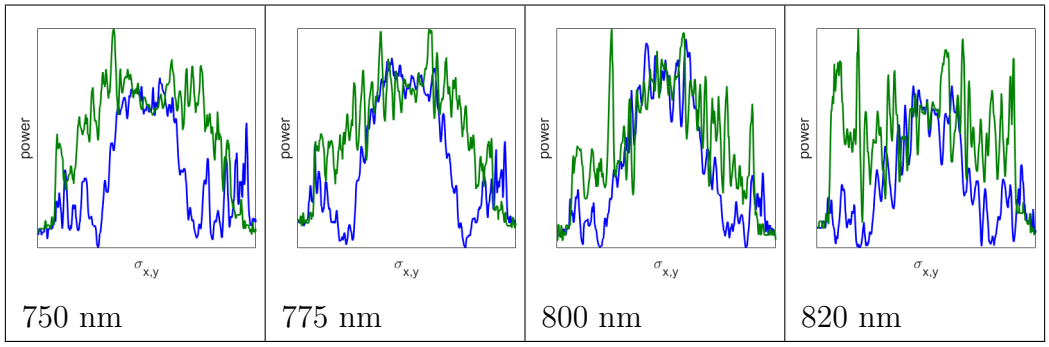

6. #R25 with radially polarised beam

a. Unnormalised reflection

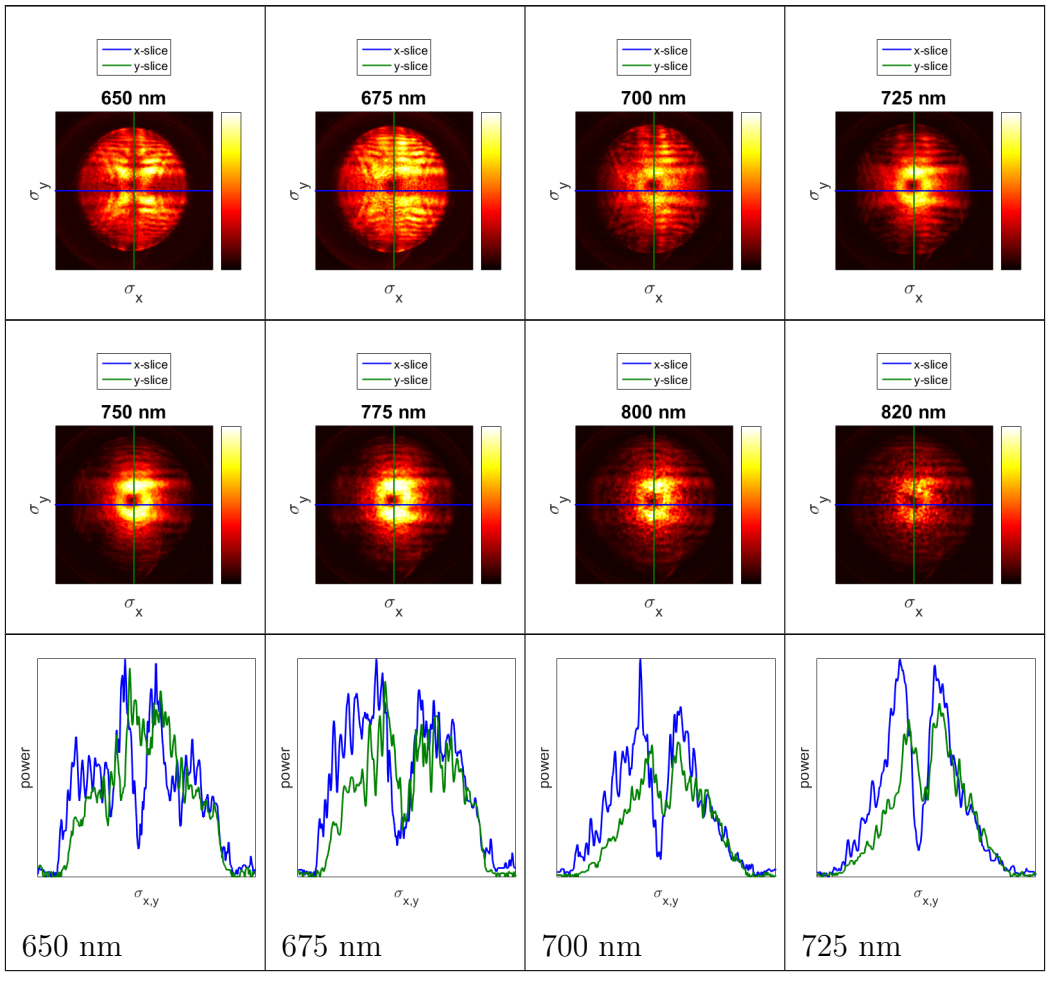

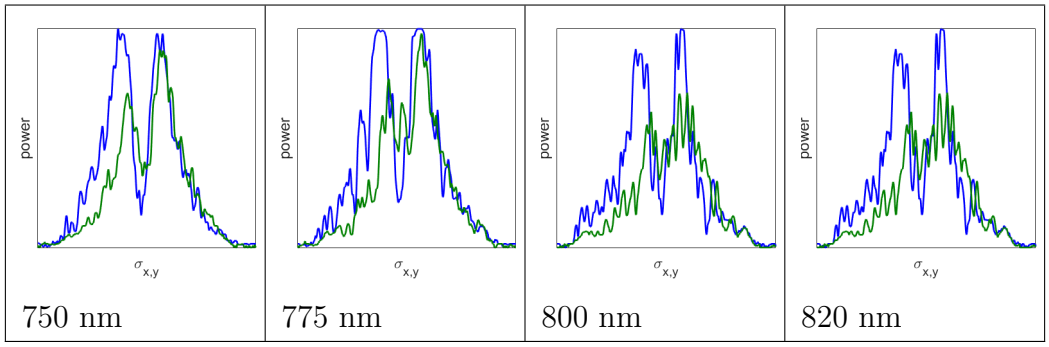

750 nm | 775 nm | 800 nm | 820 nm

b. Normalised reflection

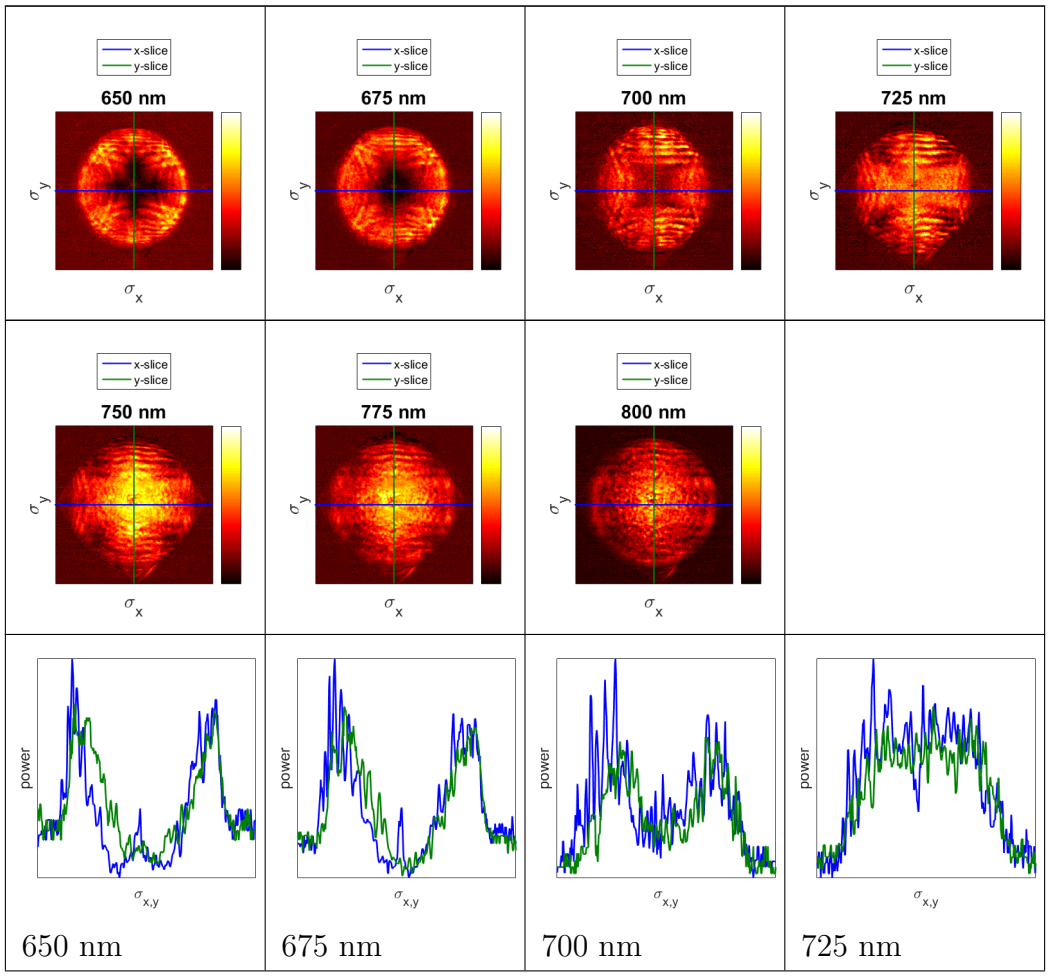

650 nm | 675 nm | 700 nm | 725 nm

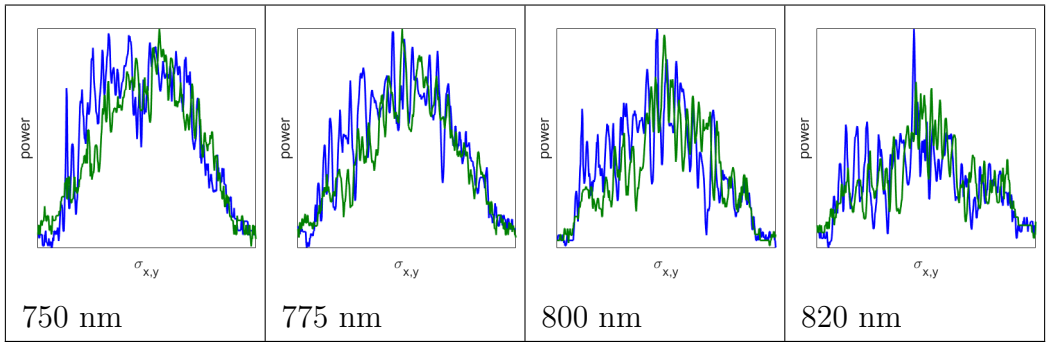
power
$\sigma_{x,y}$
750 nm
power
$\sigma_{x,y}$
775 nm
power
$\sigma_{x,y}$
800 nm
power
$\sigma_{x,y}$
820 nm